1225-0767(ISSN Print)
2287-6715(ISSN Online)
한국연구재단 우수등재학술지

Journal of Ocean Engineering and Technology

Vol. 35, No. 5 (Serial Number 162) October 2021

한국해양공학회지

KSOE

www.joet.org

KSOE The Korean Society of Ocean Engineers

Journal of Ocean Engineering and Technology
한국해양공학회지
Vol. 35 No. 5
(Serial Number 162)
October 31, 2021
www.JOET.org

Editorial Board

■ Editor-in-Chief

Joonmo Choung Inha University, Korea

■ Manuscript Editors

Hyeungsik Choi	Korea Maritime and Ocean University, Korea	**Sungwon Shin**	Hanyang University, Korea
Joon-Young Kim	Korea Maritime and Ocean University, Korea	**Woo Dong Lee**	Gyeongsang National University, Korea
Seokhwan Ahn	Jungwon University, Korea		

■ Editorial Board Members

Ahmet Ergin	Istanbul Technical University, Turkey	**Kwang-Jun Paik**	Inha University, Korea
Atilla Incecik	University of Strathclyde, UK	**Masashi Kashiwagi**	Osaka University, Japan
Beom-Seon Jang	Seoul National University, Korea	**Moo Hyun Kim**	Texas A&M University, USA
Bo Woo Nam	Seoul National University, Korea	**Narakorn Srini**	Newcastle University, UK
Chang Yong Song	Mokpo National University, Korea	**Norimi Mizutani**	Nagoya University, Japan
Chong Hyun Lee	Jeju National University, Korea	**Se-Min Jeong**	Chosun University, Korea
Do Kyun Kim	Seoul National University, Korea	**Seongim Choi**	Virginia Tech, USA
Dongho Jung	Korea Research Institute of Ships & Ocean Engineering, Korea	**Seung Min Park**	Hyein Engineering & Construction, Co., Ltd., Korea
Erkan Oterkus	University of Strathclyde, UK	**Soonchul Kwon**	Pusan National University, Korea
Geoffrey Lyons	BPP-TECH, UK	**Sungnam Hong**	Gyeongsang National University, Korea
Gökhan Tansel Tayyar	Istanbul Technical University, Turkey	**Sung-Woong Choi**	Gyeongsang National University, Korea
Gyusung Cho	Tongmyong University, Korea	**Taemin Ha**	Kangwon National University, Korea
Hee Jin Kang	Korea Research Institute of Ships & Ocean Engineering, Korea	**Taeseong Kim**	Loughborough University, UK
Hooi-Siang Kang	Universiti Teknologi Malaysia, Malaysia	**TaeSoon Kang**	GeoSystem Research Corp., Korea
Hyeon Kyu Yoon	Changwon National University, Korea	**Tak Kee Lee**	Gyeongsang National University, Korea
Hyun-Sik Kim	Tongmyong University, Korea	**Weoncheol Koo**	Inha University, Korea
Jinwhan Kim	Korea Advanced Institute of Science and Technology, Korea	**Yeon-Joong Kim**	Inje University, Korea
Jong Chun Park	Pusan National University, Korea	**Yong Uk Ryu**	Chonnam National University, Korea
Junbong Jang	Dong-A University, Korea	**Yoon Hyeok Bae**	Jeju National University, Korea
Kangsu Lee	Korea Research Institute of Ships & Ocean Engineering, Korea	**Younghun Kim**	Kyungnam University, Korea
Kideok Do	Korea Maritime and Ocean University, Korea	**Youngsub Lim**	Seoul National University, Korea
Kookhyun Kim	Tongmyong University, Korea		

Research and Publication Ethics Committee

■ Chair

Sung-Bu Suh Dongeui University, Korea

■ Research and Publication Ethics Committee Members

Han Koo Jeong	Kunsan National University, Korea	**Yong Uk Ryu**	Chonnam National University, Korea
Jinwhan Kim	Korea Advanced Institute of Science and Technology, Korea		

Published on October 31, 2021
Published by The Korean Society of Ocean Engineers (KSOE)
Room 1302, 13, Jungang-daero 180beon-gil, Dong-gu, Busan, 48821, Korea
TEL: +82-51-759-0656 FAX: +82-51-759-0657 E-mail: ksoehj@ksoe.or.kr URL: http://www.ksoe.or.kr
Printed by Hanrimwon Co., Ltd., Seoul, Korea E-mail: hanrim@hanrimwon.co.kr
ISSN(print) 1225-0767 **ISSN(online)** 2287-6715

This journal was supported by the Korean Federation of Science and Technology Societies (KOFST) grant funded by the Korean government.

© 2021 by The Korean Society of Ocean Engineers (KSOE)
This is an open access article distributed under the terms of the creative commons attribution non-commercial license (http://creativecommons.org/licenses/by-nc/4.0) which permits unrestricted non-commercial use, distribution, and reproduction in any medium, provided the original work is properly cited.

Journal of Ocean Engineering and Technology
한국해양공학회지

CONTENTS

Volume 35, Number 5 October, 2021

<Original Research Articles>

<Review Articles>

GENERAL INFORMATION

"Journal of Ocean Engineering and Technology" is the official journal published by "The Korean Society of Ocean Engineers (KSOE)". The ISO abbreviation is "J. Ocean Eng. Technol." and acronym is "**JOET**". It was launched in 1987. It is published bimonthly in February, April, June, August, October, and December each year. Supplement numbers are published at times.

Journal of Ocean Engineering and Technology (JOET) is a medium for the publication of original research and development work in the field of ocean engineering. JOET covers the entire range of issues and technologies related to the following topics:

Ships and offshore platforms: Design of marine structures; Resistance and propulsion; Seekeeping and maneuvering; Experimental and computational fluid dynamics; Ocean wave mechanics; Fatigue strength; Plasticity; Optimization and reliability; Arctic technology and extreme mechanics; Noise, vibration, and acoustics; Concrete engineering; Thermodynamics and heat transfer; Hydraulics and pneumatics;
Coastal civil engineering: Coastal structures; Port and harbor structures; Soil mechanics; Drilling and exploration; Hydraulics of estuary; Seismic engineering; Coastal disaster prevention engineering;
Ocean renewable energy platforms: Offshore wind turbines; Wave energy platforms; Tidal current energy platforms; Floating photovoltaic energy platforms;
Marine robots: Robot sensor system; Autonomous navigation; Robot equipments; Spatial information and communications; Underwater network; Design of underwater vehicles;
Multidisciplinary areas: Design for safety; IT-based design; IT-based production engineering; Welding mechanics; Control engineering; GPS and GIS; Inspection and sensor; Port and logistics; Leisure boat and deep see water; Offshore process systems engineering; Marine metallic materials; Marine organic materials; Marine Composite materials; Materials properties; Corrosion and Anti-corrosion; Tribology;

It contains original research articles, case reports, brief communications and reviews on technial issues. Conference papers, research papers, diploma papers and academic articles can be submitted.

All of the manuscripts are peer-reviewed. **JOET** has a system where two or more peer reviewers must review each submitted paper and it is operated very strictly.

JOET is an open access journal distributed under the terms of the creative commons attribution non-commercial license (http://creativecommons.org/licenses/by-nc/4.0). Therefore, all ocean engineers and researchers around the world can easily access all journal articles via the journal homepage (http://www.joet.org) and download the PDF-based original texts or view the web-based XML texts for free.

JOET is being indexed in some prominent database such as Korean Citatation Index (KCI), Google Scholar, Science Central, Korea Science and Directory of Open Access Journals (DOAJ).

For correspondences concerning business matters, author needs to contact KSOE Secretariat by email or phone (e-mail: ksoehj@ksoe.or.kr or Tel: +82 51 759 0656). Correspondences for publication matters can be asked via email to the Editor-in-Chief (email: heroeswise2@gmail.com).

Journal of Ocean Engineering and Technology 35(5), 313-326, October, 2021
https://doi.org/10.26748/KSOE.2021.063

pISSN 1225-0767
eISSN 2287-6715

Original Research Article

Evaluation of Dynamic Characteristics for a Submerged Body with Large Angle of Attack Motion via CFD Analysis

Myungjun Jeon[1], Thi Loan Mai[1], Hyeon Kyu Yoon[2], Jaekwan Ryu[3], Wonhee Lee[3] and Pyungmo Ku[4]

[1] *Ph.D. Candidante Student, Department, of Eco-friendly Offshore Plant FEED Engineering, Changwon National University, Korea*
[2] *Professor, Department, of Naval Architecture & Marine Engineering, Changwon National University, Korea*
[3] *Chief Researcher, LIG Nex1 Unmanned Systems R&D Laboratory, Korea*
[4] *Senior Researcher, LIG Nex1 Unmanned Systems R&D Laboratory, Korea*

KEY WORDS: Submerged body, Computational fluid dynamics, Large angle of attack, Virtual captive model tests, Maneuvering simulation

ABSTRACT: *A submerged body with varied control inputs can execute large drift angles and large angles of attack, as well as basic control such as straight movement and turning. The objective of this study is to analyze the dynamic characteristics of a submerged body comprising six thrusters and six control planes, which is capable of a large drift angle and angle of attack motion. Virtual captive model tests via were analyzed via computational fluid dynamics (CFD) to determine the dynamic characteristics of the submerged body. A test matrix of virtual captive model tests specialized for large-angle motion was established. Based on this test matrix, virtual captive model tests were performed with a drift angle and angle of attack of approximately 30° and 90°, respectively. The characteristics of the hydrodynamic force acting on the horizontal and vertical surfaces of the submerged body were analyzed under the large-angle motion condition, and a model representing this hydrodynamic force was established. In addition, maneuvering simulation was performed to evaluate the standard maneuverability and dynamic characteristics of large-angle motion. Considering the shape characteristics of the submerged body, we attempt to verify the feasibility of the analysis results by analyzing the characteristics of the hydrodynamic force when the large-angle motion occurred.*

Nomenclature

$O-xyz$	Earth-fixed coordinate
$o-x_b y_b z_b$	Body-fixed coordinate
U	Vehicle speed (m/s)
β	Drift angle (deg)
α	Angle of attack (deg)
u	Surge (axial) velocity (m/s)
v	Sway (lateral) velocity (m/s)
w	Heave (vertical) velocity (m/s)
p	Roll rate (deg/s)
q	Pitch rate (deg/s)
r	Yaw rate (deg/s)
δ_r	Rudder angle (deg)
δ_b	Bow plane angle (deg)
δ_s	Stern plane angle (deg)
$X_{\dot{u}}$	Derivative of X_{HD} with respect to $\dot{u}$
X_u	Derivative of X_{HD} with respect to u
$X_{u\|u\|}$	Derivative of X_{HD} with respect to $u\|u\|$
$X_{\delta_b\|\delta_b\|}$	Derivative of X_C with respect to $\delta_b\|\delta_b\|$
$X_{\delta_s\|\delta_s\|}$	Derivative of X_C with respect to $\delta_s\|\delta_s\|$
$X_{\delta_r\|\delta_r\|}$	Derivative of X_C with respect to $\delta_r\|\delta_r\|$
$Y_{\dot{v}}$	Derivative of Y_{HD} with respect to $\dot{v}$
$Y_{\dot{p}}$	Derivative of Y_{HD} with respect to $\dot{p}$
$Y_{\dot{r}}$	Derivative of Y_{HD} with respect to $\dot{r}$
Y_v	Derivative of Y_{HD} with respect to v
Y_p	Derivative of Y_{HD} with respect to p
Y_r	Derivative of Y_{HD} with respect to r
Y_{δ_r}	Derivative of Y_C with respect to δ_r
$Z_{\dot{w}}$	Derivative of Z_{HD} with respect to $\dot{w}$
$Z_{\dot{q}}$	Derivative of Z_{HD} with respect to $\dot{q}$
Z_w	Derivative of Z_{HD} with respect to w
Z_q	Derivative of Z_{HD} with respect to q

Received 20 July 2021, revised 31 July 2021, accepted 2 August 2021

Corresponding author Hyeon Kyu Yoon: +82-55-213-3683, hkyoon@changwon.ac.kr

Z_{δ_b}	Derivative of Z_C with respect to δ_b
Z_{δ_s}	Derivative of Z_C with respect to δ_s
$K_{\dot{v}}$	Derivative of K_{HD} with respect to $\dot{v}$
$K_{\dot{p}}$	Derivative of K_{HD} with respect to $\dot{p}$
$K_{\dot{r}}$	Derivative of K_{HD} with respect to $\dot{r}$
K_v	Derivative of K_{HD} with respect to v
K_p	Derivative of K_{HD} with respect to p
K_r	Derivative of K_{HD} with respect to r
K_{δ_r}	Derivative of K_C with respect to δ_r
$M_{\dot{w}}$	Derivative of M_{HD} with respect to $\dot{w}$
$M_{\dot{q}}$	Derivative of M_{HD} with respect to $\dot{q}$
M_w	Derivative of M_{HD} with respect to w
M_q	Derivative of M_{HD} with respect to q
M_{δ_b}	Derivative of M_C with respect to δ_b
M_{δ_s}	Derivative of M_C with respect to δ_s
$N_{\dot{v}}$	Derivative of N_{HD} with respect to $\dot{v}$
$N_{\dot{p}}$	Derivative of N_{HD} with respect to $\dot{p}$
$N_{\dot{r}}$	Derivative of N_{HD} with respect to $\dot{r}$
N_v	Derivative of N_{HD} with respect to v
N_p	Derivative of N_{HD} with respect to p
N_r	Derivative of N_{HD} with respect to r
N_{δ_r}	Derivative of N_C with respect to δ_r

1. Introduction

A submerged body refers to all vehicles operated in water, such as a remotely operated vehicles (ROVs), autonomous underwater vehicles (AUVs), underwater weapons, and submarines (Kim et al., 2012; Park et al., 2015). Different types of submerged bodies serve varying purposes in military or commercial applications. Because submerged bodies have distinct operational purposes, their dynamic characteristics must reflect their operational purpose, and their shapes must be designed to satisfy the required dynamic characteristics accordingly. Therefore, a submerged body must be developed with a suitable performance for each task and utilization (Jeon et al., 2017). In particular, it is difficult to monitor the state of a small submerged body with the human eye because it is often remotely controlled or autonomously driven, unlike vessels manned by humans. Therefore, the maneuverability of such a submerged body needs to be sufficiently examined during the design stage to ensure the adoption of an appropriate controller.

Studies based on experimental and analytical methods have been actively conducted on estimating the maneuverability of a submerged body. The most accurate maneuverability analysis in the design stage involves modeling the external force of maneuvering equations of motion that reflect the motion range and operational purpose of a submerged body and estimating the external force model coefficients by performing a captive model test in a towing tank. Bae and Sohn (2009) conducted a static test including a resistance test in a circular water channel for Manta-type unmanned underwater vehicles. The maneuvering equation of motion with six degrees of freedom for Manta-type unmanned underwater vehicles was established by combining certain damping coefficients determined via a static test with added mass and damping coefficients estimated theoretically, and then, maneuverability was analyzed. Kim et al. (2012) conducted a captive model test by installing a submerged body model in a large-scale controlled computerized planar motion carriage. In addition to stability analysis, resistance, static drift, static angle of attack, horizontal and vertical turning, and combined tests were performed to estimate a damping coefficient, excluding the added mass coefficient. Jung et al. (2014) estimated added mass and damping coefficients by performing a vertical planar motion mechanism test in a linear towing tank for an autonomous underwater glider. In addition, they modeled the equation of motion based on the estimated coefficients to be adopted as the plant model for a control simulation. Owing to the cylindrical shape of most submerged bodies, the roll hydrodynamic damping moment is relatively small, and it triggers a large rolling motion at a high speed if the rolling motion is not properly controlled. To estimate a rolling motion of a sensitive submerged body, Park et al. (2015) conducted a coning motion test to estimate the hydrodynamic derivative, which is related to rolling motion, and proposed a different coning motion test method. The aforementioned model test cases were conducted for submerged bodies with slender shapes, under the assumption that the drift angle and angle of attack were not large at the design speed; hence, additional research is required to reflect a large angle of attack motion.

Estimating the maneuverability of a submerged body via analytical methods can be divided into two categories. The simplest approach adopts an empirical formula. Yeo et al. (2006) deduced the effect of design factors on the stability of a submarine based on an empirical formula that assumes that the main body is a lift force generator, which they substituted with an equivalent wing. Jeon et al. (2017) analyzed the effects of shape design factors on the maneuverability of a submerged body. However, an empirical formula was used to establish a plant model for designing a controller and estimating a linear stability coefficient for stability analysis. Simulating the large attack angle motion and slow motion is limited because a nonlinear coefficient cannot be estimated. The other approach involves conducting virtual captive model tests based on computational fluid dynamics (CFD). Recently, estimating hydrodynamic derivatives by performing a CFD in the same condition as a captive model test conducted in a tank has been widely adopted, and the accuracy results are similar to that of a model test. Sung and Park (2015) conducted a CFD-based virtual captive model test for open merchant vessels, KCS (KRISO Container Ship) and KVLCC (KRISO Very Large Crude-oil Carrier) 1&2, and compared the accuracy with the free running model test results. In terms of accuracy, They produced outstanding results. Nguyen et al. (2018) calculated the hydrodynamic force acting on a full scale submarine using a CFD analysis based on the Reynolds-averaged Navier–Stokes equations (RANS), and estimated damping coefficients. Cho et al. (2020) performed a virtual captive model test using CFD for submarines equipped with an X-rudder and deduced results similar to an experimental outcome.

In general, a large attack angle motion needs to be considered in a case when a vessel is operated at a low speed when berthing at a port (Takashina, 1986; Yoon and Kim, 2005), or when lateral and vertical movements are free, such as in ROVs (Jeon et al., 2016). In this study, we analyze the dynamic characteristics of a submerged body equipped with six thrusters and six control panels. A submerged body with various control inputs has relatively more free motions than a slender-type submerged body comprising a rudder attached in the rear part, elevator, and thruster. Specifically, motions in large drift angles and large angles of attack are possible. Because the motions are in large drift angles and large angles of attack, the motion range needs to be set broadly to accurately estimate the hydrodynamic force in the analysis.

Maneuverability can be directly investigated if a virtual free-running model test is conducted using CFD; however, it requires a significant amount of computation resources, and the maneuvering equation of motion, which is a plant model used for designing controllers, cannot be determined. Therefore, a virtual captive model test was performed in this study via CFD analysis to analyze the dynamic characteristics of a submerged body with a large angle of attack motion. This method is more advantageous than a model test in terms of time and cost, and it is also more advantageous than a water vessel in terms of computation time because computation is performed in water instead of on a free surface.

Most previous studies first established a maneuvering mathematical model and then estimated maneuvering coefficients comprising the mathematic model in their analyses. However, it is challenging to establish a mathematical model when the force tendencies are not thoroughly examined, the correlation between forces and motions is difficult to predict, and the data available on the submerged body are insufficient. Therefore, this study first examined the tendency of forces by establishing the conditions of a virtual captive model test in which hydrodynamic forces including large angles of attack motion were estimated and then modeled the correlation between forces and motions.

2. Coordinate System and Test Conditions

2.1 Coordinate System

Fig. 1 presents a coordinate system comprising the Earth-fixed coordinate for expressing the motion trajectory, orientation angle, and a body-fixed coordinate for defining the equation of motion and external forces acting on a submerged body. All the symbols used in the equation of motion and coordinate system are in accordance with the symbolic notation defined by Fossen (2011).

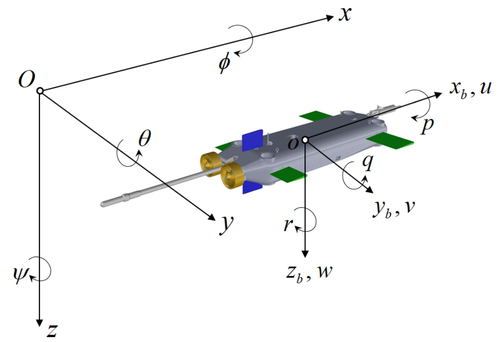

Fig. 1 Coordinate systems

2.2 Subject Submerged Body

Fig. 2 shows that the subject submerged body is equipped with two main thrusters in the rear part and four auxiliary thrusters for adjusting the depth, including a rudder for controlling directions, a bow plane for controlling depth, and a rear elevator. Here, six control inputs generate thrust and rudder force based on the large angle of attack and angle of attack motions that are possible. In addition, the principal parameters are presented in Table 1.

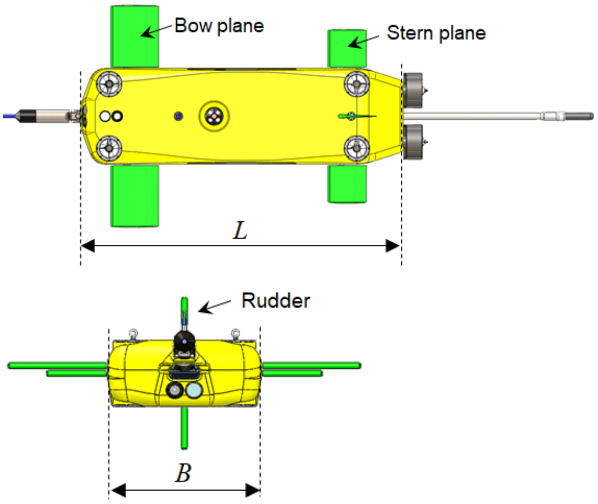

Fig. 2 Shape of a subject submerged body

Table 1 Principal parameters of the subject submerged body

Item (unit)	Symbol	Value
Length (m)	L	2.0
Beam (m)	B	0.6
Depth (m)	D	0.26
Volume (m^3)	$\bigtriangledown$	0.281
2-rudder area (m^2)	A_{rd}	0.03984
2-bow plane area (m^2)	A_{bp}	0.1158
2-stern plan area (m^2)	A_{sp}	0.0552
x-, y-, and z-axis Center of gravity (m)	$(x_g \quad y_g \quad z_g)$	(-0.082, 0.0, 0.0015)
x-, y-, and z-axis mass moment of inertia (kg·m^2)	$(I_{xx} \quad I_{yy} \quad I_{zz})$	(6.08, 65.49, 69.82)

2.3 Test Conditions

The conditions of the virtual captive model tests were configured, as presented in Table 2. Provided the CFD analysis is performed under the conditions in Table 2, all maneuvering coefficients can be obtained, excluding the coefficient related to thrust. All test conditions except a resistance test are applied with a design speed of 2.57 m/s (5 knots). Because there are two main thrusters attached in the rear part, yawing moment can be generated via steering and by thrust. Therefore, the submerged body may have a higher circular angular velocity than a submerged body that simply turns by steering, and the drift angle may also be larger because the circular angular velocity and drift angle are linked. Accordingly, a drift angle of approximately ±30° is considered when conducting a static drift test, as well as a dimensionless angular velocity of approximately 0.6. For self-propulsion, four auxiliary thrusters are attached to the hull, in addition to the main thrusters, and thrust can be freely generated in the vertical direction. Computation conditions were established considering an angle of attack of approximately ±90° because heave motions were realized by auxiliary thrusters. Hydrodynamic forces were computed using ANSYS FLUENT version 20.1, which is a commercial CFD analysis program. The analysis conditions adopted are presented in Table 3, and Fig. 3 illustrates the results obtained from mesh generation.

Table 2 Calculation matrix of virtual captive model tests

Test type	Motion variables
Resistance test	U = 1.03, 1.54, 2.06, 2.57, 3.09, 3.60 m/s (2.0, 3.0, 4.0, 5.0, 6.0, 7.0 knot)
Static drift test	β = ±2°, ±4°, ±6°, ±8°, ±10°, ±12°, ±15°, ±20°, ±25°, ±30°
Static angle of attack test	α = ±2°, ±4°, ±6°, ±8°, ±10°, ±12°, ±15°, ±20°, ±25°, ±30°, ±40°, ±50°, ±60°, ±70°, ±80°, ±90°
Horizontal circular motion test	r' = ±0.2, ±0.3, ±0.4, ±0.5, ±0.6
Vertical circular motion test	q'= ±0.2, ±0.3, ±0.4, ±0.5, ±0.6
Horizontal circular motion with drift test	β = ±2°, ±4°, ±6°, +8°, +10°, +12° r' = 0.2, 0.3, 0.4, 0.5
Vertical circular motion with angle of attack test	α = ±2°, ±4°, ±6°, -8°, -10°, -12° q' = 0.2, 0.3, 0.4, 0.5
Static rudder test	δ_r = ±3°, ±6°, ±9°, ±12°, ±15°, ±18°, ±21°
Static elevator test (bow plane)	δ_b = ±3°, ±6°, ±9°, ±12°, ±15°, ±18°, ±21°
Static elevator test (stern plane)	δ_s = ±3°, ±6°, ±9°, ±12°, ±15°, ±18°, ±21°
Roll rotating test	p' = 0.4, 0.5, 0.6, 0.7
Pure sway test	$\dot{v}'$ = 0.08, 0.16, 0.24, 0.32
Pure yaw test	$\dot{r}'$ = 0.29, 0.52, 0.76, 1.02
Pure heave test	$\dot{w}'$ = 0.08, 0.16, 0.24, 0.32
Pure pitch test	$\dot{q}'$ = 0.29, 0.52, 0.76, 1.02
Pure roll test	$\dot{p}'$ = 7.2, 14.3, 21.5, 28.6, 35.8

Table 3 Analytic methods and conditions for CFD calculation

Item	Description
Turbulence model	$k-\omega$ model
Algorithm	Semi-implicit method for pressure-linked equations (SIMPLE)
Interpolation method for pressure	Second order upwind
Number of elements	7,070,460
Number of nodes	1,309,828
Type of mesh	Tetrahedral unstructured mesh, Prism layer mesh (near hull surface)

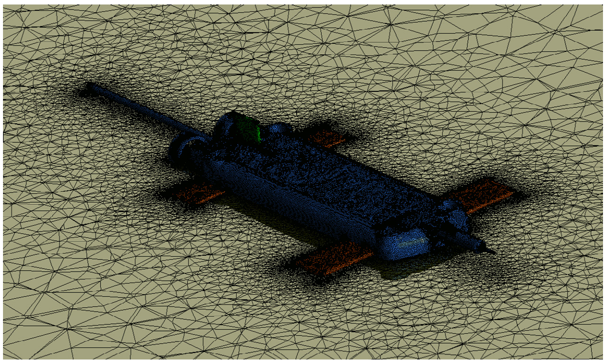

Fig. 3 Mesh generation

The $k-\omega$ model is widely used to predict hydrodynamic forces applied on maneuvering ships (Quérard et al., 2008). The $k-\omega$ model for hydrodynamic derivatives is advantageous in terms of its CPU computation time. Because CFD calculations under several conditions are required in this study, the $k-\omega$ model was selected as the turbulence model. A 3D incompressible viscous flow was assumed, and a continuity equation and RANS equations were applied as governing equations (Jeon et al., 2016). The convection term was applied with the second-order upwind method, diffusion term was discretized using a second-order central differential method, and pressure and speed were linked by the semi-implicit method for pressure-linked equations (SIMPLE).

3. Analysis Results and Modeling

3.1 Static Test

A static test estimates damping coefficients by calculating the damping force contributing to the speed of the hull and the rotation of a control plane, and it comprises resistance, static drift, static angle of attack, combined, static rudder, and static elevator tests. Details on the hydrodynamic force model of each test are presented in Table 4. The hydrodynamic force model was divided into two: a linear model in which the linearization of the force is possible because the size of perturbed state variables is small and a nonlinear model considering the nonlinearity of the force generated as motions become greater.

The results of the resistance test for estimating resistance per speed are presented in Fig. 4. When neutral buoyancy is assumed as the force proportional to the square of the advanced speed, approximately 9.8% of dead weight is assumed to be applied in the design speed. Here, dead weight refers to the product of the acceleration of gravity and the mass of the submerged body. Resistance is proportional to the square of the advanced speed, and the resistance applied on the hull can be linearized if the change in the speed is negligible, based on a design speed of 2.57 m/s (5 knots). Accordingly, Fig. 4 presents the results of the curve approximation of both linear and nonlinear models.

A static drift test calculates the damping force applied when only the sway velocity is generated; the results obtained from calculating the force by adjusting the drift angle by ±30° are presented in Fig. 5. Nondimensionalization complies with the prime system 1 defined by the Society of Naval Architecture and Marine Engineering (SNAME) (Fossen, 2011). The hydrodynamic forces were modeled according to the tendency of forces. The nonlinear model presented in Table 3 was considered appropriate, and the coefficient of determination R^2 was

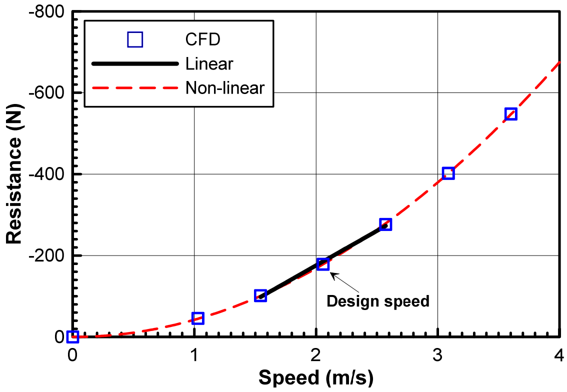

Fig. 4 Result of resistance tests

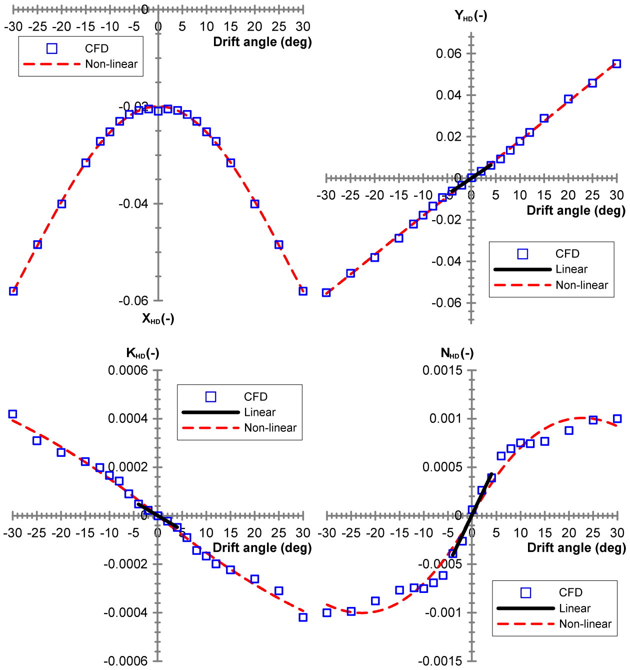

Fig. 5 Results obtained from static drift tests

Table 4 Static hydrodynamic force model for hull motion variables

Test type	Model	Formulae	R^2
Resistance	Linear	$X_{HD}=X_0+X_u u$	$R_X^2=0.9868$
	Non-linear	$X_{HD}=X_0+X_{u\lvert u\rvert}u\lvert u\rvert$	$R_X^2=0.9999$
Static drift	Linear	$\begin{cases} X_{HD}=X_0 \\ Y_{HD}=Y_0+Y_v v \\ K_{HD}=K_0+K_v v \\ N_{HD}=N_0+N_v v \end{cases}$, -4°<$\beta$<4°	$R_Y^2=0.9983$ $R_K^2=0.9904$ $R_N^2=0.9771$
	Non-linear	$\begin{cases} X_{HD}=X_0+X_{vv}v^2+X_{vvvv}v^4 \\ Y_{HD}=Y_0+Y_v v+Y_{v\lvert v\rvert}v\lvert v\rvert \\ K_{HD}=K_0+K_v v+K_{v\lvert v\rvert}v\lvert v \\ N_{HD}=N_0+N_v v+N_{v\lvert v\rvert}v\lvert v \end{cases}$	$R_X^2=0.9969$ $R_Y^2=0.9999$ $R_K^2=0.9929$ $R_N^2=0.9846$
Static angle of attack	Linear	$\begin{cases} X_{HD}=X_0 \\ Z_{HD}=Z_0+Z_w w \\ M_{HD}=M_0+M_w w \end{cases}$, -4°<$\alpha$<4°	$R_Z^2=0.9863$ $R_M^2=0.9968$
	Non-linear	$\begin{cases} X_{HD}=X_0+X_{ww}w^2+X_{wwww}w^4 \\ Z_{HD}=Z_0+Z_w w+Z_{w\lvert w\rvert}w\lvert w\rvert \\ M_{HD}=M_0+M_w w+M_{w\lvert w\rvert}w\lvert w\rvert \end{cases}$	$R_X^2=0.9193$ $R_Z^2=0.9988$ $R_M^2=0.9758$
Horizontal circular motion	Linear	$\begin{cases} X_{HD}=X_0 \\ Y_{HD}=Y_0+Y_r r \\ K_{HD}=K_0+K_r r \\ N_{HD}=N_0+N_r r \end{cases}$, $r'<0.3$	$R_Y^2=0.9988$ $R_K^2=0.9987$ $R_N^2=0.9998$
	Non-linear	$\begin{cases} X_{HD}=X_0+X_{rr}r^2 \\ Y_{HD}=Y_0+Y_r r+Y_{r\lvert r\rvert}r\lvert r\rvert \\ K_{HD}=K_0+K_r r+K_{r\lvert r\rvert}r\lvert r\rvert \\ N_{HD}=N_0+N_r r+N_{r\lvert r\rvert}r\lvert r\rvert \end{cases}$	$R_X^2=0.9810$ $R_Y^2=0.9966$ $R_K^2=0.8696$ $R_N^2=0.9900$
Vertical circular motion	Linear	$\begin{cases} X_{HD}=X_0 \\ Z_{HD}=Z_0+Z_q q \\ M_{HD}=M_0+M_q q \end{cases}$, $q'<0.3$	$R_Z^2=0.9862$ $R_M^2=0.9998$
	Non-linear	$\begin{cases} X_{HD}=X_0+X_{qq}q^2 \\ Z_{HD}=Z_0+Z_q q+Z_{q\lvert q\rvert}q\lvert q\rvert \\ M_{HD}=M_0+M_q q+M_{q\lvert q\rvert}q\lvert q\rvert \end{cases}$	$R_X^2=0.7684$ $R_Z^2=0.9974$ $R_M^2=0.9997$
Roll rotating	Linear	$\begin{cases} X_{HD}=X_0 \\ Y_{HD}=Y_0+Y_p p \\ K_{HD}=K_0+K_p p \\ N_{HD}=N_0+N_p p \end{cases}$	$R_Y^2=0.9976$ $R_K^2=0.9999$ $R_N^2=0.8563$
	Non-linear	$\begin{cases} X_{HD}=X_0+X_{pp}p^2 \\ Y_{HD}=Y_0+Y_p p+Y_{p\lvert p\rvert}p\lvert p\rvert \\ K_{HD}=K_0+K_p p+K_{p\lvert p\rvert}p\lvert p\rvert \\ N_{HD}=N_0+N_p p+N_{p\lvert p\rvert}p\lvert p\rvert \end{cases}$	$R_X^2=0.9014$ $R_Y^2=0.9977$ $R_K^2=0.9997$ $R_N^2=0.8214$
Horizontal circular motion with drift	Non-linear	$\begin{cases} X_{HD}=X_0+X_{vv}v^2+X_{vvvv}v^4 \\ \quad +X_{rr}r^2+X_{vr} \\ Y_{HD}=Y_0+Y_v v+Y_{v\lvert v\rvert}v\lvert v\rvert+Y_r r \\ \quad +Y_{r\lvert r\rvert}r\lvert r\rvert+Y_{v\lvert r\rvert}v\lvert r\rvert+Y_{\lvert v\rvert r}\lvert v\rvert r \\ K_{HD}=K_0+K_v v+K_{v\lvert v\rvert}v\lvert v+K_r r \\ \quad +K_{r\lvert r\rvert}r\lvert r\rvert+K_{v\lvert r\rvert}v\lvert r\rvert+K_{\lvert v\rvert r}\lvert v\rvert r \\ N_{HD}=N_0+N_v v+N_{v\lvert v\rvert}v\lvert v\rvert+N_r r \\ \quad +N_{r\lvert r\rvert}r\lvert r\rvert+N_{v\lvert r\rvert}v\lvert r\rvert+N_{\lvert v\rvert r}\lvert v\rvert r \end{cases}$	$R_X^2=0.9917$ $R_Y^2=0.9985$ $R_K^2=0.9528$ $R_N^2=0.9839$
Vertical circular motion with aoa	Non-linear	$\begin{cases} X_{HD}=X_0+X_{ww}w^2+X_{wwww}w^4 \\ \quad +X_{qq}q^2+X_{wq} \\ Z_{HD}=Z_0+Z_w w+Z_{w\lvert w\rvert}w\lvert w\rvert+Z_q q \\ \quad +Z_{qq}q^2+Z_{\lvert w\rvert q}\lvert w\rvert q+Z_{w\lvert q\rvert}w\lvert q\rvert \\ M_{HD}=M_0+M_w w+M_{w\lvert w\rvert}w\lvert w\rvert+ \\ \quad M_q q+M_{qq}q^2+M_{\lvert w\rvert q}\lvert w\rvert q+M_{w\lvert q\rvert}w\lvert q\rvert \end{cases}$	$R_X^2=0.9796$ $R_Z^2=0.9961$ $R_M^2=0.9949$

approximately 1. In addition, linear coefficients were identified within the drift angle range of ±4°. As previously mentioned, hydrodynamic forces were calculated by adjusting the angle of attack by up to ±90°, considering a large angle of attack; the results obtained from the static angle of attack test are presented in Fig. 6. A stall occurs at approximately ±50° and ±40° of the surge and pitch, respectively, and the tendency of forces should be modeled using the same model as the static drift test. Nonlinear coefficients constituting the nonlinear model must be analyzed using simple curve approximation results because physical implication is ambiguous. In contrast, linear coefficients comprising the linear model have a distinct physical implication, such that the effectiveness of numerical analysis results can be determined by examining the correlation among linear coefficients when there are no experimental results, as in this study. Fig. 7 presents the points of damping force applications when the sway v and heave w velocities are generated based on the linear coefficients of stability Y_v, K_v, N_v, Z_w, and M_w, identified via the static drift and static angle of attack tests.

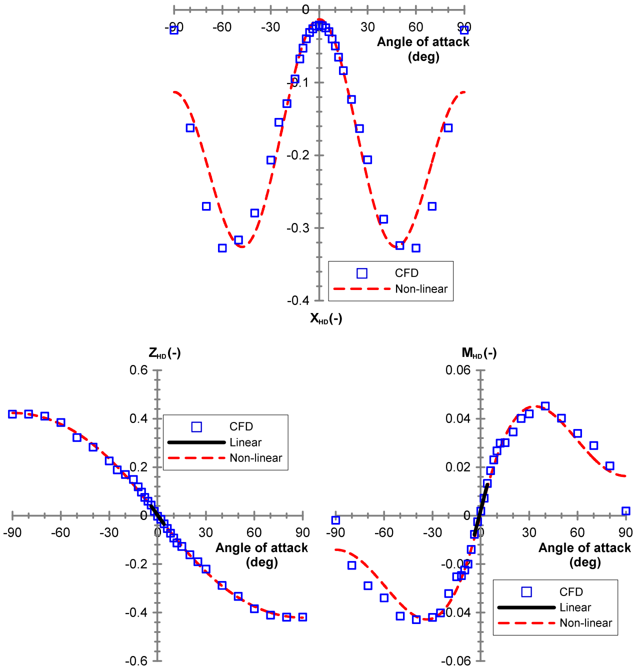

Fig. 6 Results obtained from static angle of attack tests

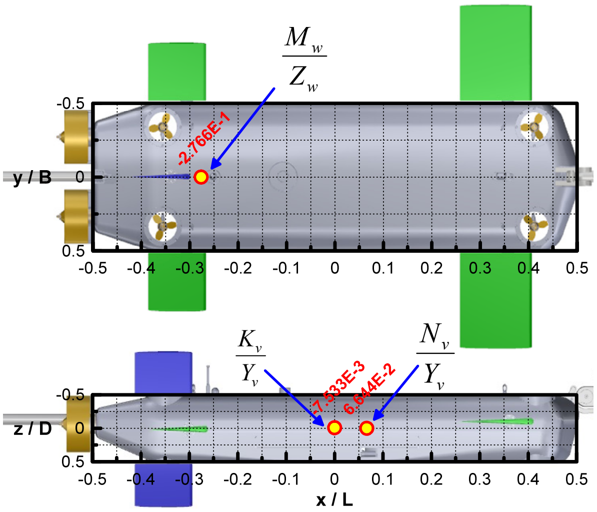

Fig. 7 Moment levers due to heave (upper) and sway (lower) velocities

The side shape of the subject submerged body exhibits a tendency in which the rear part area is predominant owing to the large rudder attached in the rear part; thus, it is predicted to exhibit relatively better results in terms of horizontal stability. Therefore, N_v/Y_v, which is the application point of the damping force in the longitudinal direction due to the sway velocity, is positioned at approximately $0.066L$ in front of the origin. Considering that the N_v/Y_v of a general slender-type vehicle such as a ship is approximately $0.25L$, the application point of the damping force moved backward considerably, toward the rear. Because the vertical shape is almost symmetrical, the application point K_v/Y_v of the damping force in the height direction is positioned slightly upward with respect to the geometrical origin; however, the size is negligible. In contrast, M_w/Z_w, which is the application point of the damping force in the longitudinal direction due to the heave velocity, is positioned approximately $0.277L$ toward the rear, with respect to the origin. A large bow plane exists in the head part, which implies that it is disadvantageous in terms of vertical stability, owing to the predominant head part.

Figs. 8 and 9 present the results obtained from horizontal and vertical turning tests, which are conducted to determine the damping force and moment related to the yaw angular velocity r and pitch velocity q. The top area is more than two times greater than the side area of the hull, and the vertical hydrodynamic moment M_{HD} is substantially greater than the horizontal hydrodynamic moment Y_{HD}. In contrast, hydrodynamic forces Y_{HD} and Z_{HD} are the forces generated from the difference in the shapes of the head and rear parts

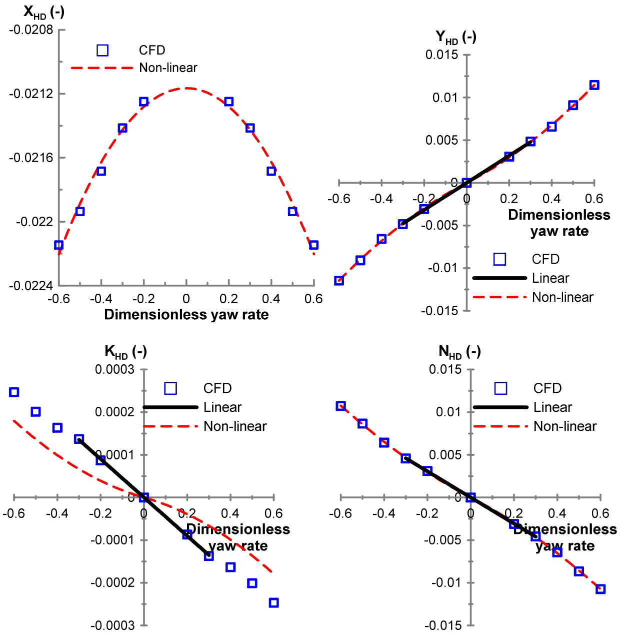

Fig. 8 Results obtained from horizontal circular motion tests

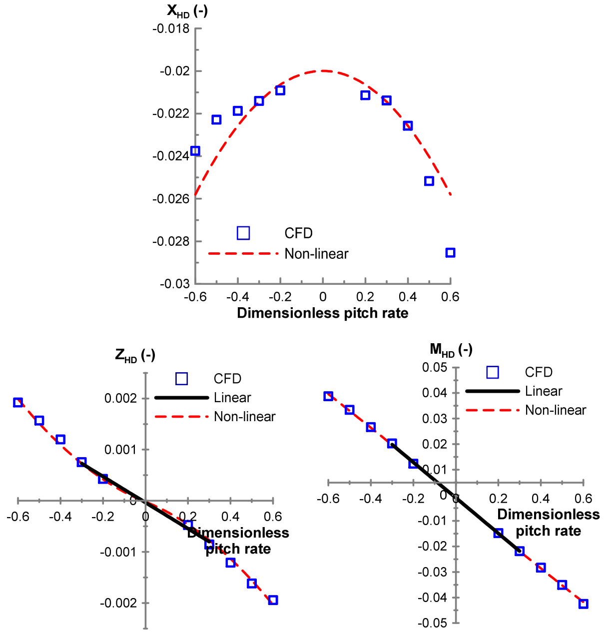

Fig. 9 Results obtained from vertical circular motion tests

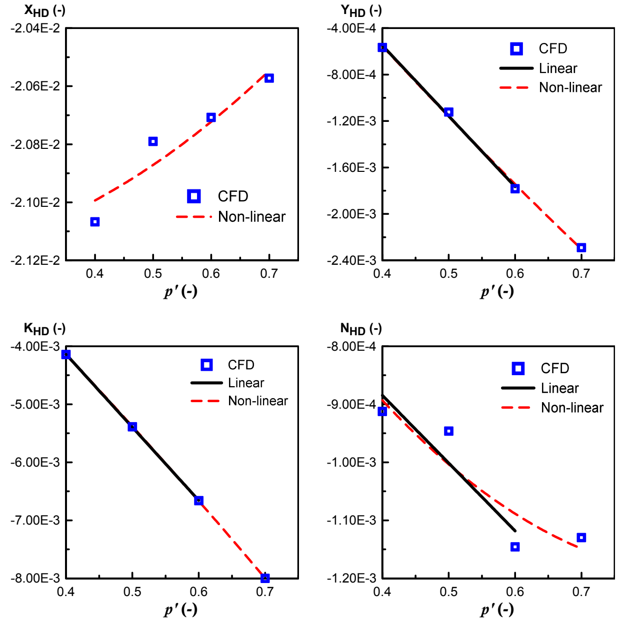

Fig. 10 Results obtained from roll rotating tests

during the rotational motions in which the asymmetry of the shapes of the head and rear parts significantly influence the horizontal hydrodynamic force Y_{HD}.

Fig. 10 presents the results of a roll rotating test, which measures the force generated by a certain roll rate p while a submerged body is advanced at speed U. Generally, a submerged body with a cylindrical shape frequently experiences a large rolling motion if a controller is not applied because the roll damping coefficient applied on the hull is relatively small. The subject submerged body in this study has a relatively flat hull top surface and a large elevator area, thus exhibiting a large roll damping moment. As shown in Fig. 10, which illustrates the roll damping moment K_{HD} for the roll rate p, the order is greater than that of the same angular motion moment N_{HD}. A large roll damping moment indicates that a roll is not large during circular motions in which favorable dynamic characteristics can be obtained from the motion control perspective. A simulation must be conducted to verify whether such a phenomenon actually occurs.

Figs. 11 and 12 present the results of the horizontal circular motion with the drift test and those of the vertical circular motion with the angle of attack test. The hydrodynamic forces measured in the static

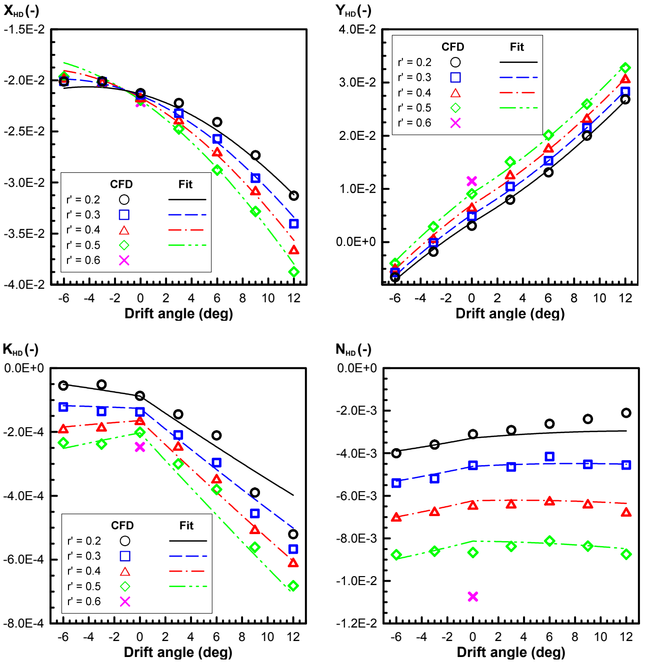

Fig. 11 Results obtained from the horizontal circular motion with drift tests

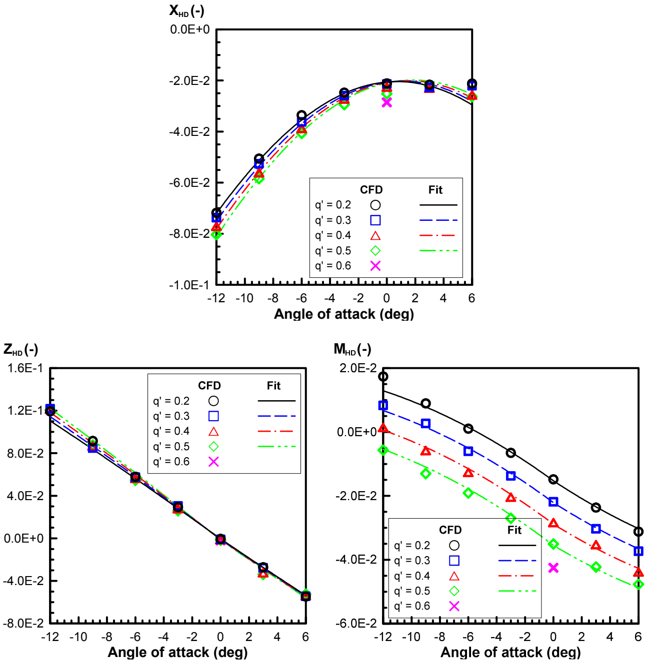

Fig. 12 Results obtained from the vertical circular motion with the angle of attack tests

drift and horizontal turning tests are also measured when the horizontal circular motion with the drift test is performed; therefore, all hydrodynamic forces applied by and can be determined. Likewise, the hydrodynamic forces measured in the static angle of attack and vertical turning tests are also measured if the vertical circular motion is performed with drift test; therefore, all hydrodynamic forces applied by w and q can be determined.

All the damping coefficients due to ship motions u, v, w, p, q, and r were estimated via the above tests. Table 5 presents the coefficient of determination of the hydrodynamic force model and corresponding models generated in the static rudder and static elevator tests. Figs. 13–14 present the results of the static rudder and static elevator tests, respectively. In general, the center of pressure of the hydrodynamic forces applied on a rudder is positioned at approximately 1/4 the point of a rudder chord. Similar to the static drift test, hydrodynamic forces and the rudder angle have a linear relationship in a region with a small rudder angle; hence, a linear coefficient can be determined to estimate the center of pressure of the rudder force. Fig. 15 presents the center of pressure on a rudder, which is estimated based on a linear coefficient when the rudder was rotated by a small angle. The center of pressure in the longitudinal direction $N_{\delta_r}/Y_{\delta_r}$ when the rudder was rotated is positioned closer to 1/4 of a rudder chord. The center of pressure in the vertical direction $K_{\delta_r}/Y_{\delta_r}$ is slightly more predominant in the top area from the side view of the hull; however, the size of $K_{\delta_r}/Y_{\delta_r}$ is negligible because the vertical shape of the hull is almost symmetrical. The centers of pressure when the bow plane and stern elevator are turned, $M_{\delta_b}/Z_{\delta_b}$ and $M_{\delta_s}/Z_{\delta_s}$, are also approximate to the 1/4 point of a

Table 5 Static hydrodynamic force model for control plane angles

Test type	Model	Formulae	R^2
Static rudder	Linear	$\begin{cases} X_{HD} = X_0 \\ Y_{HD} = Y_0 + Y_{\delta_r}\delta_r \\ K_{HD} = K_0 + K_{\delta_r}\delta_r \\ N_{HD} = N_0 + N_{\delta_r}\delta_r \end{cases}$, -4°<β<4°	$R_Y^2 = 0.9981$ $R_K^2 = 0.9517$ $R_N^2 = 0.9995$
	Non-linear	$\begin{cases} X_{HD} = X_0 + X_{\delta_r\delta_r}\delta_r^2 \\ Y_{HD} = Y_0 + Y_{\delta_r}\delta_r + Y_{\delta_r\lvert\delta_r\rvert}\delta_r\lvert\delta_r\rvert \\ K_{HD} = K_0 + K_{\delta_r}\delta_r + K_{\delta_r\lvert\delta_r\rvert}\delta_r\lvert\delta_r\rvert \\ N_{HD} = N_0 + N_{\delta_r}\delta_r + N_{\delta_r\lvert\delta_r\rvert}\delta_r\lvert\delta_r\rvert \end{cases}$	$R_X^2 = 0.9952$ $R_Y^2 = 0.9992$ $R_K^2 = 0.8317$ $R_N^2 = 0.9857$
Static elevator (Bow)	Linear	$\begin{cases} X_{HD} = X_0 \\ Z_{HD} = Z_0 + Z_{\delta_b}\delta_b \\ M_{HD} = M_0 + M_{\delta_b}\delta_b \end{cases}$	$R_Z^2 = 0.9991$ $R_M^2 = 0.9983$
	Non-linear	$\begin{cases} X_{HD} = X_0 + X_{\delta_b\lvert\delta_b\rvert}\delta_b\lvert\delta_b\rvert \\ Z_{HD} = Z_0 + Z_{\delta_b}\delta_b + Z_{\delta_b\lvert\delta_b\rvert}\delta_b\lvert\delta_b\rvert \\ M_{HD} = M_0 + M_{\delta_b}\delta_b + M_{\delta_b\lvert\delta_b\rvert}\delta_b\lvert\delta_b\rvert \end{cases}$	$R_X^2 = 0.9828$ $R_Z^2 = 0.9943$ $R_M^2 = 0.9984$
Static elevator (Stern)	Linear	$\begin{cases} X_{HD} = X_0 \\ Z_{HD} = Z_0 + Z_{\delta_b}\delta_b \\ M_{HD} = M_0 + M_{\delta_b}\delta_b \end{cases}$	$R_Z^2 = 0.9509$ $R_M^2 = 0.9177$
	Non-linear	$\begin{cases} X_{HD} = X_0 + X_{\delta_s\lvert\delta_s\rvert}\delta_s\lvert\delta_s\rvert \\ Z_{HD} = Z_0 + Z_{\delta_s}\delta_s + Z_{\delta_s\lvert\delta_s\rvert}\delta_s\lvert\delta_s\rvert \\ M_{HD} = M_0 + M_{\delta_s}\delta_s + M_{\delta_s\lvert\delta_s\rvert}\delta_s\lvert\delta_s\rvert \end{cases}$	$R_X^2 = 0.9739$ $R_Z^2 = 0.9944$ $R_M^2 = 0.9917$

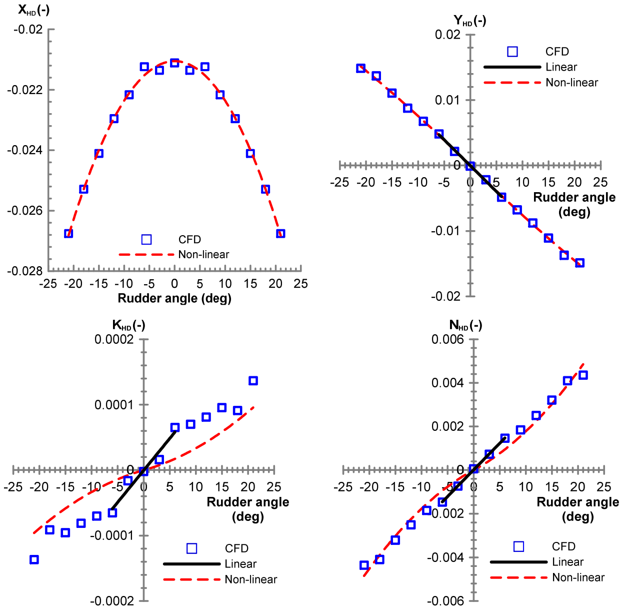

Fig. 13 Results obtained from static rudder tests

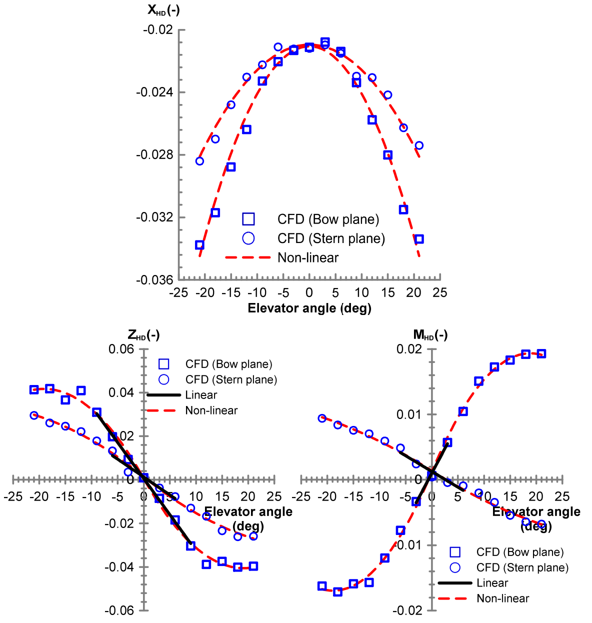

Fig. 14 Results obtained from static elevator tests

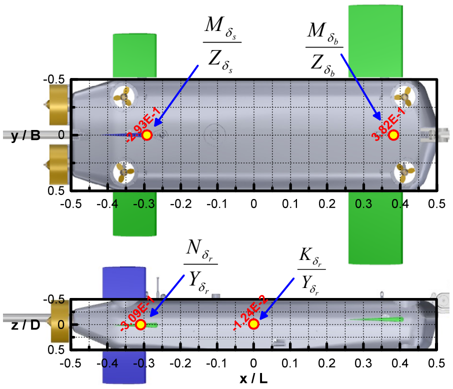

Fig. 15 Moment levers due to elevator (upper) and rudder (lower) deflections

Table 6 Dimensionless linear maneuvering mathematical model parameters ($\times 10^6$)

X-coeff.		*Y*-coeff.		*Z*-coeff.	
$X_{\dot u}$	-1872	$Y_{\dot v}$	-59564	$Z_{\dot w}$	-299190
X_u	-21472	$Y_{\dot p}$	54	$Z_{\dot q}$	-65503
		$Y_{\dot r}$	29365	Z_w	-535933
		Y_v	-89962	Z_q	-2548
		Y_p	-6083	Z_{δ_b}	-199688
		Y_r	15920	Z_{δ_s}	-94044
		Y_{δ_r}	-45209		
K-coeff.		*M*-coeff.		*N*-coeff.	
$K_{\dot v}$	-758	$M_{\dot w}$	71802	$N_{\dot v}$	2282
$K_{\dot p}$	-1004	$M_{\dot q}$	-39941	$N_{\dot p}$	-34
$K_{\dot r}$	-490	M_w	148263	$N_{\dot r}$	-10956
K_v	678	M_q	-69468	N_v	-5977
K_p	-12587	M_{δ_b}	76212	N_p	-1167
K_r	-450	M_{δ_s}	-27535	N_r	-15323
K_{δ_r}	560			N_{δ_r}	13978

rudder chord. Fig. 14 presents the results obtained from comparing the hydrodynamic forces when the bow plane was turned and when the stern elevator was turned. The area of a bow plane is approximately twice as large as the area of a stern elevator; hence, the linear control panel coefficient Z_{δ_b} provided in Table 6 is approximately twice as large as Z_{δ_s}. In contrast, moment coefficients M_{δ_b} and M_{δ_s} are associated with the distance to the pressure center of a control panel, and M_{δ_b} is at least two times greater than M_{δ_s} because the pressure center of a bow plane is far from the origin. Similarly, examining the physical relationship between linear coefficients appears to be an appropriate method for verifying the CFD analysis results when no experimental results are available.

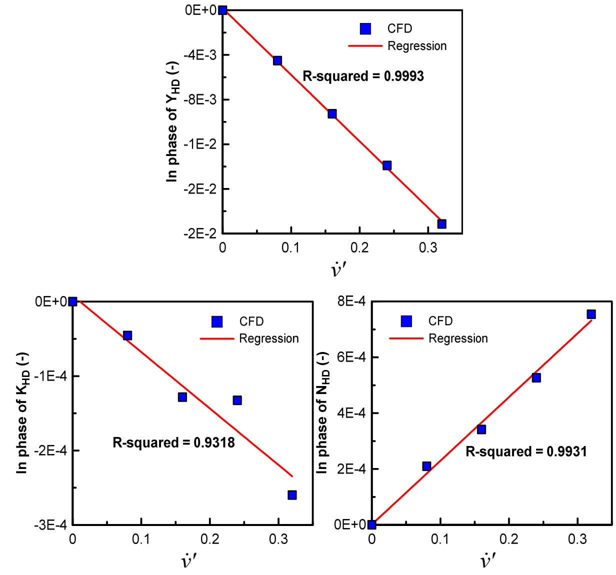

Fig. 16 Results obtained from pure sway tests

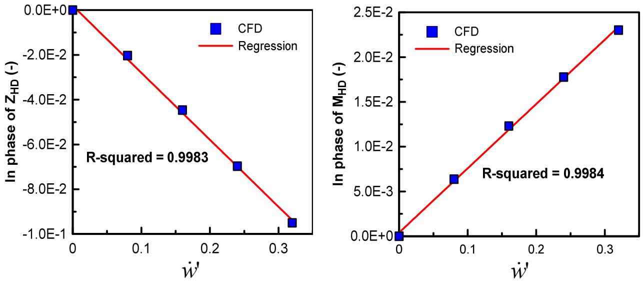

Fig. 17 Results obtained from pure heave tests

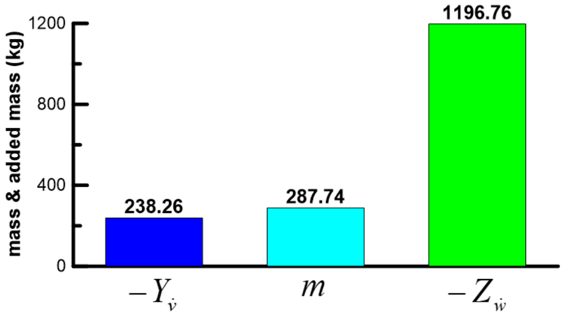

Fig. 18 Comparison of mass and added mass

3.2 Dynamic Test

A dynamic test was performed to estimate the added mass force applied on the hull and the surrounding fluid when the hull accelerates. The added mass force exhibits a linear relationship with acceleration when a vessel or a submerged body has a very small accelerated motion. Figs. 16 and 17 present the results obtained from pure sway tests for estimating the added mass force with respect to sway acceleration $\dot v$ and pure heave tests for estimating the added mass force with respect to heave acceleration $\dot w$, respectively. The added mass moment of inertia coefficients $K_{\dot v}$ and $N_{\dot v}$ for $\dot v$ are typically negligible, as well as the added mass moment of inertia coefficient $M_{\dot w}$ for $\dot w$; therefore, the sizes of $Y_{\dot v}$ and $Z_{\dot w}$ need to be examined. The results obtained from comparing the sizes of $Y_{\dot v}$ and $Z_{\dot w}$ with the mass of the submerged body are illustrated in Fig. 18. $Y_{\dot v}$ of a general ship has proportion of its mass. Furthermore, $Y_{\dot v}$ and $Z_{\dot w}$ are identical in a submerged body with symmetrical horizontal and vertical planes. However, the subject submerged body in this study is applied with a relatively greater added mass force owing to its plate shape. Considering that the top surface area is at least twice as large as the side area and the top surface shape is a plate shape, rather than a streamlined shape, it is feasible for the size of $Z_{\dot w}$ to be greater than that of $Y_{\dot v}$ and its own mass.

Figs. 19–21 illustrate the results obtained from a dynamic test for angular acceleration. Figs. 19 and 20 present the results obtained from estimating added mass coefficients for yaw angular acceleration $\dot r$ and pitch angular acceleration $\dot q$. Similar to the difference in the sizes of $Y_{\dot v}$ and $Z_{\dot w}$, the size of $M_{\dot q}$ is greater than that of $N_{\dot r}$ because the top

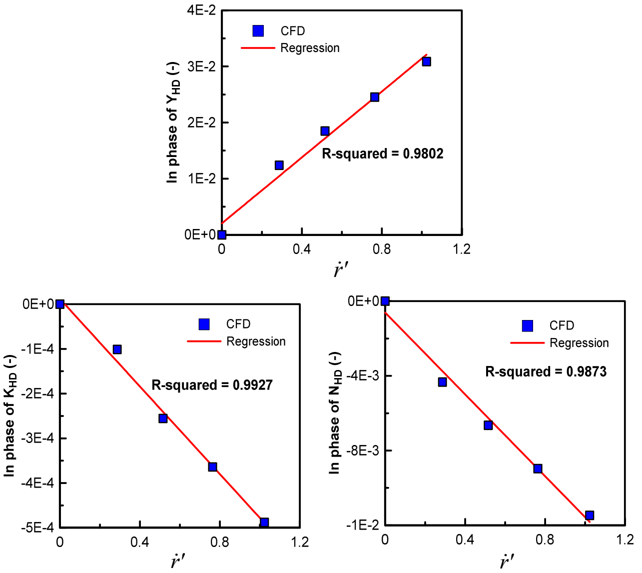

Fig. 19 Results obtained from pure yaw tests

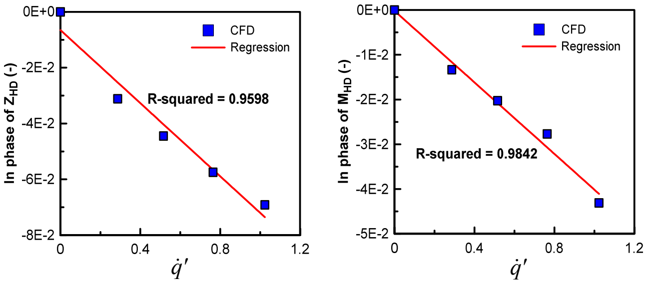

Fig. 20 Results obtained from pure pitch tests

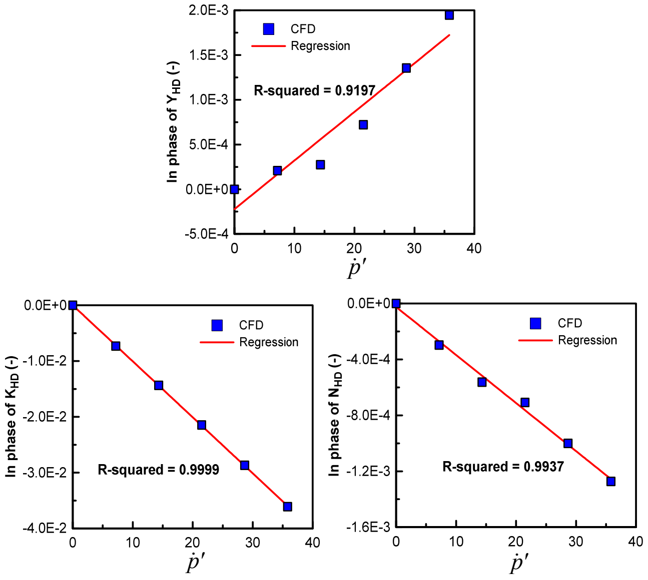

Fig. 21 Results obtained from pure roll tests

surface shape is more predominant than that of the side shape. In general, the added mass moment of inertia is sufficiently small to be negligible compared to the mass moment of inertia (I_{xx}) in a submerged body with a streamlined shape when a roll angular acceleration $\dot{p}$ is generated. However, the subject submerged body has a relatively plate-like shape, and the slenderness ratio (L/B) is relatively small. Moreover, a large hydrodynamic moment is generated by a roll angular acceleration because the areas of bow and stern elevators are large. Consequently, the yaw induced mass moment of inertia $K_{\dot{p}}$ is relatively larger than that of a general slender-type submerged body, as illustrated in Fig. 21.

3.3 Dynamics Model

The six degrees-of-freedom equations of motion based on Newton's second law of motion can be expressed as in Eq. (1).

$$\begin{cases} m\left[\dot{u}-vr+wq-x_g\left(q^2+r^2\right)+z_g\left(pr+\dot{q}\right)\right]=X \\ m\left[\dot{v}-wp+ur+z_g\left(qr-\dot{p}\right)+x_g\left(qp+\dot{r}\right)\right]=Y \\ m\left[\dot{w}-uq+vp-z_g\left(r^2+p^2\right)+x_g\left(rp-\dot{q}\right)\right]=Z \\ I_x\dot{p}+\left(I_z-I_y\right)qr-m\left[z_g\left(\dot{v}-wp+ur\right)\right]=K \\ I_y\dot{q}+\left(I_x-I_z\right)rp+m\left[z_g\left(\dot{u}-vr+wq\right)-x_g\left(\dot{w}-uq+vp\right)\right]=M \\ I_z\dot{r}+\left(I_y-I_x\right)pq+m\left[x_g\left(\dot{v}-wp+ur\right)\right]=N \end{cases} \tag{1}$$

External forces on the right side of Eq. (1) can be divided into hydrodynamic force, gravitational force, buoyant force, control force, and thrust. Hydrodynamic forces were modeled as expressed in Eqs. (2) and (3) by distinguishing linear models for designing the controller and stability analysis and nonlinear models for predicting maneuverability based on the coefficients identified via the static and dynamic tests.

$$\begin{cases} X_{HD}=X_{\dot{u}}\dot{u}+X_u u \\ Y_{HD}=Y_{\dot{v}}\dot{v}+Y_{\dot{p}}\dot{p}+Y_{\dot{r}}\dot{r}+Y_v v+Y_p p+Y_r r \\ Z_{HD}=Z_{\dot{w}}\dot{w}+Z_{\dot{q}}\dot{q}+Z_w w+Z_q q \\ K_{HD}=K_{\dot{v}}\dot{v}+K_{\dot{p}}\dot{p}+K_{\dot{r}}\dot{r}+K_v v+K_p p+K_r r \\ M_{HD}=M_{\dot{w}}\dot{w}+M_{\dot{q}}\dot{q}+M_w w+M_q q \\ N_{HD}=N_{\dot{v}}\dot{v}+N_{\dot{p}}\dot{p}+N_{\dot{r}}\dot{r}+N_v v+N_p p+N_r r \end{cases} \tag{2}$$

$$\begin{cases} X_{HD}=X_{\dot{u}}\dot{u}+X_{u|u|}u|u|+X_{vv}v^2+X_{vvvv}v^4+X_{ww}w^2+X_{wwww}w^4 \\ \qquad +X_{pp}p^2+X_{qq}q^2+X_{rr}r^2+X_{vr}vr+X_{wq}wq \\ Y_{HD}=Y_{\dot{v}}\dot{v}+Y_{\dot{p}}\dot{p}+Y_{\dot{r}}\dot{r}+Y_v v+Y_p p+Y_r r \\ \qquad +Y_{v|v|}v|v|+Y_{p|p|}p|p|+Y_{r|r|}r|r|+Y_{v|r|}v|r|+Y_{|v|r}|v|r \\ Z_{HD}=Z_{\dot{w}}\dot{w}+Z_{\dot{q}}\dot{q}+Z_*+Z_w w+Z_q q \\ \qquad +Z_{w|w|}w|w|+Z_{q|q|}q|q|+Z_{w|q|}w|q|+Z_{|w|q}|w|q \end{cases} \tag{3}$$

$$\begin{cases} K_{HD}=K_{\dot{v}}\dot{v}+K_{\dot{p}}\dot{p}+K_{\dot{r}}\dot{r}+K_v v+K_p p+K_r r \\ \qquad +K_{v|v|}v|v|+K_{p|p|}p|p|+K_{r|r|}r|r|+K_{v|r|}v|r|+K_{|v|r}|v|r \\ M_{HD}=M_{\dot{w}}\dot{w}+M_{\dot{q}}\dot{q}+Z_*+M_w w+M_q q \\ \qquad +M_{w|w|}w|w|+M_{q|q|}q|q|+M_{w|q|}w|q|+M_{|w|q}|w|q \\ N_{HD}=N_{\dot{v}}\dot{v}+N_{\dot{p}}\dot{p}+N_{\dot{r}}\dot{r}+N_v v+N_p p+N_r r \\ \qquad +N_{v|v|}v|v|+N_{p|p|}p|p|+N_{r|r|}r|r|+N_{v|r|}v|r|+N_{|v|r}|v|r \end{cases}$$

$$\begin{cases} X_C=0 \\ Y_C=Y_{\delta_r}\delta_r \\ Z_C=Z_{\delta_b}\delta_b+Z_{\delta_s}\delta_s \\ K_C=K_{\delta_r}\delta_r \\ M_C=M_{\delta_b}\delta_b+M_{\delta_s}\delta_s \\ N_C=N_{\delta_r}\delta_r \end{cases} \tag{4}$$

$$\begin{cases} X_C = X_{\delta_r\delta_r}\delta_r^2 \\ Y_C = Y_{\delta_r}\delta_r + Y_{\delta_r|\delta_r|}\delta_r|\delta_r| \\ Z_C = Z_{\delta_b}\delta_b + Z_{\delta_s}\delta_s + Z_{\delta_b|\delta_b|}\delta_b|\delta_b| + Z_{\delta_s|\delta_s|}\delta_s|\delta_s| \\ K_C = K_{\delta_r}\delta_r + K_{\delta_r|\delta_r|}\delta_r|\delta_r| \\ M_C = M_{\delta_b}\delta_b + M_{\delta_s}\delta_s + M_{\delta_b|\delta_b|}\delta_b|\delta_b| + M_{\delta_s|\delta_s|}\delta_s|\delta_s| \\ N_C = N_{\delta_r}\delta_r + N_{\delta_r|\delta_r|}\delta_r|\delta_r| \end{cases} \tag{5}$$

Unlike other external forces contributing to the surface force, gravitational force and buoyancy are body forces that contribute to the volume, which do not require a modeling process as hydrodynamic forces, and can be perfectly expressed physically. Therefore, the expressions for gravitational force and buoyancy are omitted in this study because they can be referenced in the study by Fossen (2011). A control force is a fluid force applied on the control panel and the hull when the control panel rotates. Eqs. (4) and (5) represent the control force of linear and nonlinear models, respectively. The parameters expressed in Eqs. (2)–(5) are presented in Tables 6 and 7 by distinguishing between a linear and nonlinear model.

Table 7 Dimensionless non-linear maneuvering mathematical model parameters (×10^6)

X-coeff.		*Y*-coeff.		*Z*-coeff.	
$X_{\dot{u}}$	-1872	$Y_{\dot{v}}$	-59564	$Z_{\dot{w}}$	-299190
$X_{u\|u\|}$	-43077	$Y_{\dot{p}}$	54	$Z_{\dot{q}}$	-65503
X_{vv}	-180760	$Y_{\dot{r}}$	29365	Z_{*}	1474
X_{vvvv}	113190	Y_v	-75834	Z_w	-510550
X_{ww}	-1142600	$Y_{v\|v\|}$	-146670	$Z_{w\|w\|}$	88318
X_{wwww}	1042500	Y_p	-7178	Z_q	-1664
X_{pp}	1354	$Y_{p\|p\|}$	1224	$Z_{q\|q\|}$	-2861
X_{rr}	-2883	Y_r	6663	$Z_{w\|q\|}$	-119730
X_{vr}	9883	$Y_{r\|r\|}$	16754	$Z_{\|w\|q}$	85992
X_{wq}	140360	$Y_{v\|r\|}$	-40930	Z_{δ_b}	-246238
X_{qq}	-1664	$Y_{\|v\|r}$	-21802	$Z_{\delta_b\|\delta_b\|}$	368611
$X_{\delta_r\delta_r}$	-42934	Y_{δ_r}	-45216	Z_{δ_s}	-112358
$X_{\delta_b\delta_b}$	-99899	$Y_{\delta_r\|\delta_r\|}$	10537	$Z_{\delta_s\|\delta_s\|}$	95154
$X_{\delta_s\delta_s}$	-53328				
K-coeff.		*M*-coeff.		*N*-coeff.	
$K_{\dot{v}}$	-758	$M_{\dot{w}}$	71802	$N_{\dot{v}}$	2282
$K_{\dot{p}}$	-1004	$M_{\dot{q}}$	-39941	$N_{\dot{p}}$	-34
$K_{\dot{r}}$	-490	M_{*}	1136	$N_{\dot{r}}$	-10956
K_v	926	M_w	119002	N_v	-5191
K_p	-283	$M_{w\|w\|}$	-76339	N_p	4703
K_r	-10230	M_q	4713	N_r	-2223
$K_{v\|v\|}$	-2376	$M_{q\|q\|}$	11909	$N_{v\|v\|}$	1247
$K_{p\|p\|}$	-384	$M_{w\|q\|}$	41481	$N_{p\|p\|}$	-6188
$K_{r\|r\|}$	0	M_{δ_b}	110107	$N_{r\|r\|}$	-14236
$K_{v\|r\|}$	200	$M_{\delta_b\|\delta_b\|}$	-167012	$N_{v\|r\|}$	1989
$K_{\|v\|r}$	-2923	M_{δ_s}	-29035	$N_{\|v\|r}$	-9039
K_{δ_r}	128	$M_{\delta_s\|\delta_s\|}$	18252	N_{δ_r}	7364
$K_{\delta_r\|\delta_r\|}$	363			$N_{\delta_r\|\delta_r\|}$	16017

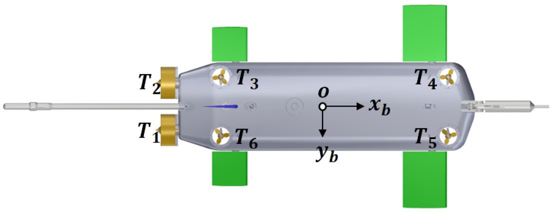

Fig. 22 Sequence of thruster

Because the system has six thrusters attached, the subjectsubmerged body can create thrust in all directions, except for the sway direction. Thrust force with six degrees of freedom generated by each thruster can be defined as expressed in Eq. (6), based on Fig. 22.

$$\begin{cases} X_T = T_1 + T_2 \\ Y_T = 0 \\ Z_T = T_3 + T_4 + T_5 + T_6 \\ K_T = y_{T_3}T_3 + y_{T_4}T_4 + y_{T_5}T_5 + y_{T_6}T_6 \\ M_T = z_{T_1}T_1 + z_{T_2}T_2 - \left(x_{T_3}T_3 + x_{T_4}T_4 + x_{T_5}T_5 + x_{T_6}T_6\right) \\ N_T = -\left(y_{T_1}T_1 + y_{T_2}T_2\right) \end{cases} \tag{6}$$

x_{T_i}, y_{T_i}, and z_{T_i} in Eq. (6) represent the distance from the origin of the i-th thruster to the x-, y-, z-axes, respectively. The thrust specified in the specifications of each thrust manufacturer was adopted as the thrust defined by T_{1-6}.

4. Dynamics Simulation

4.1 Stability Analysis

A stability analysis was conducted to evaluate the stability relative to the ship's course and depth while the control panel is fixed ($\delta_r = \delta_b = \delta_s = 0$). The sizes of the perturbation state variables v, w, q, and r were not significant when the control panel was fixed and the linearization of the equations of motion in Eq. (1) was possible; hence, the linear stability coefficients in Table 6 were adopted. Horizontal and vertical stability can be evaluated based on the stability margin, under the assumption that surge velocity u has no influence on sway, yaw, heave, or pitch. Horizontal and vertical stability margins can be defined by adopting Eqs. (7) and (8), respectively, at infinite speed.

$$G_h = 1 - \frac{N_v(Y_r - m)}{Y_v(N_r - mx_g)} \tag{7}$$

$$G_v = 1 - \frac{M_v(Z_q + m)}{Z_w(M_q - mx_g)} \tag{8}$$

Because m and x_g in Eqs. (7)–(8) are design variables, the stability margin results in Fig. 23 can be deduced for x_g under the assumption that neutral buoyancy is applied. As mentioned in Section 3, the rear is more critical with regard to the side shape of the submerged body, where it was assumed to be more important than the vertical plane in terms of stability. The analysis results indicated that G_h is greater than G_v when the center of gravity is closer to zero.

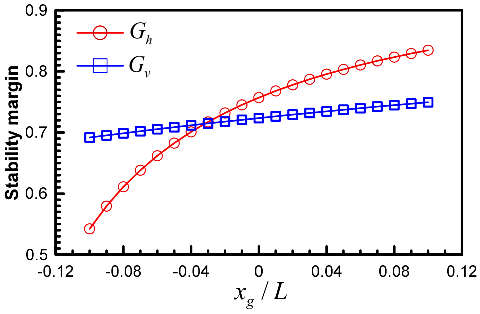

Fig. 23 Results obtained from pure roll tests

4.2 Maneuverability Analysis

Unlike a stability analysis in which the control panel is fixed, the control panel can be adjusted to the maximum angle when analyzing maneuverability, such as in turning and veering, which creates large motions such as drifting or yaw rate. Therefore, the hydrodynamic and control forces defined in Eqs. (3) and (5) are required. A turning simulation was performed by altering the rudder angle by ±5°, ±10°, and ±15° under an initial speed of 2.57 m/s, and the obtained results are illustrated in Figs. 24 and 25. The simulation results indicate that the tactical diameter is approximately 7.42 m when the rudder angle is 15°. The hull length of the subject submerged body is 2 m, and the entire length is approximately 3.7 m, including a towing poll; hence, adequate turning performance is realized owing to the small side surface area and large rudder area. Through simulations, it was verified that the roll convergence was approximately 1° during turning owing to a relatively large roll damping moment which was due to the large elevator and top surface areas of the hull, as observed in the pure roll tests mentioned in Section 3. The result of a meander test, which evaluates vertical stability in the maneuverability test of the submerged body, is illustrated in Fig. 26. The meander test investigates the stability of motions in the vertical plane direction over time, after the disturbance of a certain size is applied in the vertical plane direction (Jeon et al., 2020). After generating disturbance for a specific time in the vertical plane direction by turning the bow plane and stern elevator, the test examines whether the depth is maintained over time when the elevator is turned again at an angle of 0°. Unlike horizontal plane motions, the vertical plane motions have a restoring moment, which is expressed as the sum of gravitational force and buoyancy, and thus converges to a specific value without diverging to a pitch angle. When the subject submerged body is assumed to be under neutral buoyancy, the pitch angle converges to zero, and the depth is maintained after the rudder angle is maintained at 0° after 30 s, as illustrated Fig. 26. Vertical stability can be examined again via a meander simulation, based on the results presented in Fig. 23. The motions in a large angle of attack were simulated by generating thrust and thrust moment in heave and pitch directions, while increasing the

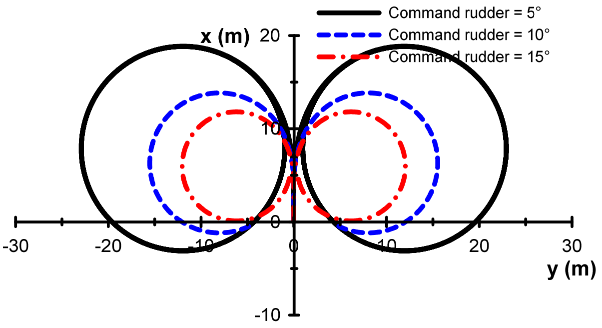

Fig. 24 Trajectories of turning tests

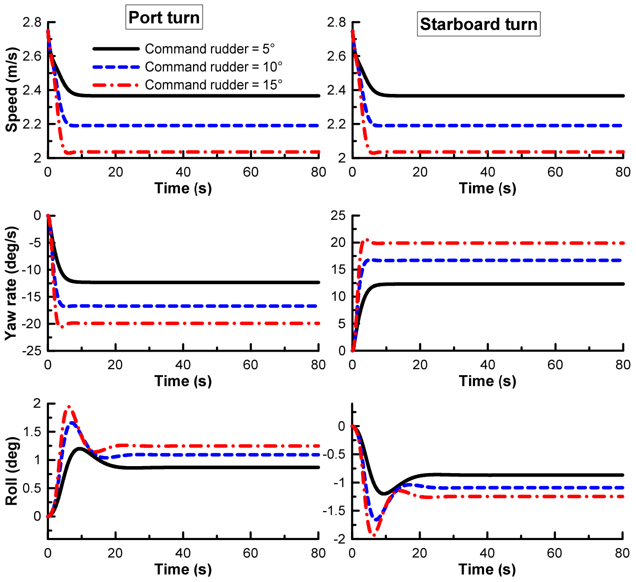

Fig. 25 Motion variables of turning tests

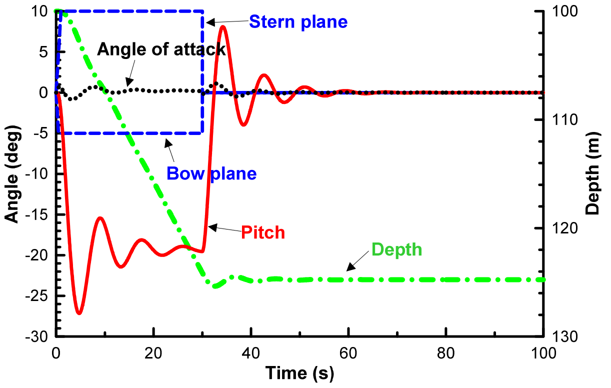

Fig. 26 Meander test

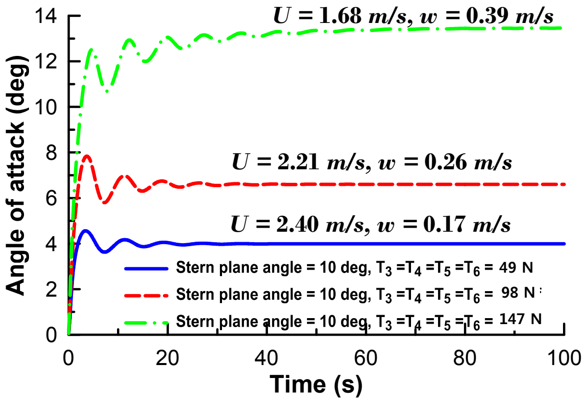

Fig. 27 Large angle of attack test

thrust of auxiliary thrusters T_3, T_4, T_5, and T_6 attached on the hull presented in Fig. 22 to 49 N, 98 N, and 147 N; the obtained results are presented in Fig. 27.

5. Concluding Remarks

Maneuvering coefficients for a hydrodynamic model were estimated by performing virtual captive model tests based on CFD for a submerged body that can exhibit large angles of attack and receives various control inputs. The conditions for the virtual captive model tests based on CFD were established by considering that the subject submerged body has a large control panel area and exhibits a large angle of attack motion. A practical inference method was established to verify the results using the linear coefficients of the submerged body because no experimental results were available. Maneuvering coefficients were identified by distinguishing a linear model from a nonlinear model, based on the results of the static test. In general, the determination coefficients of the linear model were closer to 1 than those of nonlinear coefficients in the CFD analysis results, which implied that errors occurred in a mathematical model of hydrodynamic forces as drift angle and angle of attack increased. The accuracy of the mathematical model improved as the order of hydrodynamic derivatives increased; however, the structural stability of the mathematical model of hydrodynamic forces reduced accordingly. The mathematical model was appropriately established because the determination coefficients were generally 0.95 or higher. Because linear coefficients have significant physical implications, the application point of a damping force was verified when a small perturbed motion was generated. Moreover, the application point of the damping force was realistic when the motion of the hull and rotation of the control panel occurred. Dynamic characteristics of the submerged body were evaluated by establishing a mathematical model with six degrees of freedom for thrust generated by six thrusters and hydrodynamic forces applied on the hull by a large angle of attack motion and the rotation of the control panel. Excellent turning characteristics were obtained because the rudder area was larger than the side surface area of the hull, and the stability of the vessel’s course was secured. Arbitrary thrust was applied to the auxiliary thrusters attached to the hull, and the large angle of attack motion in the vertical direction was simulated by changing the elevator; however, the effect of the design variables, including the weight of the submerged body and its center of gravity, were greater. The hydrodynamic model will be further improved by tuning various coefficients and comparing the results of an actual experiment with the results of a CFD analysis.

Funding

This research was financially supported by the Institute of Civil Military Technology Cooperation, funded by the Defense Acquisition Program Administration and Korean government Ministry of Trade, Industry, and Energy.

References

Bae, J.-Y., & Sohn, K.-H. (2009). A Study on Manoeuvring Motion Characteristics of Manta-type Unmanned Undersea Vehicle. Journal of the Society of Naval Architects of Korea, 46(2), 114–126. https://doi.org/10.3744/snak.2009.46.2.114

Cho, Y.J., Seok, W., Cheon, K.-H., & Rhee, S.H. (2020). Maneuvering Simulation of an X-plane Submarine Using Computational Fluid Dynamics. International Journal of Naval Architecture and Ocan Engineering., 12, 843-855. https://doi.org/10.1016/j.ijnaoe.2020.10.001

Fossen, T. I. (2011). Handbook of Marine Craft Hydrodynamics and Motion Control. New Jersey, USA: John Wiley & Sons.

Jeon, M., Lee, D., Yoon, H.K., & Koo, B. (2016). Modeling and Tracking Simulation of ROV for Bottom Inspection of a Ship using Component Drag Model. Journal of Ocean Engineering and Technology, 30(5), 374–380. https://doi.org/10.5574/ksoe.2016.30.5.374

Jeon, M., Nguyen, T.T., Yoon, H.K., & Cho, H.J. (2020). A Study on Verification of the Dynamic Modeling for a Submerged Body Based on Numerical Simulation. International Journal of Engineering and Technology Innovation, 10(2), 107–120. https://doi.org/10.46604/ijeti.2020.4350

Jeon, M., Yoon, H.K., Hwang, J., & Cho, H.J. (2017). Study on Maneuvering Characteristics of Submerged Body by Changing Its Design Parameters. Journal of Ocean Engineering and Technology, 31(2), 155–163. https://doi.org/10.5574/ksoe.2017.31.2.155

Jung, J.-W., Jeong, J-H., Kim, I-G., & Lee, S.-K. (2014). Experimental Study on Hydrodynamic Coefficients of Autonomous Underwater Glider Using Vertical Planar Motion Mechanism Test. Journal of Ocean Engineering and Technology, 28(2), 119–125. https://doi.org/10.5574/ksoe.2014.28.2.119

Kim, Y.-G., Yun, K.-H., Kim, S.-Y., & Kim, D.-J. (2012). Captive Model Test of Submerged Body Using CPMC. Journal of the Society of Naval Architects of Korea, 49(4), 296–303. https://doi.org/10.3744/snak.2012.49.4.296

Nguyen, T. T., Yoon, H. K., Park, Y., & Park, C. (2018). Estimation of Hydrodynamic Derivatives of Full-Scale Submarine using RANS Solver. Journal of Ocean Engineering and Technology, 32(5), 386– 392. https://doi.org/10.26748/ksoe.2018.6.32.5.386

Park, J.-Y., Kim, N., Rhee, K.-P., Yoon, H. K., Kim, C., Jung, C., ... Lee, S. (2015). Study on Coning Motion Test for Submerged Body. Journal of Ocean Engineering and Technology, 29(6), 436–444. https://doi.org/10.5574/ksoe.2015.29.6.436

Quérard, A., Temarel, P., & Turnock, S. (2008). Influence of Viscous Effects on the Hydrodynamics of Ship-Like Section Undergoing Symmetric and Anti-Symmetric Motions Using RANS. Proceedings of the 27th International Conference on Offshore Mechanics and Arctic Engineering, Estoril, Portugal, 683-692. https://doi.org/10.1115/OMAE2008-57330

Yeo, D.J., Yoon, H.K., Kim, Y.G., & Lee, C.M. (2006). Sensitivity Analysis on the Stability of a Submarine Concerning its Design Parameters. Journal of the Society of Naval Architects of Korea, 12, 843–855. https://doi.org/10.1016/j.ijnaoe.2020.10.001

Takashina, J. (1986). Ship Maneuvering Motion due to Tugboats and Its Mathematical Model. Journal of the Society of Naval Architects of Japan, 160, 93–102. https://doi.org/10.2534/jjasnaoe1968.1986.160_93

Yoon, H.K., & Kim, S.Y. (2005). A Study on the Model Test Scheme for Establishing the Mathematical Model of Hydrodynamic Force and Moment Acting on a Slowly Moving Ship. Journal of the Society of Naval Architects of Korea, 42(2), 98–104. https://doi.org/10.3744/SNAK.2005.42.2.098

Author ORCIDs

Author name	ORCID
Jeon, Myungjun	0000-0002-1655-5364
Mai, Thi Loan	0000-0002-0849-3204
Yoon, Hyeon Kyu	0000-0001-6639-0927
Ryu, Jaekwan	0000-0003-4176-3867
Lee, Wonhee	0000-0002-1063-3800
Ku, Pyungmo	0000-0003-1506-9935

KSOE

Journal of Ocean Engineering and Technology 35(5), 327-335, October, 2021
https://doi.org/10.26748/KSOE.2021.022

pISSN 1225-0767
eISSN 2287-6715

Original Research Article

Reliability Improvement of Offshore Structural Steel F690 Using Surface Crack Nondamaging Technology

Weon-Gu Lee[1], Kyoung-Hee Gu[2], Cheol-Su Kim[3] and Ki-Woo Nam[2,4]

[1]*Princial Engineer, DS Mirae-tech Co., Ltd, Gyeongnam, Korea*
[2]*Graduate Student, Department of Marine Convergence Design Engineering, Pukyong National University, Busan, Korea*
[3]*Senior researcher, Eco-friendly Transport Systems Research Institute, Pukyong National University, Busan, Korea*
[4]*Professor, Department. of Materials Science and Engineering, Pukyong National University, Busan, Korea*

KEY WORDS: Nondamaging technology, Shot peening, Compressive residual stress, Offshore structural steel, Reliability

ABSTRACT: *Microcracks can rapidly grow and develop in high-strength steels used in offshore structures. It is important to render these microcracks harmless to ensure the safety and reliability of offshore structures. Here, the dependence of the aspect ratio* (As) *of the maximum depth of harmless crack* (a_{hlm}) *was evaluated under three different conditions considering the threshold stress intensity factor* (ΔK_{th}) *and residual stress of offshore structural steel F690. The threshold stress intensity factor and fatigue limit of fatigue crack propagation, dependent on crack dimensions, were evaluated using Ando's equation, which considers the plastic behavior of fatigue and the stress ratio.* a_{hlm} *by peening was analyzed using the relationship between* ΔK_{th} *obtained by Ando's equation and* ΔK_{th} *obtained by the sum of applied stress and residual stress. The plate specimen had a width* $2W$ = *12 mm and thickness* t = *20 mm, and four value of As were considered: 1.0, 0.6, 0.3, and 0.1. The* a_{hlm} *was larger as the compressive residual stress distribution increased. Additionally, an increase in the values of As and* $\Delta K_{th(l)}$ *led to a larger* a_{hlm}. *With a safety factor (N) of 2.0, the long-term safety and reliability of structures constructed using F690 can be secured with needle peening. It is necessary to apply a more sensitive non-destructive inspection technique as a non-destructive inspection method for crack detection could not be used to observe fatigue cracks that reduced the fatigue limit of smooth specimens by 50% in the three types of residual stresses considered. The usefulness of non-destructive inspection and non-damaging techniques was reviewed based on the relationship between* a_{hlm}, a_{NDI} *(minimum crack depth detectable in non-destructive inspection),* a_{crN} *(crack depth that reduces the fatigue limit to 1/N), and As.*

1. Introduction

Offshore construction generally refers to the installation of structures and facilities in the marine environment for the production and transportation of electricity, petroleum, gas, and other resources. The shipbuilding industry is growing globally owing to the increasing freight volume, and drilling rigs are also actively being constructed for the development of marine resources (Lee et al., 2011; Song et al., 2013; Kim and Kim, 2018). High-strength steels are used to construct these offshore structures as they are becoming increasingly large and the environments in which they are used are becoming increasingly harsh. However, the possibility of microcracks developing in high-strength steels is high in harsh environments (variable load action), and cracks that have formed can grow rapidly. Microcracks can develop when processing materials and when transporting and installing these structures. To ensure the safety and reliability of offshore structures, initial defects that lead to microcracking should be rendered harmless.

Recently, many researchers have been actively attempting to render cracks harmless using peening. Peening effectively induces a compressive residual stress in high-strength steel (Al-Hassani, 1982; Al-Obaid, 1990; Harada et al., 2007) and increases its fatigue life and strength (Lee and Kim, 1997; Benedetti et al., 2002). As the heat-affected zone of welds is prone to cracking, studies have been conducted on improving fatigue life and rendering cracks harmless by peening the weld toe (Houjou et al., 2013a; Fueki et al., 2015; Fueki et al., 2019). Furthermore, studies simulating the behavior of steels with existing microcracks have been conducted to investigate the use of peening to render cracks harmless (Takahashi et al., 2012; Houjou et al., 2013b). A crack is determined to be harmless using the relationship

Received 11 May 2021, revised 21 June 2021, accepted 9 July 2021

Corresponding author Ki-Woo Nam: +82-51-629-6358, namkw@pknu.ac.kr

between the stress intensity factor and the crack size based on the acting stress and compressive residual stress (Nakagawa et al., 2014; Ando et al., 2021; Nam et al., 2021). Each stress intensity factor is evaluated using the Newman–Raju equation (Newman and Raju, 1981) and API-RP579's equation (American Petroleum Institute, API, 2000). Equations to determine the threshold stress intensity factor of a microcrack have been proposed by El Haddad et al. (1979), Tange et al. (1991), and Ando et al. (2019). In particular, Ando et al. proposed an evaluation equation that depends on the crack size, considering the peculiar plastic behavior and stress ratio of fatigue in high-strength steels. This equation can be used to evaluate the fatigue limit and the threshold stress intensity factor of microcracks in high-strength steels (Ando et al., 2020; Ando et al., 2021; Park et al., 2020; Park et al., 2021; Kim et al., 2020).

This study aimed to evaluate the dependence of the maximum depth of a harmless crack (a_{hlm}) in needle peening (NP)-applied offshore structural steel F690 on the compressive residual stress distribution, threshold stress intensity factor range for large cracks ($\Delta K_{th(l)}$), and crack aspect ratio (As). Furthermore, we evaluated the maximum allowable crack depth at an assumed safety factor (N) (a_{crN}), the minimum detectable crack depth via nondestructive inspection and a_{hlm} (a_{NDI}), and the crack aspect dependence of a_{hlm}.

2. Materials and Experimental Methods

2.1 Materials and Model Specimens

This study investigated high-strength steel DNV F690, which is used in offshore structures. Table 1 describes the chemical composition of DNV F690 and Table 2 lists its mechanical properties. As shown in Fig. 1, the model specimen has a plate width $2W = 12$ mm and a thickness $t = 20$ mm; a four-point bending fatigue stress with a stress ratio $R = 0.1$ is applied, as in a previous study (Kim et al., 2021). A semicircular crack with a surface crack length ($2c$) and depth (a) exists at the center of the specimen. We assumed four crack aspect ratios ($As = a/c$): 1.0, 0.6, 0.3, and 0.1.

Table 1 Chemical compositions of DNV F690 (wt.%)

C	Si	Mn	P	S	Cr	Ni	Mo	Al	Cu	Nb	V	Ti
0.18	0.46	1.6	0.025	0.025	0.18	0.36	0.05	0.045	0.28	0.038	0.03	0.02

Table 2 Mechanical properties of DNV F690

Yield strength (MPa)	Tensile strength (MPa)	Elongation (%)
851	876	15.2

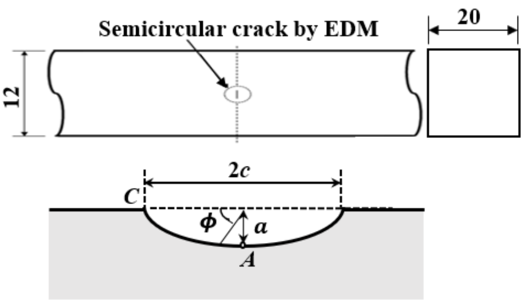

Fig. 1 Schematic of a finite plate containing a semicircular crack

2.2 Residual Stress Distribution

Three types of compressive residual stress ①, ②, and ③ induced by NP were assumed in order to evaluate their effect on a_{hlm}, as shown in Fig. 2. Residual stress ② was obtained in an experiment (Kim et al., 2021). Residual stress ① was the surface compressive residual stress of residual stress ② + 100 MPa, and residual stress ③ was the surface compressive residual stress of residual stress ② − 150 MPa. In the figure, σ_s is the compressive residual stress of the surface, $\sigma_{\max}$ is the maximum compressive residual stress, $d_{\max}$ is the depth at which the maximum compressive residual stress is observed, and d_0 is the point where the compressive residual stress is 0. Table 3 summarizes these values. The fatigue limit of the smooth specimen was 740 MPa and that of the NP smooth specimen was 750 MPa (Kim et al., 2021). $\Delta K_{th(l)}$ of the smooth specimen obtained experimentally was 6.5 $\mathrm{MPa}\sqrt{\mathrm{m}}$, but we assumed three values (3, 5, and 7 $\mathrm{MPa}\sqrt{\mathrm{m}}$) to evaluate the effect of $\Delta K_{th(l)}$. In general, $\Delta K_{th(l)}$ is related to the hardness of a material, and as the hardness increases, $\Delta K_{th(l)}$ decreases. In this study, considering that the hardness of F690 varies depending on the heat treatment applied, we selected the three values of $\Delta K_{th(l)}$. The fatigue limit of the NP smooth specimen depends on the residual stress distribution and $\Delta K_{th(l)}$, but we assumed that the fatigue limit of the NP smooth specimens was identical to evaluate the dependence of a_{hlm} on the residual stress distribution and $\Delta K_{th(l)}$.

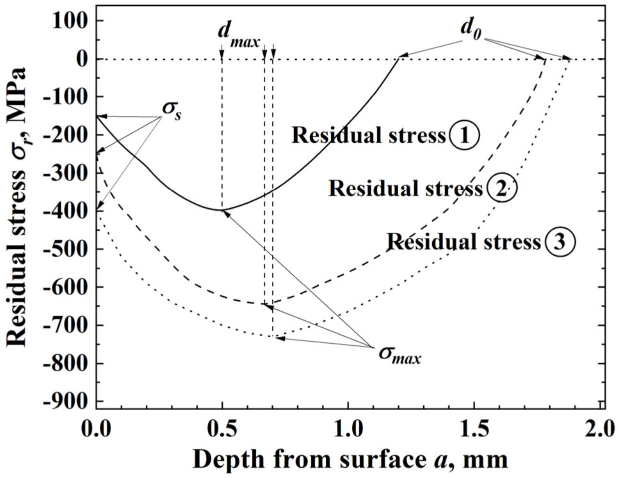

Fig. 2 Three types of residual stresses considered in this study

Table 3 Parameters of considered residual stresses

	σ_s (MPa)	$\sigma_{\max}$ (MPa)	$d_{\max}$ (mm)	d_0 (mm)
RS1	-150	-400	0.5	1.2
RS2	-250	-647	0.676	1.784
RS3	-400	-731	0.697	2.150

2.3 Evaluation Method

In this study, we used Eq. (1), which was originally proposed by Ando et al. (Ando et al., 2019). This equation describes the dependence of the threshold stress intensity factor range (ΔK_{th}) on crack length when an existing crack in an infinite plate propagates under fatigue stress.

$$\Delta K_{th} = 2\beta\Delta\sigma_w \sqrt{\frac{a}{\pi}}\, cos^{-1}\left\{\frac{\pi}{8\beta^2 a}\left(\frac{\Delta K_{th(l)}}{\Delta\sigma_w}\right)^2 + 1\right\}^{-1} \tag{1}$$

$$\beta = \frac{H\left(\frac{a}{t}, \frac{a}{c}, \frac{c}{b}, \phi\right) F\left(\frac{a}{t}, \frac{a}{c}, \frac{c}{b}, \phi\right)}{\sqrt{Q\left(\frac{a}{c}\right)}}$$

where a is the crack length, $\Delta K_{th(l)}$ is the threshold stress intensity factor range for large cracks, $\Delta\sigma_w$ is the fatigue limit of the non-peened smooth specimen, β is a function of ϕ in Fig. 1 and a shape factor obtained by the Newman–Raju equation (Newman and Raju, 1981). In contrast, the fatigue limit of the cracked specimen ($\Delta\sigma_{wc}$) can be evaluated using Eq. (2).

$$\Delta K_{th} = \Delta\sigma_{wc}\sqrt{\pi a} \tag{2}$$

Eqs. (1)–(2) are used to determine ΔK_{th} and $\Delta\sigma_{wc}$ for the deepest part of the crack (point A) in the cracked specimen to which bending stress is applied. To determine these values on the outermost surface (point C), a can be replaced with c in Eqs. (1) and (2).

We evaluated the crack depths corresponding to fatigue limit reduction rates of 25% and 50% in the smooth specimens. These crack depths are denoted by a_{25} and a_{50}. In our evaluation, the safety factor (SF) for the fatigue limit was set to 2.0, as suggested in the standard established by the American Society of Mechanical Engineers (ASME). As a_{25} decreases till SF reaches 1.5, these cracks can always be detected via nondestructive inspection. Furthermore, in the case of $SF = 2.0$, the maximum crack depth that can exist after a certain period is a_{50}. Therefore, if there are no internal defects, surface crack nondamaging technology can ensure the safety of the cracks of a_{50} by peening.

a_{25} and a_{50} were evaluated using Eq. (3):

$$\Delta K_{ap} = \Delta K_{th(s)} \tag{3}$$

where ΔK_{ap} is the stress intensity factor based on bending stress; it can be calculated using the Newman–Raju equation (Newman and Raju, 1981). In other words, ΔK_{ap} is a stress intensity factor obtained by considering a 25% and 50% lower stress than the fatigue limit of the smooth specimen. In this case, ΔK_{ap} was evaluated at points A and C in Fig. 1, and a small crack size was used.

In contrast, the stress intensity factor of the NP specimen was evaluated using Eq. (4):

$$\Delta K_{Tr} = \Delta K_{ap} + K_r \tag{4}$$

where the stress intensity factor K_r based on the compressive residual stress was calculated using a stress intensity factor evaluation equation for surface cracks, considering the stress distribution shown in a four-order polynomial provided by API-RP579 (API, 2000). The stress intensity factor of a semi-circular crack existing in a plate is represented by Eq. (5):

$$K_r = \left[G_0\sigma_0 + G_1\sigma_1\left(\frac{a}{t}\right) + G_2\sigma_2\left(\frac{a}{t}\right)^2 + G_3\sigma_3\left(\frac{a}{t}\right)^3 + G_4\sigma_4\left(\frac{a}{t}\right)^4\right]\sqrt{\frac{\pi a}{Q}}\, f_w \tag{5}$$

$$Q = 1.0 + 1.464\left(\frac{a}{c}\right)^{1.65}$$

$$f_w = \left\{\sec\left(\frac{\pi c}{2W}\sqrt{\frac{a}{t}}\right)\right\}^{0.5}$$

where $G_0 - G_4$ are the shape correction factors of the stress intensity factor determined by API-RP579. a and c represent the depth and surface length of the semi-circular crack, respectively. W and t are the width and thickness of the plate, respectively. $\sigma_0 - \sigma_4$ are the factors obtained from the fourth-order polynomial approximation of the residual stress distribution.

$$\sigma(x) = \sigma_0 + \sigma_1\left(\frac{x}{t}\right) + \sigma_2\left(\frac{x}{t}\right)^2 + \sigma_3\left(\frac{x}{t}\right)^3 + \sigma_4\left(\frac{x}{t}\right)^4 \tag{6}$$

where x is the distance along the depth direction from the surface to the crack. In this study, the fourth-order polynomial approximation was used for the three types of compressive residual stress distributions shown in Fig. 2 to evaluate K_r. Table 4 lists the factors $\sigma_0 - \sigma_4$ obtained from the fourth-order polynomial approximation of residual stress distribution.

Table 4 Factors obtained from fourth-order polynomial of residual stress distribution

	σ_4	σ_3	σ_2	σ_1	σ_0
RS1	-8.46E+07	8.56E+06	1.03E+05	-1.64E+04	-1.48E+02
RS2	-1.75E+07	-8.74E+05	4.82E+05	-2.56E+04	-2.69E+02
RS3	2.89E+07	-6.04E+06	5.98E+05	-2.36E+04	-4.05E+02

Eq. (7) expresses the determining condition of a_{hlm} of the NP specimen:

$$\Delta K_{Tr} = \Delta K_{th(s)} \tag{7}$$

Eq. (7) was reviewed at points A and C, in Fig. 1, and a small crack size was determined with a_{hlm}.

The detection probability of a semi-circular fatigue crack was studied by Rummel et al. (1974). They reported that the ultrasonic detection method showed the best detection probability of fatigue cracks. According to them, cracks with a 100% detection probability in the optimal conditions of the laboratory using this method had $2c = 12$ mm and $a = 4$ mm. Moreover, cracks with a 50% detection probability had $2c = 1.2$ mm and $a = 0.26$ mm. The minimum crack dimensions were $c = a = 0.17$ mm. Recently, other researchers detected stress corrosion cracking with a depth (a) of 0.4 mm (Ochiai et al., 2006); however, since they did not mention the length, it was assumed to be a semi-circular crack. In this study, based on the above literature, we assumed that the ultrasonic detection method can sufficiently detect a semi-circular crack of $2c = 0.6$ mm and $a = 0.3$ mm. Among ultrasonic testing methods, the echo reflection method's echo intensity depends on the crack area. The area (S) of a semi-circular crack can be represented by Eq. (8):

$$S = \pi ac/2 \tag{8}$$

In other words, if the area of a semi-circular crack (S) is the same, even if the crack aspect ratio (As) changes, the crack detection probability remains the same. Therefore, if the area of a semi-circular crack of $2c = 0.6$ mm and $a = 0.3$ mm is S_{NDI}, then the relationship between the maximum crack size a_{NDI} that can be detected from S_{NDI} and As can be expressed by Eq. (9):

$$S_{NDI} = \pi a_{NDI}^2 / 2As \tag{9}$$

3. Results and Discussion

Fig. 3 shows the crack depth (a) dependence of ΔK_{th} and ΔK_{Tr} for residual stresses ①, ②, and ③ in the case of $As = 1.0$. Fig. 3(a) shows the results at point A, and Fig. 3(b) shows the results at point C. Eq. (7) expresses the condition for determining the maximum harmless crack dimensions using NP, and the small crack dimensions of point A and point C are selected. These crack dimensions are marked with ●. In the case of $As = 1.0$, a_{hlm} values of residual stresses ①, ②, and ③ were determined at point C for all $\Delta K_{th(l)}$.

Fig. 4 shows the crack depth (a) dependence of ΔK_{th} and ΔK_{Tr} for residual stresses ①, ②, and ③ in the case of $As = 0.6$. Fig. 4(a) shows the results at point A, and Fig. 4(b) shows the results at point C. In this case also, the crack dimensions that determine the maximum harmless crack dimensions are marked with ●. In the case of $As = 0.6$, a_{hlm} of residual stress ① was determined at point A for all $\Delta K_{th(l)}$. While a_{hlm} of residual stress ② was determined at point A in the cases of $\Delta K_{th(l)} = 3$ MPa$\sqrt{\text{m}}$ and $\Delta K_{th(l)} = 5$ MPa$\sqrt{\text{m}}$, it was determined at point C in the case of . In contrast, of residual stress ③ was determined at point A in the case of $\Delta K_{th(l)} = 3$ MPa$\sqrt{\text{m}}$ and at point C in the cases of

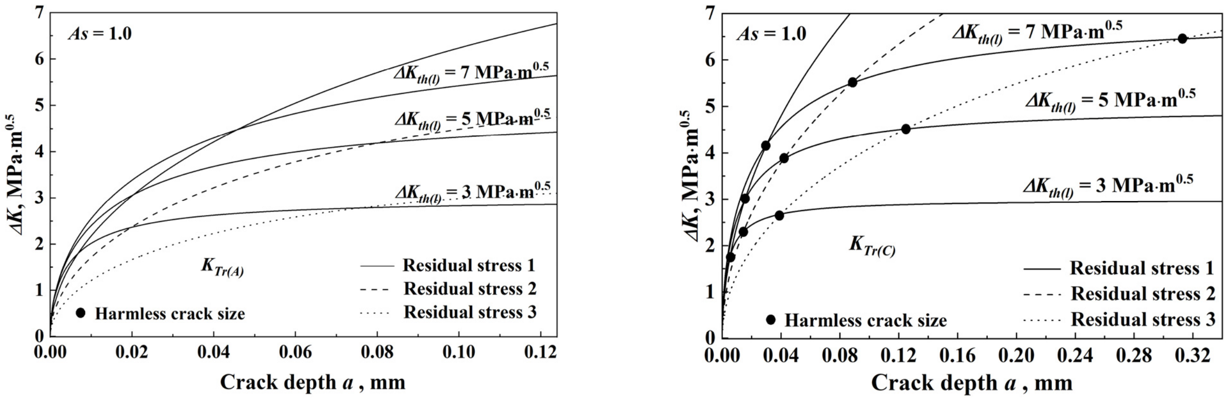

(a) (b)

Fig. 3 Crack depth dependence of ΔK_{th} and ΔK_{Tr} at (a) point A and (b) point C in the case of $As = 1.0$

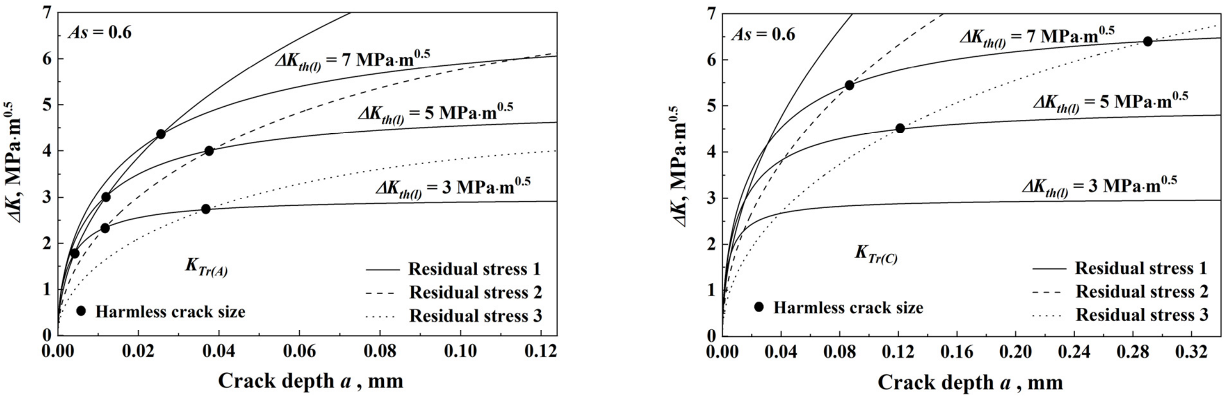

(a) (b)

Fig. 4 Crack depth dependence of ΔK_{th} and ΔK_{Tr} at (a) point A and (b) point C in the case of $As = 0.6$

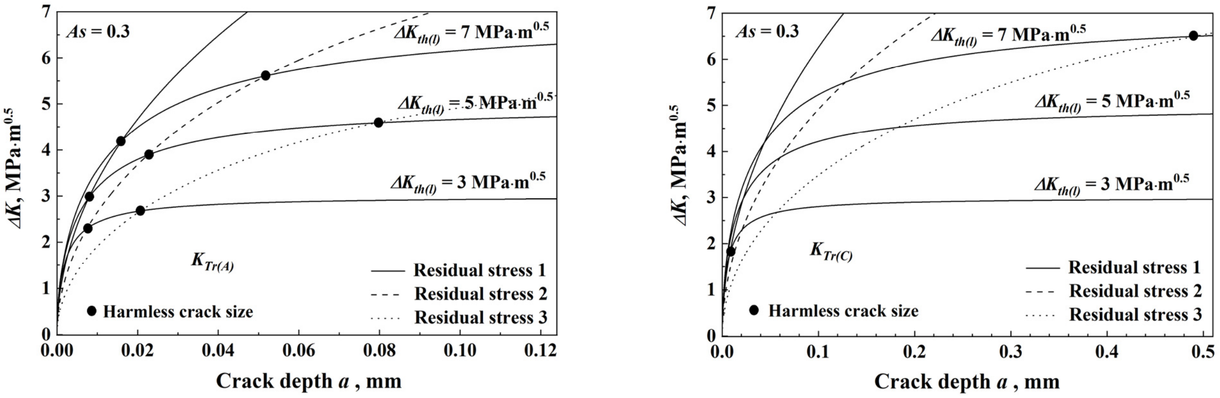

(a) (b)

Fig. 5 Crack depth dependence of ΔK_{th} and ΔK_{Tr} at (a) point A and (b) point C in the case of As = 0.3

$\Delta K_{th(l)} = 5$ MPa$\sqrt{\text{m}}$ and $\Delta K_{th(l)} = 7$ MPa$\sqrt{\text{m}}$.

Fig. 5 shows the crack depth (a) dependence of ΔK_{th} and ΔK_{Tr} in the case of As = 0.3 for residual stresses ①, ②, and ③. Fig. 5(a) shows the results at point A, Fig. 5(b) shows the results at point C. In this case also, the crack dimensions that determine the maximum harmless crack dimensions are marked with ●. In the case of As = 0.3, of residual stress ① was determined at point A when $\Delta K_{th(l)}$ = 5 MPa$\sqrt{\text{m}}$ and $\Delta K_{th(l)}$ = 7 MPa$\sqrt{\text{m}}$, but it was determined at point C when $\Delta K_{th(l)}$ = 3 MPa$\sqrt{\text{m}}$. a_{hlm} of residual stress ② was determined at point A for all $\Delta K_{th(l)}$. In contrast, a_{hlm} of residual stress ③ was determined at point A when $\Delta K_{th(l)}$ = 3 MPa$\sqrt{\text{m}}$ and $\Delta K_{th(l)}$ = 5 MPa$\sqrt{\text{m}}$ and at point C when $\Delta K_{th(l)}$ = 7 MPa$\sqrt{\text{m}}$.

Fig. 6 shows the crack depth (a) dependence of ΔK_{th} and ΔK_{Tr} in the case of As = 0.1 for residual stresses ①, ②, and ③. Fig. 6(a) shows the results at point A, and Fig. 6(b) shows the results at point C. In this case also, the crack dimensions that determine the maximum harmless crack dimensions are marked with ●. In the case of As = 0.1, a_{hlm} values of residual stresses ① and ② were determined at point A for all $\Delta K_{th(l)}$. However, a_{hlm} of residual stress ③ was determined at point A in the cases of $\Delta K_{th(l)}$ = 3 MPa$\sqrt{\text{m}}$ and $\Delta K_{th(l)}$ = 5 MPa$\sqrt{\text{m}}$ and at point C in the case of $\Delta K_{th(l)}$ = 7 MPa$\sqrt{\text{m}}$.

The surface crack nondamaging technology using NP is employed to ensure safety of structures. Fig. 7 shows the crack aspect ratio dependence of a_{hlm} when using NP. In Figs. 7(a), 7(b), and 7(c), $\Delta K_{th(l)}$ values are 3, 5, and 7 MPa$\sqrt{\text{m}}$, respectively. a_{hlm} was larger when the residual stress distribution was larger and deeper, indicating that a_{hlm} was considerably affected by the residual stress distribution. Furthermore, As and $\Delta K_{th(l)}$ increased, a_{hlm} increased.

Fig. 7 shows the crack depths corresponding to fatigue limit reduction rates of 25 % and 50% (a_{25}, a_{50}) in the non-NP specimens. The crack depth showed a decreasing tendency As decreased. Furthermore, the figure shows the relationship between a_{NDI} and As, which was evaluated using Eq. (9).

In Fig. 7(a), since a_{hlm} of residual stress ① is below a_{50}, it cannot be rendered harmless. Since a_{hlm} of residual stress ② is below a_{50}, it can not be rendered harmless; however, since it is above a_{25}, it can be rendered harmless. Meanwhile, since a_{hlm} of residual stress ③ is above a_{50}, it can be rendered harmless. Based on this, residual stress ③ can ensure the safety of structures that use this material via the surface crack nondamaging technology. In contrast, the crack detection ability (◆) determined by the above-assumed non-destructive inspection is above a_{50}. Therefore, it is difficult to detect cracks of a_{50} by using this non-destructive inspection, and it is necessary to apply a more sensitive non-destructive inspection technique.

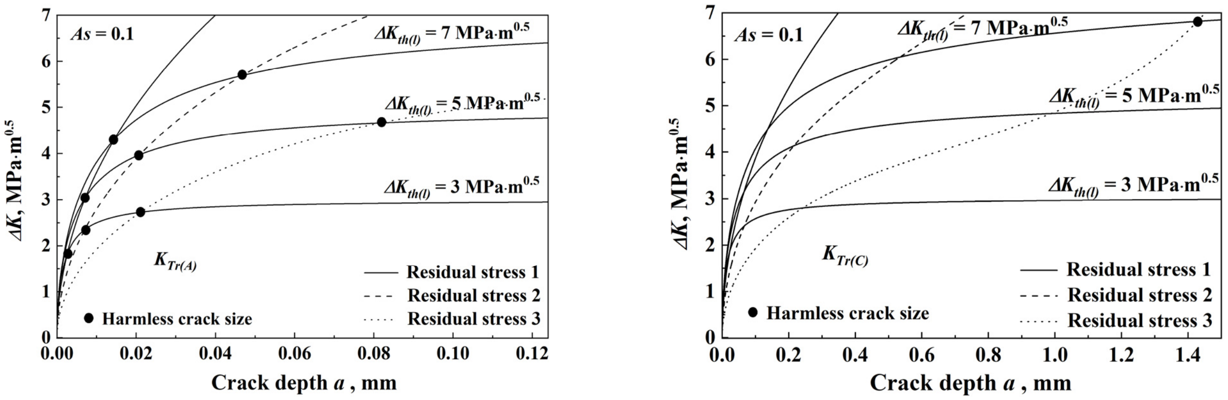

(a) (b)

Fig. 6 Crack depth dependence of ΔK_{th} and ΔK_{Tr} at (a) point A and (b) point C in the case of As = 0.1.

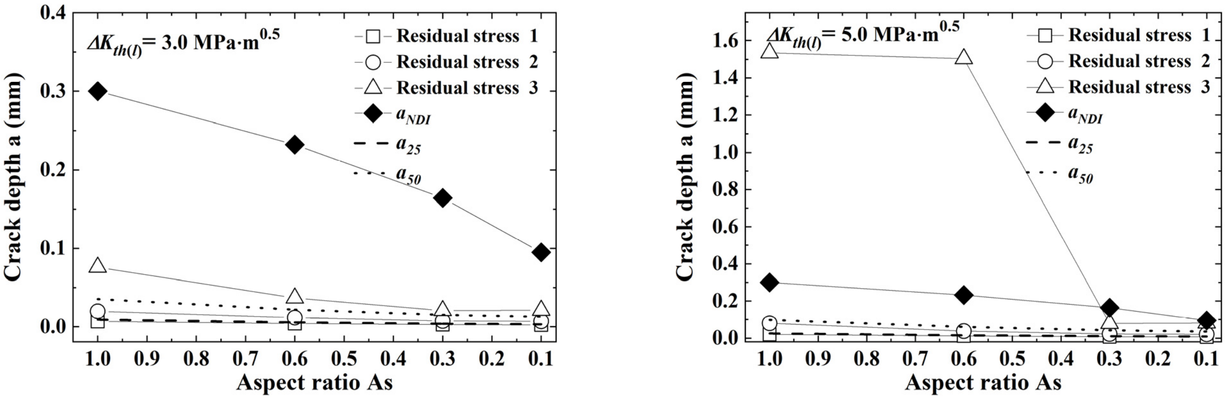

(a) $\Delta K_{th(l)} = 3.0$ MPa$\sqrt{\text{m}}$ (b) $\Delta K_{th(l)} = 5.0$ MPa$\sqrt{\text{m}}$

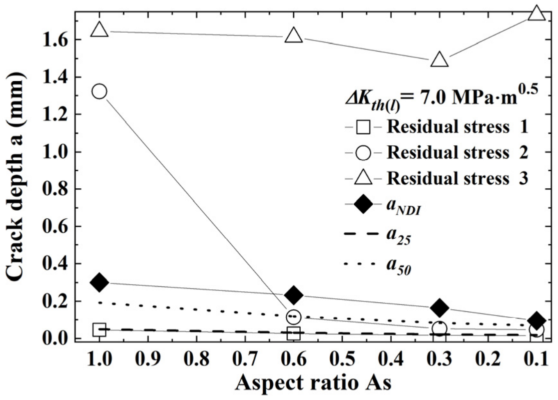

(c) $\Delta K_{th(l)} = 7.0$ MPa$\sqrt{\text{m}}$

Fig. 7 Effect of As on the rendered harmless crack depth (a_{hlm}), a_{25} and a_{50}

In Fig. 7(b), since a_{hlm} of residual stress ① is below a_{25}, it can not be rendered harmless. Since a_{hlm} of residual stress ② is above a_{25}, it can be rendered harmless. However, since it is below a_{50}, it cannot be rendered harmless. a_{hlm} of residual stress ③ can be rendered harmless since it is above a_{50}. Based on this, residual stress ③, determined using the surface crack nondamaging technology, can ensure the safety of structures that use this material. In contrast, the crack detection ability (◆) determined by the above-assumed non-destructive inspection is above a_{50}. Therefore, it is difficult to detect cracks of a_{50} by using this non-destructive inspection, and it is necessary to apply a more sensitive non-destructive inspection technique.

In Fig. 7(c), since a_{hlm} of residual stress ① is below a_{25}, it cannot be rendered harmless. Furthermore, since a_{hlm} of residual stress ② is above a_{25}, it can be rendered harmless; however, since it is below a_{50} except for a_{hlm} of As = 1.0, it cannot be rendered harmless. a_{hlm} of residual stress ③ can be rendered harmless since it is above a_{50}. Based on this, residual stress ③ can ensure the safety of structures that use this material via the surface crack nondamaging technology. In contrast, the crack detection ability (◆) determined by the above-assumed non-destructive inspection is above a_{50}. Therefore, it is difficult to detect cracks of a_{50} by using this non-destructive inspection, and it is necessary to apply a more sensitive non-destructive inspection technique.

Based on this, residual stress ①, determined by the surface crack nondamaging technology, cannot ensure the safety of structures that use this material; however, residual stress ② with As = 1.0 and residual stress ③ can ensure the safety of structures. In contrast, since the crack detection ability (◆) determined by the non-destructive inspection assumed for residual stresses ② and ③ is above a_{50}, this non-destructive inspection cannot detect cracks of a_{50}.

In Fig. 8, examination results of the maintenance and reliability of fatigue failure using non-destructive inspection and surface crack nondamaging technology (Nam et al., 2021) are shown. The schematic diagrams in Figs. 8(a)–8(d) show a_{hlm} and a_{NDI} determined when using NP and the relationship between the crack depth (a_{crN}), which reduces the fatigue limit to 1/N, and the crack aspect ratio (As) when the safety factor is N. In Fig. 8(a), the condition is $a_{crN} < a_{hlm} < a_{NDI}$. Under this condition, the surface crack nondamaging technology can facilitate appropriate maintenance, but the non-destructive inspection cannot facilitate appropriate maintenance. In Fig. 8(b), the condition is $a_{NDI} < a_{crN} < a_{hlm}$. Under this condition, both non-destructive inspection and the surface crack nondamaging technology can facilitate appropriate maintenance. If NP is performed after non-destructive inspection to ensure complete safety, it can contribute greatly to the shortening of the periodic inspection period because it is required to detect only cracks that are deeper than the crack depth

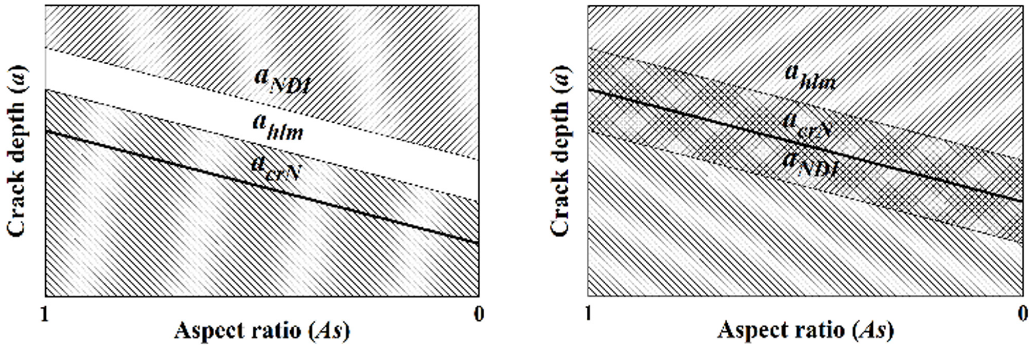

(a) $a_{crN} < a_{hlm} < a_{NDI}$ (b) $a_{NDI} < a_{crN} < a_{hlm}$

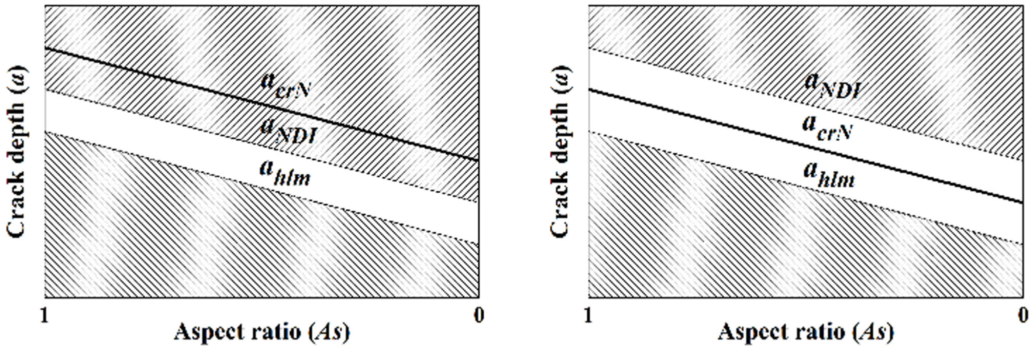

(c) $a_{hlm} < a_{NDI} < a_{crN}$ (d) $a_{hlm} < a_{crN} < a_{NDI}$

Fig. 8 Schematic diagram of the application of surface crack nondamaging techniques and nondestructive inspection to material integrity

corresponding to a_{hlm}. In Fig. 8(c), the condition is $a_{hlm} < a_{NDI} < a_{crN}$. Under this condition, non-destructive inspection alone can facilitate appropriate maintenance, and the surface crack nondamaging technology cannot facilitate appropriate maintenance. In Fig. 8(d), the condition is $a_{hlm} < a_{crN} < a_{NDI}$. Under this condition, since a_{crN} is very small, it pertains to structural ceramics, and appropriate maintenance is impossible with non-destructive inspection and the surface crack nondamaging technology. However, peening forms significant residual stress in structural ceramics. Quality assurance can be provided for cracks caused by peening after self-healing.

4. Conclusion

In the case of varying $\Delta K_{th(l)}$ and three types of residual stresses of offshore structural high-strength steel F690, we evaluated As dependence of $\Delta K_{th(l)}$ and As dependence of crack depths (a_{25} and a_{50}) corresponding to fatigue limit reduction rates of 25 % and 50% in Non-NP specimens. Furthermore, in the case where the fatigue crack surface is the same irrespective of As, we evaluated the As dependence of a_{NDI} using high-performance non-destructive inspection. Based on the results, we examined how the surface crack nondamaging technology will contribute to the longevity of F690 and the reliability of maintenance. The conclusions drawn are as follows.

(1) a_{hlm} was larger when the residual stress distribution was larger and deeper, indicating that a_{hlm} was considerably affected by the residual stress distribution. Furthermore, as As and $\Delta K_{th(l)}$ increased, a_{hlm} increased.

(2) At $\Delta K_{th(l)}$ = 3, 5, and 7 $\mathrm{MPa}\sqrt{\mathrm{m}}$, a_{hlm} of residual stress ③ is above a_{50}, and at $\Delta K_{th(l)}$ = 7 $\mathrm{MPa}\sqrt{\mathrm{m}}$ in the case of residual stress ②, a_{hlm} of As = 1.0 is above a_{50}. Therefore, in the case of N = 2.0, the safety and reliability of F690 used for a long time can be ensured when using NP.

(3) Since the crack detection ability (◆) determined by the assumed non-destructive inspection cannot detect a_{50} at residual stresses ①, ②, and ③, it is necessary to apply a more sensitive non-destructive inspection technique.

(4) With the relationship of a_{hlm}, a_{NDI}, and a_{crN} with As, we examined the usefulness of non-destructive inspection and the crack nondamaging technology.

Funding

This work was supported by a Research Grant of Pukyong National University (2021).

References

Al-Hassani, S.T.S. (1982). The Shot Peening of Metals—Mechanics and Structures. SAE Transactions, 91(4), 4513–4525. Retrieved July 27, 2021, from http://www.jstor.org/stable/44634444

Al-Obaid, Y.F. (1990). A Rudimentary Analysis of Improving Fatigue Life of Metals by Shot-Peening. Journal of Applied Mechanics, 57(2), 307–312. https://doi.org/10.1115/1.2891990

Ando, K., Fueki, R., Nam, K.W., Matsui, K., & Takahashi, K. (2019). A Study on the Unification of the Threshold Stress Itensity Factor for Micro Crack Growth. Transactions of Japan Society for Spring Engineers, 2019(64), 39–44. https://doi.org/10.5346/trbane.2019.39

Ando, K., Nam, K.W., Kim, M.H., Ishii, T., & Takahashi, K. (2020). Analysis of Peculiar Fatigue Fracture Behavior of Shot Peened Steels Focusing on Threshold Stress Intensity Factor Range. Transactions of Japan Society for Spring Engineers, 2020(65), 35–41. https://doi.org/10.5346/trbane.2020.35

Ando, K., Kim, M.H., & Nam, K.W. (2021). Analysis on Peculiar Fatigue Fracture Behavior of Shot Peened Metal Using New Threshold Stress Intensity Range Equation. Fatigue & Fracture of Engineering Materials & Structures, 44(2), 306–316. https://doi.org/10.1111/ffe.13356

American Petroleum Institute (API). (2000). Recommended Practice 579, Fitness for Service. American Petroleum Institute, C3–C10.

Benedetti, M., Fontanari, V., Höhn, B.R., Oster, P., & Tobie, T. (2002). Influence of Shot Peening on Bending Tooth Fatigue Limit of Case Hardened Gears. International Journal of Fatigue, 24(11), 1127–1136. https://doi.org/10.1016/S0142-1123(02)00034-8

EI Haddad, M.H., Topper, T.H., & Smith, K.N. (1979). Prediction of non Propagating Cracks. Engineering Fracture Mechanics, 11(3), 573–584. https://doi.org/10.1016/0013-7944(79)90081-X

Fueki, R., Takahashi, K., & Houjou. K. (2015). Fatigue Limit Prediction and Estimation for the Crack Size Rendered Harmless by Peening for Welded Joint Containing a Surface Crack. Materials Sciences and Applications, 6(6), 500–510. https://doi.org/10.4236/msa.2015.66053

Fueki, R., Takahashi, K., & Handa, M. (2019). Fatigue Limit Improvement and Rendering Defects Harmless by Needle Peening for High Tensile Steel Welded Joint. Metals, 9(2), 143, https://doi.org/10.3390/met9020143

Harada, Y., Fukaura, K., & Haga, S. (2007). Influence of Microshot Peening on Surface Layer Characteristics of Structural Steel. Journal of Materials Processing Technology, 191(1–3), 297–301. https://doi.org/10.1016/j.jmatprotec.2007.03.026

Houjou, K., Takahashi, K., Ando, K., & Sekiguchi, Y. (2013a). Improvement of Fatigue Limit and Rendering Crack Harmless by Peening for Rolled Steel Containing a Crack at the Weld Toe Zone. Transactions of the Japan Society of Mechanical Engineers A, 79(797), 110–114. https://doi.org/10.1299/kikaia.79.110

Houjou, K., Takahashi, K., & Ando, K. (2013b). Improvement of Fatigue Limit by Shot Peening for High-Tensile Strength Steel Containing a Crack in the Stress Concentration Zone. International Journal of Structural Integrity, 4(2), 258–266. https://doi.org/10.1108/17579861311321726

Kim, J.H., & Kim, Y.I. (2018). Numerical Simulation on the Response of Moored Semi-submersible Under Ice Load. Journal of Ocean Engineering and Technology, 32(3), 177–183. https://doi.org/10.26748/KSOE.2018.6.32.3.177

Kim, M.H., Hyun, J.Y., & Nam, K.W. (2020). Evaluation of Harmless Crack Size using Ando's Equation. Journal of Mechanical Science and Technology, 34, 1971–1977. https://doi.org/10.1007/s12206-020-0418-7

Kim, M.H., Lee, W.G., Kim, C.S., Takahashi, K., Handa, M., & Nam, K.W. (2021). Evaluation of Fatigue Limit and Harmless Crack Size of Needle Peened Offshore Structure Steel F690. Journal of Mechanical Science and Technology, 35(9), 3855–3862. https://doi.org/10.1007/s12206-021-2109-4

Lee, J.G., & Kim, J.K. (1997). Influence of Residual Stress Due to Shot Peening on Fatigue Strength and Life. Transactions of the Korean Society of Mechanical Engineers A, 21(9), 1498–1506. https://doi.org/10.22634/KSME-A.1997.21.9.1498

Lee, K.Y., Choi, H.S., Lee, E.J., & Yoon, T.S. (2011). Future Vision Through NL Tensioner Technology Development and Domestic Equipment Fabrication. Journal of Ocean Engineering and Technology, 25(2), 127–133. https://doi.org/10.5574/KSOE.2011.25.2.127

Nakagawa, M., Takahashi, K., Osada, T., Okada, H., & Koike, H. (2014). Improvement in Fatigue Limit by Shot Peening for High-Strength Steel Containing Crack-like Surface Defect (Influence of Surface Crack Aspect Ratio). Japan Society of Spring Engineers, 2014(59), 13–18. https://doi.org/10.5346/trbane.2014.13

Nam, K.W., Ando, K., Kim, M.H., & Takahashi, K. (2021). Improving Reliability of High Strength Steel Designed Against Fatigue Limit using Surface Crack Nondamaging Technology by Shot Peening. Fatigue & Fracture of Engineering Materials & Structures, 44(6), 1062–1610. https://doi.org/10.1111/ffe.13460

Newman, J.C.Jr., & Raju, I.S. (1981). An Empirical Stress-Intensity Factor Equation for the Surface Crack. Engineering Fracture Mechanics, 15(1–2), 185–192. https://doi.org/10.1016/0013-7944(81)90116-8

Ochiai, M., Miura, T., & Yamamoto, S. (2006). Laser-Ultrasonic Nondestructive Testing and Its Application to Nuclear Industry. Toshiba Review, 61(1), 44–47.

Park, H.S., Kim, M.H., & Nam, K.W. (2020). A Study on the Threshold Stress Intensity Factor and Fatigue Limit of Short Crack Growth. Transactions of the Korean Society of Mechanical Engineers A, 44(11), 781–786. https://doi.org/10.3795/KSME-A.2020.44.11.781

Park, H.S., Kim, M.H., & Nam, K.W. (2021). Study of Threshold Stress Intensity Factor and Fatigue Limit for Through Crack in Infinite Plate and Semi-Elliptical Surface Crack in Finite Plate. Transactions of the Korean Society of Mechanical Engineers A, 45(2), 133–139. https://doi.org/10.3795/KSME-A.2021.45.2.133

Rummel, W.D., Todd, P.H. Jr., Frecska, S.A., & Rathke, R.A. (1974). The Detection of Fatigue Cracks by Nondestructive Testing Methods (Report NASA-CR-2369). NASA Contractor.

Song, C.Y., Choi, H.Y., & Shim, S.H. (2013). Structural Safety Evaluation of Marine Loading Arm Using Finite Element Analysis. JJournal of Ocean Engineering and Technology, 27(1), 43–50. https://doi.org/10.5574/KSOE.2013.27.1.043

Takahashi, K., Okada, H., & Ando, K. (2012). Effects of Shot Peening on the Torsional Fatigue Limit of High-Strength Steel Containing an Artificial Surface Defect. International Journal of Structural Integrity, 3(3), 274–284. https://doi.org/10.1108/17579861211264389

Tange, A., Akutu, T., & Takamura, N. (1991). Relation Between Shot-Peening Residual Stress Distribution and Fatigue Crack Propagation Life in Spring Steel. Transactions of Japan Society for Spring Engineers, 1991(36), 47–53. https://doi.org/10.5346/trbane.1991.47

Author ORCIDs

Author name	ORCID
Lee, Weon-Gu	0000-0002-3098-4018
Gu, Kyoung-Hee	0000-0001-5364-4713
Kim, Cheol-Su	0000-0002-8057-8771
Nam, Ki-Woo	0000-0001-7019-358X

KSOE

Journal of Ocean Engineering and Technology 35(5), 336-346, October, 2021
https://doi.org/10.26748/KSOE.2021.021

pISSN 1225-0767
eISSN 2287-6715

Original Research Article

Prediction of Significant Wave Height in Korea Strait Using Machine Learning

Sung Boo Park[1], Seong Yun Shin[1], Kwang Hyo Jung[2] and Byung Gook Lee[3]

[1]*Graduate student, Department of Naval Architecture and Ocean Engineering, Pusan National University, Busan, Korea*
[2]*Professor, Department of Naval Architecture and Ocean Engineering, Pusan National University, Busan, Korea*
[3]*Professor, Department of Computer Engineering, Dongseo University, Busan, Korea*

KEY WORDS: Machine learning, Significant wave height, Korea Strait, Feedforward neural network, Long short-term memory, Pearson correlation coefficient

ABSTRACT: *The prediction of wave conditions is crucial in the field of marine and ocean engineering. Hence, this study aims to predict the significant wave height through machine learning (ML), a soft computing method. The adopted metocean data, collected from 2012 to 2020, were obtained from the Korea Institute of Ocean Science and Technology. We adopted the feedforward neural network (FNN) and long-short term memory (LSTM) models to predict significant wave height. Input parameters for the input layer were selected by Pearson correlation coefficients. To obtain the optimized hyperparameter, we conducted a sensitivity study on the window size, node, layer, and activation function. Finally, the significant wave height was predicted using the FNN and LSTM models, by varying the three input parameters and three window sizes. Accordingly, FNN (W48) (i.e., FNN with window size 48) and LSTM (W48) (i.e., LSTM with window size 48) were superior outcomes. The most suitable model for predicting the significant wave height was FNN(W48) owing to its accuracy and calculation time. If the metocean data were further accumulated, the accuracy of the ML model would have improved, and it will be beneficial to predict added resistance by waves when conducting a sea trial test.*

1. Introduction

Metocean data are essential in the marine industry, such as in the transportation, installation, operation, and survival of offshore structures. They are also adopted to determine the departure time and route of merchant vessels, as well as new renewable energy development projects, and offshore constructions. Shipboard measurements began in 1854 for time-series observations of wind speed and wave height, while marine buoy was introduced in the 1970s for metocean observations. Owing to the emergence of marine observation satellites in the late 1970s, elucidating the phenomena of wind and waves became possible, and approximately 30 years of data covering the entire globe were collected with the steady development of technologies (Meucci et al., 2020). These accumulated measurement data have been harnessed to generate the re-analysis and hindcast data calculated via energy balance equations for wind and waves, including several ocean wave models and mathematical techniques (e.g., the differential equation of wave energy). Furthermore, owing to the consistent advancement of numerical models, predicting metocean conditions worldwide has become possible.

The European Centre for Medium-Range Weather Forecasts and the National Oceanic and Atmospheric Administration are well-known agencies that provide metocean predictions. In addition, the statistical analysis of metocean data enables the prediction of extreme values in extensive return periods (e.g., 10, 20, and 100 years) for the operation and survival of merchant vessels and offshore structures during their life cycle (Park et al., 2020). However, terrain and sea surface wind are required as input conditions when numerical wave models are used. Furthermore, temporal and spatial changes in waves are estimated according to the laws of physics; hence, they do not have a sufficient level of precision to replace the observed data. To address these issues, a study was conducted to estimate wave height through machine learning (ML; Kumar et al., 2018).

Conventionally, to enable computers solve a specific problem, humans digitize (e.g., define functions and assign boundary conditions) this problem using mathematical and statistical techniques. Conversely, using ML, humans provide the machine with information related to the problem they attempt to solve, and the machine learns

Received 7 May 2021, revised 8 July 2021, accepted 9 July 2021
Corresponding author Kwang Hyo Jung: +82-51-510-2343, kjung@pusan.ac.kr

and decipher the rules for the solution to the problem. That is, ML is a data-driven modeling technology that enables machines to grasp the relationship between the input and output by learning by itself, without adopting any specific mathematical forms to solve the problem. From 1940 to 1950, scientists from various fields began the discussion on the possibility of an artificial brain. However, it was not until 1956 that the term artificial intelligence (AI) was officially used. Afterward, this technology passed through a period of technological renaissance, followed by a period of stagnation. Currently, it is called machine learning, artificial neural network (ANN), or deep learning and is currently being incorporated into various academic and industrial fields. With the enhancements in big data technology and computer performance, ML is expected to continue expanding into other fields at an increasing rate (Haenlein and Kaplan, 2019). LeCun et al. (2015) introduced conventional ML models, such as feedforward neural network (FNN), convolutional neural network (CNN), recurrent neural network (RNN), and long-short term memory (LSTM). They also mentioned that these ML models can be applied in areas ranging from simple regression problems to image and voice recognition, language processing, and the medical industry. Moreover, studies have been conducted to detect oil spills using FNN (Kim and Kim, 2017) and to predict the path of a typhoon (Kim et al., 2019), as well as the volume of goods transported using LSTM (Kim and Lee, 2020).

Jain and Deo (2006) presented previous studies that have utilized FNN in the field of ocean engineering. These studies include metocean (e.g., wave height, wave period, wind speed, and tidal level) predictions, as well as predictions of environmental forces acting on marine structures, damage to offshore structures, ship motions, and hull design. Among them, research that utilizes FNN to predict marine weather at a single location is being actively conducted. Moreover, a study was conducted on predicting wave variables (i.e., significant wave height and wave period) in the near future, using the past wave data measured using a buoy (Deo and Naidu, 1998; Makarynskyy, 2004). A study was also performed on predicting wave variables using FNN (Mandal and Prabaharan, 2006). Furthermore, research was conducted to predict wave variables via FNN, using previously collected wind data (e.g., wind speed and wind direction) at a single location (Deo et al., 2001; Kim, 2020). Malekmohamadi et al. (2011) predicted significant wave heights using various soft computing methods (support vector machines (SVMs), Bayesian networks (BNs), and adaptive neuro-fuzzy inference system (ANFIS)), including FNN. In addition, they demonstrated that FNN produces better results than other models. To improve the accuracy of wave prediction, a hybrid-type model known as an empirical orthogonal function (EOF)-wavelet-neural network, which incorporated the ML model into the conventional statistical method, was proposed (Oh and Suh, 2018). Furthermore, a convolutional long short-term memory (ConvLSTM) model was developed by combining CNN and LSTM models, and the ConvLSTM model was proposed to solve the problem with the prediction of sea surface temperature (Jung et al., 2020). However, to perform ML for metocean predictions, it remains impossible for machines to handle the entire process unassisted. The input data for solving problems, selection of a suitable ML model, and tuning of hyperparameters are crucial in ML. However, human intervention is still required in this process, and it takes a significant amount of trial and error to create a ML model that can make excellent metocean predictions.

This paper proposes a ML model that predicts significant wave heights using the metocean data obtained from an oceanographic buoy at the Korea Strait, which was provided by the Korea Institute of Ocean Science and Technology (KIOST). The types and number of input data were classified into three cases by considering the Pearson correlation coefficient of the collected metocean data. The FNN and LSTM models that have incorporated the concept of window size were adopted as the ML model. The numbers of nodes and layers, including the activation functions for the hidden layer, were varied to derive the combination of hyperparameters that minimize the mean absolute error (MAE) between the predicted and measured values for the validation set. An ML model that predicts significant wave heights using the input variables, as well as the selected hyperparameters and their characteristics, were regarded as the outcome of this study.

2. Collection of Metocean Data and Statistical Analysis

The metocean data were collected from the Korea Strait oceanographic buoy provided by KIOST. The Korea Strait is one of the representative sea areas where sea trials are conducted on domestically built vessels before delivery. Fig. 1 illustrates the location of the Korea Strait oceanographic buoy. Its latitude and longitude are 34°55′0″ N and 129°07′16″ E, respectively. The Korea Strait oceanographic buoy commenced observations in September 2012 and has been in operation since then. The data adopted in this study span a total period of 9 years (from 2012 to 2020). The collected data comprise 13 categories and is organized in intervals of 30 min. These categories include surface current speed,

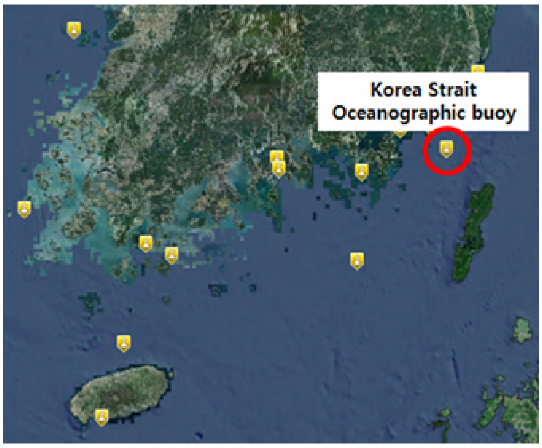

Fig. 1 Location of Korea Strait oceanographic buoy (Korea Institute of Ocean Science and Technology (KIOST), 2021)

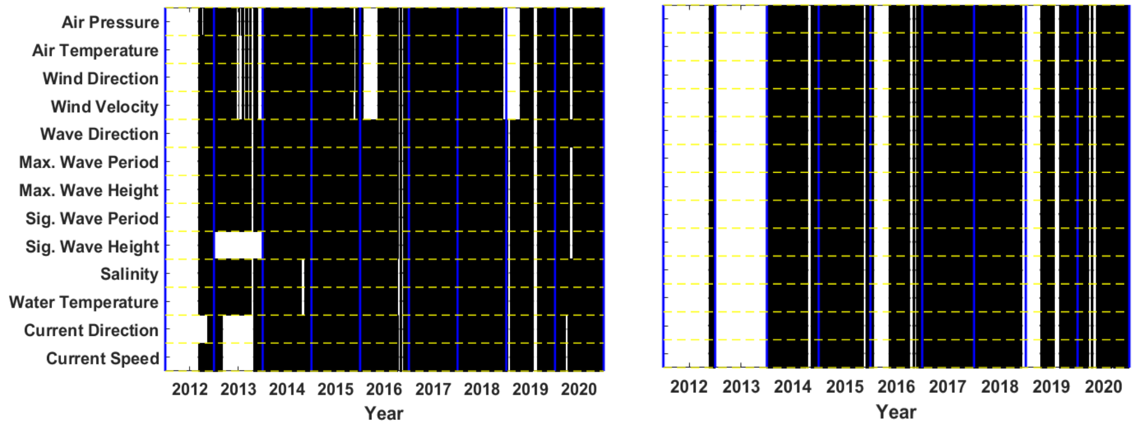

(a) Raw data (b) Filtered data

Fig. 2 Metocean data (2012~2020) of Korea Strait oceanographic buoy

Table 1 Data availability of metocean data of Korea Strait oceanographic buoy

Year	No. of raw data	No. of outlier data (‘NaN’, ‘-’, ‘0’, ‘99.99’)	No. of filtered data	Data availability (%)
2012	17,568	15,413	2,155	12.3
2013	17,520	17,520	0	0.0
2014	17,520	1,842	15,678	89.5
2015	17,520	2,536	14,984	85.5
2016	17,568	7,718	9,850	56.1
2017	17,521	1,061	16,460	93.9
2018	17,520	1,572	15,948	91.0
2019	17,520	7,304	10,216	58.3
2020	17,568	3,982	13,586	77.3
Total	157,825	58,948	98,877	-

surface current direction, water temperature, salinity, significant wave height, significant wave period, maximum wave height, maximum wave period, wave direction, wind speed, wind direction, air temperature, and air pressure. For the raw data, approximately 17,500 data sets are measured and stored each year on average, and the total number of data sets over the 9-year period is 157,825. There were outliers in the raw data because of the malfunction of the measuring equipment and facility repairs, owing to bad weather conditions. For time period that contain outliers (‘NaN’, ‘-’, ‘0’, ‘99.99’), all environment variables, including the time period, were discarded from the dataset. Fig. 2 and Table 1 present the number of data for each year for the raw and filtered data from where the outliers have been eliminated. The number of filtered data in 2012 and 2013 is significantly low because the buoy commenced its operation in September 2012, and significant wave height and current information were not stored in 2013 owing to an inherent problem with the measuring equipment. Excluding the data for 2012 and 2013, the amount of usable data is approximately 78% of the total data.

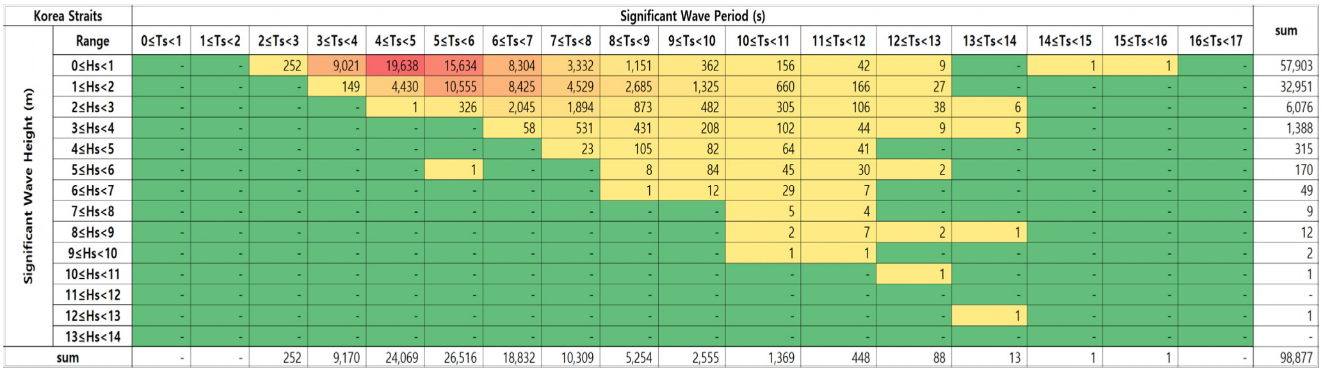

Korea Straits		Significant Wave Period (s)																	sum
	Range	0≤Ts<1	1≤Ts<2	2≤Ts<3	3≤Ts<4	4≤Ts<5	5≤Ts<6	6≤Ts<7	7≤Ts<8	8≤Ts<9	9≤Ts<10	10≤Ts<11	11≤Ts<12	12≤Ts<13	13≤Ts<14	14≤Ts<15	15≤Ts<16	16≤Ts<17	
Significant Wave Height (m)	0≤Hs<1	-	-	252	9,021	19,638	15,634	8,304	3,332	1,151	362	156	42	9	-	1	1	-	57,903
	1≤Hs<2	-	-	-	149	4,430	10,555	8,425	4,529	2,685	1,325	660	166	27	-	-	-	-	32,951
	2≤Hs<3	-	-	-	-	1	326	2,045	1,894	873	482	305	106	38	6	-	-	-	6,076
	3≤Hs<4	-	-	-	-	-	-	58	531	431	208	102	44	9	5	-	-	-	1,388
	4≤Hs<5	-	-	-	-	-	-	-	23	105	82	64	41	-	-	-	-	-	315
	5≤Hs<6	-	-	-	-	-	1	-	-	8	84	45	30	2	-	-	-	-	170
	6≤Hs<7	-	-	-	-	-	-	-	-	1	12	29	7	-	-	-	-	-	49
	7≤Hs<8	-	-	-	-	-	-	-	-	-	-	5	4	-	-	-	-	-	9
	8≤Hs<9	-	-	-	-	-	-	-	-	-	-	2	7	2	1	-	-	-	12
	9≤Hs<10	-	-	-	-	-	-	-	-	-	-	1	1	-	-	-	-	-	2
	10≤Hs<11	-	-	-	-	-	-	-	-	-	-	-	-	1	-	-	-	-	1
	11≤Hs<12	-	-	-	-	-	-	-	-	-	-	-	-	-	-	-	-	-	-
	12≤Hs<13	-	-	-	-	-	-	-	-	-	-	-	-	-	1	-	-	-	1
	13≤Hs<14	-	-	-	-	-	-	-	-	-	-	-	-	-	-	-	-	-	-
sum		-	-	252	9,170	24,069	26,516	18,832	10,309	5,254	2,555	1,369	448	88	13	1	1	-	98,877

Fig. 3 Wave scatter diagram

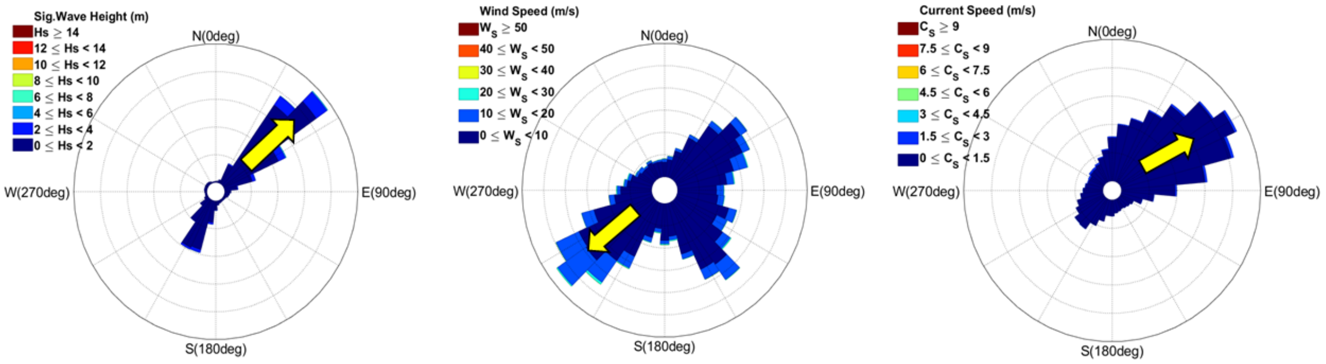

(a) Wave (b) Wind (c) Current

Fig. 4 Rose diagram for wave, wind, and current

The statistical analysis was performed using approximately 98,000 filtered data. Fig. 3 presents the wave scatter diagram(WSD) for the significant wave height and significant wave period, and Fig. 4(a) presents the wave rise with significant wave height and wave direction. In addition, Fig. 4(b) presents the wind rose with the wind speed and wind direction, while Fig. 4(c) illustrates the current rose diagram with the surface current speed and surface current direction.

The WSD presents the frequency of the significant wave height at intervals of 1 m, as well as the frequency of the significant wave period at intervals of 1 s. The wave condition with the most frequency is between 0 m and 1 m for the significant wave height, and between 4 s and 5 s for the significant wave period. The direction the waves, winds, and currents move toward is depicted using a rose diagram and is divided into the east (90°), south (180°), and west (270°), in a clockwise direction from the true north (0°). According to the KIOST, the direction the waves and currents move toward and the direction the wind blows from are defined as the direction of each environmental variable. However, the definition of wind direction was altered to match the definition of wave and current direction and to adopt the direction as an input variable for the ML model. The most dominant directions of wave, wind, and currents in 16 azimuths are the northeast (NE), southwest (SW), and east-northeast (ENE) directions, respectively. For the wind direction, the frequency of the winds blowing toward the southeast (SE) direction is high as well, and it is presumed to be the effect of the northwest wind, which blows during the winter season in Korea.

In Fig. 5, the remaining categories, water temperature, salinity, air temperature, and air pressure are presented in histograms, which represent probabilities. The histogram for water temperature presents a uniform distribution, mostly between 10 ℃ and 30 ℃, and the salinity histogram exhibits a unimodal probability distribution at approximately 5 psu. Similarly, the histograms for air temperature and air pressure exhibit unimodal probability distributions at approximately 20 ℃ and 1010 hPa, respectively. In the air temperature case, an unrealistic temperature of approximately -60 ℃ was intermittently measured. Nevertheless, it is challenging to determine a reasonable threshold that can distinguish outliers in metocean data. However, an advantage of ML is that a small number of outliers do not have a significant effect on

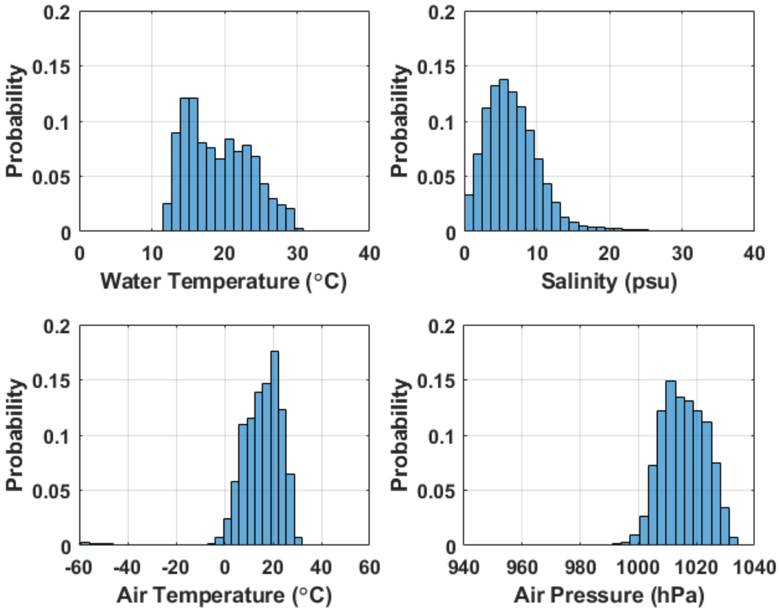

Fig. 5 Probability histogram for water temperature, salinity, air temperature, and air pressure

the ML results (Jain and Deo, 2006). Therefore, the existing small number of outliers for air temperature (2% of the total data) was not discarded. Finally, the maximum wave height and maximum wave period were not adopted as input variables in this study; hence, they are not presented separately.

3. Machine Learning (ML) Methodology

The basic structure of an artificial neural network is created by imitating the human brain, which generates an output when a certain threshold is exceeded at a synapse junction between neurons. In this study, FNN and LSTM were adopted as the ML models. FNN is the simplest ML model that comprises input, hidden, and output layers, and LSTM exhibits an excellent performance in time-series learning. The first FNN layer is an input layer, and the number of nodes in the input layer is set to match the number of input variables. The final layer is the output layer, and it has the same number of nodes as the number of predictor variables. The layers between the input and output layers are called hidden layers, and the product of the input variables and weights are calculated using the arithmetic operation of the activation function. As the number of hidden layers increases, the neural network is called the multi-layer FNN or deep learning.

Datasets are generally classified into a training and a test sets or training, validation, and test sets for machine learning. Recently, the rectified linear unit (ReLU), sigmoid, and hyperbolic tangent (Tanh) functions have been widely adopted as the activation function of hidden layers (LeCun et al., 2015). A linear function is used as the activation function for the output layer when there is no limit on the output value range. The result obtained from the arithmetic operations of the activation function in the output layer is the predicted value, and this value is compared with the measured value. The mean squared error (MSE) or the MAE is often adopted as the error function for this process. ML updates the weights and bias to minimize the error between the predicted and measured values. This process can be performed using an error backpropagation algorithm in a multi-layer neural network. The error backpropagation algorithm progresses from the output layer to the input layer, and it updates the weights and bias values of each layer of the neural network by using the partial derivatives of the error function. In addition, the error backpropagation algorithm can control the learning speed based on the learning rate. If the learning rate is quite high, the global minima cannot be attained. In contrast, the learning slows down if the learning rate is quite low, and the gradient descent falls into the local minima, which prevents it from reaching the global minima. An advanced gradient descent method known as the Adam optimizer is widely adopted in programming. A previous study adopted the concept of momentum to prevent the gradient descent from falling into the local minima, and this method can quickly and accurately determine the point where the differential gradient is the minimum (Cho, 2020).

LSTM is suitable for time-series data because it is configured with a feedback connection. It was devised to address the vanishing gradient or exploding gradient problem of RNN, which has a multi-layered structure. Hochreiter and Schmidhuber (1997) first developed LSTM by altering the internal nodes of the RNN with a complex structure

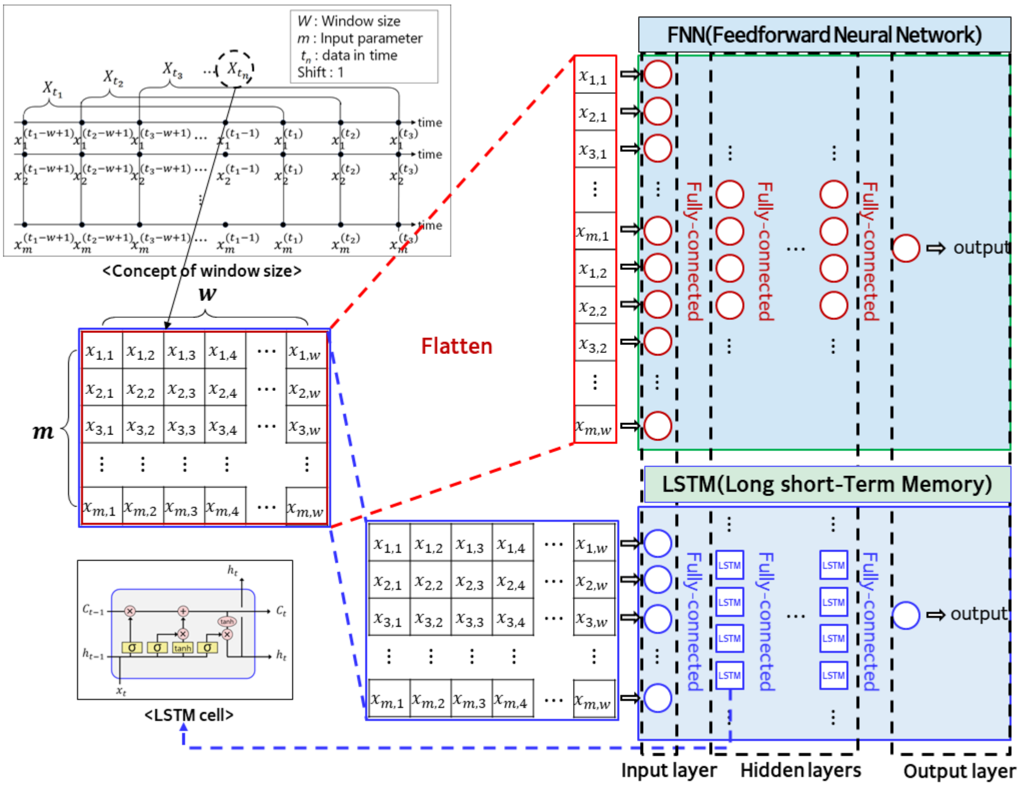

Fig. 6 FNN and LSTM architecture with window size

called a memory cell. It was improved by Gers et al. (1999), and the improved version is currently adopted as the ML model. LSTM is similar to FNN; however, the two models differ because three gates and the internal nodes share the same weight in LSTM. The three gates include the input, forget, and output gates, and they play the role of determining the extent to which the input information is memorized and are updated with new results based on this information (Ann, 2016; Jung et al., 2020). The LSTM structure comprises the input, hidden, and output layers. In addition, LSTM updates the weights and bias values using the error backpropagation algorithm to determine the predicted value with the minimum error, relative to the measured value.

FNN and LSTM can both adopt sequence data as an input variable, and the number of sequence data is defined by the window size. Fig. 6 illustrates the FNN and LSTM that have incorporated the concept of window size.

In this study, the ML development environment comprised Python 3.7.10, TensorFlow 2.4.1, and Keras 2.4.0. Significant wave heights were predicted using the FNN that uses data from a single time point as an input, including the FNN and LSTM that have incorporated the concept of window size. The dataset was divided into training, validation, and test sets for the performance evaluation of ML models; in addition, the holdout validation was performed. The proportion of the training (2012–2018), validation (2019), and test (2020) sets is approximately 76:10:14. The sensitivity analysis was conducted based on the changes to the window size for the input data, the number of nodes and layers for the hidden layers, and the activation function (Eqs. (1)–(3)). In addition, the result with the smallest MAE (Eq. (4)) between the predicted and measured values in the validation set was selected as the optimal hyperparameter combination using the Adam optimizer.

$$ReLU : f(z) = \max(0, z) \tag{1}$$

$$Sigmoide : f(z) = \frac{1}{1+e^{-z}} \tag{2}$$

$$Tanh : f(z) = \frac{e^{z}-e^{-z}}{e^{z}+e^{-z}} \tag{3}$$

$$MAE = \frac{1}{N}\sum_{i=1}^{N}\left|\hat{Y}_i - Y_i\right| \tag{4}$$

In Eq. (4), N, $\hat{Y}_i$, and Y_i represent the total number of data points in the dataset, predicted value, and measured value, respectively.

3.1 Input Layer Selection

The Pearson correlation coefficient (r) of Eq. (5) was derived for the collected metocean data to select the variables for the input layer of the ML model (Fig. 7).

$$r_{pq} = \frac{\sum_{i=1}^{n}(p_i - \bar{p})(q_i - \bar{q})}{\sqrt{\sum_{i=1}^{n}(p_i - \bar{p})^2}\sqrt{\sum_{i=1}^{n}(q_i - \bar{q})^2}} \tag{5}$$

In Eq. (5), p_i and q_i represent individual values of the metocean data for calculating the correlation coefficient, while $\bar{p}$ and $\bar{q}$ are the average values of the selected metocean data. Here, n denotes the number of metocean data.

The significant wave height (Hs), a predictor variable, was most correlated with the maximum wave height ($Hmax$), with a correlation coefficient of 0.97. The $Hmax$ was followed by the significant wave period (Ts) and the maximum wave period ($Tmax$) in the correlation coefficient order. However, the wave data with the same characteristics as the significant wave height were not used as the input data in this study. Instead, in addition to the wave data, the remaining environmental variables were adopted to devise an ML model for predicting the significant wave height. Excluding the wave data, the order of the absolute value of the correlation coefficient, from the highest to lowest, is wind speed, wind direction, current direction, and water temperature. Based on this result, the input variable conditions were divided into three categories in Table 2. In addition, to solve the discontinuity problem with the direction (0°–360°) for the current and wind directions, the method of expressing the direction was changed from the polar coordinate system to the Cartesian coordinate system (x, y), using Eq. (6). Afterward, the current and wind directions were adopted as the input variables (Table 2). The input variables were standardized using the feature scaling method (Eq. (7)). The gradient descent method was optimally applied by making the features of the distribution between the input variables the same.

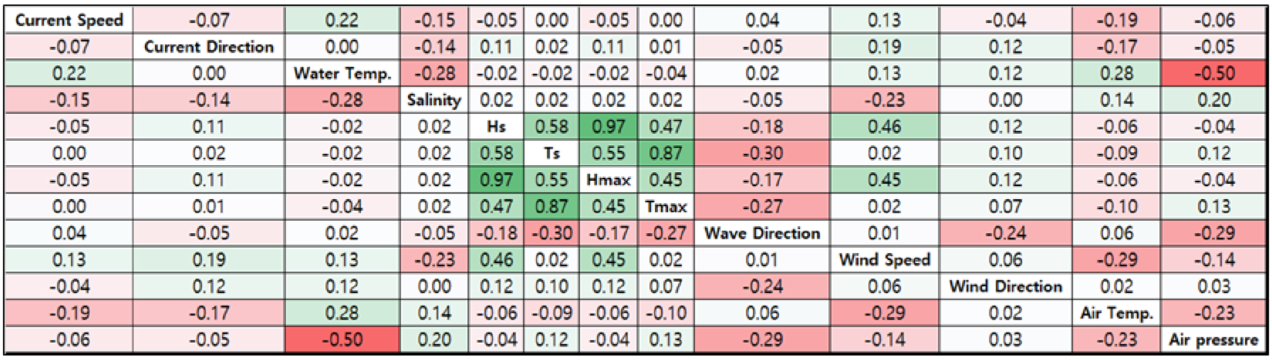

Current Speed	-0.07	0.22	-0.15	-0.05	0.00	-0.05	0.00	0.04	0.13	-0.04	-0.19	-0.06
-0.07	**Current Direction**	0.00	-0.14	0.11	0.02	0.11	0.01	-0.05	0.19	0.12	-0.17	-0.05
0.22	0.00	**Water Temp.**	-0.28	-0.02	-0.02	-0.02	-0.04	0.02	0.13	0.12	0.28	-0.50
-0.15	-0.14	-0.28	**Salinity**	0.02	0.02	0.02	0.02	-0.05	-0.23	0.00	0.14	0.20
-0.05	0.11	-0.02	0.02	**Hs**	0.58	0.97	0.47	-0.18	0.46	0.12	-0.06	-0.04
0.00	0.02	-0.02	0.02	0.58	**Ts**	0.55	0.87	-0.30	0.02	0.10	-0.09	0.12
-0.05	0.11	-0.02	0.02	0.97	0.55	**Hmax**	0.45	-0.17	0.45	0.12	-0.06	-0.04
0.00	0.01	-0.04	0.02	0.47	0.87	0.45	**Tmax**	-0.27	0.02	0.07	-0.10	0.13
0.04	-0.05	0.02	-0.05	-0.18	-0.30	-0.17	-0.27	**Wave Direction**	0.01	-0.24	0.06	-0.29
0.13	0.19	0.13	-0.23	0.46	0.02	0.45	0.02	0.01	**Wind Speed**	0.06	-0.29	-0.14
-0.04	0.12	0.12	0.00	0.12	0.10	0.12	0.07	-0.24	0.06	**Wind Direction**	0.02	0.03
-0.19	-0.17	0.28	0.14	-0.06	-0.09	-0.06	-0.10	0.06	-0.29	0.02	**Air Temp.**	-0.23
-0.06	-0.05	-0.50	0.20	-0.04	0.12	-0.04	0.13	-0.29	-0.14	0.03	-0.23	**Air pressure**

Fig. 7 Pearson correlation coefficient for metocean data

Table 2 Input variables for the input layer

No. of input data	Input variables	Note
3	Wind speed, wind direction (x,y)	Wind data only
5	Wind speed, wind direction (x,y) Current direction (x,y)	Data (r > 0.1)
10	Wind speed, wind direction (x,y) Current speed, current direction (x,y) Water temperature, salinity, Air temperature, air pressure	All data, excluding wave data

$$\theta = [(x = \cos\theta), (y = \sin\theta)] \tag{6}$$

$$X_{new} = \frac{X - \mu}{\sigma} \tag{7}$$

In Eq. (6), θ denotes the angle, while X in Eq. (7) represents the input variable. In addition, μ and σ represent the mean and standard deviation, respectively. The input variables were categorized into 3, 5, and 10, and the category with three input variables comprised the wind speed and wind direction. This is because wind speed and wind direction are the most important factors for predicting waves in the FNN (Mohjoobi et al., 2008). Therefore, it is determined that estimating the wave height with only wind data is a substantially rational approach. The categories with 5 and 10 input variables were classified to identify the effect of the correlation coefficient between the output and input variables.

3.2 Hidden Layer Selection

The number of nodes and layers in the hidden layers are hyperparameters related to the capacity of the model for the training set. If the capacity is low, underfitting occurs such that errors cannot be sufficiently reduced during the learning process. However, if the model's capacity is quite high, overfitting may occur, where the model learns patterns that are unrelated to the prediction of the test set. There is no clear standard for determining the number of layers and nodes for the hidden layers corresponding to the input variables. Although several empirical formulas (Huang and Foo, 2002) exist, the optimal hyperparameters need to be determined via repeated experimentations, as well as through trial and error. Therefore, sensitivity analysis was performed on the number of layers and nodes in the hidden layers, and the test matrix is presented in Table 3. The Adam optimizer and MAE were adopted as the optimizer and error function, respectively, while the number of batches and epochs were fixed at 256 and 200, respectively. To prevent overfitting, the early stopping technique was applied to stop the learning when the validation error reaches the minimum value in the iterative learning process. In addition, the learning rate was set to 0.001 (Kingma and Ba, 2014), and a linear function was used as the activation function for the output layer.

A total of 720 FNN and LSTM models were generated based on the changes to the hyperparameters, and training was performed on each model. The MAE between the predicted and measured values of the validation set was compared for each epoch, and the lowest result was

Table 3 Test matrix for the sensitivity analysis

ML model	Input layer		Hidden layer		Activation function
	No. of data (m)	Window size for sequence data (W)	No. of node	No. of layer	
FNN	3 5 10	1 (30 min) 48 (1 day) 720 (15 day) 1440 (30 day)	1 10 30 50 100	1 2 3 4	ReLU Sigmoid Tanh
LSTM			1 4 8 12 16		

Table 4 Summary of ML models and hyperparameter

ML model	Input layer		Hidden layer		Activation function	Cost function	Batch	Epochs
	No. of data (m)	Window size for sequence data (W)	No. of node	No. of layer				
FNN (W1)	3 5 10	1 (30 min)	30	3	ReLU	MAE	256	200
FNN (W48)		48 (1 day)						
LSTM (W48)		48 (1 day)	8	2	Tanh			

selected as the representative value. Among the 720 calculated results, the combination with the smallest MAE was selected as the optimal hyperparameter.

The FNN (W1), which was trained with the training set comprising the input and predictor variables at a single time point, was selected as the baseline performance. From each ML model, the FNN (W48) and LSTM (W48), with a window size of 48 (1 day) each, had the lowest MAE for the corresponding hyperparameters (Table 4).

4. Results of Significant Wave Height Predictions Using the ML Model

Significant wave heights were predicted using three types of ML models (i.e., FNN (W1), FNN (W48), LSTM (W48)), three cases of input variables (i.e., 3, 5, 10), and a combination of the optimal hyperparameters (Table 4). The ML models were evaluated using the test set. The predicted values calculated by inputting the input variables of the test set and the predictors in the test set were compared using a time-series graph and a histogram.

Fig. 8 presents time-series graphs for the three methods of the ML model and three conditions for input variables. In addition, the MAE between the predicted and measured values is presented in the upper-right corner of each graph. In general, the calculated MAE of the model with only the wind variable (input variable 3) was the smallest. Furthermore, it can be observed that the FNN (W48) and LSTM (W48) with window sizes of 48 each generated better results than FNN (W1). Kim (2020) predicted the significant wave heights through FNN (W1) using the wind speed, wind direction, and wave direction data from the data collected by the Oeyeondo oceanographic buoy and obtained outstanding results with a MAE of 0.283 m. It is presumed that outstanding results could be obtained using only the FNN (W1) because the wind speed, which was adopted as the input variable, was highly correlated ($r > 0.8$) with the significant wave height. In the FNN (W48), the MAE tends to increase as the number of input variables gradually increases. However, the input variables (5 and 10) yield the same MAE in the case of the LSTM (W48).

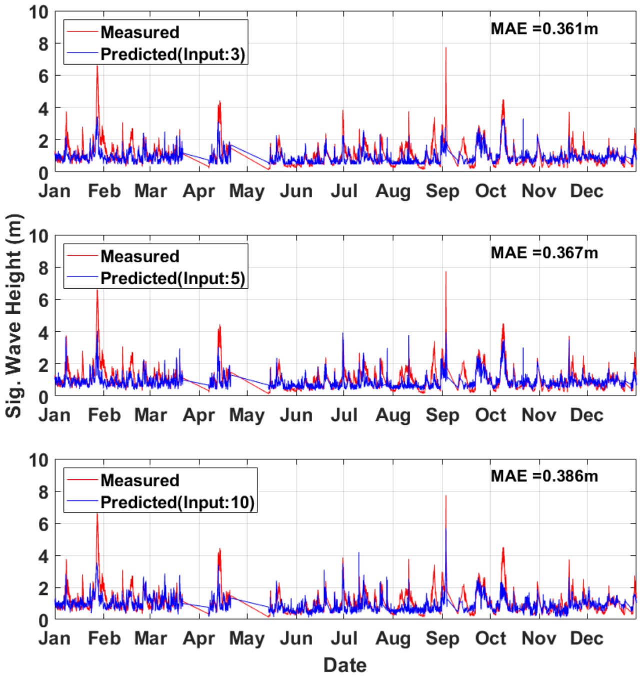

(a) FNN (W1)

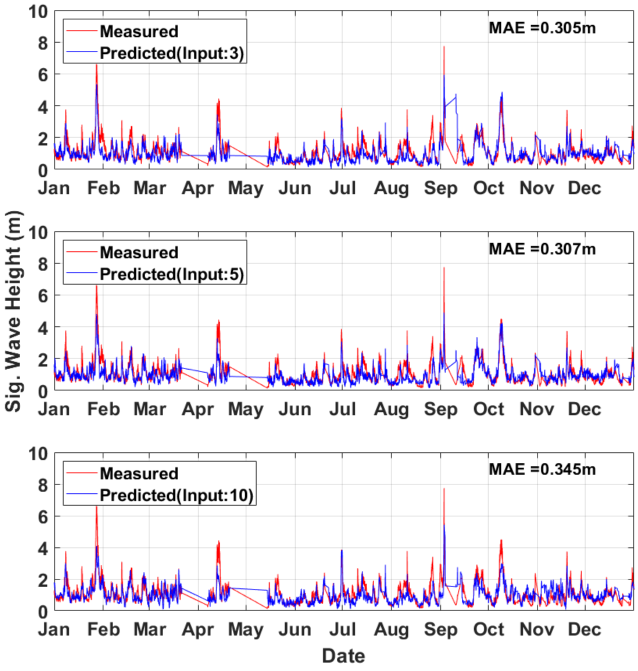

(b) FNN (W48)

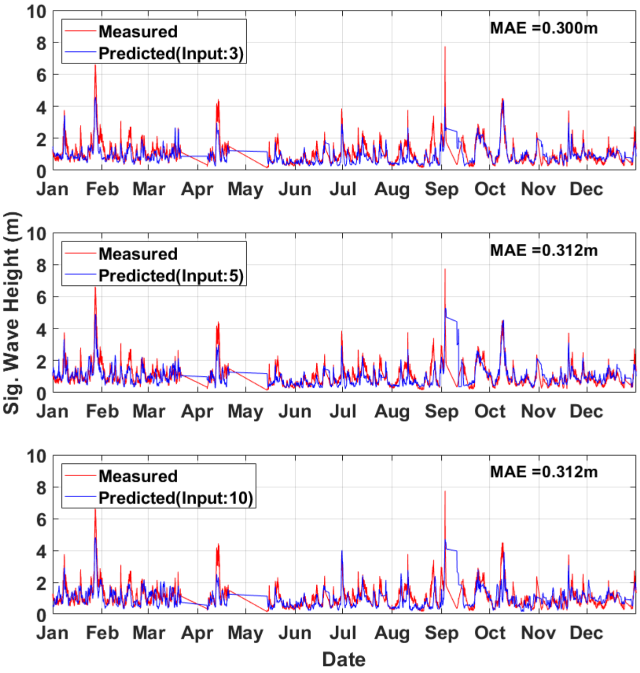

(c) LSTM (W48)

Fig. 8 Comparison between the measured and predicted values in time series varied with input nodes and ML models

To check the frequency of the predicted values relative to the measured values for each wave height, the probability histogram of two values for the significant wave height is presented in Fig. 9. The graphs on the left-hand side show the probability histogram for the entire data of each ML model. The graphs on the right-hand side present magnified histograms for the data with a significant wave height of 2 m or higher, which have low probability. In FNN (W1), the predicted values have a higher frequency than the measured values around the significant wave height of 0.6 m, where the frequency of the measured values is the highest. In contrast, the predicted values have a lower frequency than the measured values for a wave height of 2 m or higher. For both the FNN (W48) and LSTM (W48) models, the predicted values at approximately 0.6 m, where the frequency of the measured values is the highest, exhibit a frequency similar to the measured values. Although the probability of the occurrence of a high wave (with height of 5 m or higher) is low for the measured values, it was verified that a difference exists between the measured and predicted values in the area where the wave height is 5 m or higher for all three ML models.

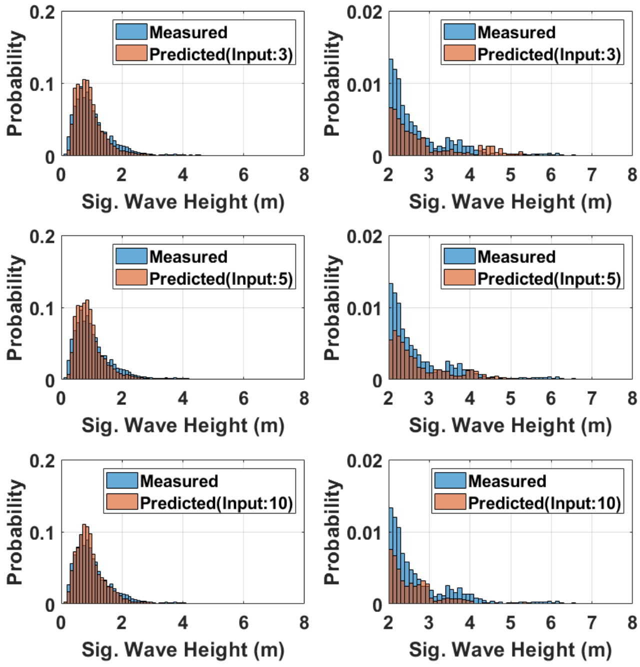

(a) FNN (W1)

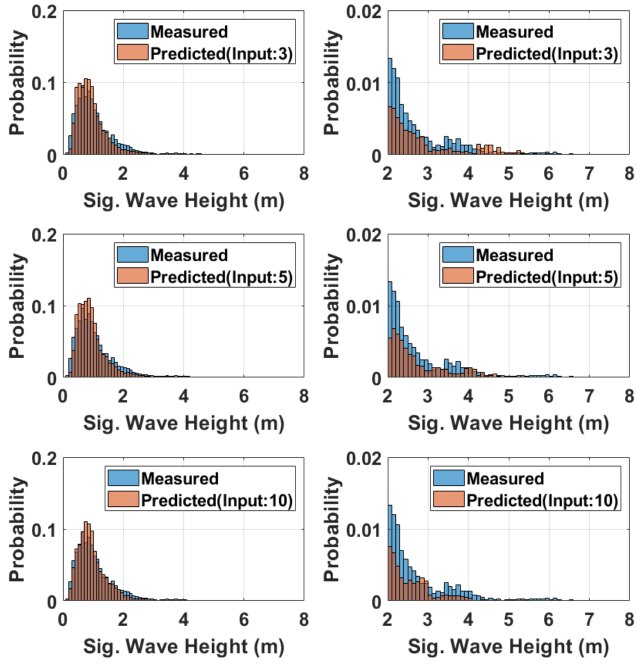

(b) FNN (W48)

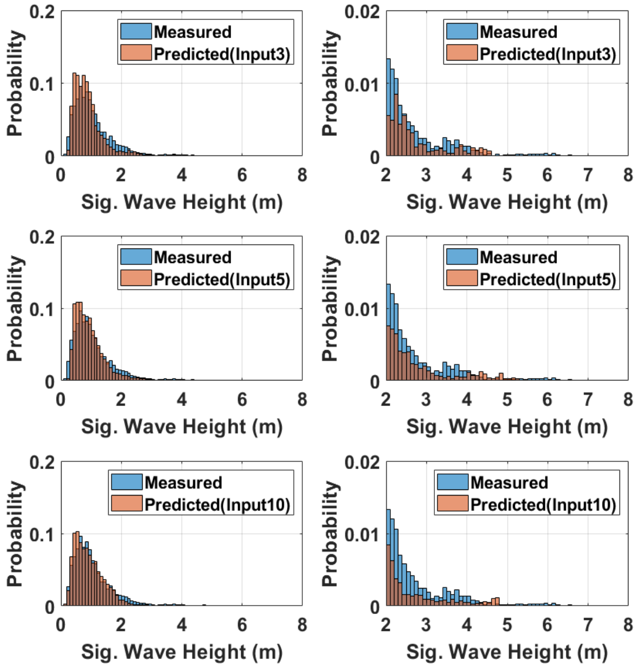

(c) LSTM (W48)

Fig. 9 Comparison between the measured and predicted values varied with input nodes and ML models using the histogram

Finally, the difference between the predicted and the measured values was analyzed by introducing the concept of the sea state (SS). The SS code, which the World Meteorological Organization (WMO) classified into grades 0–9, was adopted (Table 5). Significant wave heights of the measured values used as the test set are distributed between the SS2 grade and the SS7 grade, as provided by the WMO.

Table 5 WMO sea state code (3700) (WMO, 2019)

Sea State	Wave height (m)	Median wave height (m)	Characteristics
0	0.00	-	Calm (glassy)
1	0.00–0.10	0.050	Calm (rippled)
2	0.10–0.50	0.300	Smooth (wavelets)
3	0.50–1.25	0.875	Slight
4	1.25–2.50	1.875	Moderate
5	2.50–4.00	3.250	Rough
6	4.00– 6.00	5.000	Very rough
7	6.00–9.00	7.500	High
8	9.00–14.00	11.500	Very high
9	Over 14.00	-	Phenomenal

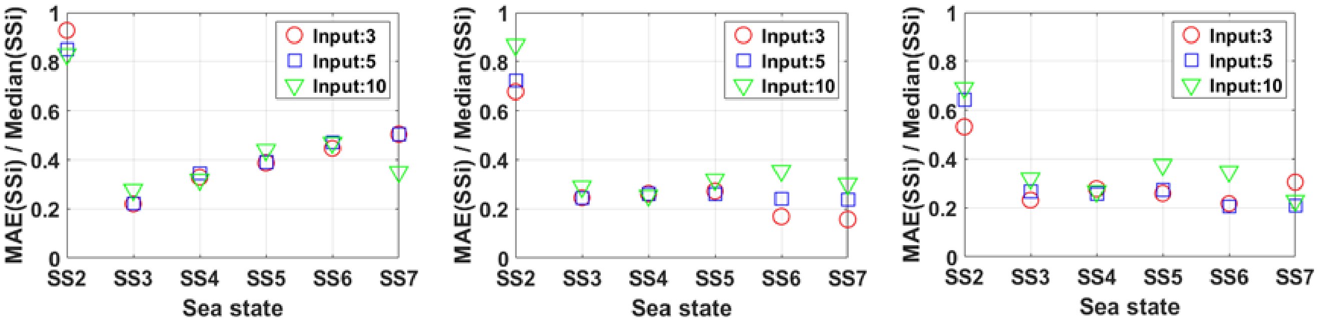

(a) FNN (W1) (b) FNN (W48) (c) LSTM (W48)

Fig. 10 Nondimensionalization of the MAE with sea state

The MAE between the predicted and the measured values in each SS range was nondimensionalized by the median of the corresponding SS, and its results are presented in Fig. 10.

In general, the result of input variable 3, which solely adopted wind as the input variable, exhibits a smaller MAE value , compared to those of input variables 5 and 10. Using the variable with a correlation coefficient greater than 0.1 (input variable 5) yields the second-best result. Contrary to our expectations, a relatively large error was generated when the results were calculated by adding water temperature, salinity, air temperature, and air pressure, compared to using input variables 3 and 5. It is presumed that variables that have low correlation coefficients but with the significant wave height are recognized as noise during training, and they cause overfitting. In the FNN (W1), it can be verified that the difference between the predicted and measured values tend to increase steadily as the significant wave height of the measured value gradually increases according to the SS. The LSTM (W48) model exhibits better prediction performance than the other two models for the SS2 grade of low wave heights. However, excluding the results for the SS2 grade with relatively low absolute error, it is determined that the FNN (W48) with input variable 3 is the best prediction model. In addition, the FNN (W48) model exhibit a higher prediction accuracy than the LSTM (W48) model for the SS6 and SS7 grades, and its computation speed is more than twice as fast. Therefore, considering the prediction accuracy and computation time, the FNN (W48) is proposed as a model for predicting significant wave heights in the Korea Strait.

5. Conclusion

In this paper, an ML model for predicting significant wave heights was proposed using the metocean data collected from the Korea Strait oceanographic buoy of KIOST. The ML model adopted FNN and LSTM network models. Based on the Pearson correlation analysis between the metocean data, three cases of input variables were selected. In addition, the hyperparameter combination with the minimum MAE was obtained via the sensitivity analysis of the window size, number of nodes in the hidden layers, number of layers, and activation function. The Adam optimizer was adopted as the optimizer in this process, and the number of batches and epochs were fixed at 256 and 200, respectively. Significant wave height prediction results of the FNN (W1) with a window size of 1 (30 min), the FNN (W48) with a window size of 48 (1 day), and the LSTM (W48) with a window size of 48 were compared with the measured values using time-series charts and histograms. In addition, the SS code was incorporated to compare the MAE nondimensionalized by the median of each SS for each model and input variable. The MAE of the prediction results was the smallest when the input variables solely comprised wind data. When environment variables that exhibit negligible correlation with the significant wave height ($r < 0.1$) were adopted, the MAE exhibited a tendency to increase. In the comparison of the FNN (W1) and the FNN (W48), which are the same FNN models, the FNN (W48) exhibited a smaller MAE for the test set. In the comparison between the FNN (W48) and LSTM (W48), using two models with the same window size, the LSTM (W48) exhibited a slightly smaller mean absolute error for the test set. However, when the MAE was compared based on the SS, the FNN (W48) with input variable 3 demonstrated better results between the SS3 and SS7 grades, except for the SS2 grade. In addition, the FNN (W48) was twice as fast as the LSTM (W48) in terms of computation time. Therefore, by comprehensively considering factors such as the accuracy of significant wave height predictions and computation speed, the FNN (W48) was evaluated to be the suitable ML model for predicting significant wave heights in the Korea Strait. When predicting significant wave heights, selecting input variables using correlation coefficients can produce outstanding results in machine learning. In addition, it is determined that optimal prediction models can be created using only wind data (e.g., wind speed and wind direction). However, the prediction accuracy was slightly lower in high wave areas with a significant wave height of 4 m or higher. It is inferred that the high wave prediction exhibits lower performance because the amount of high-wave data owing to typhoons is insufficient. To address this problem, it is necessary to expand the high-wave data when typhoons occur or develop an ML model that efficiently utilizes limited high-wave data. Finally, The ML model that predicts significant wave heights using only wind data can be utilized at the practical work where is adjusting the engine's power considering the added resistance of the ship, owing to the waves according to the SS, during sea trials. In the future, we plan to continue our research and enhance the accuracy of the model for predicting significant wave heights in the Korea Strait by adopting the data obtained from other oceanographic buoys near the Korea Strait oceanographic buoy, or the hindcast data, as input variables.

Funding

This study was supported by the following technology innovation programs: of "R&D Platform Establishment of Eco-Friendly Hydrogen Propulsion Ship Program (No. 20006636)" and "the Global Advanced Engineer Education Program for Future Ocean Structures (P0012646)", which were funded by the Ministry of Trade, Industry & Energy (MOTIE, Korea).

References

Ahn, S. (2016). Deep Learning Architectures and Applications. Journal of Intelligence and Information Systems, 22 (2), 127–142.

Cho, T. (2020). Deep Searning for Everyone (2nd ed.). Gibut, ISBN 979-11-6521-039-7, 368.

Deo, M.C., Jha, A., Chaphekar, A.S., & Ravikant, K. (2001). Neural Networks for Wave Forecasting. Ocean Engineering, 28(7), 889–898.

Deo, M.C., & Naidu, C.S. (1998). Real Time Wave Forecasting Using Neural Networks. Ocean Engineering, 26(3), 191–203.

Gers, F.A., Schmidhuber, J., & Cummins, F. (1999). Learning to Forget: Continual Prediction with LSTM.

Haenlein, M., & Kaplan, A. (2019). A Brief history of Artificial Intelligence: On the Past, Present, and Future of Artificial Intelligence. California management review, 61(4), 5–14.

Hochreiter, S., & Schmidhuber, J. (1997). Long Short-term Memory. Neural Computation, 9(8), 1735–1780.

Huang, W., & Foo, S. (2002). Neural Network Modeling of Salinity Variation in Apalachicola River. Water Research, 36(1), 356–362.

Jain, P., & Deo, M.C. (2006). Neural Networks in Ocean Engineering. Ships and Offshore Structures, 1(1), 25–35.

Jung, S., Kim, Y.J., Park, S., & Im, J. (2020). Prediction of Sea Surface Temperature and Detection of Ocean Heat Wave in the South Sea of Korea Using Time-series Deep-learning Approaches. Korean Journal of Remote Sensing, 36(5–3), 1077–1093.

Kim, D.H., & Lee, K. (2020). Forecasting the Container Volumes of Busan Port Using LSTM. Journal of Korea Port Economic Association, 36(2), 53–62.

Kim, G.D., & Kim Y.H. (2017). A Survey on Oil Spill and Weather Forecast Using Machine Learning Based on Neural Networks and Statistical Method

Kim, T.Y. (2020). A Study on the Prediction Technique for Wind and Wave Using Deep Learning. Journal of the Korean Society for Marine Environment & Energy, Vol, 23 (3), 142–147.

Kim, Y.J., Kim, T.W., Yoon, J.S., & Kim, I.H. (2019). Study on Prediction of Similar Typhoons through Neural Network Optimization. Journal of Ocean Engineering and Technology, 33 (5), 427–434.

Kingma, D.P., & Ba, J. (2014). Adam: A Method for Stochastic Optimization. arXiv Preprint arXiv:1412.6980.

Korea Institute of Ocean Science and Technology (KIOST). (2021). Location of Korea Strait Oceanographic Buoy. Retrieved 17 April 2021 from http://www.khoa.go.kr/oceangrid/khoa/koofs.do

Kumar, N.K., Savitha, R., & Al Mamun, A. (2018). Ocean Wave Height Prediction Using Ensemble of Extreme Learning Machine. Neurocomputing, 277, 12–20.

LeCun, Y., Bengio, Y., & Hinton, G. (2015). Deep Learning. Nature, 521(7553), 436–444.

Mahjoobi, J., Etemad-Shahidi, A., & Kazeminezhad, M.H. (2008). Hindcasting of Wave Parameters Using Different Soft Computing Methods. Applied Ocean Research, 30(1), 28–36.

Makarynskyy, O., 2004. Improving Wave Predictions with Artificial Ueural Networks. Ocean Engineering, 31(5–6), 709–724.

Malekmohamadi, I., Bazargan-Lari, M.R., Kerachian, R., Nikoo, M.R., & Fallahnia, M. (2011). Evaluating the Efficacy of SVMs, BNs, ANNs and ANFIS in Wave Height Prediction. Ocean Engineering, 38(2–3), 487–497.

Mandal, S., & Prabaharan, N. (2006). Ocean Wave Forecasting Using Recurrent Neural Networks. Ocean Engineering, 33(10), 1401–1410.

Meucci, A., Young, I. R., Aarnes, O.J., & Breivik, Ø. (2020). Comparison of Wind Speed and Wave Height Trends from Twentieth-century Models and Satellite Altimeters. Journal of Climate, 33(2), 611–624.

Oh, J., & Suh, K.D. (2018). Real-time Forecasting of Wave Heights Using EOF–wavelet–neural Network Hybrid Model. Ocean Engineering, 150, 48–59.

Park, S.B., Shin, S.Y., Jung, K.H., Choi, Y.H., Lee, J., & Lee, S.J. (2020). Extreme Value Analysis of Metocean Data for Barents Sea. Journal of Ocean Engineering and Technology, 34(1), 26–36.

World Meteorological Organization (WMO). (2019). Manual on Codes: International Codes I. 1, part A—Alphanumeric Codes.

Author ORCIDs

Author name	**ORCID**
Park, Sung Boo	0000-0001-9587-2183
Shin, Seong Yun	0000-0001-6665-9092
Jung, Kwang Hyo	0000-0002-8229-6655
Lee, Byung Gook	0000-0003-0725-0355

Journal of Ocean Engineering and Technology 35(5), 347-359, October, 2021
https://doi.org/10.26748/KSOE.2021.058
pISSN 1225-0767
eISSN 2287-6715

Original Research Article

Analysis of Dynamic Response Characteristics for 5 MW Jacket-type Fixed Offshore Wind Turbine

Jaewook Kim[1,2], Sanghwan Heo[3] and WeonCheol Koo[4]

[1]*Graduate Student, Department of Navel Architecture & Ocean Engineering, Inha University, Incheon, Korea*
[2]*Principal Engineer, Daewoo Shipbuilding & Marine Engineering Co. Ltd., Seoul, Korea*
[3]*Postdoctoral Researcher, Department of Navel Architecture & Ocean Engineering, Inha University, Incheon, Korea*
[4]*Professor, Department of Navel Architecture & Ocean Engineering, Inha University, Incheon, Korea*

KEY WORDS: Offshore wind turbine, Jacket, Tower, Dynamic response, Combined wind and wave load, Fourier analysis, Turbulent wind

ABSTRACT: *This study aims to evaluate the dynamic responses of the jacket-type offshore wind turbine using FAST software (Fatigue, Aerodynamics, Structures, and Turbulence). A systematic series of simulation cases of a 5 MW jacket-type offshore wind turbine, including wind-only, wave-only, wind & wave load cases are conducted. The dynamic responses of the wind turbine structure are obtained, including the structure displacement, rotor speed, thrust force, nacelle acceleration, bending moment at the tower bottom, and shear force on the jacket leg. The calculated time-domain results are transformed to frequency domain results using FFT and the environmental load with more impact on each dynamic response is identified. It is confirmed that the dynamic displacements of the wind turbine are dominant in the wave frequency under the incident wave alone condition, and the rotor thrust, nacelle acceleration, and bending moment at the bottom of the tower exhibit high responses in the natural frequency band of the wind turbine. In the wind only condition, all responses except the vertical displacement of the wind turbine are dominant at three times the rotor rotation frequency (considering the number of blades) generated by the wind. In a combined external force with wind and waves, it was observed that the horizontal displacement is dominant by the wind load. Additionally, the bending moment on the tower base is highly affected by the wind. The shear force of the jacket leg is basically influenced by the wave loads, but it can be affected by both the wind and wave loads especially under the turbulent wind and irregular wave conditions.*

1. Introduction

Owing to the increasing global environmental regulations and energy crisis, wind energy is gaining global interest as eco-friendly alternative renewable energy that can be sustained. The wind power generation technology that converts fluid kinetic energy into electric energy has already been technologically verified, and large land-based wind turbines have been constructed worldwide since the 1980s (Jang and Sohn, 2011).

However, constructing large land-based wind turbines causes various issues such as spatial limitations, noise, radio interference, and visual discomfort. Moreover, high energy generation efficiency is difficult to obtain in land-based wind power generation owing to low wind speed and turbulence caused by interference from surrounding terrain features (Li et al., 2018). Offshore wind power generation results in high power generation efficiency because the offshore wind speed is, on average, at least 70% higher than that on land, and large wind turbines can be installed because wide installation spaces are available (Park et al., 2021).

Consequently, offshore wind turbines have recently been installed and operated in numerous regions, and many fixed type wind turbines have been installed in relatively shallow coastal areas. Particularly, in South Korea, the Jeju Tamla Offshore Wind Farm was constructed in 2017 and has ten 3 MW wind turbines in operation, and the Offshore Wind Farm in the Southwestern Coast of Yellow Sea was constructed in 2019 and has twenty 3 MW wind turbines in operation (Jeong et al., 2020; Oh et al., 2020).

As the demand for offshore wind turbines increases, studies on them have been actively conducted. Shi et al. (2011) carried out dynamic response analysis according to the shapes of the substructures of a 5 MW offshore wind turbine and reported that the load and dynamic response acting on a monopile-shaped substructure have larger values

Received 16 June 2021, revised 18 July 2021, accepted 2 August 2021
Corresponding author WeonCheol Koo: +82-32-860-7348, wckoo@inha.ac.kr
It is noted that this paper is revised edition based on proceedings of KAOST 2021 in Incheon.

than those acting on tripod- and jacket-shaped substructures. Kim et al. (2015) carried out a design load analysis for a 5 MW offshore wind turbine system using various numerical analysis techniques and analyzed the qualitative results. Zwick and Muskulus (2015) conducted a study for reducing errors from the input variables of numerical analysis and performing efficient simulations when turbulent winds and irregular waves act on a 5 MW jacket-type offshore wind turbine. Song and Yoo (2017) carried out dynamic response analysis according to the shapes (monopile, jacket, and dolphin) of substructures for a 2.5 MW offshore wind turbine and found that the wave load acting on the jacket-type substructure had the smallest value. Kim et al. (2019) examined a technique for predicting the wake of a wind turbine to remedy the weaknesses of the aerodynamic analysis model of the Fatigue, Aerodynamics, Structures and Turbulence (FAST) program (Jonkman, 2007) developed in the National Renewable Energy Laboratory (NREL) and conducted a study on the optimization of wind turbine arrangements. Tran et al. (2021) conducted a study on the bending performance of a substructure when sea winds, waves, and ocean currents act on a 3 MW jacket-type offshore wind turbine as environmental external forces.

Unlike a land-based wind turbine, a fixed wind turbine installed on the sea has motion responses of the structure by incident waves. Moreover, the motion responses of the wind turbine by combined environmental loads are fairly complex because the incident waves and wind speed act together. The effect of individual environmental loads (incident wave or wind speed) on the structure and motion response characteristics of the structure must be identified for the optimal design and stable operation of the offshore wind turbine. The authors of this paper, however, found only a few studies that analyzed the precise motion response characteristics of fixed wind turbines for individual environmental loads such as incident wave-only effects or wind speed-only effects and combined wave-wind effects.

In this study, therefore, the response characteristics of a 5 MW jacket-type fixed offshore wind turbine for environmental external forces acting on the wind turbine structure, namely, individual environmental loads such as the effects of regular waves and irregular waves (wave loads) or the effects of the presence of winds, wind speed changes, and turbulent winds (wind loads) were systematically analyzed and their features were identified. It is difficult to evaluate the dynamic responses accurately and objectively in strong wind and high wave conditions due to the mixed effects of the environmental loads; therefore, the wind speed, wave height, and wave period were set to small values to precisely analyze the response characteristics of the structure corresponding to each load based on the blade element momentum (BEM) theory. The FAST program of the NREL that is widely used in analysis studies on wind turbines and is expected to derive reliable results was used to obtain time-domain calculation results for each environmental load. These results were converted into frequency responses by fast Fourier transform (FFT) analysis to identify the responses of the structure for the individual environmental loads and analyze their characteristics. The goal of this study is to acquire the basic information required to design and operate a wind turbine by precisely identifying and analyzing the response characteristics of the structure according to the magnitude of each environment load and whether the effect of the load is dominant.

2. Fixed Offshore Wind Turbine

2.1 Fixed Substructure

The substructure of an offshore wind turbine can be either fixed or floating depending on its installation environment conditions. Floating offshore wind turbines are installed on the deep sea, whereas fixed offshore wind turbines are adopted as a more suitable form on shallow coasts. Conventionally, fixed substructures directly supported on the seabed largely fall into four categories monopile, tripod, jacket, and gravity-base (de Vries et al., 2011).

The jacket-type wind turbine substructure considered in this study is fixed on the seabed with piles after connecting thin braces to three or four cylindrical legs in a lattice structure. The load acting on the entire structure is axially distributed through structural members to stably withstand the relatively high vertical and lateral loads. Song and Yoo (2017) found that the jacket-type receives fewer wave loads than the monopile or dolphin types. Moreover, the jacket-type can be installed in relatively deep water up to a water depth of 50 m, whereas the monopile or improved tripod types can be installed only on shallow coasts.

2.2 Load Analysis of Wind Turbine

Aerodynamic and hydrodynamic analysis according to each external force condition are required to conduct the load analysis for an offshore wind turbine. The force applied to the tower of the wind turbine is an aerodynamic external force created by wind. The BEM theory using the blade element momentum is applied to calculate the speed and load acting on the wind turbine rotors according to the wind speed, rotor rotation speed, and pitch angle (Agarwal and Manuel, 2008). The generalized dynamic wake (GDW) was developed for the aerodynamic analysis of high-speed blades such as helicopters (Peters et al., 1989; Suzuki, 2000; Kim et al., 2019). In this study, the results were derived by applying wind speeds below the rated speed to accurately identify the response characteristics of a wind turbine by the wind. Therefore, the BEM results were used for the aerodynamic analysis of slowly moving blades and were compared with the GDW results suitable for high-speed rotation to determine their difference.

The BEM theory, developed by Glauert in 1935, is based on normal flow, namely non-turbulent flow, and assumes that all annular shapes are independent (Fenu et al., 2020). The BEM theory finely divides a blade into element units and then calculates the lift (dL, N) and drag (dD, N) forces applied to the two-dimensional airfoil of each element to calculate the force and moment applied to the entire wind turbine using the sum of longitudinal forces (Faltinsen, 1993). The force acting on the blade can be obtained using the induced velocity vector

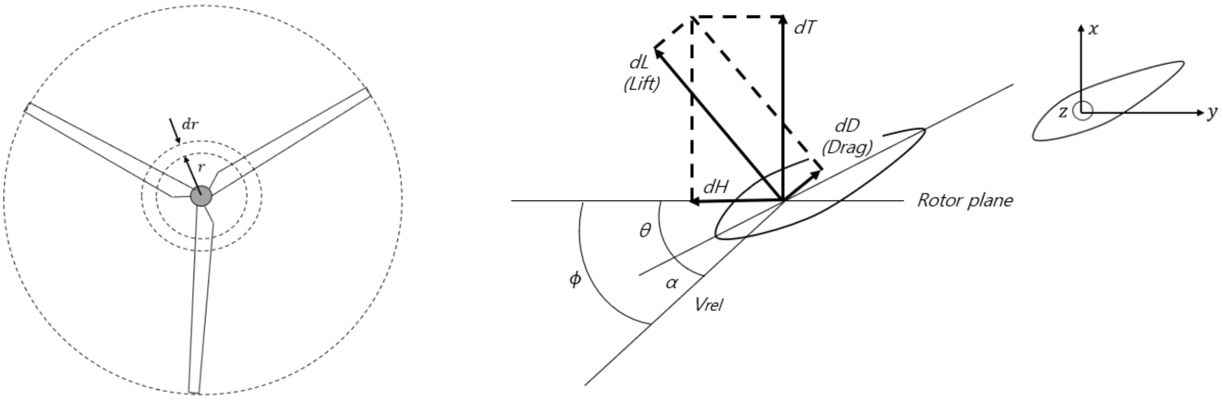

Fig. 1 Annular plane and forces components at blade element

W of the cross-section of the blade in the momentum conservation equation based on the momentum and angle, and the torque and power applied to the rotor shaft based on the force acting on the blade (Snel, 2003). The relative velocity V_{rel} can be separated and expressed as follows.

$$V_{rel.y} = V_y + W_y - \omega x \tag{1}$$

$$V_{rel.z} = V_z + W_z \tag{2}$$

where x is the vertical direction with respect to the rotational axis of the rotor and z is the longitudinal direction of the blade. ω represents the angular velocity of the rotor, and the angle of attack (α) and inflow angle (ϕ) on the airfoil plane in Fig. 1 can be expressed as in the following equations using the torsional angle (θ) and pitch angle (θ_p) (Burton et al., 2001).

$$\alpha = \phi - (\theta + \theta_p) \tag{3}$$

$$\phi = -\tan^{-1}\frac{V_{rel,z}}{V_{rel,y}} \tag{4}$$

Finally, the thrust (dT, N) that is applied to the blade element and obtained by numerical calculation can be expressed as in Eq. (5), and the torque (dQ, N・m) can be expressed as in Eq. (6) based on the horizontal force (dH, N), where ρ is the air density (kg/m^3), V_{rel} is the wind speed (m/s), B is the number of blades, r is the distance (m) from the hub to the blade sector, c is the chord length, and the lift coefficient c_l and drag coefficient c_d are dimensionless coefficients of the airfoil associated with the Reynolds number (Lanzafame and Messina, 2007).

$$dT = B\frac{1}{2}\rho V_{rel}^{2}(c_l cos\phi + c_d sin\phi)cdr \tag{5}$$

$$dQ = rdH = B\frac{1}{2}\rho V_{rel}^{2}(c_l sin\phi - c_d scos\phi)crdr \tag{6}$$

An external force that is hydrodynamically created has a horizontal incident wave force applied to the vertical substructure of the offshore wind turbine; this force consists of the inertial force by the acceleration of wave particles, the drag force by boundary conditions, and the frictional force. Morison's equation as in Eq. (7) was used to numerically calculate the wave loads applied to slender bodies with smaller structure diameters than the wavelength, namely, structures whose diffraction parameter is smaller than 0.2 (Morison et al., 1950; Wei et al., 2014).

$$F = F_d + F_i = \frac{1}{2}\rho C_d A u^2 + \rho C_m V\frac{du}{dt} \tag{7}$$

where C_d is the drag coefficient and C_m is the inertial coefficient. The load of a fixed structure created by accelerating the fluid particles is expressed as an inertial force as in Eq. (8).

$$dF_i = \rho C_m \frac{\pi D^2}{4}\frac{du}{dt} \tag{8}$$

The wave load by Morison's equation that considers the wave elevation η and water depth d can be obtained using the water particle velocity u as in Eq. (9) below.

$$F = \int_{-d}^{\eta}\rho C_m\frac{\pi D^2}{4}\frac{du}{dt}dz + \int_{-d}^{\eta}\frac{\rho}{2}C_d u|u| D dz \tag{9}$$

3. Calculation Results and Analysis

3.1 Numerical Analysis

FAST v.8.16.00a-bjj, an open-source code program, was used in our numerical analysis. A 5 MW offshore wind turbine was modeled by referring to the NREL reference model. The jacket OC4 (offshore code comparison collaboration continuation) project structure, one of the fixed models that can meet the characteristic and environmental conditions of the seas around Korea, was applied to the substructure. The system components of the FAST program are illustrated in Fig. 2.

Six module programs were used for the fixed wind turbine simulation analysis, and AeroDyn was used for the wind load

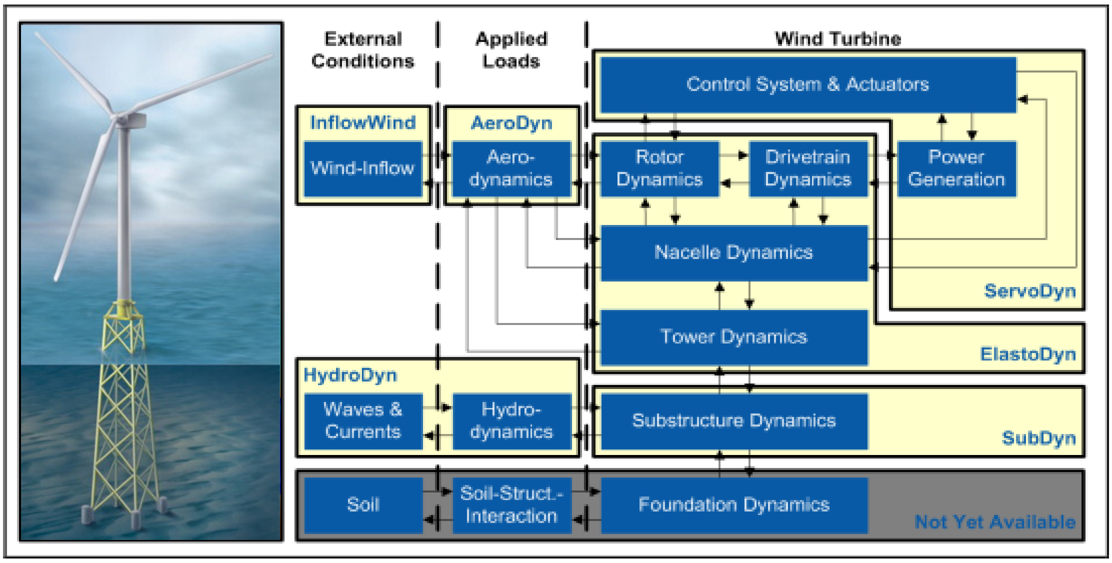

Fig. 2 System of FAST program for a fixed-bottom wind turbine structure (Jonkman and Buhl, 2005)

calculation. The analysis code, AeroDyn, calculates the aerodynamic loads of the tower and blades, considering a wind speed and wind direction inputted via InflowWind in a BEM-based wind force analysis mode (Jonkman et al., 2015). The two-dimensional force and moment of each node were calculated as distributed loads per unit length, and the sum of these loads was used to calculate the three-dimensional aerodynamic load of the horizontal axis applied to the entire tower in the time domain. The unit wind speed acting on the blades or tower nodes is determined as in Eq. (10) below (Moriarty and Hansen, 2005; IEC, 2019).

$$V(z)=V_{hub}\left(\frac{Z}{z_{hub}}\right)^{\alpha} \tag{10}$$

where $V(z)$ is the wind speed at a spot where the vertical displacement from the mean water level is z. V_{hub} represents the wind speed at the hub height z_{hub}. The hub height of the NREL 5 MW wind turbine used as a calculation model in this paper is 90 m. α represents the wind shear index indicating an abrupt change in the wind speed or direction. The international standard for designing fixed wind turbines recommends that an α value of 0.14 be used (IEC, 2019), but this value is set to 0 in this study to linearly increase the wind speed from the water surface.

The hydrodynamic load applied to the substructure (jacket) of the wind turbine is calculated using HydroDyn, an independent analysis module for calculating hydrodynamic loads based on the maritime information of an inputted region such as the wave height, wave period, and waveform (regular wave or irregular wave) (Jonkman et al., 2014). The calculation for wave motion was done in the area between the still water level and flat seabed, whereas the dynamic load analysis for each substructure node within the corresponding area was carried out in the time domain. The governing equation of motion used for the analysis is given as Eq. (11) below. *M* and *K* are global matrices consisting of the element unit mass matrix and stiffness matrix of the substructure, respectively. *U* represents the displacement and *F* is the external force (Damiani et al., 2015).

$$[M]\{\ddot{U}\}+[C]\{\dot{U}\}+[K]\{U\}=\{F\} \tag{11}$$

The three-direction displacement (*x*-axis direction displacement, *x*-*z*-direction rotational displacement, and *z*-direction vertical displacement) of the fixed wind turbine was designated as the main motion response for analyzing the calculation results because this motion response is most affected by winds and waves entering in the *x*-direction. It is also important to examine the rotor rotation speed and

Table 1 Specifications of 5 MW wind turbine (Jonkman et al., 2009)

Property	Specification
Rated power	5 MW
Rotor orientation, Configuration	Upwind, 3 Blades, 61.5 m length
Rotor, Hub diameter	126 m, 3 m
Hub height	90 m
Cut-in Vin, Rated, Cut-out Vout wind speed	3 m/s, 11.4 m/s, 25 m/s
Cut-in, Rated rotor speed	6.9 rpm, 12.1 rpm
Drivetrain concept	Geared
Gearbox ratio	97:1
Overhang, Shaft tilt, Precone	5 m, 5°, 2.5°
Rotor mass	110,000 kg
Nacelle mass	240,000 kg
Tower mass	347,460 kg
Tower base diameter	6 m
Tower top diameter	3.87 m
CM location	-0.2 m, 0.0 m, 64.0 m
Control system	Variable-speed & Collective pitch

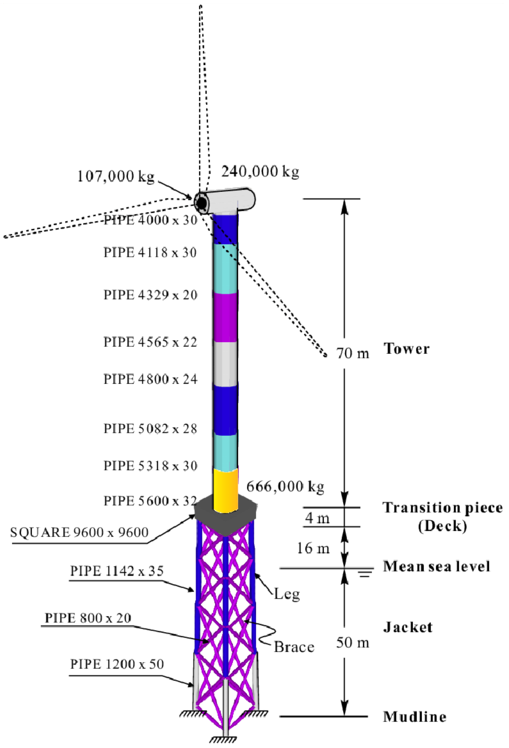

Fig. 3 Design of fixed wind turbine

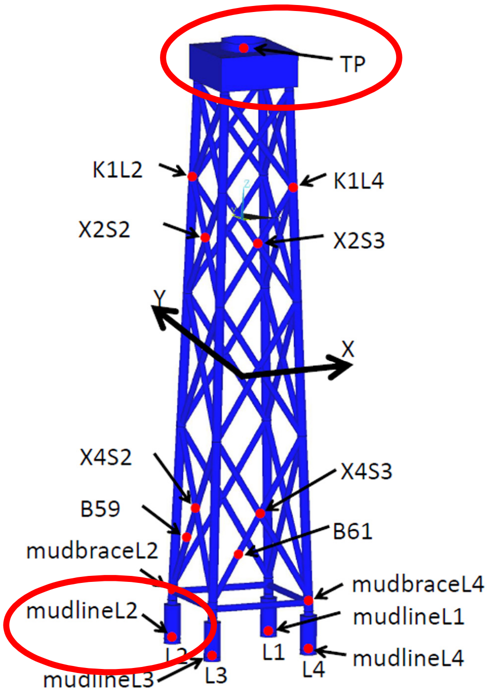

Fig. 4 Jacket support structure element (Popko et al., 2012)

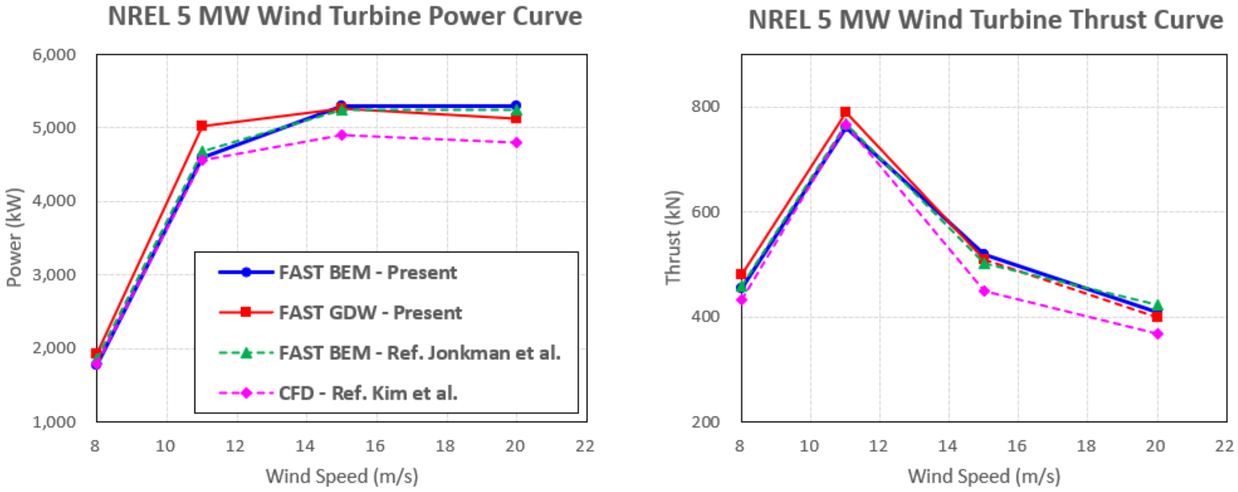

Fig. 5 Comparison of rotor power (left) and thrust (right) for various methods

thrust determined according to the effect of the wind and the nacelle acceleration directly connected to the actual power generation efficiency of the wind turbine. Another important result to be analyzed in this study is the bending moment of the base connection of the tower created by fore-aft shearing loads, the largest force acting on the turbine. Lastly, the effects of the wind and wave forces were compared by checking the shear force in the *x*-direction to identify changes in the force applied to the jacket. Specific information on the model used in this study is described through Table 1 and Figs. 3–4.

Fig. 5 shows the results of comparing the rotor power and thrust according to the wind speeds by various analysis methods. The FAST results of Jonkman et al. (2009) and the three-dimensional CFD analysis results of Kim et al. (2015) were compared to verify the FAST calculation results of the fixed 5 MW offshore wind turbine mentioned above. The calculation results overall matched the previous results. The BEM results of the same analysis program (FAST) are very close, and the GDW results suitable for high-speed rotation as in a helicopter are fairly close except for the wind speed of 11 m/s. The CFD results deviate from the rest owing to computational differences caused by the absence of information on some input values and model configuration differences caused by the different analysis programs.

The analysis model is for 5 MW turbines, hence, the rotor power rapidly increases up to 11 m/s and tends to converge to 5 MW after that. It can be inferred that the model has the highest efficiency at the wind speed of 11 m/s because the thrust is the largest at the corresponding wind speed. The application of GDW analysis is recognized as a general method for reducing errors to carry out numerical analysis that considers the abnormal characteristics of wind because such characteristics are severe in extreme design wind speed conditions; however, the wind speed, wave height, and wave period were set to low values to precisely analyze the response characteristics of the structure corresponding to the input values based on the BEM theory because the effects of environmental factors are mixed in such analysis under strong wind and high and rough wave conditions, which makes it difficult to objectively conduct accurate response analysis.

3.2 Design Load Case

Various design load cases (DLCs) were selected as in Table 2 and the analysis was carried out to identify the response characteristics according to the wind speed and wave state of the 5 MW fixed jacket-type offshore wind turbine. DLCs 1-5 were examined to check the natural response characteristics of the fixed wind turbine, and DLCs 6-9 were selected and examined to identify the effects in the load conditions where waves and winds are combined.

To analyze the cases, constant speeds (V_{Steady}) were inputted for steady winds, and the results calculated by turbulent wind simulations with designated speeds ($V_{Turbulence}$) were used as input values for the turbulent winds. The wind speeds were set based on the point of the hub height of 90 m. In the windless scenario (DLC 1), the wind turbine was in a parked condition and the analysis was carried out in the state where the rotors were fixed. The fixed wave height and wave period values were inputted for regular incident waves, and the significant wave height H_S and peak period T_P were designated by applying the JONSWAP spectrum for irregular incident waves.

In DLCs 1-5, to check the natural response characteristics, regular waves or steady winds were applied to carry out numerical analysis on single loads for 1,000 s, and the time series results were used for the last 100 s, considering the transient effect. In DLCs 6-9 in which combined loads, irregular waves, and turbulent winds are applied, the numerical analysis was carried out for one hour (3,600 s) to derive more precise interrelations and reliable results; FFT analysis was carried based on the results of the last 300 s; and the time step of each case was set to 0.01 s. There was little difference in the results although the FFT analysis interval was extended to a maximum of 1 h. The graphs of the results of the cases were generated and comparative analysis was carried out by extracting the time series results of the latter half to remove the transient interval, minimize convergence value variability, and increase the legibility of the time series and frequency data trend.

3.3 Analysis of Calculation Results

3.3.1 Wave Only Case

The incident wave with a six-second period (0.17 Hz) was substituted in a windless state to identify the response characteristics of the wind turbine structure for the incident wave. In Fig. 6, the response frequencies of the horizontal displacement, vertical displacement, *x*-*z*-direction rotational displacement, and jacket shear force of the structure match the wave frequency of 0.17 Hz, and the thrust, nacelle acceleration, and bending moment have the same frequency response as the wave frequency in the windless state. There is also a response at 0.32 Hz, which represents the natural frequency of the analysis model as reported by Jonkman et al.(2009). Therefore, the tower of the wind turbine has a considerable response in the natural frequency band even in the windless state simply by the effect of the incident wave.

Fig. 7 compares the changes in the bending moment of the base connection of the tower according to different incident wave conditions (DLCs 1-3) to examine the response changes of the wind turbine structure according to the incident wave height and wave period changes. The response frequency point changes to 0.17 Hz and 0.13 Hz (1/7.5 s) with wave periods of 6 and 7.5 s, respectively. Fig. 7 (right) also shows that the bending moment response of the tower base is rapidly amplified as a result of setting the incident wave period to 3 s (near the natural frequency of the model) to accurately analyze the response of the bending moment because the response of the bending moment was considerable even in the band of the natural frequency (0.32 Hz) as mentioned above in connection with Fig. 6. Although the wave height increased from 2 m to 4 m, a large response was absent, but a large impact was created when the incident wave period matched

Table 2 Design load cases

Case	Description	Waves	Wind	Turbine condition
1	Regular wave	Reg., H = 2.0 m, T = 6.0 s	-	Parked
2	Regular wave	Reg., H = 2.0 m, T = 3.0 s	-	Parked
3	Regular wave	Reg., H = 4.0 m, T = 7.5 s	-	Parked
4	Steady wind	-	Steady, V_{Steady} = 6.0 m/s	Operating
5	Steady wind	-	Steady, V_{Steady} = 12.0 m/s	Operating
6	Operational	Reg., H = 2.0 m, T = 6.0 s	Steady, V_{Steady} = 6.0 m/s	Operating
7	Operational	Reg., H = 2.0 m, T = 6.0 s	Turb., $V_{Turbulence}$ = 6.0 m/s	Operating
8	Operational	Irreg., H_S = 2.0 m, T_P = 6.0 s	Steady, V_{Steady} = 6.0 m/s	Operating
9	Operational	Irreg., H_S = 2.0 m, T_P = 6.0 s	Turb., $V_{Turbulence}$ = 6.0 m/s	Operating

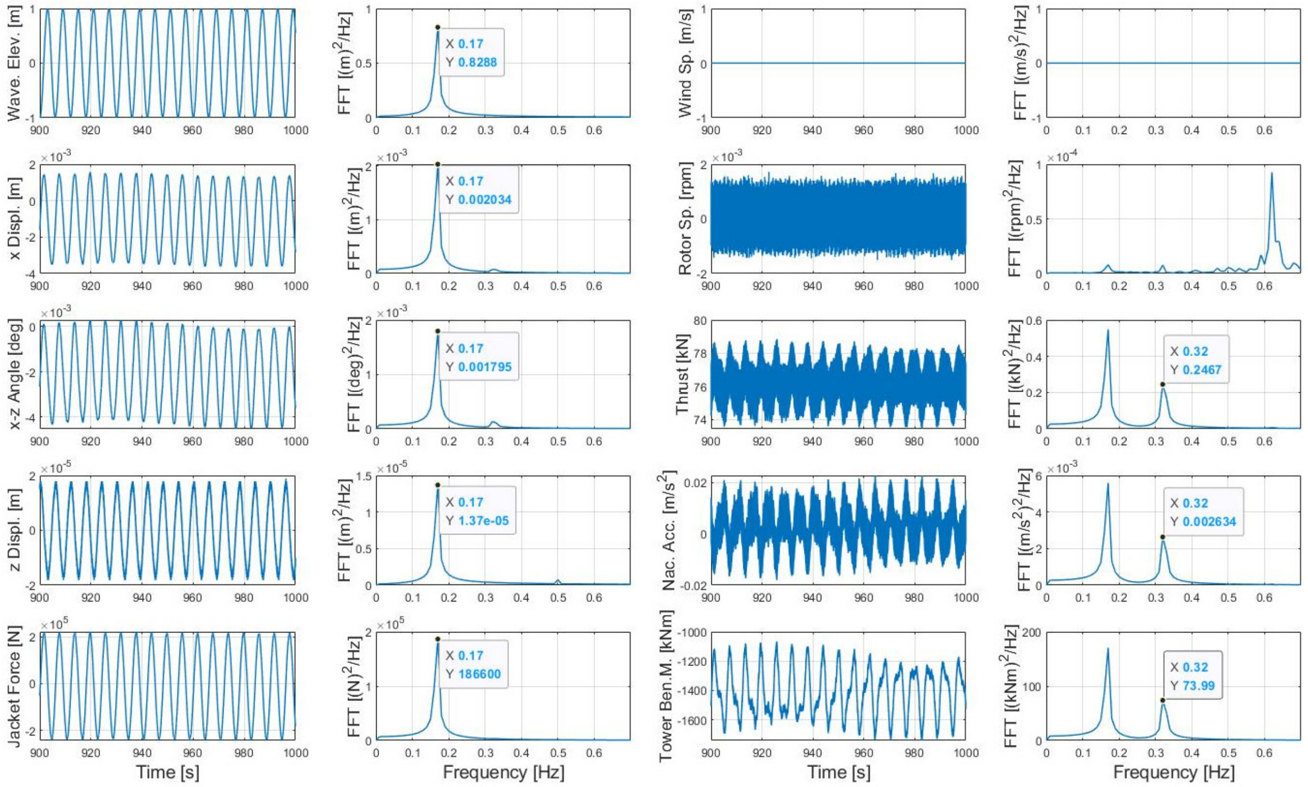

Fig. 6 Response to DLC #1, regular wave only (H = 2.0 m, T = 6.0 s, No wind)

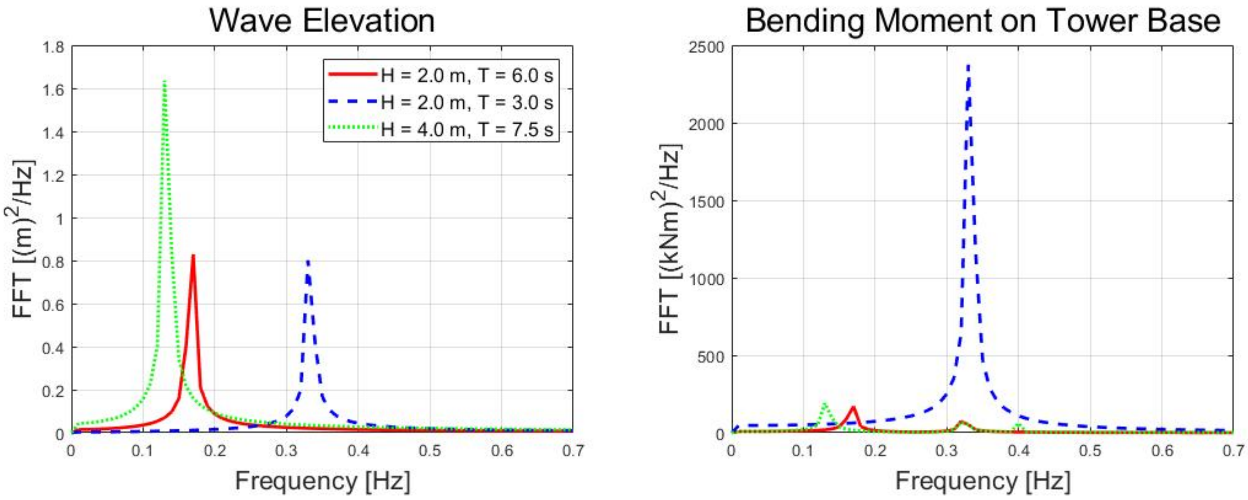

Fig. 7 Comparison of tower bending moment for DLC #1, #2 & #3, regular wave only cases

the natural frequency band of the structure.

3.3.2 Wind Only Case

The wind speed (6 m/s) below the rated speed was substituted to identify the response characteristics of the 5 MW jacket-type wind turbine structure by the wind while the structure was not affected by the wave (Fig. 8). All responses of the tower and jacket were maximum at 0.39 Hz (rpm = 7.88/60 s × 3 blades) corresponding to a frequency increase by the number of blades caused by the rotation of each blade at the rotor rotation speed (7.88 rpm) output by the wind speed (6 m/s). Therefore, the response of the wind turbine structure by the wind is closely related to the rotor rotation. The vertical displacement of the structure is quite small and converges to 0 even in the time series results; thus, it can be inferred that the vertical displacement caused by the wind is absent in the fixed wind turbine structure.

The results of DLCs 4 and 5 are compared in Fig. 9 to identify changes in the response characteristics of the structure caused by wind speed changes. The rotating speed of the rotor is derived by the steady wind in the absence of incident waves, which causes a response at the frequency increased by the number of blades. The maximum response of the thrust occurs at the frequency of 0.39 Hz resulting from

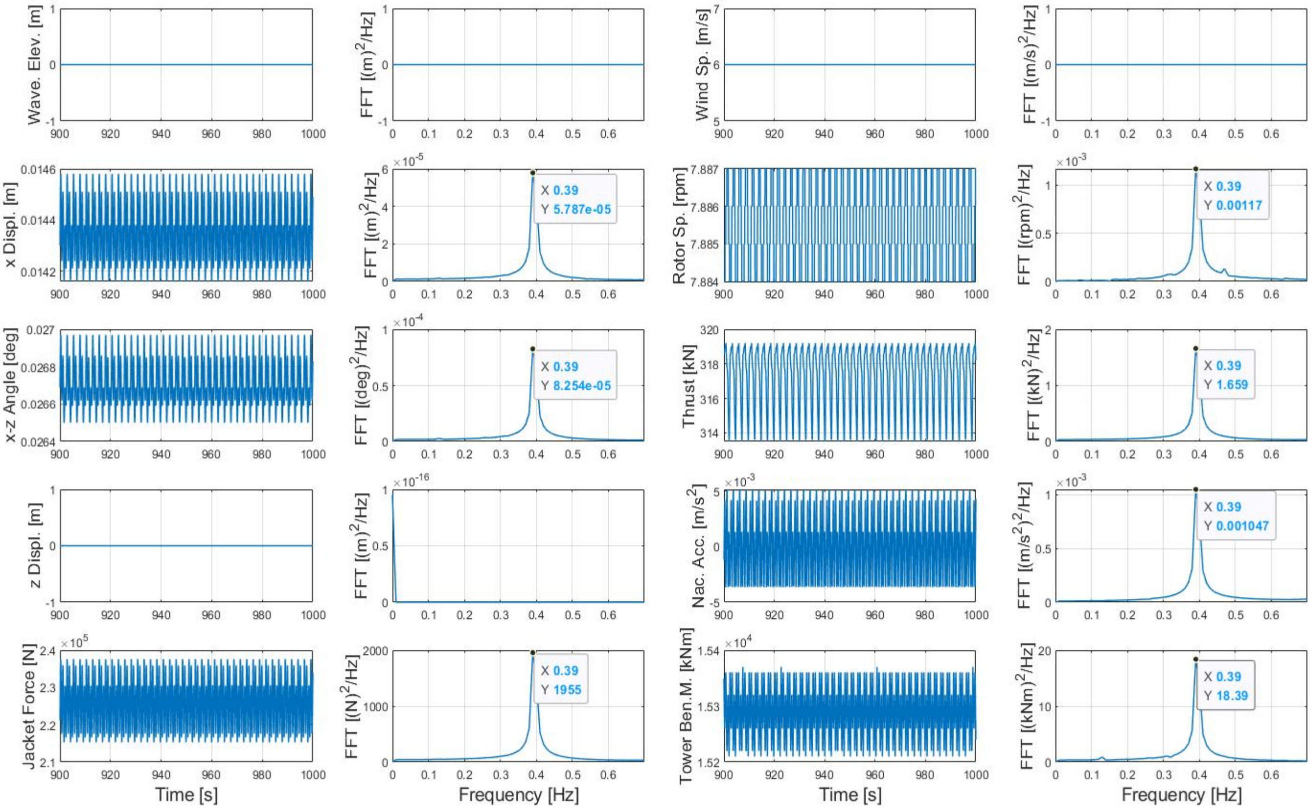

Fig. 8 Response to DLC #4, steady wind only (No wave, V_{Steady} = 6 m/s)

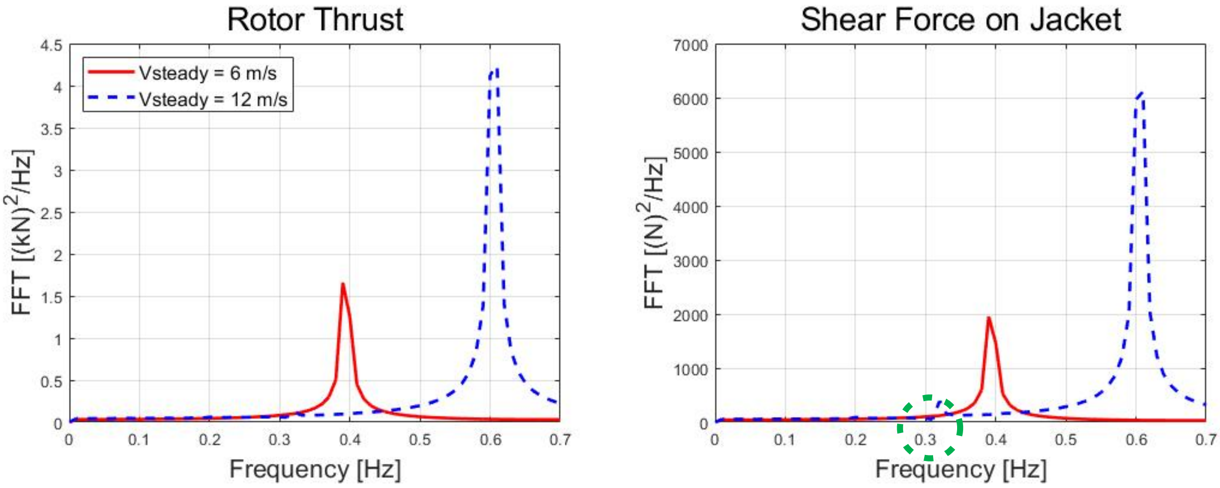

Fig. 9 Comparison of rotor thrust and shear force on jacket for DLC #4 & #5, steady wind only cases

multiplying the rotor rotation speed (7.88 rpm) by the number (3) of blades with the wind speed of 6 m/s and frequency of 0.61 Hz (rpm = 12.1/60 s × 3 blades) resulting from multiplying 12.1 rpm by the number (3) of blades with the wind speed of 12 m/s. Similar to the thrust, the shear force applied to the jacket is also significantly affected by the wind. Additionally, as the wind speed increases two folds from 6 m/s to 12 m/s, the thrust and shear force increase approximately three folds. The wind speed of 12 m/s also caused a weak response at the natural frequency (0.32 Hz) of the wind turbine structure (green circle). This means that the response of the structure also occurs in the natural frequency band from the increasing force acting on the structure as the wind speed increases.

3.3.3 Response to Combined Wind and Wave Case

In the previous section, the effect of the incident wave on the response of the fixed jacket-type wind turbine structure and the effect on the wind were identified. Based on this finding, the response characteristics of the structure are to be evaluated in an environmental load where the incident wave and wind are mixed. First, the steady wind speed (V_{Steady}) and turbulent wind speed ($V_{Turbulence}$) of 6 m/s were

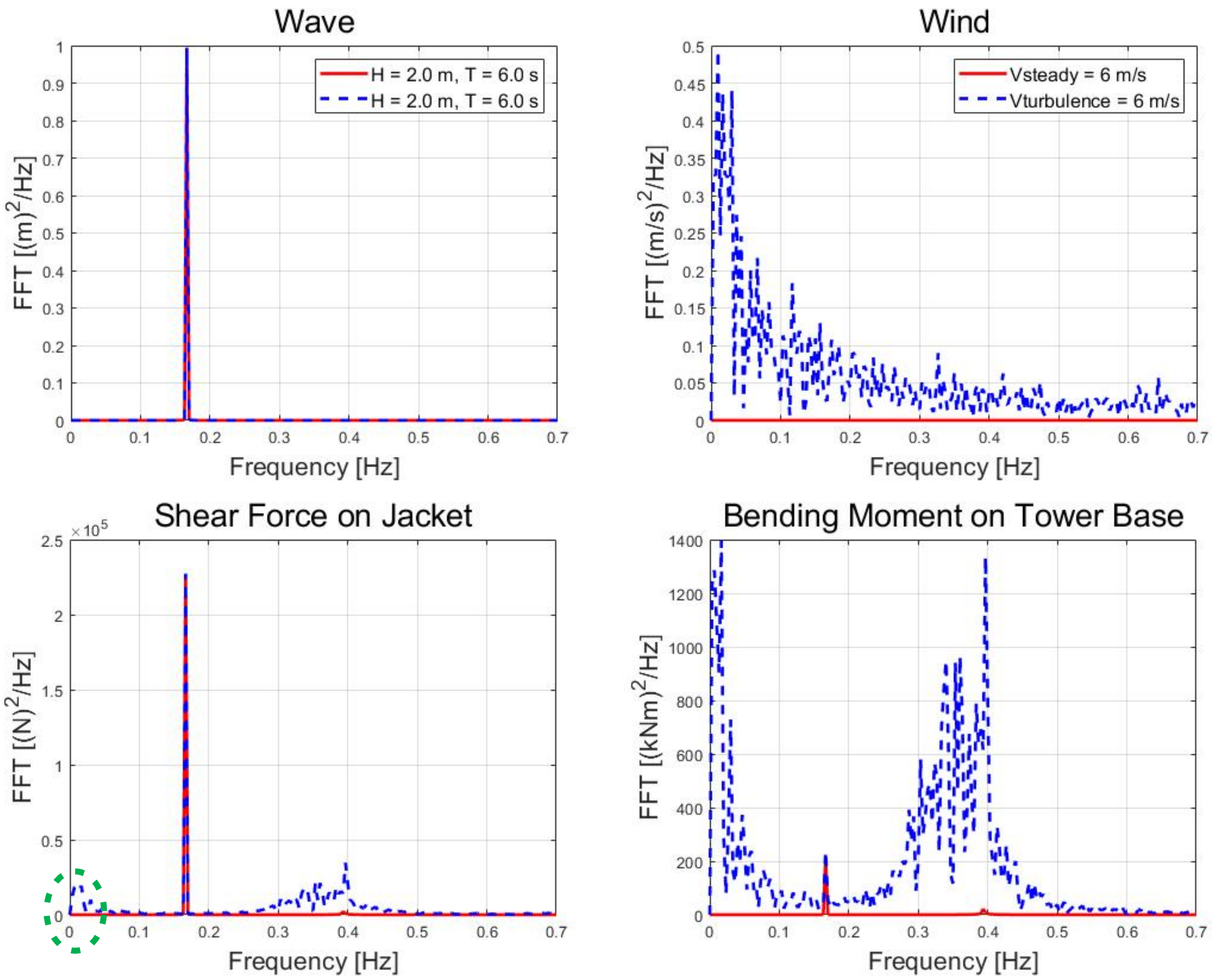

Fig. 10 Comparison of shear force on jacket and tower bending moment for DLC #6 & #7, regular wave with different wind types

substituted in the regular wave condition ($H = 2$ m, $T = 6$ s) in Fig. 10 to compare the response changes in the difference between the steady wind and turbulent wind in the regular incident wave condition (DLCs 6 and 7). The turbulent wind spectrum is dominant at a low frequency in comparison to the incident wave frequency, and the frequency change from a Fourier analysis is 0 because a constant-speed wind was inputted for the steady wind.

The shear force applied to the jacket was predominantly affected by the incident wave in a condition where the same regular wave entered (period: 6 s, frequency: 0.17 Hz), and the effect of the turbulent wind was approximately 8% in comparison to the maximum response at the corresponding point in the low-frequency interval (green circle). A small response of approximately 13% was also derived at the frequency of 0.39 Hz (rpm = 7.8/60 s × 3 blades) by the rotor rotation speed (7.8 rpm) and the number of blades at a wind speed of 6 m/s. This is because the same frequency as the rotor blade rotation frequency verified in the previous results, is included in the frequencies of the turbulent wind. However, the bending moment in the tower base has a small response of approximately 14% at the incident wave frequency of 0.17 Hz in comparison to its maximum frequency response. However, it has a maximum frequency response at the frequency of 0.39 Hz by the low-frequency interval affected by the turbulent wind and rotor rotation. Therefore, the bending moment in the tower base has a considerable response in the frequency (0.39 Hz) band by the low-frequency interval of the turbulent wind, the natural frequency (0.32 Hz) of the structure, and the rotor rotation.

Fig. 11 compares the response characteristics of the bending moment and shear force when the stead wind (6 m/s) and turbulent wind are applied in a condition where the same irregular wave enters (DLCs 8 and 9). The shear force has a high response at a low frequency of the turbulent wind spectrum, the peak frequency of the irregular wave, and the frequency of 0.39 Hz by the rotor rotation speed; it has its maximum response at the peak frequency region (0.1−0.2Hz) of the irregular wave regardless of the form of wind. As verified by the regular wave condition in Fig. 10, the shear force of the jacket is predominantly affected by the incident wave. However, because the significant wave height (average of top 1/3 wave heights) is applied to the irregular wave, a wide response spectrum results in approximately 0.17 Hz and the maximum response is reduced to approximately 1/4 in comparison to the regular wave, to be similar to the response by the turbulent wind. Similar to Fig. 10, the bending moment response of the tower base is slightly affected by the incident wave and is

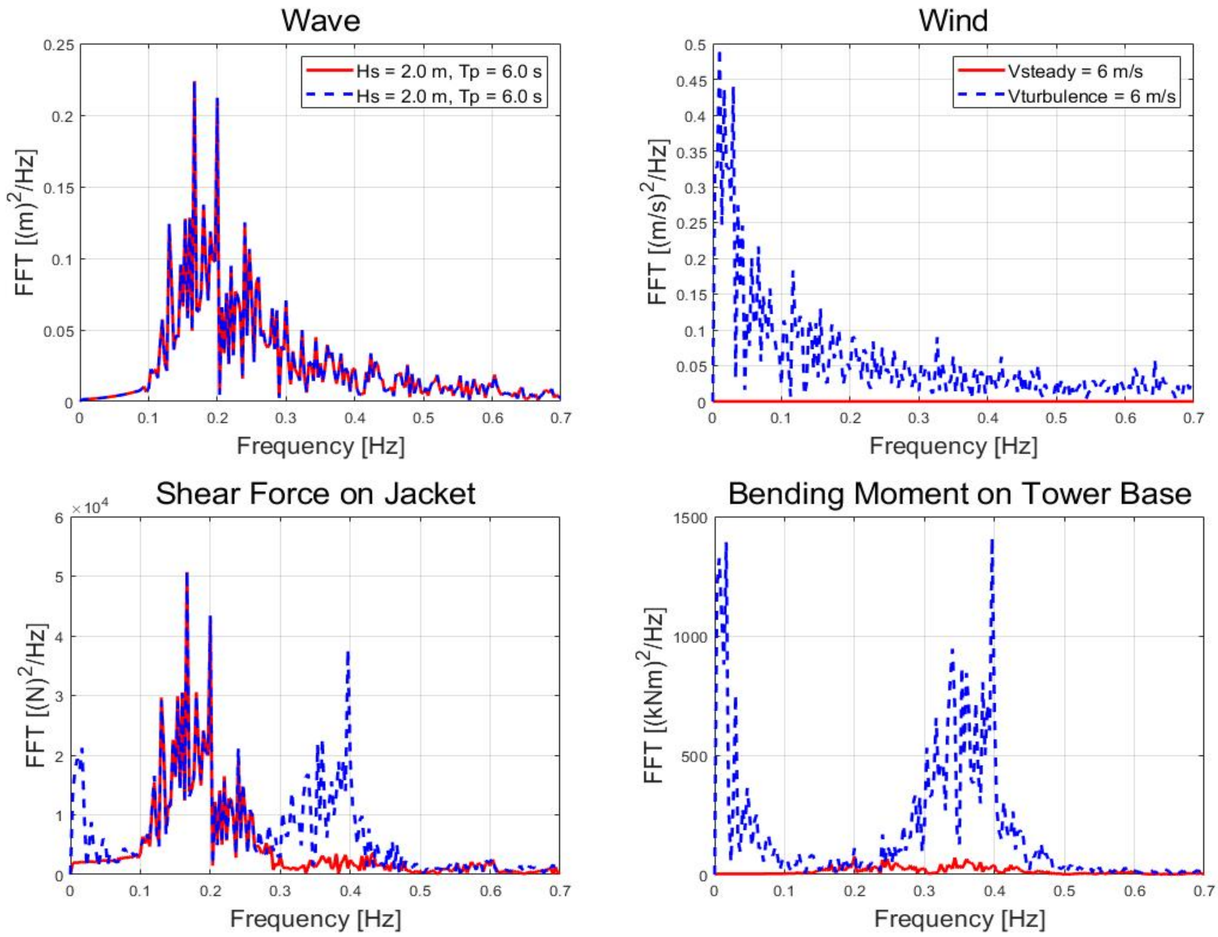

Fig. 11 Comparison of shear force on jacket and tower bending moment for DLC #8 & #9, irregular wave with different wind types

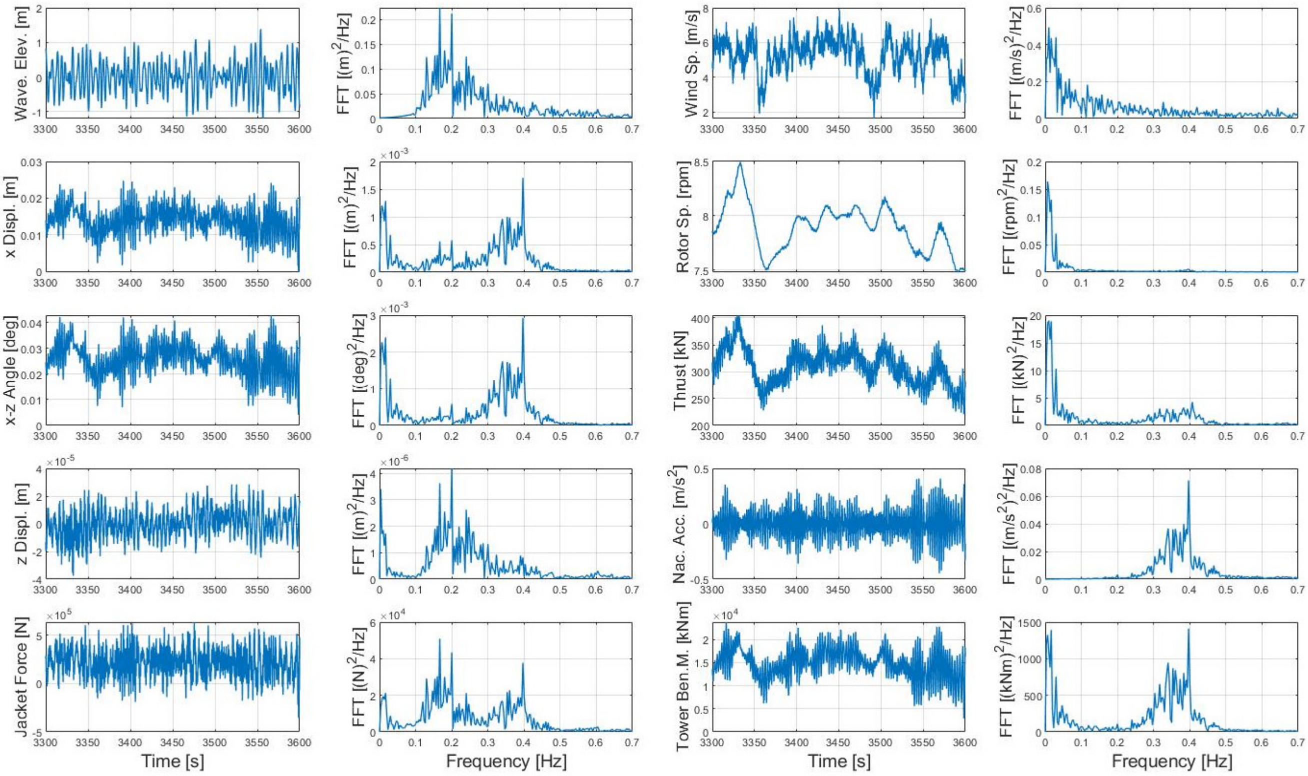

Fig. 12 Response to DLC #9, combined wind and wave condition (H_S = 2.0 m, T_P = 6.0 s, $V_{Turbulence}$ = 6 m/s)

predominantly affected by the wind, judging from the maximum response in the low-frequency region of the turbulent wind spectrum and the frequency region of the rotor rotation speed.

In Fig. 12, the overall response characteristics of the structure for the irregular incident wave were identified in the turbulent wind speed ($V_{Turbulence}$ = 6 m/s) condition. All the responses of the analysis model are affected by the low-frequency turbulent wind speed. The vertical displacement is relatively less affected because the wind turbine is a fixed structure. The shear force of the jacket and vertical displacement have their maximum responses at the incident wave peak frequency (period of 6 s, 0.17 Hz), which means that they are significantly affected by the incident wave. However, the horizontal displacement and *x-z*-direction rotational displacement of the structure have their maximum responses near 0.4 Hz outside the low-frequency region, which indicates that they are predominantly affected at a frequency of 0.39 Hz (rpm = 7.8/60 s × 3 blades) resulting from multiplying the rotor rotation speed frequency by the number of blades at the inputted wind speed ($V_{Turbulence}$) of 6 m/s. The shear force also has a large value at the same frequency.

The rotor rotation speed and thrust have dominant responses in the same low-frequency region by the application of the turbulent wind spectrum. Particularly, the rotor rotation speed is expressed with a spectrum of a very slow long waveform by the turbulent wind speed ($V_{Turbulence}$) of 6 m/s. The nacelle acceleration has its maximum response at 0.39 Hz resulting from multiplying the rotor rotation speed of 7.8 rpm by the number of the blades. The bending moment of the tower has a large response at the frequency (0.39 Hz) by the rotor rotation and low-frequency region of the turbulent wind spectrum and shows a trend similar to the *x-z*-direction rotational displacement response, which shows a correlation between the bending moment and rotational displacement.

Therefore, all the responses of the jacket-type wind turbine are affected by the low frequency of the turbulent wind spectrum. Particularly, the horizontal displacement, rotational displacement, nacelle acceleration, and bending moment are significantly affected at the frequency (0.39 Hz) by the rotor rotation from the wind. The effect of the incident wave frequency is dominant in the vertical displacement of the structure. The shear force of the jacket is predominantly affected in all the frequency regions above.

4. Conclusions

In this study, the dynamic response characteristics corresponding to each environmental external force of a 5 MW fixed jacket-type offshore wind turbine model were analyzed. The characteristics of the frequency responses were compared by analyzing the FFTs of the time series results calculated using the FAST program. The motion responses of the analysis model were analyzed by applying single environmental conditions such as an incident wave-only condition and a wind-only condition to identify the characteristics of the motion responses of the analysis model. The external force that predominantly affects the combined load was identified.

(1) In the incident wave-only condition, the motion response and load response of the wind turbine structure were dominant at the wave frequency; the rotor thrust, nacelle acceleration, and bending moment of the tower base had high responses in the natural frequency band of the structure.

(2) In the wind-only condition, all the responses except for the vertical displacement of the structure were dominant at the frequency resulting from multiplying the rotor rotation frequency caused by the wind and number of blades.

(3) In a combined external force where the wind and wave are simultaneously applied, the vertical displacement of the structure was mainly affected by the incident wave; the shear force applied to the jacket was affected by both the wind and incident wave; the bending moment in the tower base was predominantly affected by the wind.

The response analysis results of the fixed offshore wind turbine according to the wind and wave that were obtained in this study are expected to help in deriving more suitable models for installation in sea areas and developing improved designs by response performance comparison with different types of fixed or floating substructures in the future. It is difficult to state that the FAST program used in this study always derives accurate analysis results. However, it is currently widely used in areas related to wind turbine analysis, is open source code, and is useful in identifying the overall trend of the motion response of a structure.

Funding

This study was supported by grants of the Korean-English Offshore Plant Global Expert Training Project of the Ministry of Trade, Industry and Energy and the Korea Institute for Advancement of Technology and Technology Study Abroad of Daewoo Shipbuilding Engineering Co., Ltd. This study was also supported by a grant of the Basic Research Project in Science and Engineering Areas of the National Research Foundation of Korea (NRF-2018R1D1A1B07040677).

References

Agarwal, P., & Manuel, L. (2008). Extreme Loads for an Offshore Wind Turbine Using Statistical Extrapolation from Limited Field Data. Wind Energy, 11(6), 673–684. https://doi.org/10.1002/we.301

Burton, T., Sharpe, D., Jenkins, N., & Bossanyi, E. (2001). Wind Energy Handbook. New York: Wiley.

Damiani, R., Jonkman, J., & Hayman, G. (2015). SubDyn User's Guide and Theory Manual (Technicla Report NREL/TP-5000-63062). USA: National Renewable Energy Laboratory. https://doi.org/10.2172/1225918

de Vries, W., Vemula, N.K., Passon, P., Fischer, T., Kaufer, D., Matha, D., & Vorpahl, F. (2011). Final Report WP4.2: Support Structure Concepts for Deep Water (UpWind_WP4_D4.2.8).

Faltinsen, O. (1993). Sea Loads on Slips and Offshore Structures. USA: Cambridge University Press.

Fenu, B., Attanasio, V., Casalone, P., Novo, R., Cervelli, G., Bonfanti, M., ... & Mattiazzo, G. (2020). Analysis of a Gyroscopic-Stabilized Floating Offshore Hybrid Wind-Wave Platform. Journal of Marine Science and Engineering, 8(6), 439. https://doi.org/10.3390/jmse8060439

International Electrotechnical Commission (IEC). (2019). Wind Energy Generation Systems－Part 3-1: Design Requirements for Fixed Offshore Wind Turbines (IEC 61400-3-1). IEC.

Jang, J.S., & Sohn, J.H. (2011). Analysis of Dynamic Behavior of Floating Offshore Wind Turbine System. Transactions of the Korean Society of Mechanical Engineers A, 35(1), 77–83. https://doi.org/10.3795/KSME-A.2011.35.1.077

Jeong, S.M., Oh, U.G., Lee, Y.C., Lim, J.T., Lee, K.B., & Choi, J.S. (2020). A Study on the Evaluation of the Economics and Environmental Contribution to the Jeju Power System from Tamla Offshore Wind Farm. The Transactions of The Korean Institute of Electrical Engineers, 69(7), 955–963. https://doi.org/10.5370/KIEE.2020.69.7.955

Jonkman, J.M. (2007). Dynamics Modeling and Loads Analysis of an Offshore Floating Wind Turbine (Technicla Report NREL/TP-500-41958). USA: National Renewable Energy Laboratory.

Jonkman, J.M., & Buhl, Jr., M.L. (2005). FAST User's Guide (Technical Report, NREL/EL-500-38230). USA: National Renewable Energy Laboratory.

Jonkman, J.M., Butterfield, S., Musial, W., & Scott, G. (2009). Definition of a 5-MW Reference Wind Turbine for Offshore System Development (NREL/TP-500-38060), USA: National Renewable Energy Laboratory.

Jonkman, J.M., Hayman, G.J., Jonkman, B.J., Damiani, R.R., & Murray, R.E. (2015). AeroDyn v15 User's Guide and Theory Manual. USA: National Renewable Energy Laboratory.

Jonkman, J.M., Robertson, A.N., & Hayman, G.J. (2014). HydroDyn User's Guide and Theory Manual. USA: National Renewable Energy Laboratory.

Kim, H.K., Han, W.S., & Lee, S.G. (2019). Wind Farm Layout Optimization Considering Dynamic Characteristic of Floating Wind Turbine. New & Renewable Energy, 15(3), 1–10. https://doi.org/10.7849/ksnre.2019.9.15.3.001

Kim, K.H., Kim, D.H., Kwak, Y.S., & Kim, S.H. (2015). Design Load Case Analysis and Comparison for a 5MW Offshore Wind Turbine Using FAST, GH Bladed and CFD Method. The KSFM Journal of Fluid Machinery, 18(2), 14–21. https://doi.org/10.5293/kfma.2015.18.2.014

Lanzafame, R., & Messina, M. (2007). Fluid Dynamics Wind Turbine Design: Critical Analysis, Optimization and Application of BEM Theory. Renewable Energy, 32(14), 2291-2305. https://doi.org/10.1016/j.renene.2006.12.010

Li, L., Gao, Y., Hu, Z., Yuan, Z., Day, S., & Li, H. (2018). Model Test Research of a Semisubmersible Floating Wind Turbine with and Improved Deficient Thrust Force Correaction Approach. Renewable Energy, 119, 95–105. https://doi.org/10.1016/j.renene.2017.12.019

Moriarty, P.J., & Hansen, A.C. (2005). AeroDyn Theory Manual (NREL/TP-500-36881). USA: National Renewable Energy Laboratory. https://doi.org/10.2172/15014831

Morison, J., Johnson, J., & Schaaf, S. (1950). The Force Exerted by Surface Waves on Piles. Journal of Petroleum Technology, 2, 149–154. https://doi.org/10.2118/950149-G

Oh, H.T., Yeo, M.Y., Jung, H.E., & Shim, J.M. (2020). Status and Improvement of Environmental Impacts Assessment on the Marine Endangered Species Around the Coastal Area of Offshore Wind Energy – Case Study of the Marine Mammals and Sea Birds. Journal of fishries and Marine Sciences Education, 32(6), 1428–1444. https://doi.org/10.13000/JFMSE.2020.12.32.6.1428

Park, M.K., Park S.G., Seong, B.C., Choi, Y.J., & Jung, S.H. (2021). Current Status and Prospective of Offshore Wind Power to Achieve Korean Renewable Energy 3020 Plan. Journal of Korean Society of Environmental Engineers., 43(3), 196–205. https://doi.org/10.4491/KSEE.2021.43.3.196

Peters, D.A., Boyd, D.D., & He, C.J. (1989). Finite-State Induced-Flow Model for Rotors in Hover and Forward Flight. Journal of the American Helicopter Society, 34(4), 5–17. https://doi.org/10.4050/JAHS.34.5

Popko, W., Vorpahl, F., Zuga, A., Kohlmeier, M., Jonkman, J., Robertson, A., ... & von Waaden, H. (2012). Offshore Code Comparison Collaboration Continuation (OC4), Phase 1-Results of Coupled Simulations of an Offshore Wind Turbine with Jacket Support Structure. In The Twenty-second International Offshore and Polar Engineering Conference, Rhodes, Greece, ISOPE-I-12-117.

Shi, W., Park, H.C., Chung, C.W., & Kim, Y.C. (2011). Comparison of Dynamic Response of Monopile, Tripod and Jacket Foundation System for a 5-MW Wind Turbine. In the Twenty-first International Offshore and Polar Engineering Conference. Maui, Hawaii, USA, ISOPE-I-11-266.

Snel, H. (2003). Review of Aerodynamics for Wind Turbines. Wind Energy, 6(3), 203–211. https://doi.org/10.1002/we.97

Song, C.Y., & Yoo, J. (2017). Dynamic Response Analyses of Fixed Type Substructures for 2.5 MW Class Offshore Wind Turbine. Journal of Advanced Research in Ocean Engineering, 3(1), 15–24. https://doi.org/10.5574/JAROE.2017.3.1.015

Suzuki, A. (2000). Application of Dynamic Inflow Theory to Wind Turbine Rotors (Ph. D. thesis). University of Utah.

Tran, T.T., Kang, S., Lee, J.H., & Lee, D. (2021). Directional Bending Performance of 4-Leg Jacket Substructure Supporting a 3MW Offshore Wind Turbine. Energies, 14(9), 2725. https://doi.org/

10.3390/en14092725

Wei, K., Sanjay, R.A., & Myers, A.T. (2014). Incremental Wind-Wave Analysis of the Structural Capacity of Offshore Wind Turbine Support Structures under Extreme Loading. Engineering Structures, 79, 58–69. https://doi.org/10.1016/j.engstruct.2014.08.010

Zwick, D., & Muskulus, M. (2015). The Simulation Error Caused by Input Loading Variability in Offshore Wind Turbine Structural Analysis. Wind Energy, 18(8), 1421–1432. https://doi.org/10.1002/we.1767

Author ORCIDs

Author name	**ORCID**
Kim, Jaewook	0000-0002-7652-7314
Heo, Sanghwan	0000-0003-0033-5022
Koo, WeonCheol	0000-0002-4384-0996

Journal of Ocean Engineering and Technology 35(5), 360-368, October, 2021
https://doi.org/10.26748/KSOE.2021.062

pISSN 1225-0767
eISSN 2287-6715

Original Research Article

Mechanism Development and Heading Control of Catamaran-type Sail Drone

Dong-Woo Man[1] and Hyun-Sik Kim[2]

[1]*Graduate Student, Department of Mechanical System Engineering, Tongmyong University, Busan, Korea*
[2]*Professor, School of Mechanical Engineering, Tongmyong University, Busan, Korea*

KEY WORDS: Sail drone, Catamaran-type, Heading control, Fuzzy logic controller, Perfromance estimation, Speed and duration

ABSTRACT: *The need for energy harvesting in marine environments is gradually increasing owing to the energy limitation of marine robots. To address this problem, a catamaran-type sail drone (CSD), which can harvest marine energies such as wind and solar, was proposed in a previous study. However, it was designed and manufactured without considering the stability, optimal hull-form, and maintenance. To resolve these problems, a CSD with two keels, a performance estimator, V-shape hulls, and modularized components is proposed and its mechanism is developed in this study. To verify the performance of the CSD, the performance estimation using smoothed-particle hydrodynamics (SPH) and the heading control using fuzzy logic controller (FLC) are performed. Simulation results show the attitude stability of the CSD and the experimental results show the straight path of the CSD according to wind conditions. Therefore, the CSD has potential applications as an energy harvesting system.*

1. Introduction

In recent years, the interest in oceans has been increasing due to the Fourth Industrial Revolution for Oceans, wind power, offshore photovoltaic power plants, and Antarctic and Arctic exploration bases. Accordingly, interest in the importance of maritime domain awareness (MDA) has also been increasing (Kim et al., 2016).

Research on marine robots for efficient mission performance in oceans has increased with the increasing interest in MDA (Yeu et al., 2019, Park et al., 2021). In the case of autonomous marine robots, there is a problem of energy insufficiency because of the size limitation. The energy insufficiency leads to severe problems, such as loss or damage of the robots caused by the lack of energy when the robots are conducting highly difficult missions and the activity radius is limited (Park et al., 2019).

To solve this problem, diverse studies have been conducted on marine-energy harvesting-based robots such as wave gliders and underwater gliders in South Korea and abroad. Among them, sailing-type robots, which have strengths in terms of speed and duration, stand out (Meinig et al., 2015).

A sail drone, a sailing-type robot, is a system that is propelled by wind and is heavily affected by wind direction and speed. Hence, it has a disadvantage that the straight path movement is not excellent because of the cross-flow forces produced by wind (Sa et al., 2019).

To solve this problem, research was conducted in South Korea on a type of sail drone, to which a keel, a cross-flow force prevention device, was attached; however, the manufacturing and maintenance costs were high because the attitude stability and modularization for maintenance and repair were not considered in the design and manufacturing process (Man et al., 2020). Furthermore, they did not consider suitable sailing control techniques for the sail drone.

In this study, therefore, we developed a performance estimation tool that can ensure attitude stability using previously produced 3D design results and the smoothed-particle hydrodynamics (SPH) method, thereby securing attitude stability in the design process. Furthermore, we considered a V-model of the bow for speed improvement and modularization for robot maintenance and repair.

We considered the shape of the catamaran-type sail drone (CSD) to increase the attitude stability and considered a hybrid propulsion method, in which the sail is used as the main propulsion method and an electric propeller is used as the auxiliary propulsion method.

Recently, studies have used neural network (NN) methods (Fang et al., 2017) and deep learning (Sun and Gao, 2020) for the heading control of marine robots. However, owing to the complexity of sailing techniques, marine robots need expert systems that operate based on expert knowledge and are sensitive to wind direction and speed, thus

Received 13 July 2021, revised 2 September 2021, accepted 15 September 2021
Corresponding author Hyun-Sik Kim: +82-51-629-1565, hyunskim@tu.ac.kr

requiring more robust controllers.

Therefore, this study proposes a fuzzy logic controller (FLC), which has more robust control characteristics and is easy to reflect an expert system.

Section 2 presents information related to the development of the mechanism of the CSD, and Section 3 presents the performance estimation tool created to secure the attitude stability in the design process. Section 4 describes the FLC for the heading control of the CSD. Section 5 discusses the experiments and results for the validation of the developed CSD mechanism and the proposed controller's performance, and Section 6 summarizes the conclusions.

2. Development of CSD Mechanism

The development of the CSD mechanism focuses on facilitating wind propulsion using the sails—the main propulsion method—and the attachment of solar panels. In the future, we plan to construct the system using solar panels for energy supply and the electric thruster as an auxiliary propulsion system while the sails are folded when the CSD enters a no-go zone.

The previously developed CSD ver.1.0 was not modularized and had high manufacturing and maintenance costs. Therefore, we configured the CSD ver.2.0 to facilitate easy disassembly and assembly of each module to increase the efficiency of manufacturing and maintenance. Fig. 1(a) shows the final design result of the CSD ver.2.0, and Fig. 1(b) shows the design considering the modularization, as mentioned earlier.

The keel was modularized to facilitate disassembly and assembly for the keel selection test and maintenance/repair, and the cross-sectional design of the keel was performed using a ship equipment design method.

The newly developed CSD ver.2.0 uses the same sails as the previously developed ver.1.0, but it is configured for better performance (Man, 2021).

Table 1 lists the performance and specifications of the CSD ver.1.0 and 2.0. It can be seen that because the bow of ver.2.0 was designed considering the V-model, the payload increased by approximately 1.4 times, despite the fact that the CSD's breadth and length decreased. Furthermore, as the size of the body decreased with the same area of the sails, the speed increased by approximately 1.1–1.4 times at a wind speed of 3–5 m/s, which was under the gentle breeze category in the Beaufort wind force scale. Moreover, when propelled by electricity, the speed increased by approximately 1.3 times.

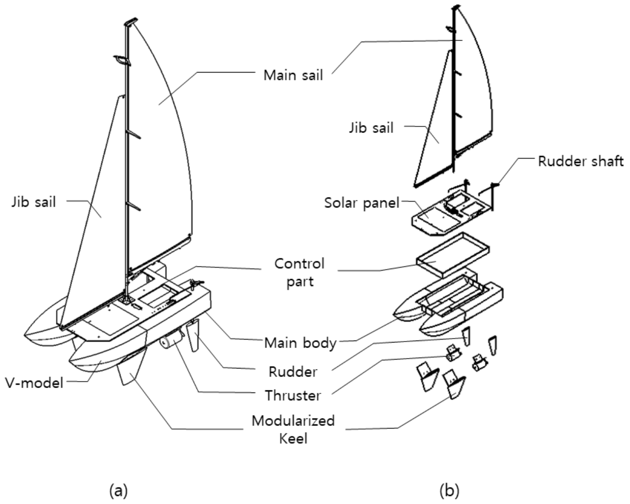

Fig. 1 Mechanism of buoy robot

Table 1 CSD ver.1.0 and 2.0 performance and specifications comparison

			Ver.1.0	Ver.2.0
Size	Weight(on air)	(kg)	3.4	2.0
	Payload	(kg)	1.12	1.5
	Length over all (*L*)	(cm)	60	50
	Moulded Brdadth (*B*)	(cm)	33.4	26.5
	Depth (*D*)	(cm)	16	16.3
	Height (*H*)	(cm)	113	112.6
Speed (Gentle breeze)	Downwind	(m/s)	0.205	0.233
	Crosswind	(m/s)	0.291	0.389
	Upwind	(m/s)	0.318	0.437
Speed	Electric propulsion (Max Speed)	(m/s)	0.2	0.255

Fig. 2 Prototype of CSD ver.2.0

Fig. 2 shows the shape of the completed prototype, which was produced as a scale model for the convenience of fabrication and experiments. We used CATIA, a 3D design tool, for modeling, based on which the prototype was fabricated using a 3D printer. The control box and body cover unit were fabricated with acrylic using a laser machine.

It was equipped with an attitude heading reference system (AHRS) for heading control and a weathervane for detecting wind direction. Additionally, it was configured to save data on an SD card and backup data through Bluetooth and on the host PC through wireless communication.

3. Development of Performance Estimation Tool

We developed a performance estimation tool to examine the attitude stability of the CSD before constructing it using the final 3D design data. Various sensors and devices are required to check the attitude stability using the fabricated equipment. However, if the performance estimation tool is used, it is easy to attach and use the sensors, without incurring costs.

The performance estimation tool was created using the SPH method, which allows real-time rendering based on the interaction between each particle of the fluid. Therefore, we developed the performance estimation tool using NVIDIA FleX that implemented the SPH method and using Unreal Engine 4 (UE4), which supported it.

The performance estimation tool developed based on the UE4 should convert the design files into files that can be recognized by the UE4 and receive the model as input. When UE4 receives the final model as an input, the inside of the model is empty, as shown in Fig. 3(a); further, because the final model cannot be recognized as a Flex object, the fluid particles do not interact with the model and pass through it. Therefore, conversion of the model into Flex objects is required, as shown in Fig. 3(b). The Flex objects contained inside and the fluid particles are configured in the same size. Table 2 lists the performance and specifications of the performance estimation tool.

For the performance estimation tool, we chose the water tank size, frames per second (FPS), maximum size and maximum quantity of particles, and life cycle to facilitate real-time rendering. The water tank size reflected the real experimental environment as much as possible. However, if the water tank size, particle size, maximum quantity, or FPS changes, the computation amount increases, causing difficulty in real-time rendering. Therefore, we determined their values through tests to facilitate real-time rendering.

We constructed the experimental water tank in a rectangular shape to examine the movement by allowing the fluid to enter in three directions. Fig. 4 shows an execution screen of the developed performance estimation tool. It provides a total of seven views, including the front, left, right, and top.

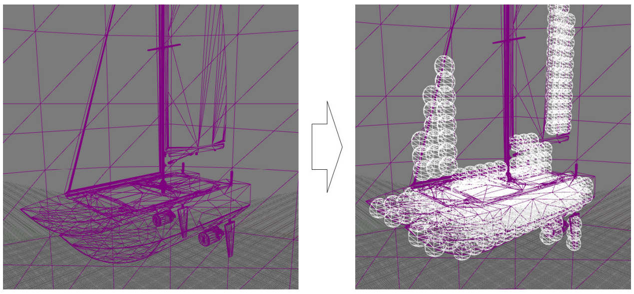
(a) (b)

Fig. 3 Conversion result of Flex object

Table 2 Performance and specifications of performance estimation tool

Max particles (ea)	400,000
Particle radius (mm)	2.50
FPS (fps)	60
Lift cycle (s)	60
Water tank size (Width × Length) (mm × mm)	3,000 × 1,855

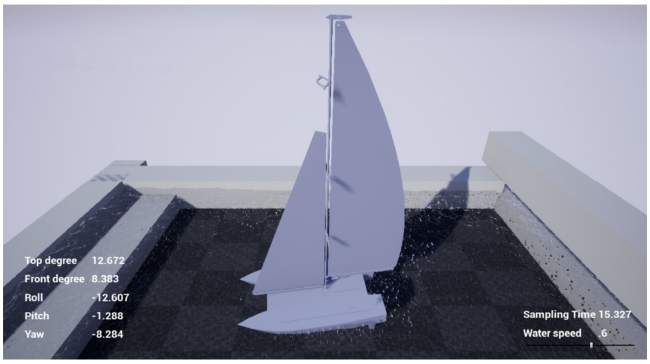

Fig. 4 Performance estimation of developed CSD

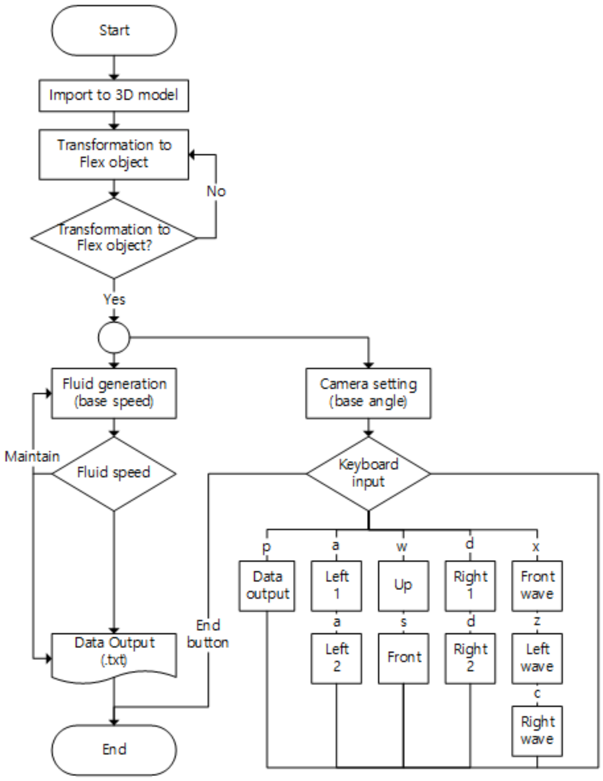

Fig. 5 Flowchart of performance estimation algorithm

Fig. 5 shows the algorithm flowchart. The inflow speed of the fluid can be controlled using the mouse wheel, and the flowing direction of the fluid can be controlled using the z, x, and c keys. Furthermore, to check the CSD's attitude stability using the sensors attached to the CSD, the roll, pitch, and yaw values are output to the screen and a text file.

Figs. 6–8 show the roll, pitch, and yaw values with and without the keel in the CSD ver.2.0, which are results of the performance estimation tool. The solid line represents the case where the keels exist, and the dashed line represents the case where the keels do not exist.

As shown in Fig. 6, when there was no keel, the roll motion occurred up to approximately −50° as the fluid entered from the side at

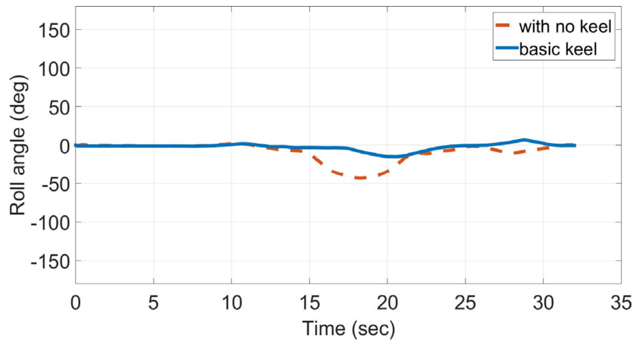

Fig. 6 Verification of attitude stability (Roll)

approximately 10 s. Furthermore, the roll motion occurred up to 10° at 25 s. In contrast, when there were keels, a maximum roll motion of ±10° occurred. This shows that keels result in better performance in terms of roll damping.

In Fig. 7, a similar performance of a maximum of approximately ±10° is shown regardless of whether the keels exist or not; it is confirmed that keels do not have a significant impact on the pitch motion.

As shown in Fig. 8, when there are keels, there is a movement of approximately 10° at 12 and 20 s, and the maximum movement is approximately 15°. When there are no keels, the maximum movement is approximately 10°. It is determined that as the keels at the bow collide with the particles first, there is more movement.

The performance estimation tool shows that the keels are helpful in terms of roll damping, through which the attitude stability can be secured.

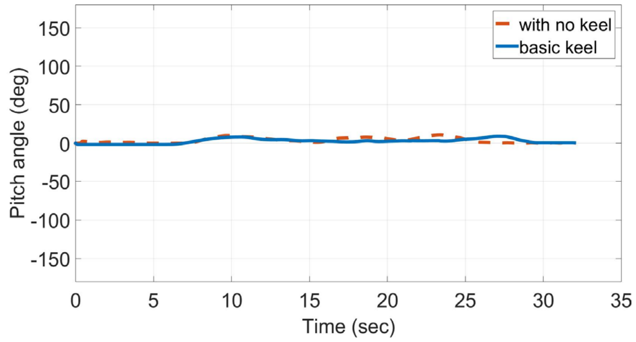

Fig. 7 Verification of attitude stability (Pitch)

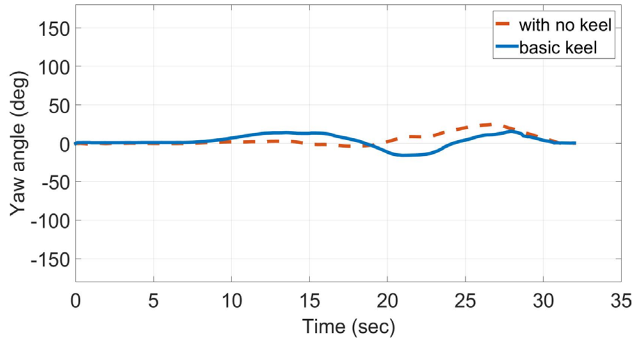

Fig. 8 Verification of attitude stability (Yaw)

4. Design of Heading Control Part

Sailing yachts cannot go straight through no-go zones, where the wind blows from the proceeding direction. They have to use a technique such as tacking to proceed in a zig-zag manner. Furthermore, because the speed and direction change as the angle of attack, at which the wind is met, changes according to the degree of spreading the sails, the degree of spreading the sails should be based on expert knowledge. Therefore, this paper proposes a simplified method, a hybrid technique in which the consequent comes out as a constant.

For the proposed control parts, we considered two parts: the heading control part and sail angle control part. In the heading control part, the part of the helm angle is considered using the heading value of the AHRS, whereas in the sail angle control part, the spreading angle of the sails is controlled using the heading value of the AHRS.

The fuzzy rule of the proposed heading control part is configured using the heading value error e_r and its differential $\dot{e}_r$, as presented in Table 3. The fuzzy rule is configured with NB (negative big), NS (negative small), Z0 (zero), PS (positive small), and PB (positive big), and it has a simple and basic format.

Table 3 Definition of fuzzy rule (Heading)

$\dot{e}_r$ e_r	PB	PS	Z0	NS	NB
PB	1.0	1.0	0.8	0.5	0.0
PS	1.0	0.8	0.5	0.0	-0.5
Z0	0.8	0.5	0.0	-0.5	-0.8
NS	0.5	0.0	-0.5	-0.8	-1.0
NB	0.0	-0.5	-0.8	-1.0	-1.0

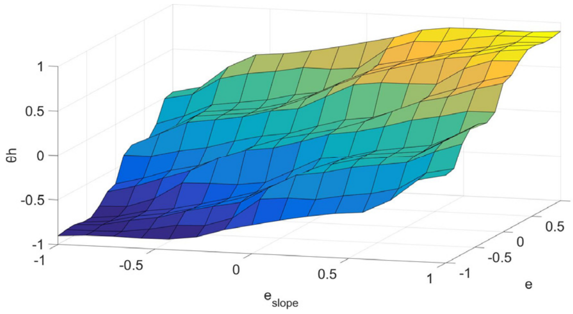

Fig. 9 Control surface of proposed FLC (Heading)

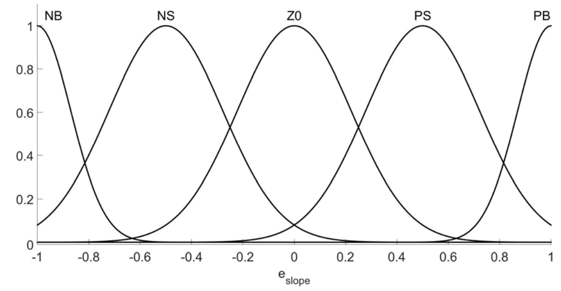

Fig. 10 Membership function of proposed FLC (Heading)

Table 4 Proposed fuzzy rule (Sail angle)

e_r θ_w	Small	Medium	Large
No-go	0.0	0.0	0.0
Up	0.0	1.0	0.5
Cross	0.8	1.0	0.5
Down	0.5	0.8	1.0
Deadrun	0.5	1.0	0.5

Fig. 9 shows the control surface that represents the fuzzy input and output relationship regarding the proposed fuzzy rule. For the membership function of the fuzzy input part, which uses the heading value error and error change rate as input values, we used a Gaussian form, as shown in Fig. 10.

The fuzzy rule of the proposed sail angle control part is configured using the measured wind direction angle θ_w and the heading value error e_r, as illustrated in Table 4. The fuzzy rule divides e_r into small, medium, and large by size. The wind direction is defined for five cases with the no-go zone as the baseline: No-go; Up, which is a case of wind blowing from the front in the straight-ahead direction; Cross, which is a case of crosswind; Down, which is a case of wind blowing from the back; and deadrun, which is a case of wind blowing from a rear direction of ±170° relative to the straight-ahead direction. In other words, we configured them based on the criteria used by experts in common sailing methods.

Fig. 11 shows the control surface that represents the fuzzy input and output relationship regarding the proposed fuzzy rule. For the membership function of the fuzzy input part, which uses the heading value error and wind direction as input values, we used a Gaussian form, as shown in Fig. 12.

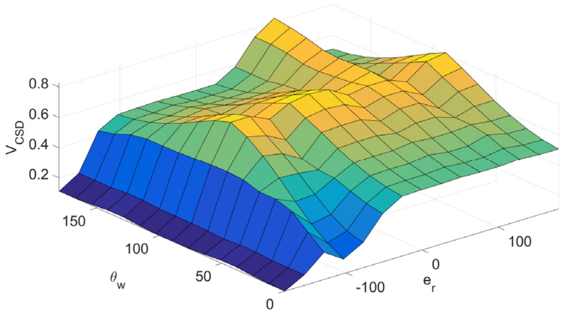

Fig. 11 Control surface of proposed FLC (Sail angle)

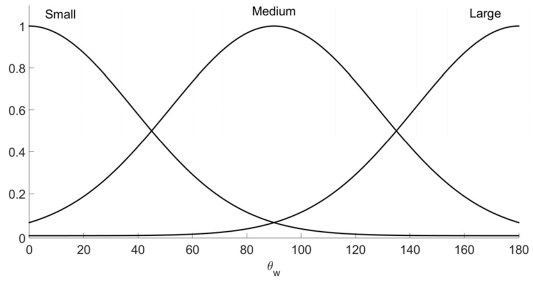

Fig. 12 Membership function of proposed FLC (Sail angle)

$$F = \sum_{i=1}^{N} W_i c_i \Big/ \sum_{i=1}^{N} W_i \qquad (1)$$

The non-fuzzification of the proposed FLC for the heading control uses a center of gravity method, as shown in Eq. (1). Here, F denotes the output value based on the center of gravity method, N is the number of fuzzy rules, W_i denotes the membership value for the i-th output variable, and c_i denotes the i-th output set single value.

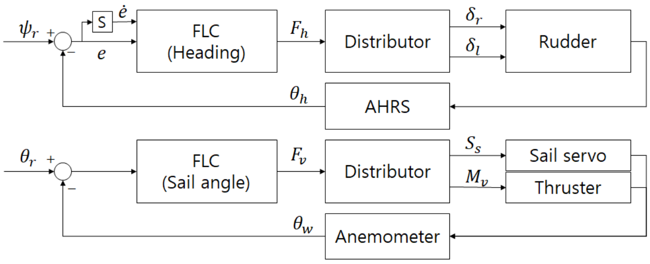

Fig. 13 Block diagram of proposed FLC

Fig. 13 shows the control block diagram of the proposed FLC. The upper part comprises the heading control part, whereas the lower part comprises the sail angle control part. Because the sails are pushed by the cross-flow force, we used the heading value error to configure the heading and sail angle control parts. Based on the above process, we completed the design of the algorithm that uses FLC for heading control.

5. Experiments and Discussion

For the performance evaluation of the constructed CSD and proposed controllers, we compared the FLC and P controller that controls the helm angle using the heading value error. The experimental environment was set up as shown in Fig. 14.

An experimental water tank constructed with a size of 3.66 m and a depth of approximately 1 m was used indoors, and a camera was used

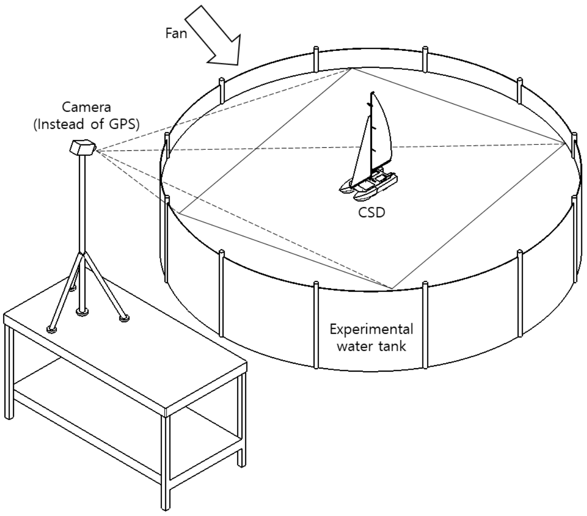

Fig. 14 Experimental enviroment

Table 5 Scenario for Test and Evaluation

Wind velocity	Wind direction		
	Downwind	Crosswind	Upwind
Gentle breeze (3–5 m/s)	Non-fuzzy / Fuzzy (D-G case)	Non-fuzzy / Fuzzy (C-G case)	Non-fuzzy / Fuzzy (U-G case)
Fresh breeze (8–10 m/s)	Non-fuzzy / Fuzzy (D-F case)	Non-fuzzy / Fuzzy (C-F case)	Non-fuzzy / Fuzzy (U-F case)

as a substitute for the GPS. The images were corrected by a perspective transform, and according to the measurement results after the image processing, 1 pixel corresponded to approximately 1 cm. Furthermore, image processing for obtaining the location information of the CSD was implemented to distinguish and track the red color using RGB for convenience of use. Furthermore, the system was configured to output the coordinate data and processed images to files.

Table 5 presents a brief overview of the test and evaluation scenarios. Here, based on the Beaufort wind force scale and the results of measuring the wind speed using a weathervane 2 m away, the wind speeds were classified into gentle breeze (a wind speed of 3–5 m/s) and fresh breeze (8–10 m/s). Furthermore, the wind direction was classified into Upwind (wind blowing at approximately 50° from the front based on the proceeding direction of the CSD), Crosswind (wind blowing at 90° from the side), and Downwind (wind blowing at 130° from the rear side.

In all the experimental results, the solid line represents a case using the FLC, and the dashed line represents a case not using it. The desired target point in the image coordinates is (0, 165).

Fig. 15 shows the D-G case. In (a), the heading value graph, the maximum error is 20° identically. In the case of the dashed line, it can be seen that the direction is continuously maintained in a trajectory that has been pushed away once. The solid line shows that the direction is maintained by veering at 4 s and 8 s.

In the image coordinate trajectories of Fig. 15(b), the dashed line shows that the direction was maintained properly for a while, but it deviated near the destination, and the vessel arrived at a position approximately 16 cm away. However, the solid line shows that the vessel arrived at the desired destination, confirming that its performance is better.

Fig. 16 shows the D-F case, in which the wind speed increased, resulting in numerous errors in the heading values and a trajectory significantly pushed away. Fig. 16(a) shows that the maximum error was 25° in the case of the dashed line, but it decreased to 20° in the case of the solid line, where the FLC was used. Furthermore, because it veered at 5 s and maintained the direction properly, it can be seen that the response speed increased.

In the image trajectories of Fig. 16(b), the solid line shows that the CSD proceeded in the desired direction and arrived at a position approximately 14 cm away, but the dashed line shows that it arrived at a completely different location because the cross-flow force occurred significantly.

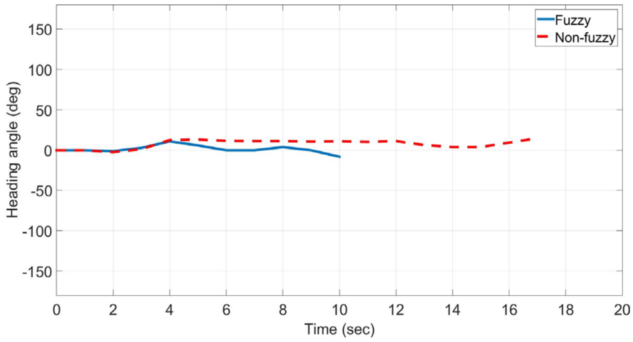

(a) Heading angle

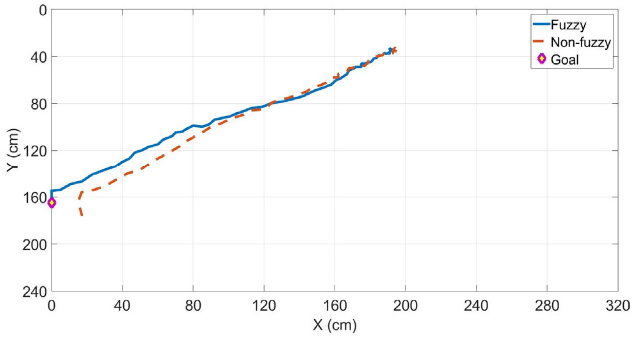

(b) Position

Fig. 15 Performance of heading control (D-G case)

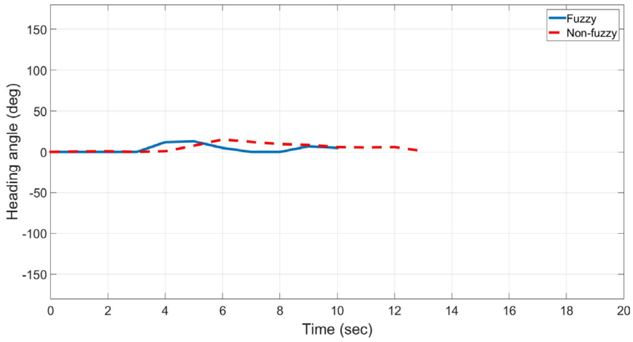

(a) Heading angle

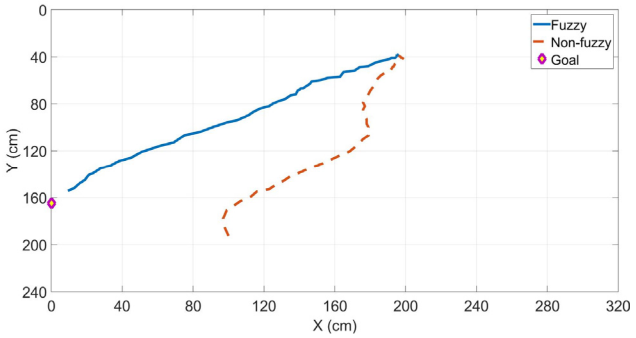

(b) Position

Fig. 16 Performance of heading control (D-F case)

Fig. 17 shows the C-G case. The crosswind, the wind blowing from the side, occurs typically, where the cross-flow force occurs the most. However, in the case of a gentle breeze, the cross-flow force was not large because the wind speed was low.

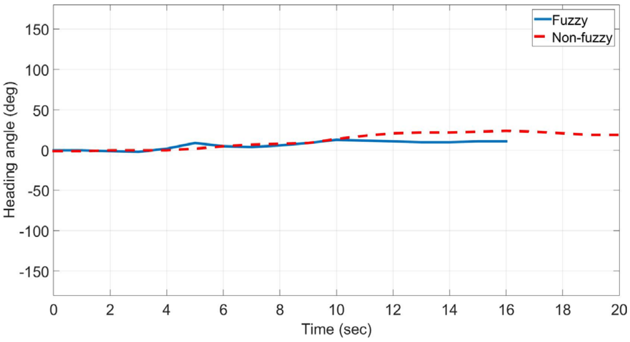

(a) Heading angle

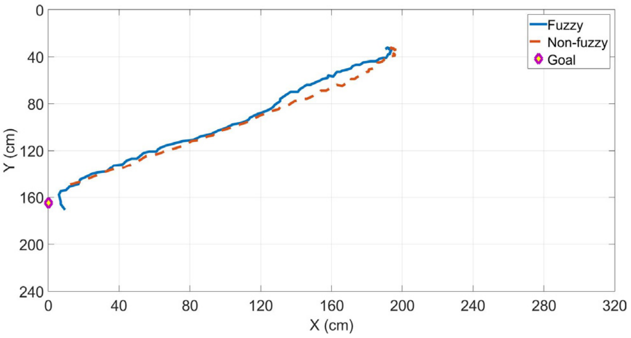

(b) Position

Fig. 17 Performance of heading control (C-G case)

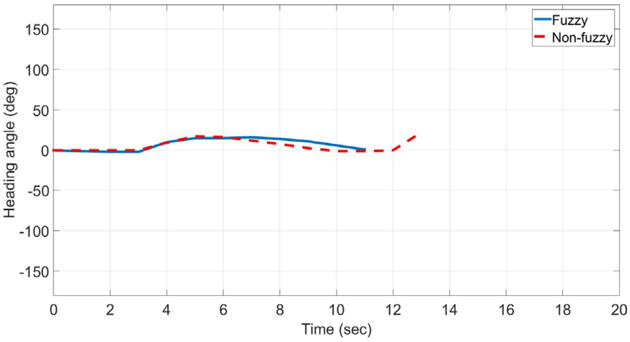

(a) Heading angle

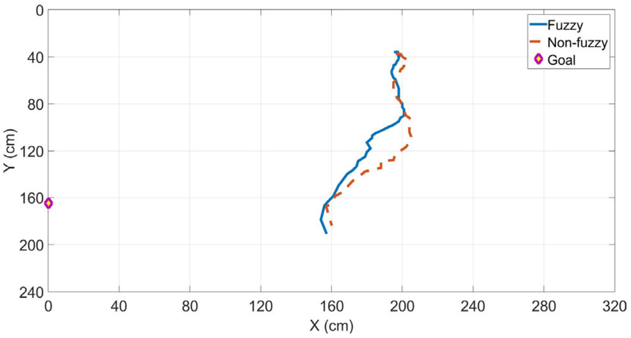

(b) Position

Fig. 18 Performance of heading control (C-F case)

Fig. 17(a) shows that the maximum error of the heading values is 30° in the case of the dashed line. In the solid line, it can be seen that errors occurred up to 15° at 5 s and 10 s, but the direction was maintained by veering.

In the image coordinate trajectories of Fig. 17(b), it can be observed that the desired direction was well-maintained in both cases. In the case of the solid line, the CSD arrived at a position approximately 5 cm away, and in the case of the dashed line, it arrived at a position approximately 20 cm away.

Fig. 18 shows the C-F case. As mentioned earlier, it is a case where the cross-flow force occurs the most. When the heading values are compared in Fig. 18(a), it is found that the maximum error is 20°. The solid line shows that direction is well-maintained through veering. In the case of the dashed line, however, the value increases up to 24°.

The image trajectories of Fig.18 (b) show that the CSD was pushed away by the cross-flow force in both cases, and it was pushed away less when the proposed controller was used compared to before using it. Nevertheless, it was pushed significantly to the side in both cases, proceeding in directions different from the desired direction.

Fig. 19 shows the U-G case. In the heading values in Fig. 19(a), the dashed line shows that the direction started to turn at 6 s, turning 30° at the end. However, the solid line shows that a maximum error of 18° occurred at 6 s, but the direction was maintained by veering.

The comparison of the solid line and dashed line in the image trajectories of Fig. 19(b) shows similar performances. The dashed line shows arrival at a position approximately 8 cm away with a trajectory, which was pushed further away to the side compared to the solid line. The solid line shows that the direction was maintained, and the CSD arrived at the target position.

Fig. 20 shows the U-F case. In the heading values in Fig. 20(a), errors occurred significantly irrespective of the controller. The dashed line shows that an error of approximately 30° occurred, and toward the

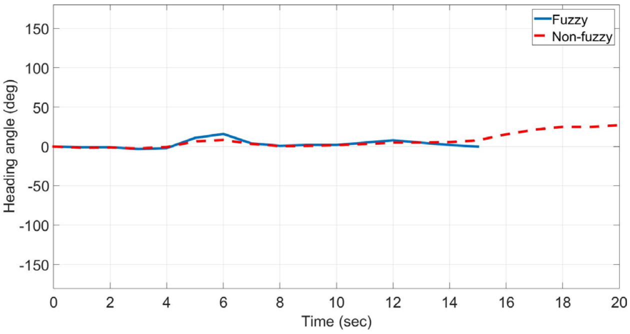

(a) Heading angle

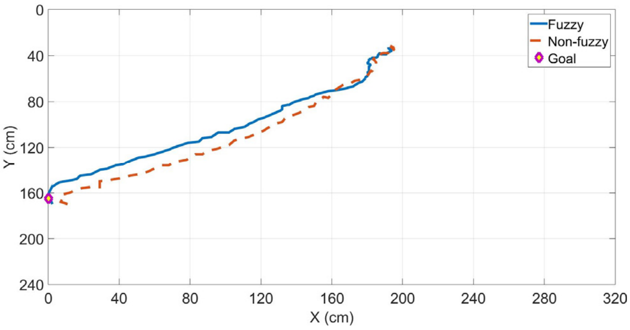

(b) Position

Fig. 19 Performance of heading control (U-G case)

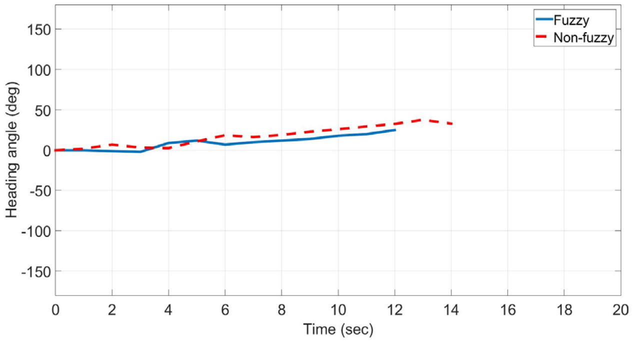

(a) Heading angle

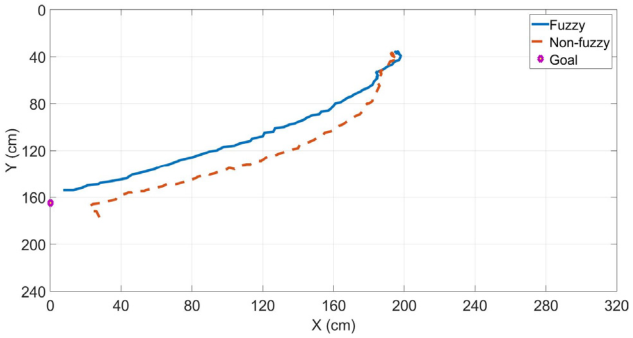

(b) Position

Fig. 20 Performance of heading control (U-F case)

Table 6 Result of Test & Evaluation

		FLC	D-G	D-F	C-G	C-F	U-G	U-F
Max. error (heading)	(°)	×	20	25	30	24	30	45
		○	20	20	15	20	18	30
	Decrease rate (%)		0	20	50	17	40	33
Maintaining heading		×	○	×	○	×	○	×
		○	○	○	○	×	○	○
Spending time	(s)	×	17	13	20	13	20	14
		○	10	10	16	11	15	12
	Decrease rate (%)		40	23	20	15	25	14

end, the maximum error increased to 45°. In the case of the solid line using the FLC, the maximum error was 30°.

In the image trajectories of Fig. 20(b), the dashed line shows the arrival at a position approximately 22 cm away from the target position, but in the case of the solid line, it can be observed that the CSD proceeded in the desired direction properly, arriving at a position approximately 14 cm away.

Table 6 summarizes the overall results. The heading value errors show that the use of the proposed controller reduced the maximum error by 50% overall. Furthermore, because the time spent decreased by 14–40%, it is confirmed that the speed increased.

When the capability for maintaining the heading was compared using the image coordinate values, we found that the path was well maintained overall when the proposed controller was used, except in the C-F case. Furthermore, the D-F case was the case that exhibited the greatest difference in performance, whereby the direction was maintained to the desired destination only when the proposed controller was used.

6. Conclusion

In this study, we investigated a novel CSD system that considers the maintenance/repair and model of a ship, a performance estimation tool that can check the attitude stability in the CSD design process, and an FLC that reflects the expert knowledge-based sailing operation method.

The newly developed CSD considering the model of a ship and the maintenance showed better performance than the conventional CSD. Furthermore, the proposed performance estimation tool can be used to check the attitude stability before manufacturing.

To validate the proposed expert knowledge-based FLC, the heading was controlled for three types of wind direction and two types of wind speed. As indicated by the experimental results of validating the heading control, the response speed and CSD's speed for maintaining the heading increased in all cases, showing the performance of the proposed controller.

In this study, we have prepared a foundation for research in CSD in South Korea. In the future, we will adopt various intelligent control methods to compare the performance and continue research on the improvement of straight path movement for the cases of crosswind and fresh breeze. Furthermore, the developed performance estimation tool was studied based on the limited size of the experimental water tank for real-time rendering. However, in the future, we plan to conduct research related to simulations that reflect the real-world maritime domain environment by improving the program.

References

Kim, H.S., & Cho, G.S. (2016). Study on Advanced Development and Application of Micro Marine Robot for Maritime Domain Awareness. ICIC Express Letters, Part B: Applications, 7(3), 571–576. https://doi.org/10.24507/icicelb.07.03.571

Yeu, T.K., Choi, H.T., Lee, Y., Chae, J., Lee, Y., Kim, S.S., ... Lee, T.H. (2019). Development of Robot Platform for Autonomous Underwater Intervention. Journal of Ocean Engineering and Technology, 33(2), 168–177. https://doi.org/10.26748/KSOE.2019.021

Park, J.H., Shin, M.S., Jeon, Y.H., & Kim, Y.G. (2021). Simulation-Based Prediction of Steady Turning Ability of a Symmetrical Underwater Vehicle Considering Interactions Between Yaw Rate and Drift/Rudder Angle. Journal of Ocean Engineering and Technology, 35(2), 99–112. https://doi.org/10.26748/ksoe.2020.067

Park, H.G., Man, D.W., Jo, Y.J., & Kim, H.S. (2019). Lighting Buoy type Marine Charging Robot Base on Marine Energy Harvesting.

Proceedings of KIIEE (Busan・Ulsan・Kyungnam Branch) Annual Conference, 59-62.

Meinig, C., Lawrence-Slavas, N., Jenkins, R., & Tabisola, H.M. (2015). The Use of Saildrones to Examine Spring Conditions in the Bering Sea: Vehicle Specification and Mission Performance. Proceedings of OCEANS 2015 - MTS/IEEE Washington. https://doi.org/10.23919/oceans.2015.740434 8

Sa, Y.M., Cho, G.S., & Kim, H.S. (2019). Study on Autonomous Surface Robot Based on Marine Energy Harvesting. ICIC Express Letters, Part B: Applications, 10(3), 243-249. https://doi.org/ 10.24507/icicelb.10.03.243

Man, D.W., Cho, G., & Kim, H.S. (2020). Comparative Study on Keel Effects of Catamaran-Type Sail Drone. ICIC Express Letters, Part B: Applications, 11(3), 261-266. https://doi.org/10.24507/icicelb.11.03.261

Fang, Y., Pang, M., & Wang, B. (2017). A Course Control System of Unmanned Surface Vehicle (USV) Using Back-propagation Neural Network (BPNN) and Artificial Bee Colony (ABC) Algorithm. Procedia Computer Science, 111, 361-366. https://doi.org/10.1016/j.procs.2017.06.035

Sun, W., & Gao, X. (2020). Predicting the Trajectory Tracking Control of Unmanned Surface Vehicle Based on Deep Learning. Artificial Intelligence in China, 591-598. https://doi.org/10.1007/ 978-981-15-0187-6_70

Man, D.W. (2021). Study on System Development and Heading Control of Catamaran-type Sail Drone (Ph.D. Thesis). University of Tongmyong, Busan, Korea

Author ORCIDs

Author name	ORCID
Man, Dong-Woo	0000-0002-9155-4935
Kim, Hyun-Sik	0000-0003-4821-9784

Journal of Ocean Engineering and Technology 35(5), 369-381, October, 2021
https://doi.org/10.26748/KSOE.2021.060

pISSN 1225-0767
eISSN 2287-6715

Review Article

Review of Ice Characteristics in Ship-Iceberg Collisions

Tak-Kee Lee[1] and Hyun-Jin Park[2]

[1]Professor, Department of Naval Architecture & Ocean Engineering, Gyeongsang National University, Tongyeong, Korea
[2]Graduate Student, Department of Ocean System Engineering, Graduate School, Gyeongsang National University, Tongyeong, Korea

KEY WORDS: Iceberg, Ship-iceberg collision accident, Masses of iceberg, Mechanical properties of iceberg, Ice extents

ABSTRACT: *The International Ice Patrol (IIP) was established after the Titanic collided with an iceberg off the eastern coast of Canada in 1912 and sank, killing more than 1,500 people. Recently, the IIP has analyzed satellite images and provided safe operation information to vessels by tracking the occurrence and movement of icebergs. A large number of recent arctic studies mainly deal with sea ice formed by freezing seawater related to sea routes and resource development. The iceberg that collided with the Titanic was land-based ice that dislodged from a glacier and fell into the sea. The properties of these two types of ice are different. In addition, vessels operating in ice-covered waters such as the Arctic sea have an ice-breaking function or minimum ice-strengthened functions. Ships operating on transatlantic routes including the eastern coast of Canada do not necessarily require ice-strengthened functions. Hundreds to thousands of icebergs are discovered each year near the area where the Titanic sank. In this study, the status of ship-iceberg collision accidents was investigated to provide useful information to researchers, and the physical and mechanical characteristics of icebergs were investigated and summarized.*

1. Introduction

Over 100 years have passed since the Titanic, one of the world's most widely known ships, sank after hitting an iceberg. According to Dasgupta(2019), the International Ice Patrol (IIP) was established to properly monitor icebergs generated in the wake of the accident. However, in his article describing 10 ships that sank due to a collision with an iceberg, Dasgupta emphasized that the Titanic was not the first ship that sank after striking an iceberg and would not be the last one to suffer such an accident, either.

Ship collisions are considered an important problem in maritime accidents (Wikipedia, 2021). First, ship collisions can result in the loss of human lives. The Titanic hit an iceberg and sank in the North Atlantic Ocean about 740 km south of Newfoundland, Canada, on April 14, 1912, causing an estimated maximum of 1,522 deaths (Hill, 2001 - 1,503 people; Bigg and Billings, 2014 - 1,514 people; Dasgupta, 2019 - 1,522 people). Ship collisions can also cause environmental disasters, including oil spills. In 1989, the Exxon Valdez ran aground off the coast of Alaska and leaked 41,640 kL of crude oil into the sea, causing an ecological disaster that threatened the local marine ecosystem. Analysis data on the cause of the accident (Paik, 1992) revealed that it was related to a glacier: the ship ran aground on a reef while trying to steer clear of a group of floating ice packs that broke off from a glacier. Ship collisions generally entail substantial financial losses for ship owners. In 1989, the Trave Ore paid about 4 million dollars for ship repair alone after it struck a bergy bit (Hill, 2001). This amount did not include the amount of compensation for the loss of cargo or the operating deficit for ship operations.

Icebergs are chunks of ice that float above the water surface and have broken off from land-based ice. They are made of frozen fresh water with little salt, they are lighter than sea water and are more likely to float above the water surface than sea ice. For smaller icebergs, the fractions exposed above the water surface generally have a length of several meters, so they are not easily detected by instruments such as radar. However, the total mass, including the mass of the portion below the water surface, is tremendous, so an iceberg can generate huge energy when it collides with a ship. This energy is very dangerous when ship-iceberg collisions occur. When the iceberg responsible for the sinking of the Titanic was reconstructed based on the accounts of survivors, it was estimated to have a depth of 100 m and a length of 125 m, and its mass was estimated to be as large as over 2 million tonnes (Bigg and Billing, 2014).

This study reviews the data of previous investigations to investigate

Received 17 June 2021, revised 20 August 2021, accepted 21 August 2021
Corresponding author Tak-Kee Lee: +82-55-772-9193, tklee@gnu.ac.kr

the characteristics of ice related to ship-iceberg collisions. For this purpose, we first reviewed statistical data on ship-iceberg collision accidents. This review was conducted to gain a proper understanding of the historical status and the overall characteristics of the occurrences of ship-iceberg collision. In addition, among major ice parameters related to ship-iceberg collision accidents, key properties such as the size, mass, shape, and strength of icebergs were reviewed with focus on previous research data. This analysis is expected to serve as a starting point for a more practical engineering approach to the problem of ship-iceberg collision. Finally, current efforts to prevent ship collision accidents due to icebergs were briefly summarized.

2. Statistics on Ship-Iceberg Collision Accidents

Table 1 shows 10 ships that collided with an iceberg (Dasgupta, 2019) based on the number of fatalities. Among the 10 accidents, the exact causes have not yet been clarified for the Naronic and the Hans Hedtoft, but since they are presumed to have been caused by icebergs, they were also included in the article. The 2,857-ton freighter Hans Hedtoft set out on a voyage bearing the prideful label of the "safest afloat," but when the accident happened, the fishing boat that arrived at the location after receiving a distress signal did not find any traces of the ship, and the mystery remains unsolved. As shown in Table 1, aside from the Islander, 9 accidents occurred in the North Atlantic, and they mostly occurred between January and April regarding the seasonal time of the accident.

The National Research Council of Canada (NRC) has built an iceberg-ship collision database using MS Access. This database includes 670 collision accidents that occurred in the Northern Hemisphere (Hill, 2001; Hill, 2006). Most of these accidents occurred in the Grand Banks area southeast of Newfoundland Island in Canada (Fig. 1). Hill (2001) analyzed the number of ship-iceberg collisions per year and the extent of sea ice using data from the database for a period of almost 200 years from 1810 to 2004. The results showed significant correlation between collisions and sea ice (Fig. 2). Kujala (1991), Hanninen (2005), Marchenko (2012), and Marchenko (2014) provided related information for ship-iceberg collision accidents outside the east coast of Canada or the northwestern part of the North Atlantic.

Table 1 10 ships sunk by accident with iceberg

Ship name	Accident date	Accident location	Life loss (people)
Titanic	1912.4.14	Newfoundland, Canada	1,522
Pacific	1856.1.23	Fr. Liverpool to New York	186
John Rutledge	1856.2.19	Fr. Liverpool to New York	133
Maria	1949.5.10	St. Paul's Island, Canada	109
Hans Hedtoft	1959.1.30	Cape Farewell, Greenland	95
Vaillant	1897.4.13	Newfoundland, Canada	78
Naronic	1893.2.11	Fr. Liverpool to New York	74
Hannah	1849.4.29	Fr. Newry (Ireland) to Quebec	50
William Brown	1841.4.19	Newfoundland, Canada	50
Islander	1901.8.15	Alaska, USA	40

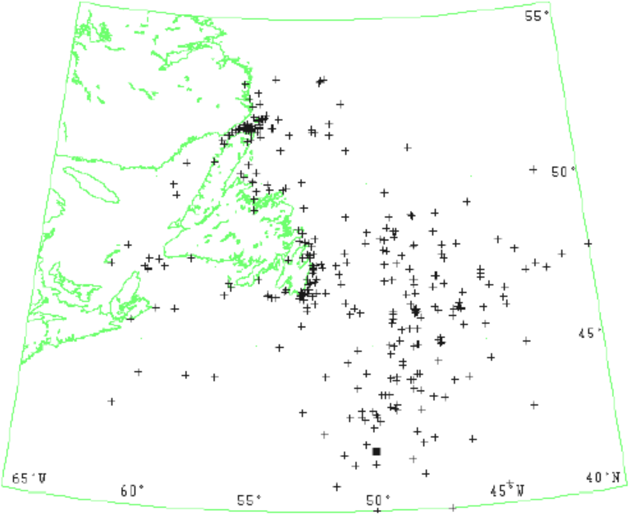

Fig. 1 Chart of the approximately 300 known locations of iceberg collisions off Newfoundland with the Titanic location marked as a square (Hill, 2001)

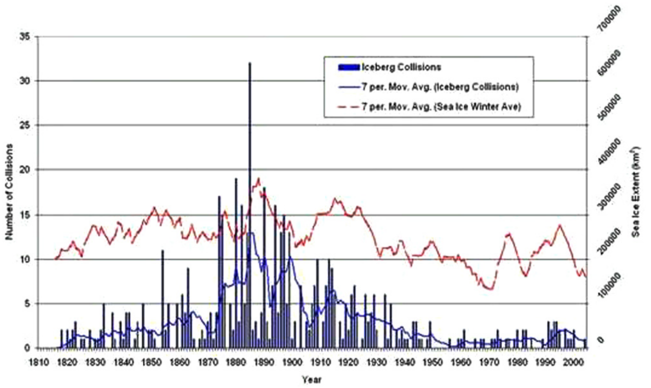

Fig. 2 Inter-annual variation of iceberg collisions and sea ice extent with a 7-year period moving average (Hill, 2006)

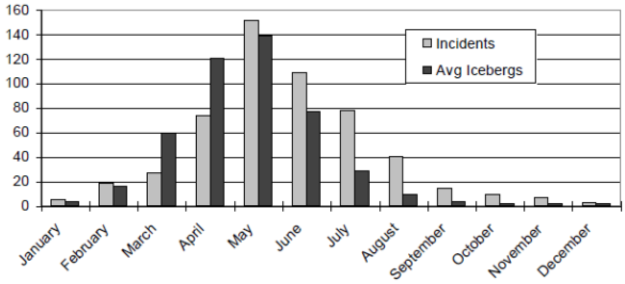

Fig. 3 Comparison of 545 incidents in the North Atlantic sorted by month and the average monthly iceberg count (Hill, 2001)

Hill (2001) presented the monthly distributions of the number of collisions and the average number of icebergs, as shown in Fig. 3. It can be seen that the monthly distributions of the two variables show close similarity. However, as pointed out by the author, this data does not include changes in the marine traffic volume. In addition, Fig. 2 shows that the number of collisions reached a maximum of 31 at the end of the 19th century, but it has largely remained at a low level with a maximum of 3 collisions per year since the 1940s. The analysis of the types of ships that crashed into an iceberg using this database showed that ships colliding with an iceberg were mostly passenger ships and general cargo ships until 1940, but fishing vessels and bulk carriers have made up a large proportion of them since 1990. In addition, there have been no casualties due to a collision with an iceberg since the 1960s (Hill, 2006).

Marchenko (2014) investigated ship accidents caused by floating ice from the accident of the icebreaker Admiral Lazarev in the East Siberian Sea in 1965 to the accident of the Akademik Shkalskiy in the Antarctic Ocean in 2013. He classified these accidents into three types: ice floe hit, nipping/trapping by ice, and ice jet. “Ice floe hit” refers to cases where a ship sailing at a relatively high speed collides with solid sea ice in a situation where a small number of pieces of sea ice are floating in the sea at a sea-ice concentration lower than about 15-20%, and visibility is reduced by fog. “Nipping/trapping by ice” refers to cases where a ship is trapped in sea ice and is unable to move. This type of accident occurred frequently in the early 20th century, which was the early pioneering period of the Arctic sea routes, but it rarely occurs in the waters with floating icebergs dealt with in this study. “Ice jet” refers to cases where a ship collides with floating ice moving at a relatively high speed (about 0.5–1 m/s), and this type of accident is known to occur mainly in straits and bays.

Fig. 4 shows the relative moving directions of a ship and floating ice with respect to each other. Ship-iceberg collisions can be divided into cases where the bow structure of a ship sailing at a relatively high speed collides with the edge of an iceberg in a situation of poor visibility due to fog or other factors and cases where the iceberg is pressed against the side shell of the ship. In cases similar to Fig. 4(a), the impact force is determined by the ship speed and the angle of impact, and the shape and mass of the iceberg are important factors in the collision. In the case shown in Fig. 4(b), static ice load can be increased if the side shell and the iceberg move slowly in directions perpendicular to each other.

Fig. 5 shows a vessel that collided with ice at a high speed and sustained damage in the bulbous bow, even though the accident occurred in July, a summer month when ice becomes weak. This seems to correspond to the case in Fig. 4(a), and the high speed of the ship actually seems to be the main cause of the damage of the vessel (Canadian Coast Guard, 2012). In addition, the Reduta Ordona, a bulk carrier, collided with an iceberg in July 1996 and sustained heavy damage in the ship-length direction on the side shell on the forebody, which can be considered an example of the case shown in Fig. 4(b). Yu and Amdahl (2021) presented Fig. 6 as an example of sliding damage, which happens along the direction in which the ice slides

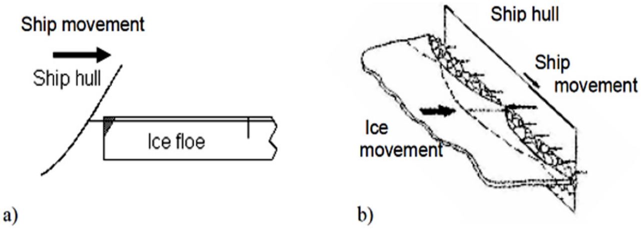

Fig. 4 (a) Ship moves and hits an ice floe or (b) ice is pressed against ship side (Jalonen et al., 2005)

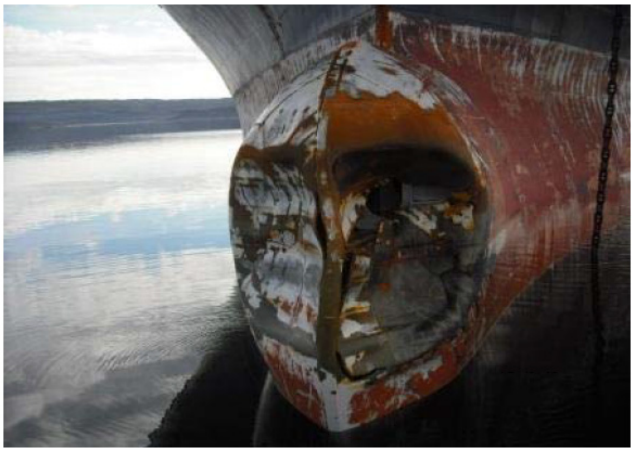

Fig. 5 Bulbous bow of a cargo vessel with a Lloyd's 100 A1 Ice Class 1A damaged in ice en route Iqaluit, Nunavut, in July (Canadian Coast Guard, 2012)

Fig. 6 Damaged side structure of bulk carrier Reduta Ordona by collision with a growler in Hudson Strait on its way from Poland to Churchill, Manitoba, July 21, 1996. Quebec City, MIL Davie shipyard (Foumler et al., 2020).

A ship that recently sank due to a collision with sea ice was the MS Explorer registered in Liberia, which was a Det Norske Veritas (DNV) 1A1 Ice-A class ice-strengthened vessel (Bureau of Maritime Affairs, Liberia, 2009). Although this accident was related to sea ice and not icebergs, we describe it briefly since it occurred recently. The ship was a cruise ship built in Finland in 1969 and operated around Ernest Shackleton via the Drake Passage in the Antarctic Ocean, which is known for rough waves (see Fig. 7 for the sea route of the ship). When the accident occurred, the ship collided with sea ice in the Bransfield

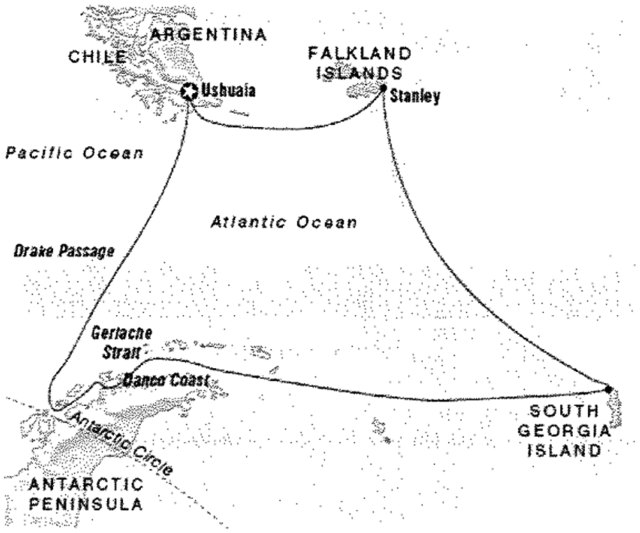

Fig. 7 Route for Spirit of Shackleton Tour by the MS Explorer (Bureau of Maritime Affairs, Liberia, 2009)

Fig. 8 The Explorer lying over its side after collision with ice wall (BBC News, 2007)

Strait near King George Island and sustained a gash similar to a deep cut, which caused seawater to flood into the ship. This ship eventually capsized, as shown in Fig. 8, but 154 people aboard including passengers and the crew were all rescued.

A final report on the investigation of the accident stated that damage of punctures and slices with a minimum length of 3.6 m occurred along with the shell plating in the longitudinal direction of the ship (Bureau of Maritime Affairs, Liberia, 2009). The report mainly attributed the accident to misjudgment based on the experience of the ship operator, who entered the ice-covered waters despite the fact that the sea ice that formed in the accident location was thicker and harder than general first-year sea ice. In connection with this, the Sea Ice Nomenclature of the World Meteorological Organization (WMO) (WMO, 2015) classifies first-year sea ice as three types according to the thickness: thin, medium, and thick first-year ice. First-year ice with a thickness of 30−70 cm is classified as thin, first-year ice with a thickness of 70-120 cm as medium, and first-year ice with a thickness of more than 120 cm as thick.

3. Characteristics of Colliding Ice and Sea Ice Extents

3.1 Size of Ice with a High Likelihood of Colliding with a Ship

Generally, floating ice can be classified according to size. “Growlers” are smaller pieces of floating ice with the size of a truck or grand piano. They have a height of less than 3 ft (about 0.91 m) above the sea surface but cover a large area of up to about 215 ft2 (about 20 m^2). “Bergy bits” are larger than them and typically have a height of 3−16 ft (about 0.91−4.9 m) above the sea surface and an area of approximately 1,000−3,000 ft^2 (about 93−279 m^2). Pieces of floating ice larger than bergy bits are referred to as icebergs (Bigg and Billing, 2014). Fig. 9 shows a comparison between the sizes of an iceberg, bergy bit, and growler, which can be figuratively described as follows (Thompson-Munson, 2021):

- Growler : Human-sized or smaller
- Bergy bit : Car-sized to house-sized
- Iceberg : Building-sized or larger

Icebergs are chunks of ice that have broken off from land-based glaciers into the sea and are made of fresh-water ice. The specific gravity of an iceberg ranges from 0.85 to 0.91, so the portion visible above the sea surface is merely a fraction of the iceberg. Since the specific gravity of sea water is generally about 1.03, approximately 12−17% of the total mass of an iceberg floats above the sea surface. Icebergs are mainly created around the western coast of Greenland in the Northern Hemisphere and on the ice cap of Antarctica in the Southern Hemisphere (Choi, 2013; Jacka and Giles, 2007). Other regions where icebergs are formed include Axel Heiberg Island, Svalbard, and Novaya Zeml'ya. Icebergs are not found in Arctic seas since they originate in the mentioned regions and are moved south by the wind and currents (Palmer and Croasdale, 2013).

According to the WMO Sea Ice Nomenclature (WMO, 2015), floating ice refers to all types of ice floating in water and is classified as lake ice, river ice, and sea ice. Data related to river ice were published by Korzhavin (1971/2002) and the US Army Corps of Engineers (2002/2005). Sea ice refers to the ice formed from the freezing of sea water and discovered in the sea. With respect to the classification of floating ice by size, the terms floe and iceberg are related to the formation process of floating ice. Floes are formed as sea

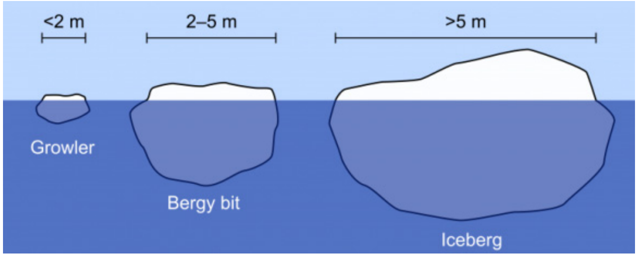

Fig. 9 Three iceberg size categories: growler, bergy bit, and iceberg (Thompson-Munson, 2021)

ice adheres together, while icebergs are chunks of ice that have broken off from glaciers. Floes are classified according to the length in the horizontal direction as follows: floe giant (10 km or more), floe vast (2–10 km), floe big (0.5–2 km), floe medium (100–500 m), floe small (20–100 m), ice cake (20 m or less), and small ice cake (2 m or less). Although it was published quite a long time ago, the book by Sanderson (1988) is one of the best books on sea ice mechanics, and another useful book currently available is that by Cammaert and Muggeridge (1988). Sea ice is not fully dealt with in this study, and further information concerning sea ice can be found in the two books.

Icebergs are classified according to size as follows based on the height and length of the part of the iceberg visible above the sea surface. Icebergs with a sail height of 75 m or greater and a length of 200 m or greater are classified as very large icebergs, those with a sail height of 46–75 m and a length of 121–200 m are large icebergs, those with a sail height of 16–45 m and a length of 61–120 m are medium icebergs, and those with a sail height of 5–15 m and a length of 15–60 m are small icebergs. Bergy bits refer to large pieces of floating glacier ice with a sail height of 1–5 m and an area of 100–300 m^2, and growlers are defined as smaller pieces of ice than bergy bits (WMO, 2015).

In dealing with the problem of ship-iceberg collision, Addario et al. (2014) argued that it is a valid approach to estimate the size of icebergs, which is a major variable, from the size of detectable icebergs. They thought that since detectable icebergs can be avoided, they no longer pose hazards to ships. Based on the results of previous investigations, they determined that the size of icebergs identifiable by airborne radar is about 20 m. In addition, they also mentioned that it may be difficult to detect icebergs with a height less than 2 m in the sea conditions commonly encountered in the Arctic region. Based on these factors, they presumed that the maximum size of icebergs that are highly likely to collide with a ship is a sail height of 2 m and a waterline length of 20 m. The DNV data (Mejlaelander-Larsen and Hysing, 2006) considers the length of icebergs identifiable by airborne radar to be 15 m or more. In addition, explanation data on icebergs from the National Snow and Ice Data Center in the U.S. (NSIDC, 2021) states that only icebergs with an area of 500 m^2 or larger can be tracked.

Fig. 10 shows a diagram of the appropriate navigation method when bergy bits (relatively large fragments of ice that have broken off from glaciers) are present together with icebergs. It is advised that a ship sail in the windward direction with respect to the iceberg to the left of the ship. In addition, the Canadian Coast Guard (2012) recommends taking extra care in monitoring bergy bits and growlers since they pose a great danger in that it is difficult to discern them from white caps in the open sea, as shown in Fig. 11, and they are sometimes hidden in rubbed ice in ice-covered waters. Even relatively large ones are difficult to detect by marine radar because the freeboard above the sea surface is small, and the sides of bergy bits and growlers reflect radar energy away from the antenna. For these reasons, bergy bits and growlers are considered to present the greatest hazard to ships in ice-covered waters (Canadian Coast Guard, 2012).

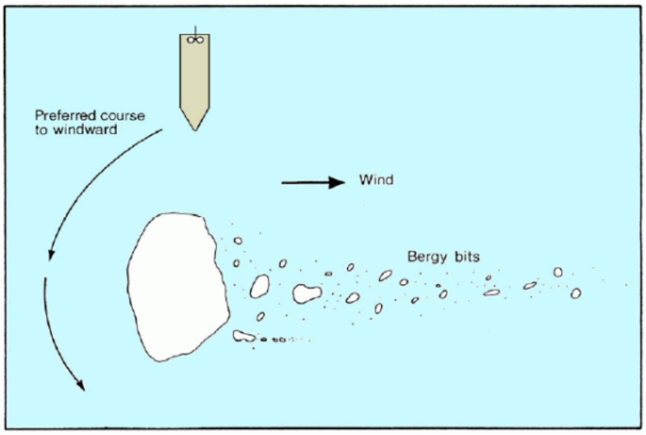

Fig. 10 Navigating around an iceberg and bergy bits (Canadian Coast Guard, 2012).

Fig. 11 Iceberg and growlers in the open sea (Canadian Coast Guard, 2012)

3.2 Shape of Colliding Icebergs

The actual shape of icebergs varies widely. Studies that performed measurements of shape data of these icebergs are summarized in Table 2. McKenna (2004) conducted shape characterization of icebergs by developing a method that allows us to connect the parts above and below the water surface in a consistent manner, satisfy hydrostatic considerations, and express the relationships between measured values of waterline length, waterline width, sail height, keel depth, and mass. Fig. 12 shows a representation of the overall shape of the iceberg named “Julianna” among the icebergs measured by the Dynamics of Iceberg Grounding and Scouring (DIGS) project. The iceberg had a waterline length of 292 m, a waterline width of 258 m, a sail height of 70 m, and a keel depth of 170 m (McKenna, 2005). McKenna (2005) also derived the relationships between the major parameters mentioned above for engineering application of the shape of icebergs.

Liu (2011) described the following three possibilities in his analysis on the shape of icebergs in terms of the potential damage to the hull structure:

(1) Icebergs with a sharp protrusion have the potential to cause great damage.

(2) A blunt surface of icebergs may be less likely to cause damage since it has a large energy dissipation capacity. However, since it has greater energy at the same time, it may cause deformation of the internal structure.

Table 2 Summary of measured iceberg shape data (McKenna, 2004)

Source	Type of data
Fenco (1971)	Aerial photogrammetry, ship based above water photographs
Intera (1981)	Aerial photogrammetry
Atlantic Survey (1982)	Aerial photogrammetry
Bercha (1983)	Aerial photogrammetry
ICE Eng. (1983a)	Ship-based above-water photographs, limited underwater sonar profiles not tied in
ICE Eng. (1983b)	Ship-based above-water photographs, limited underwater sonar profiles not tied in
Bercha (1984)	Aerial photogrammetry
Dobrocky Seatech (1984)	Ship-based above-water photographs, underwater sonar profiles tied in
ICE Eng. (1984)	Ship-based above-water photographs, limited underwater sonar profiles not tied in
Dobrocky Seatech (1985)	Ship-based above-water photographs, limited underwater sonar profiles
ICE Eng. (1985)	Ship-based above-water photographs, limited underwater sonar profiles not tied in
Smith and Donaldson (1987)	Ship-based above-water photographs, limited underwater sonar profiles tied in
Hodgson et al. (1988) -DIGS	Aerial photographs, ship-based above-water photographs, underwater sonar profiles tied in
Oceans Ltd. (2004)	Ship-based above-water photographs, underwater sonar profiles tied in

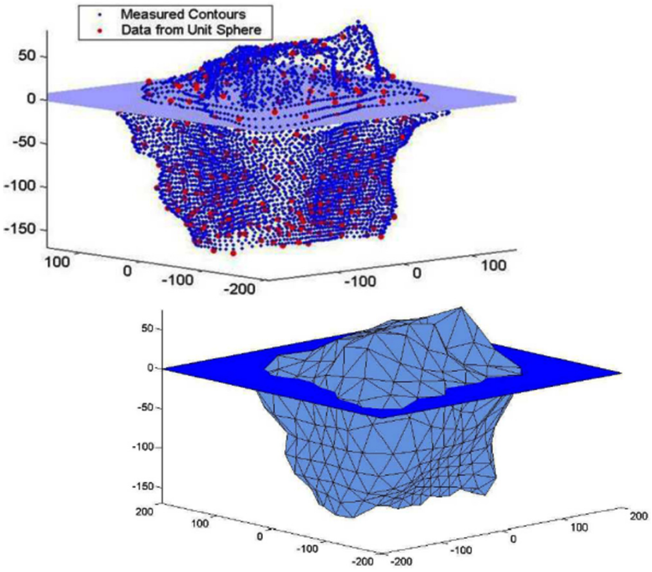

Fig. 12 Iceberg "Julianna" showing measured contours and surface points associated with radial representations; triangular patch representation of surface points.

(3) The shape that can inflict the greatest damage to a ship may be somewhere between the shapes described in (1) and (2).

In connection with these possibilities, Addario et al. (2014) posited the three shapes of icebergs shown in Fig. 13 and conducted a collision analysis. Icebergs can also be classified according to the shape, as shown in Fig. 14 (Turnbull et al., 2015), which is important for the record of iceberg detections by ships. In this regard, materials on the method of classification of icebergs according to the shape can be easily found on the Internet. Generally, the data also includes the average ratio of the sail height to the keel depth.

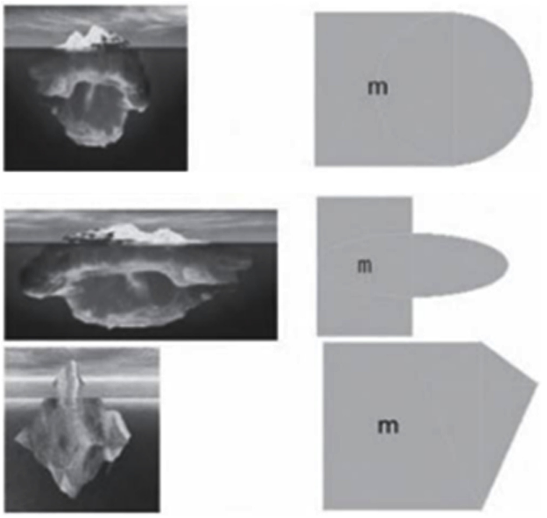

Fig. 13 Selected shapes of iceberg (Addario et al., 2014)

Shape	Average height to draft ratio	Shape	Average height to draft ratio
Tabular	1:5	Wedge	1:5
Non-Tabular	1:5	Drydock	1:1
Domed	1:4	Blocky	1:5
Pinnacle	1:2		

Photos: Masterfile ©

Fig. 14 Sample photographs of seven standard icebergs shapes and their sail height to keel depth ratios (Turnbull et al., 2015)

In an ice collision analysis for LNG vessels, Suh et al. (2008) assumed that the shape of a bergy bit as a striking body is classified as three types: conical, spherical, and cubic. This is based on the data of DNV (Mejlaelander-Larsen and Hysing, 2006), and they are typical shapes of bergy bits that are likely to collide with LNG vessels sailing on the sea routes from Murmansk to the coast of the United States. For the bergy bit with a conical shape, it was assumed that the cone angle with the horizontal plane was 60°, the diameter of the base was 2.5 m, and the diameter at the water surface was 1.15 m. For the bergy bit with a spherical shape, it was posited that the diameter was 5.1 m, and the diameter at the water surface was 4.05 m to consider the characteristics of general icebergs.

3.3 Mass of Icebergs

Among the laws of physics related to general collisions, the law of conservation of energy is considered the most fundamental principle. This law means that the energy of the entire system must be conserved regardless of the situation in which a striking body collides with a struck body. Let us consider a situation immediately before a collision occurs in relation to the ship-iceberg collision problem. Presumably, the most reasonable scenario is to assume that the ship and the iceberg are both in motion. It is likely that the ship is naturally moving toward its destination and that the iceberg is moving slowly under the influence of currents and the wind. A huge problem in this situation is the enormous mass effect of the iceberg.

As mentioned earlier, the mass of the iceberg that collided with the Titanic was estimated to be about 2 million tonnes. Even if an iceberg with such a huge mass moves very slowly, its kinetic energy would be very large. The portion of an iceberg exposed above the sea surface is typically only 12–17% of the total volume, and the size of the fraction exposed above the water surface is generally measured. Therefore, the mass of an iceberg is estimated based on the size and shape of the fraction of the iceberg above the water surface. Rudkin et al. (2005) presented a simple estimation formula for the mass M (units: t) of icebergs:

$$M = 7.12 \times L \times W \times H \times sf \qquad (1)$$

where L represents the waterline length (m), W denotes the waterline width (m), and H indicates the sail height (m). Also, sf represents the shape factor for the diverse shapes of icebergs presented in Fig. 14. Turnbull et al. (2015) presented values of shape factors ranging from 0.15 to 0.5 for the icebergs observed in the Grand Banks, Canada, as shown in Table 3. Taking into consideration the situations in which only one side of icebergs can generally be photographed when taking photographs of icebergs, Turnbull et al. (2015) suggested a modified form of Eq. (1) by substituting L^2 for $L \times W$.

Table 3 Iceberg shapes and their shape factors (Rudkin et al., 2005)

Iceberg shape	Shape factor
Tabular	0.5
Non-tabular	0.41
Domed	0.41
Pinnacle	0.25
Wedge	0.33
Drydock	0.15
Blocky	0.5

Table 4 Calculated iceberg dimensions and mass based on photographic measurement (Ralph et al., 2008)

Berg ID	Shape	Dimensions (m)			Mass (t)			
		Length	Width	Height	Eq. (1)	$0.3L^3$	*R. cont*1)	*uw cont*2)
05	wedge	73.5	23.6	12.9	19915	119120	22045	-
14	dome	16.6	11.3	3.1	1698	1525	1911	2173
16	dome	18.4	14.2	4.3	3280	2077	2838	966
17	dome	32.7	22.4	3.9	8339	11655	8526	9076
18	dome	12.1	7.9	1.4	391	591	590	-

1)Revolved contour
2)Underwater contour

The mass of a blocky iceberg with a waterline length of 20 m and a sail height of 2 m posited by Addario et al. (2014) is calculated to be about 2,848 ton by Eq. (1). Sanderson (1988) presented a table of classification of icebergs according to the size and provided the estimated mass of each type of iceberg. According to Sanderson (1988), the mass of a growler is about 100 tons, and that of a bergy bit is about 1,000 tons. When the mass of a bergy bit with maximum size is calculated by this formula (for a sail height of 5 m and a length of 15 m), the mass of the bergy bit is determined to be about 4,000 tons. Gagnon (2007) conducted a numerical analysis of an impact experiment using an actual growler, and the growler used in the experiment was reported to have a size of 1.73 m × 0.88 m × 0.98 m and a mass of 1,068 kg.

Canada's National Research Council Institute for Ocean Technology (NRC/IOT) conducted an experiment on bergy bit impact using the Terry Fox, a Canadian Coast Guard ice breaker, near St. Anthony on the northeast coast of Newfoundland in June 2001. During this experiment, data on icebergs was collected by methods such as aerial photography, exploration by sonar, and stereo photography. Ralph et al. (2008) calculated the size of icebergs using the data and presented the estimated mass of icebergs from several methods. Table 4 shows the mass of 5 icebergs with all dimension values among a total of 18 icebergs studied by Ralph et al. (2008). In Table 4, " $0.3L^3$" indicates an empirical equation derived from measured data and is a useful estimation formula for mass when only the maximum waterline dimension values are given. *R. cont* indicates "revolved contour" and was considered to produce the best estimates by Ralph et al. (2008). It starts from the assumption that if an iceberg is homogeneous in density in all parts, the total volume (V) and the volume of the fraction exposed above the water surface (V_a) are proportional to the density of surrounding water and the difference between the density of sea water and that of ice. In addition, *uw cont* represents "underwater contour" and is the mass calculated using the profile of the iceberg obtained by multibeam sonar.

3.4 Strength of Iceberg, River Ice, and Sea Ice

According to the US Army Corps of Engineers (2002, 2005), the elastic modulus varies depending on the measurement techniques. Specifically, they reported that the measured values of elastic modulus obtained by in-situ measurements ranged from 0.4 to 9.8 GPa, the elastic modulus values of freshwater ice grown in a large laboratory tank ranged from 4.3 to 8.3 GPa, and the measured values of small specimens used for laboratories were higher. Yu and Amdahl (2021) conducted a numerical analysis of glacial ice impact, and for this purpose, ice density was posited to be 900 kg/m3 based on ISO 19906 (2019). Also, the elastic modulus and Poisson's ratio were assumed to be 9.5 GPa and 0.3, respectively, based on the study by Timco and Weeks (2010). A friction coefficient of 0.15 was also used.

The mechanical properties of ice are known to vary depending on the measurement environment, such as in situ measurements and the laboratory, as well as the specimen size. Thus, to standardize a cold room test, Kim (2007) focused on the uniaxial compression test of fresh water ice grown in a laboratory. He reported that ductile failure occurred when the strain rate was 10^{-5}–10^{-4} (1/s) or lower.

According to a review study on the mechanical properties of ice and snow (Petrovic, 2003), the tensile strength of ice ranges from 0.7 to 3.1 MPa, and the compressive strength ranges from 5 to 25 MPa. In addition, as the temperature decreases or as the strain rate increases, compressive strength increases. Tensile strength is not very sensitive to these variables, and as the ice grain size increases, the tensile strength decreases. In addition, elastic modulus ranges from 9.7 to 11.2 GPa, and Poison's ratio ranges from 0.29 to 0.32, which is summarized based on previous data (Haynes, 1978; Gold, 1988; Lee and Schulson, 1988; Schulson, 1999).

Glacial ice in which icebergs originate is formed from snow, which gradually changes into ice. This change depends on temperature and pressure, and ice is formed at a density of about 830 kg/m^3. The density of pure ice is about 917 kg/m^3, and air bubbles can be formed within ice at up to 10% of the total volume of the ice (Daley and Veitch, 2000). The density of freshly deposited snow is 50-300 kg/m^3, and the density of wet snow or firm snow is about 400-830 kg/m^3 (Paterson, 1994). The average density estimated from the measured porosity values of 5 icebergs that drifted to the coast of Newfoundland was about 893±7 kg/m^3, and the grain size was measured to be about 15 mm (Gammon et al., 1983).

Gammon et al. (1983) performed a uniaxial compression test for glacial ice at an average temperature of -4.2℃ and a constant strain rate of 1.085×10^{-3}(1/s). The average values of elastic modulus and uniaxial compressive strength were 6.092 GPa and 5.34 MPa, respectively. They also carried out experiments on freshwater ice and found that the strength of glacier ice is about 35% higher. Gagnon and Gammon (1995) performed a flexural strength test using specimens obtained from icebergs, and the average density estimated from the measured value of porosity was 895 kg/m^3. Another study repeatedly performed the flexural strength test 24 times under the conditions of a strain rate of 10^{-3}/s and a temperature of −1 to −16℃. The flexural strength S_f (MPa) was temperature dependent, as shown in the equation below (Veitch and Daley, 2000):

$$S_f = 0.8827 - 0.0738T - 0.00213T^2 \tag{2}$$

where T represents the temperature (℃). For example, the flexural strength at -10℃ is calculated to be 1.41 MPa by Eq. (2).

Jang et al. (1997) proposed a crushable ice model of spherical icebergs when they conducted an iceberg collision simulation for ice-class shuttle tankers. This model has the form of a sphere and a rigid shell element with an external surface covered with a crushable solid element that has constant thickness. The material properties of icebergs assigned to the crushable solid element were as follows: elastic modulus of 9.5 GPa, Poisson's ratio of 0.3, yield strength of 10 MPa, hardening modulus of 95 MPa, and maximum plastic strain of 0.01. These elements were also adopted in an ice collision analysis by Suh et al. (2008) for a membrane tank-type LNG carrier. They adopted the nominal ice crushing strength of the winter season of 4–5 MPa (Meilaelander-Larsen and Hysing, 2006).

Korzhavin (1971, 2002) presented a summary of the material properties of river ice in the USSR region for the period up to the 1950s. The data includes the values of the stress-strain curve, elastic modulus, shear modulus, and ultimate strength. The elastic modulus of river ice was reported to be a maximum of 206 MPa under bending conditions, a maximum of 491 MPa under expansion conditions, and a maximum of 824 MPa under compression conditions. The shear modulus measured under a torsion load was a maximum of 177 MPa.

Timco and Weeks (2010) examined engineering characteristics of sea ice through an extensive investigation. They found that the material properties of sea ice are affected by the degree of salt content (that is, salinity and porosity related to the formation and growth of ice). In addition, they reported that the properties of sea ice vary according to the formation period or whether it is first-year or multi-year sea ice. Among the properties of sea ice, salinity depends on the thickness of ice, and porosity depends on salinity and temperature. For example, the average salinity (S_i) of first-year sea ice can be determined by the empirical equation below:

$$S_i = 4.606 + (91.603/h_i) \tag{3}$$

where h_i denotes the thickness of ice (cm), and the maximum value is considered to be 200 cm.

Timco and Weeks (2010) reported that first-year sea ice had a density of 920 kg/m^3 and multi-year sea ice showed a density of 910-915 kg/m^3. In addition, it was found that the tensile strength of first-year sea ice is 0.2–0.8 MPa in the direction horizontal to the sea ice sheet, which increases up to 2 MPa when a load is applied in the direction parallel to the growth direction of columnar sea ice. The flexural strength of first-year ice decreases as porosity increases, and the maximum value is about 1.5 MPa, but collected data revealed that flexural strength at a medium level of porosity was 0.3–0.8 MPa. Generally, compressive strength is greatly affected by the loading strain rate, and the compressive strength of first-year sea ice ranges from 0.4 to 5 MPa.

The borehole jack test is widely used to measure ice strength in situ. A borehole jack is lowered into a hole from the surface of ice, and an ice core sample with a diameter of 15-20 cm is collected from the ice sheet. Borehole ice strength refers to the degree of resistance of ice in this process, and this method has a great advantage in that there is no need to remove the ice sample from the ice sheet. The mid-winter ice strength value of first-year sea ice is generally 25–30 MPa, and since the value varies significantly depending on the temperature, the ice strength level in July is about 10% of the mid-winter ice strength level.

Timco and Weeks (2010) reported that first-year sea ice has an elastic modulus in the range of 7–10 GPa, and the elastic modulus of multi-year sea ice was shown to be 5% lower. Generally, the average value of Poisson’s ratio is 0.295±0.009, but it may vary depending on the stress rate, and the maximum value of Poisson’s ratio was 0.48 at 0.01 MPa/s. In addition, they argued that in the calculation of short-term bearing capacity (50 kPa/s), an effective Poisson's ratio of 0.42 is more appropriate than the dynamic value of 0.33. However, they reported that it changes to 0.25 in painted steel and 0.45 in corroded steel, and they pointed out that there is still a considerable lack of understanding of Poisson’s ratio, as in the case of friction, which was found to range from 0.2 to 0.6.

Jia et al. (2009) used sea ice material data provided by the Safe Ice project. According to the data, sea ice has a yield stress of 35 MPa, elastic modulus of 7 GPa, Poisson’s ratio of 0.34, and density of 920 kg/m^3. In addition, Høyland et al. (2020) described ice characteristics that changed from those in the first edition of ISO 19906 (the international standard related to ice action on polar offshore structures) in the second edition (ISO, 2019). These include physical properties of ice such as temperature, salinity, porosity, density, and coefficient of friction, as well as mechanical properties, such as the elastic modulus and Poisson’s ratio.

3.5 Ice Extents

Fig. 15 shows three limits of floating ice in the Grand Banks region of eastern Canada. First, the dotted line in Fig. 15 indicates the sea ice limit in April based on statistical data from the period of 1979–2013. The dashed line represents the sea ice limit of the region for the early 20th century, which was also applied in 1912 when the Titanic accident occurred. Finally, the solid line represents the limit connecting the areas where icebergs appeared during the total period of the 20th century. In Fig. 15, the region marked as 48°N latitude represents an area in the vicinity of the city of St. John's, and the bold “x” symbol represents the spot where the Titanic collided with an iceberg. The shades of blue indicate different ocean depths, and the lightest blue regions represent continental shelves with a water depth of 1,000 m or less (Bigg and Billings, 2014).

1,038 icebergs were observed at 48°N latitude in 1912 when the Titanic sank following a collision with an iceberg. This number corresponds to 90% of the average number of observed icebergs per year during the past 112-year period since 1900. In 112 years of observations, there were 14 cases in which the 90% value was exceeded and the number of detected icebergs has risen since the mid-1970s. In 2009, 1,200 icebergs were detected. The iceberg that sank the Titanic was reported to be a relatively large one. Based on survivors’ reports and general characteristics of icebergs, the iceberg is estimated to have a depth of 90-185 m and a length of 125 m. The mass of the iceberg was eventually estimated to be about 2 million tonnes (Bigg and Billings, 2014), and thus, it would have had a very large impact.

In addition, the International Ice Patrol (IIP) creates iceberg charts that represent the analysis of the status of icebergs in the region on the

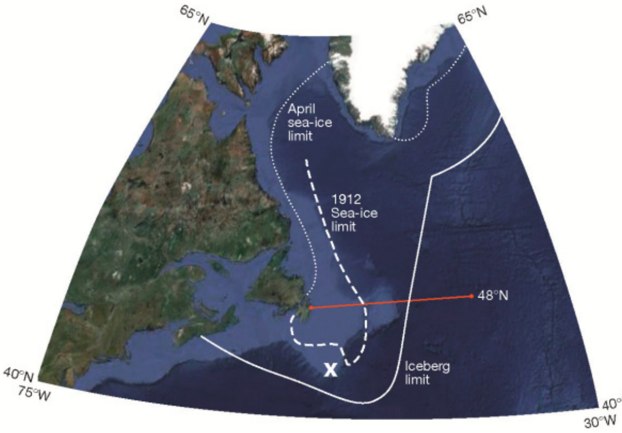

Fig. 15 The average sea-ice limit for April 1979–2013 (dotted line), a typical Newfoundland maximum sea-ice limit for early 20th century (dashed line and denoted as 1912), and the maximum iceberg limit for 1900–2000 (Bigg and Billings, 2014).

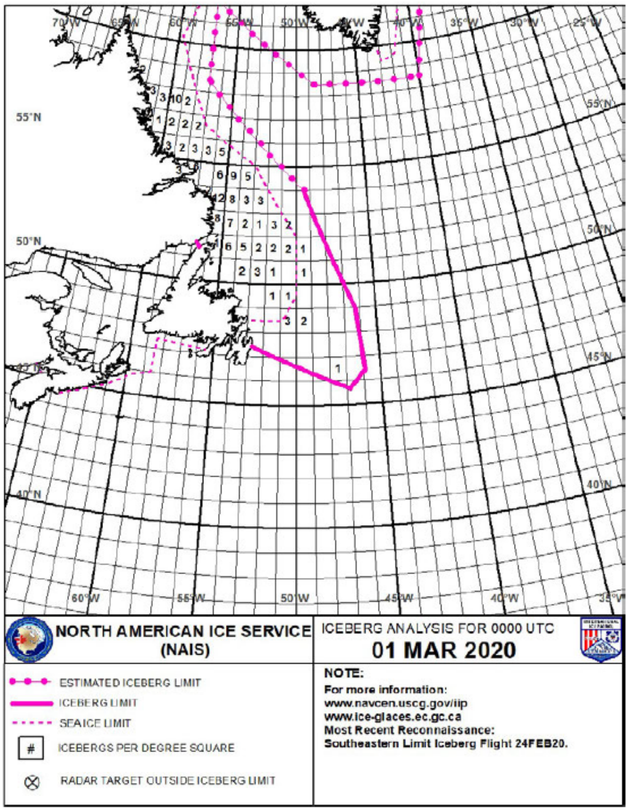

Fig. 16 Semi-monthly iceberg charts by IIP (USCG, 2020)

first and 15th days of each month, as shown in Fig. 16. These charts show the number of icebergs discovered by dividing the sea area into grid cells and present the limits of icebergs and sea ice.

4. Activities for Prevention of Iceberg Collisions

Currently, ice hazard warning services in the Northwestern Atlantic region are provided by the IIP, some commercial companies, and ice and weather forecast service agencies. The IIP was established in 1914 to watch icebergs in the Atlantic and Arctic Oceans and report their movements for safety. It is operated by the United States Coast Guard (USCG) with the financial support of 13 countries related to transatlantic sailing, including Canada, the United Kingdom, and France (USCG, 2020). This organization provides data by combining sightings, satellite imagery, and radar surveillance and iceberg trajectory models (Bigg and Billings, 2014). It has contributed to a dramatic reduction in the number of ship-iceberg collisions since 1913.

The IIP has collected data on sea-ice extents and iceberg locations to provide ships in the waters around the Grand Banks of Newfoundland with ice navigation hazard warnings. In earlier days, reports from ships around the region and dedicated cruises were used for observation, and in the mid-20th century, aircraft patrol was mainly used for observation. Recently, satellite image analysis and iceberg modeling were introduced for observation.

Since 2013, the number of icebergs discovered on the transatlantic sea routes was lowest in the 2020 ice year (October 2019 to September 2020) according to a recent report of the IIP (USCG, 2020). The number of icebergs that drifted into the routes of ships in the 2020 ice year was 169, which is the second-lowest number after 13 ships in 2013. These figures are based on 48°N latitude in the waters near Newfoundland, Canada.

Fig. 17 shows the changes in the number of icebergs that moved south below 48°N latitude in the region. The average number of icebergs per year was 498 for the period of 1900 to 2019 and 795 for the period of 1983 to the present day. As shown in Fig. 17, the number of icebergs discovered in 2019 was as much as 1,515. The IIP distinctively refers to the period from 1983 to the present day as the modern reconnaissance era and presents statistics by classifying icebergs detected by other sources such as satellites and aircraft.

Fig. 18 shows a bar graph representing the monthly number of icebergs moving south below 48°N latitude in the 2020 ice year. Out of the total of 169 icebergs, the highest proportion of them (76 icebergs) was discovered in May, and 98.8% appeared between March and June. The red solid line represents the average monthly number of icebergs for 120 years from 1900 to the present day, and the green solid line represents the value for the modern reconnaissance era since 1983. The average monthly number of icebergs discovered in the 2020 ice year was significantly lower than the average numbers for the two periods.

The U.S. National Ice Center is also using satellites to track large icebergs found near Antarctica. In addition, the Canadian Ice Service also provides information on ice sheets in the waters around Canada. In recent years, efforts have been continuously made to achieve highly accurate detection of even small icebergs using the image data from synthetic aperture radar (SAR), which allows us to obtain high-resolution images of extensive regions regardless of weather conditions or the time of day or night (Frost et al., 2016; Choi, 2018; Barbat et al., 2019; Soldal et al., 2019; Bailey et al., 2021).

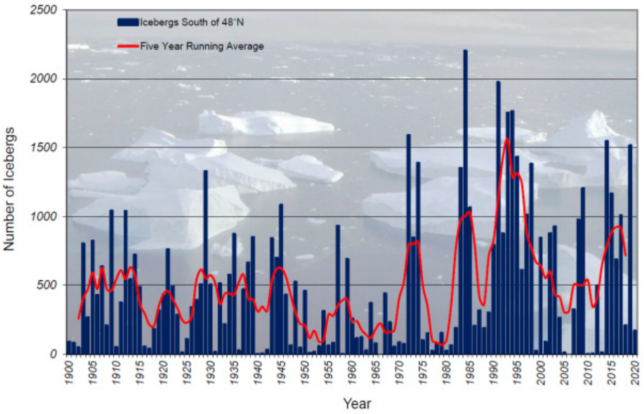

Fig. 17 Icebergs crossing 48°N by year (blue bars) and five-year running average for 1900–2019 (red line) (USCG, 2020)

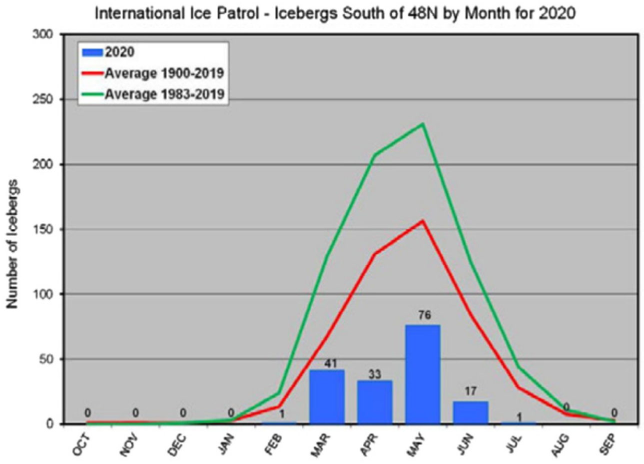

Fig. 18 Icebergs south of 48°N by month for 2020 (USCG, 2020)

5. Summary and Conclusions

It has been more than 100 years since the Titanic sank with the loss of over 1,500 lives, but the danger of ship-iceberg collisions is still present. Technological advances that allow more accurate detection of icebergs, such as marine radar, satellite image analysis, and aircraft patrol, have made the North Atlantic safer, but an average of 15,000 icebergs are formed each year. 2% of them move down to the area where the Titanic sank, and ships still continue to operate in the vicinity of the area (Sosnowski, 2012). Bergy bits and growlers, which refer to small icebergs, are difficult to detect by radar or satellites, so they are highly likely to present hazards for the operation of ships.

In this study, statistical data on ship-iceberg collision accidents were reviewed, and it was found that an average of three accidents occur per year, even in recent years. Additionally, in relation to such accidents, the characteristics of icebergs generated when chunks of ice break off from land-based glaciers were examined through a review of previous studies. Specifically, the size, shape, and mass of icebergs were included in the analysis. Also, properties related to ice strength were examined, such as density, elastic modulus, and Poisson's ratio, , and the tensile strength and bending strength were also investigated. Finally, overall activities to prevent accidents related to ship-iceberg collisions were described, such as the investigation of ice extents and collection and analysis of data on the generation, distribution, and movement of icebergs.

According to NASA, an average of 402 gigatonnes of mountain glaciers and ice caps disappear every year, and Professor Wadhams at Cambridge University stated that in the past 10 years, the downhill flow rate of glaciers in Greenland has doubled over the past decade. A number of icebergs are being generated, resulting in more icebergs floating in the sea than in 1912, when the accident of the Titanic occurred (Sosnowski, 2012). In this situation, ship-iceberg collision accidents are likely to occur at any time. In particular, it should be noted that despite cutting-edge technologies and continued patrol efforts, it is still possible for ships to sustain heavy damage due to a collision or contact with small icebergs that are difficult to detect, such as bergy bits and growlers.

References

Addario, N., Rizzuto, E., & Prestileo, A. (2014). Ship Side Damage Due to Collision with Icebergs. in G. Soares, and L. Pena, (Eds.), Developments in Maritime Transportation and Exploitation of Sea Resources. London: Taylor & Francis Group.

Atlantic Survey. (1982). Iceberg Aerial Reconnaissance. Atlantic Survey Report for Mobil Hibernia Development Studies.

Bailey, J., Marino, A., & Akbari, V. (2021). Comparison of Target Detectors to Identify Icebergs in Quad-polarimetric L-band Synthetic Aperture Radar Data. Remote Sensing, 13(9). 1753. https://doi.org/10.3390/rs13091753

Barbat, M.M., Wesche, C., Werhli, A.V., & Mata, M.M. (2019). An Adaptive Machine Learning Approach to Improve Automatic Iceberg Detection From SAR Images. Journal of Photogrammetry and Remote Sensing, 156, 247–259. https://doi.org/10.1016/ j.isprsjprs.2019.08.015

BBC News. (2007, November 24). Stricken Antarctic Ship Evacuated. BBC News. Retrieved from http://news.bbc.co.uk/2/hi/americas/7108835.stm

Bercha, F.G. (1983). Iceberg Aerial Reconnaissance 1983. F.G. Bercha and Associates Report for Mobil Hibernia Development Studies.

Bercha, F.G. (1984). Iceberg Aerial Reconnaissance 1984. F.G. Bercha and Associates Report for Mobil Hibernia Development Studies.

Bigg, G., & Billings, S. (2014). The Iceberg Risk in the Titanic Year of 1912: Was It exceptional?. Significance, 11(3), 6–10. https://doi.org/10.1111/j.1740-9713.2014.00746.x

Bureau of Maritime Affairs, Liberia. (2009), Report of Investigation in the Matter of Sinking of Passenger Vessel EXPLORER (O.N. 8495) on 23 November 2007 in the Bransfield Strait near the South Shetland Islands. Retrieved from http://www.photobits.com/dl/Explorer%20 -%20Final%20Report.PDF

Cammaert, A.B., & Muggeridge, D.B. (1988). Ice Interaction with Offshore Structures. New York: Van Nostrand Reinhold.

Canadian Coast Guard. (2012). Ice Navigation in Canadian Waters (Cat. Fs154-31/2012E-PDF). Retrieved June 8 2021 from https://www.ccg-gcc.gc.ca/publications/icebreaking-deglacage/ice-navigation-glaces/page05-eng.html

Choi, J. (2018). Iceberg-ship Classification in SAR Images Using Convolutional Neural Network with Transfer Learning. Journal of Internet Computing and Services, 19(4), 35–44. https://doi.org/10.7472/jksii.2018.19.4.35

Choi, K. (2013). Sea Ice in Polar Regions. Seoul, Korea: GeoBook Publishing Co.

Dasgupta, S. (2019, October 11). 10 Ships Sunk by Accident with Iceberg, Maritime History. Retrieved from https://www.marineinsight.com/maritime-history/10-ships-sunk-by-accident-with-iceberg/

Daley, C., & Veitch, B. (2000). Iceberg Evolution Modeling: A Background Study (PERD/CHC Report, OERC Report 2000-05-06). National Research Council of Canada. https://doi.org/10.4224/12341002

Dobrocky Seatech. (1984). Iceberg Field Survey 1984. Mobil Hibernia Development Studies.

Dobrocky Seatech. (1985). Iceberg Dimensions and Shape Field Survey 1985. Terra Nova Development Studies.

Fenco. (1971). Iceberg Dynamics Project. Report by Fenco (Newfoundland) Ltd.

Foumler, M., Lasserre, F., Beveridge, L., & Tetu, P.L. (2020). A European Shipping Companies Survey on Arctic Shipping: Expectation vs. Reality. Quebec Council for Geopolitical Studies (CQEG). Retrieved from http://hdl.handle.net/20.500.11794/39514

Frost, A., Ressel, R., & Lehner, S. (2016). Automated Iceberg Detection Using High Resolution X-band SAR Images. Canadian Journal of Remote Sensing, 42(4), 354–366. https://doi.org/10.1080/ 07038992.2016.1177451

Gagnon, R.E. (2007). Results of numerical simulations of growler impact tests, Cold Regions Science and Technology, 49(3), 206–214. https://doi.org/10.1016/j.coldregions.2007.03.016

Gagnon, R.E., & Gammon, P.H. (1995). Charaterization and Flexural Strength of Iceberg and Glacier Ice. Journal of Glaciology, 41(137), 103–111. https://doi.org/10.3189/S0022143000017809

Gammon, P.H., Gagnon, R.E., Bobby, W., & Russell, W.E. (1983). Physical and Mechanical Properties of Icebergs. Proceedings of the Offhsore Technology Conference, Houston, Texas, 143–150. https://doi.org/10.4043/4459-MS

Gold, L.W. (1988). On the Elasticity of Ice Plates. Canadian Journal of Civil Engineering, 15(6), 1080–1084. https://doi.org/10.1139/l88-140

Hanninen, S. (2005). Incidents and Accidents in Winter Navigation in the Baltic Sea, Winter 2002-2003 (Research Report 54). Winter Navigation Research Board, Finnish and Swedish Maritime Administration. Retrieved from https://arkisto.trafi.fi/filebank/a/1352716465/5666a0c12549e09d1f84c3075353d3de/10732-No_54_incidents_and_accidents_2003.pdf

Haynes, F.D. (1978). Effect of Temperature on the Strength of Snow-ice (CRREL Report 78–27). Hanover, New Hampshire: Department of the Army, Cold Regions Research and Engineering Laboratory, Corps of Engineers.

Hill, B. (2001). Ship Collisions with Icebergs: an Historical Record of Collisions in the Seas Around North America and Greenland. Proceedings of the 16th International Conference on Port and Ocean Engineering Under Arctic Conditions, Ottawa, Canada, 2, 997–1002.

Hill, B. (2006). Ship Collision with Iceberg Database (ICETECH06-117-RF). National Research Council of Canada. https://www.researchgate.net/profile/Brian-Hill-6/publication/44084643_Ship_Collision_with_Iceberg_Database/links/02e7e5346dc8b41281000000/Ship-Collision-with-Iceberg-Database.pdf

Hodgson, G.J., Lever, J.H., Woodworth-Lynas, C.M., & Lewis, C.F. (1988). The Dynamics of Iceberg Grounding and Scouring (DIGS) Experiment and Repetitive Mapping of the Eastern Canadian Cntinental Self (ESRF Report 09). Ottawa: Environmental Studies Research Funds.

Høyland, K.V., Kim, E., Marchenko, A., Lishman, B., & Barrette, P. (2020), Ice Properties in ISO 19906's (2nd ed.). Proceedings of 25th IAHR International Symposium on Ice, Trondheim, Virtual Conference.

ICE Engineering Ltd. (1983a). Iceberg Field Survey. Ice Engineering Report for Mobil Hibernia Development Studies.

ICE Engineering Ltd. (1983b). A Survey of Icebergs in the Strait of Belle Isle. Ice Engineering Report to Bedford Institute of Oceanography.

ICE Engineering Ltd. (1984). Iceberg Survey – Grand Banks – Hibernia, Contract Report Prepared for BIO.

ICE Engineering Ltd. (1985). Iceberg Survey – Grand Banks – Hibernia, Contract Report Prepared for BIO.

Intera. (1981). Iceberg Dimensions by Aerial Photography. Intera Environmental Consultants Ltd., Report for Mobile Hibernia Development Studies.

International Standards Organization (2019), Petroleum and Natural Gas Industries — Arctic Offshore Structures (ISO 19906).

Jacka, T.H., & Giles, A.B. (2007), Antarctic Iceberg Distribution and Dissolution from Ship-based Observations. Journal of Glaciology, 53(182), 341–356. https://doi.org/10.3189/002214307783258521

Jalonen, R., Riska, K., & Hanninen, S. (2005). A Preliminary Risk Analysis of Winter Navigation in the Baltic Sea (Rsearch Report 57). Winter Navigation Research Board, Finnish and Swedish Maritime Administration. Retrieved from https://arkisto.trafi.fi/filebank/a/1352716465/403d393475700af91c1f06711532924c/10735-No_57_A_preliminary_risk_analysis.pdf

Jang, K.B., Che, J.S. and Choo, I.H. (1997). Iceberg Collision Simulation for Ice Class Shuttle Tanker. Samsung Internal Technical Report M37 KR 96001.

Jia, Z., Ringsberg, J.W., & Jia, J. (2009). Numerical Analysis of Nonlinear Dynamic Structural Behaviour of Ice-loaded Side-shell Structures. International Journal of Steel Structures, 9, 219–230. https://doi.org/10.1007/BF03249496

Kim, J.H. (2007). A Study on Standardization of Ice Mechanics Experimental Techniques with a Cold Room (Master thesis). Korea Maritime University.

Korzhavin, K.N. (2002). Action of Ice on Engineering Structures. New York: Books for Business. (Original work published 1971)

Kujala, P. (1991). Damage Statistics of Ice-strengthened Ships in the Baltic Sea 1984-1987 (Research Report 50). Winter Navigation Research Board, Finnish and Swedish Maritime Administration. Retrieved from https://arkisto.trafi.fi/filebank/a/1352716465/2c77653e6c15301e82555185992ed8a0/10728-No_50_Damage_statistics_of_ice-strengthened_ships_in_the.pdf

Lee, R.W., & Schulson, E.M. (1988). The Strength and Ductility of Ice Under Tension. Journal of Offshore Mechanics and Arctic Engineering, 110(2), 187–191. https://doi.org/10.1115/1.3257049

Liu, Z. (2011). Analytical and Numerical Analysis of Iceberg Collisions with Ship Structures (Doctoral theses). NTNU. http://hdl. handle.net/11250/238036

Marchenko, N. (2012). Russian Arctic Seas: Navigational Conditions and Accidents. Heidelberg: Springer Science & Business Media.

Marchenko, N. (2014). Floating Ice Induced Ship Casualties. Proceeding of 22nd IAHR International Symposium on Ice, Singapore.

McKenna, R.F. (2004). Development of Iceberg Shape Characterization for Risk to Grand Banks Installations (PERD/CHC Report 20-73). https://doi.org/10.4224/12340897

McKenna, R.F. (2005). Iceberg Shape Charaterization. Proceedings 18th International Conference on Port and Ocean Engineering under Arctic Conditions, 2, 555–564.

Mejlaelander-Larsen, M., & Hysing, T. (2006). Ice Collision Scenario (Technical Report 2006-0672). DNV.

NSIDC. (2021). Quick Facts on Icebergs - Why Are Icebergs Important?. https://nsidc.org/cryosphere/quickfacts/icebergs.html

Oceans Ltd. (2004). Determination of Iceberg Draft and Shape (PERD/CHC Report). Oceans Ltd.

Paik, J.K. (1992). Lessons from Grounding Accident of Exxon Vadez. Bullutin of Society of Naval Architects of Korea, 29(2), 27–31.

Palmer, A., & Croasdale, K. (2013). Arctic Offshore Engineering.

Singapore: World Scientific Publishing.

Paterson, W.S.B. (1994). The Physics of Glaciers (3rd ed.), Oxford: Elsevier Science Ltd.

Petrovic, J.J. (2003). Review Mechanical Properties of Ice and Snow. Journal of Materials Science, 38, 1–6. https://doi.org/10.1023/A:1021134128038

Ralph, F., McKenna, R,& Gagnon, R. (2008). Iceberg Characterization for the Bergy Bit Impact Study. Cold Regions Science and Technology. 52(1), 7–28. https://doi.org/10.1016/j.coldregions.2007.04.016

Rudkin, P., Young, C., Barron Jr., P., & Timco, G. (2005). Analysis and Results of 30 Years of Iceberg Management. Proceedings of 18th International Conference on Port and Ocean Engineering under Arctic Conditions (POAC'05), 2, 595–604. Potsdam, NY, USA. Retrieved from https://nrc-publications.canada.ca/eng/view/accepted/?id7deaaa28-c001-4bf1-8261-1628c0802627

Sanderson, T.J.O. (1988). Ice Mechanics: Risks to Offshore Structures. London: Graham & Trotman.

Schulson, E.M. (1999). The Structure and Mechanical Behavior of Ice. Journal of Minerals, Metals, Materials Society, 51, 21–27. https://doi.org/10.1007/s11837-999-0206-4

Smith, S.D., & Donaldson, N.R. (1987). Dynamic Modelling of Iceberg Drift Using Current Profiles. Canadian Technical Report of Hydrography and Ocean Sciences 91, Bedford Institute of Oceanography.

Soldal, I., Dierking, W., Korosov, A., & Marino, A. (2019). Automatic Detection of Small Icebergs in Fast Ice Using Satellite Wide-swath SAR Images, Remote Sensing, 11(7), 806. https://doi.org/10.3390/ rs11070806

Sosnowski, A. (2012). Icebergs Still Threaten Ships 100 Years After Titanic. AccuWeather, Retrieved from https://www.scientificamerican.com/article/icebergs-still-threaten-ships-100-years-after-titanic/

Suh, Y., Ito, H., Chun, S., Han, S., Choi, J., & Urm, H. (2008). Ice Collision Analysis for Membrane Tank Type LNG Carrier. Journal of Ship & Ocean Technology, 12(1), 35–44.

Thompson-Monsen, M. (2021). Icebergs. Retrieved from http://www.antarcticglaciers.org/glacier-processes/glacier-types/icebergs/

Timco, G.W., & Weeks, W.F. (2010). A Review of the Engineering Properties of Sea Ice. Cold Regions Science and Technology, 60(2), 107–129. https://doi.org/10.1016/j.coldregions.2009.10.003

Turnbull, I.D., Fournier, N., Stolwijk, M., Fosnaes, T., & McGonigal, D. (2015). Operational Iceberg Drift Forecasting in Northwest Greenland. Cold Regions Science and Technology, 110, 1–18. https://doi.org/10/1016/j.coldregions.2014.10.006

US Army Corps of Engineers. (2005). Engineering and Design: Ice Engineering. Honolulu, Hawaii. USA: University Press of the Pacific. (Original work published 2002)

USCG. (2020). Report of the International Ice Patrol in the North Atlantic, 2020 Season Bulletin, 106, CG-188-75, U.S. Homeland Security, U.S. Coast Guard.

Wikipedia. (2021). Ship Collision. Retrieved from https://en.wikipedia.org/wiki/Ship_collision

WMO (2015), Sea Ice Nomenclature. World Meteorological Organization. https://library.wmo.int/doc_num.php?explnum_id 4651

Yu, Z., & Amdahl, J. (2021). A Numerical Solver for Coupled Dynamic Simulation of Glacial Ice Impacts Considering Hydrodynamic-ice- Structure Interaction. Ocean Engineering, 226. https://doi.org/ 10.1016/j.oceaneng.2021.108827

Author ORCIDs

Author name	**ORCID**
Lee, Tak-Kee	0000-0002-5944-156X
Park, Hyun-Jin	0000-0002-6058-4330

KSOE

Review Article

Journal of Ocean Engineering and Technology 35(5), 382-392, October, 2021
https://doi.org/10.26748/KSOE.2021.061

pISSN 1225-0767
eISSN 2287-6715

Prospects and Economics of Offshore Wind Turbine Systems

Thi Quynh Mai Pham[1], Sungwoo Im[2] and Joonmo Choung[3]

[1]*Researcher, Department of Naval Architechture and Ocean Engineering, Inha University, Incheon, Korea*
[2]*Research Professor, Department of Naval Architechture and Ocean Engineering, Inha University, Incheon, Korea*
[3]*Professor, Department of Naval Architechture and Ocean Engineering, Inha University, Incheon, Korea*

KEY WORDS: Floating offshore wind turbine, Bottom-fixed offshore wind turbine, Levelized cost of energy, Plant-level cost, Integrated cost, Social cost

ABSTRACT: *In recent years, floating offshore wind turbines have attracted more attention as a new renewable energy resource while bottom-fixed offshore wind turbines reach their limit of water depth. Various projects have been proposed with the rapid increase in installed floating wind power capacity, but the economic aspect remains as a biggest issue. To figure out sensible approaches for saving costs, a comparison analysis of the levelized cost of electricity (LCOE) between floating and bottom-fixed offshore wind turbines was carried out. The LCOE was reviewed from a social perspective and a cost breakdown and a literature review analysis were used to itemize the costs into its various components in each level of power plant and system integration. The results show that the highest proportion in capital expenditure of a floating offshore wind turbine results in the substructure part, which is the main difference from a bottom-fixed wind turbine. A floating offshore wind turbine was found to have several advantages over a bottom-fixed wind turbine. Although a similarity in operation and maintenance cost structure is revealed, a floating wind turbine still has the benefit of being able to be maintained at a seaport. After emphasizing the cost-reduction advantages of a floating wind turbine, its LCOE outlook is provided to give a brief overview in the following years. Finally, some estimated cost drivers, such as economics of scale, wind turbine rating, a floater with mooring system, and grid connection cost, are outlined as proposals for floating wind LCOE reduction.*

1. Introduction

The share of offshore wind power has increased steadily in recent years because large offshore wind farms can be developed with the advantages of faster and steadier wind speeds. In particular, bottom-fixed offshore wind farms are now becoming more competitive due to significant cost reduction. According to the 2019 IRENA (International Renewable Energy Agency) report, the LCOE (levelized cost of electricity) for onshore wind power was reported to be about 50-170 USD/MWh (IRENA, 2019) which is competitive compared to that of fossil fueled power. The report revealed that the LCOE of bottom-fixed offshore wind power was 53-94 USD/MWh in the European wind farms. The ARENA report predicted that the LCOE will be lower than that of fossil fuels.

As reported by Wind Europe, approximately 80% of potential offshore wind power is distributed in offshore area deeper than 60 m water depth (Wind Europe, 2017). This equates to 4,000 GW in Europe, 2,450 GW in the United States, and 500 GW in Japan, respectively. Larger foundation substructures and higher strength steels are necessary at such a water depth, which inevitably induce for the bottom-fixed offshore wind turbines to be less economical. Therefore, the interest in floating offshore wind turbines (FOWT) is growing rapidly as an alternative to untapped offshore wind potential.

Floating offshore wind power is a method of generating electricity by combining a wind generator and a floating substructure called a floater, which is not fixed to the seabed. The floating offshore wind started in 2009 with the installation of the first prototype in the world called the Hywind Demo, which is a 2.3-MW floating turbine with a rotor diameter of 82.4 m in the southeast of Karmoy in Norway at a water depth of about 220 m. After the commission of the Hywind Demo, the total installed floating offshore wind capacity has increased speedily and reached about 124 MW in 2020 (Spearman and Strivens, 2020). The pilot FOWT projects are in commissioning or have been completed. They are mainly located in Norway, Portugal, England, France, Japan, and the United States.

The FOWTs are capable of not only increasing the total production

Received 9 July 2021, revised 12 August 2021, accepted 24 August 2021
Corresponding author Joonmo Choung: +82-33-860-7346, heroeswise2@gmail.com

of renewable energy at deep sea areas but also minimizing ecosystem degradation, civil complaints, noise problems, etc. Consequently, it has shown a trend of focusing on floating offshore wind power all over the world.

In spite of those advantages of the FOWTs, they remain nascent technically compared to the bottom-fixed offshore wind turbines. It still makes investors very concerned about its economic feasibility. In this context, the LCOEs of floating and bottom-fixed offshore wind power were analyzed to understand the economic feasibility. In addition, we intended to identify major LCOE cost drivers of floating offshore wind power generation through an analysis, and we outlined some suggestions.

2. Floating Offshore Wind Market Reviews

2.1 Global Market Reviews

After the commissioning of the world’s first floating offshore wind turbine, the Hywind Demo, in 2009, the total electricity production by floating offshore wind turbines has grown steadily up to 124 MW in 2020 of which 90% of total installations is in Europe. The United States, Japan, and Korea are preparing to carry out pilot projects, and they are expected to accelerate the development of floating offshore wind power by the early 2020s (Table 1). Installation of FOWT is forecasted to reach 10-30 GW in 2030 and up to 250 GW in 2050 (Fig. 1 and Table 2).

Among the FOWT pilot projects, the Equinor's Hywind and the PPI's WindFloat are considered as the most pioneering ones. After the success of the Hywind Demo in 2009, Equinor constructed a pilot park called Hywind Scotland to demonstrate world's first offshore floating wind farm (Fig. 2). The Hywind Scotland finished installation of five 6 MW capacity wind turbines mounted on a spar type of floater at depth of 95−120 m in October 2017, and it has been actively operating since then.

PPI installed a 2 MW capacity wind turbine on a semi-submersible type of floater, which is called the WindFloat 1 project. The successful completion of the project paved the way for the development of a FOWT wind farm, the WindFloat Atlantic project (Fig. 3). The new floating offshore wind farm is located 20 km off the coast of Portugal

Table 1 Floating offshore wind farms expected to be commissioned by 2022 (Spearman and Strivens, 2020)

Project	Country	Capacity [Turbine rating]	Commissioning date
Hywind Scotland	UK	30 MW [6 MW × 5]	2017 (in operation)
Wind Float Atlantic	Portugal	25 MW [8.3 MW × 3]	2020 (in operation)
Kincardine	UK	50 MW [2 MW × 1, 9.6 MW × 5]	2021
Groix and Belle-lle	France	28.5 MW [9.5 MW × 3]	2021/2022
EFGL	France	30 MW [10 MW × 3]	2021/2022
EolMed	France	30 MW [10 MW × 3]	2021/2022
PGL wind farm	France	25.2 MW [8.4 MW × 3]	2021/2022
Goto City	Japan	22 MW [2MW × 1, 5 MW × 4]	2021/2022
Hywind Tampen	Norway	88 MW [8 MW × 11]	2021/2022

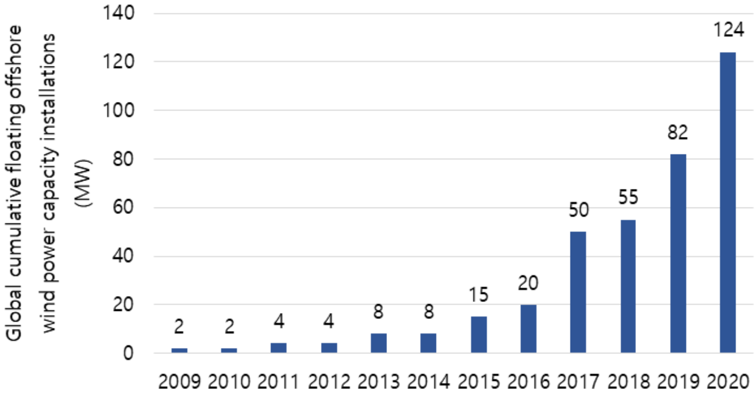

Fig. 1 Global cumulative floating offshore wind power capacity installation (Spearman and Strivens, 2020)

Table 2 Global wind energy growth (IRENA, 2019)

Wind turbine type	2030	2050
Onshore wind	1,787 GW	5,044 GW
Bottom-fixed offshore wind	228 GW	1,000 GW
Floating offshore wind	5-30 GW	250 GW

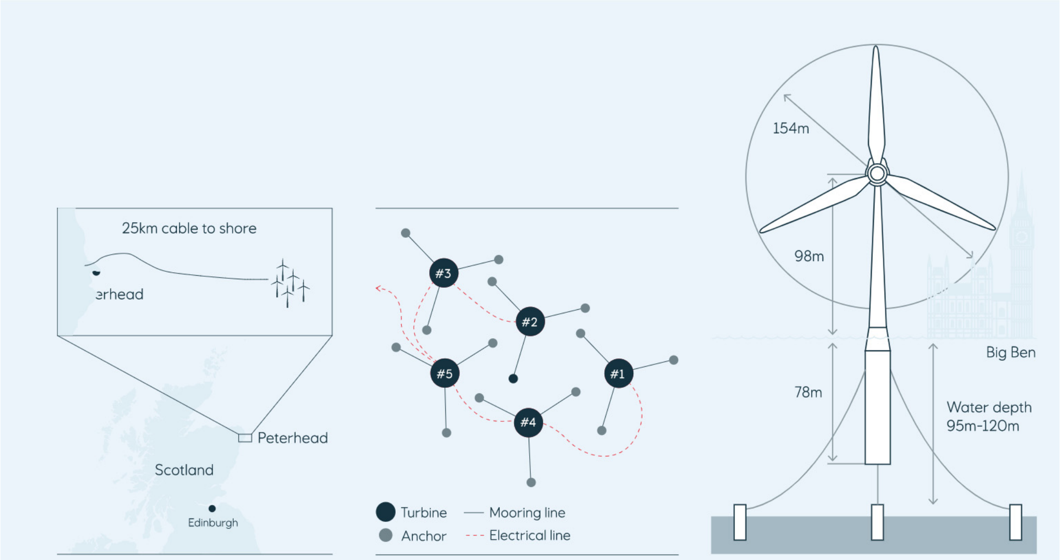

Fig. 2 Hywind Scotland floating wind turbine concept by Equinor

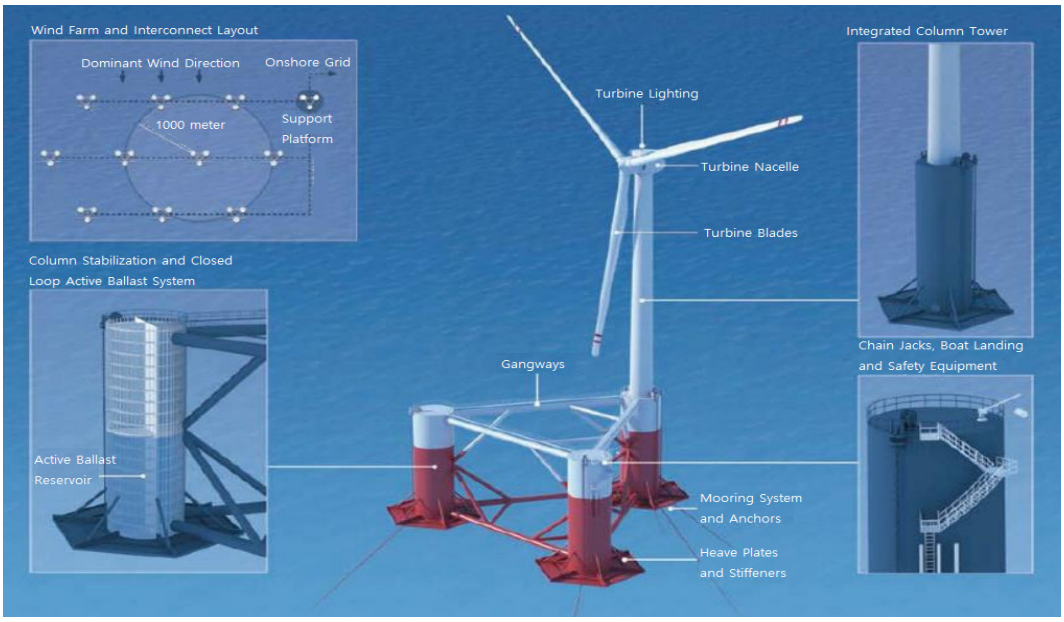

Fig. 3 WindFloat Atlantic floating wind turbine concept by PPI

and was commissioned in the middle of 2020. The project is considered to be the world's first semi-submersible floating wind farm to include three 8.4 MW capacity wind turbines.

During first 5 years of operation, the WindFloat 1 generated more than 11 GWh of electricity with a five-year average capacity factor of 47% (Weinstein, 2014). It experienced an extreme wave height of 18 m for this period and no structural damages were reported. The Hywind Demo has survived against 19 m wave height and produced about 55 GWh of electricity with an annual average capacity factor of about 50% in 2011 (Equinor, n.d.). After the commission in 2017, the Hywind Scotland recorded a capacity factor of up to 65% for the first three months and an average factor of 56% for first two years of operation (Equinor, 2020). With such huge capacity factors, floating offshore wind power has shown strong competitiveness compared to bottom-fixed offshore wind power which has a capacity factor of less than 40%.

2.2 Korean Market Reviews

According to data from the Korea Energy Agency (2020), the potential capacity of offshore wind power in the Korean Peninsula is estimated to be 41 GW based on the minimum economic feasibility. The potential of offshore wind resources on the Korean Peninsula is estimated to be 41GW based on the minimum economic feasibility. The sea area southeast of the Korean Peninsula and offshore area of the Jeju Island have a wide continental shelf for which water depth is suitable for floating offshore wind power generation. The average annual wind speed in these areas is over 8 m/s, and it is known as the best places for floating offshore wind power generation as shown in Fig. 4.

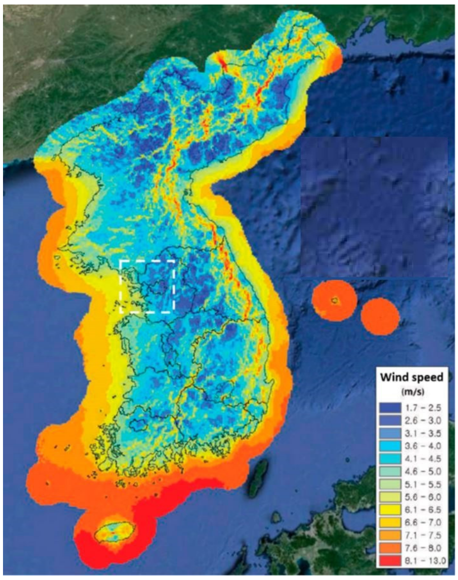

Fig. 4 Wind resource map of Korean Peninsula of mean wind speed at 100 m height above ground (Korea Institute of Energy Research, 2015)

As of 2019, 28 units of offshore wind turbines with 72 MW capacity were installed at 5 locations, accounting for 4.8% of the total installed wind power capacity (Korea Energy Agency, 2020). In the same year, the Korean government supported development of the first 750-kW FOWT project, which will be installed in the sea at 2.6 km in front of Sin-ri, Ulju-gun, Metropolitan Ulsan (Fig. 5). Since then, the development research of a MW-size FOWT has been continuously promoted. Recently, the government has continuously funded 50 billion KRW for the project of developing and manufacturing the Korea's first 8 MW FOWT from 2020 to 2026. In the report of the Ministry of Trade, Industry and Energy (MOTIE), the government also plans to install a 200 MW floating offshore wind farm in 2023, a 1.4 GW FOWT farm in Ulsan, and a 4.6 GW FOWT farm in the southeast region after 2030 (Ministry of Trade, Industry and Energy, 2020).

3. LCOE of FOWT

The economics of energy resources are based on LCOE which is the average power generation cost over the lifetime of the generator and means the average real power generation cost (KRW) per unit of power (kWh) produced by a power plant (Lee and Kim, 2020). LCOE is calculated as the ratio between the present value of the total cost of the generator and the present value of the total amount of electricity generated (Lee, 2017) and is expressed as Eq. (1):

$$LCOE = \frac{\sum_{t=1}^{n} \frac{C_t}{(1+i)^t}}{\sum_{t=1}^{n} \frac{Q}{(1+i)^t}} \tag{1}$$

Where C_t is the total cost for energy generation in year t, Q_t is the total generated electricity during year t and i is the discount rate. As specified by Samadi (2017), the costs related to power generation can be divided into three levels: power plant costs, systems integration costs, and social costs (or external costs).

3.1 Power Plant Cost

Power plant costs include capital costs, fuel costs, operating and maintenance costs, and market costs of greenhouse gas (GHG) emissions (Samadi, 2017). In the case of renewable energy, such as floating offshore wind power, only capital costs and operating and maintenance costs are considered because fuel costs and market costs of greenhouse gas emissions are not produced. Table 3 shows the main components of capital costs through reference analyses (Harries and Grace, 2015; Rhodri and Marc, 2015; Benveniste, et al., 2016; Valpy et al., 2017; Tyler et al., 2019, Lerch, 2019). The capital cost comparison between bottom-fixed and floating offshore wind power may not be accurate since the data is collected from different sizes of installations, but some general conclusions can be drawn.

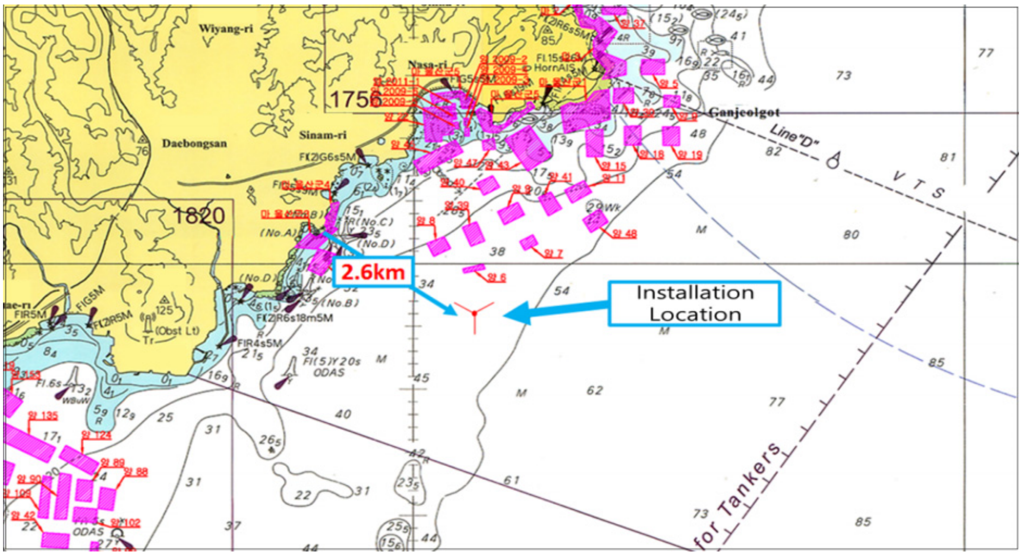

Fig. 5 Installation location of the first 750-kW floating offshore wind turbine in Korea

Table 3 Capex break-down according to some researches

Research	Bottom-fixed wind	Floating wind	Note
Harries and Grace, 2015	- Development: 4% - Windturbine: 45% - Balance of plant: 33% - Installation: 18%	- Development: 2% - Windturbine: 21% - Balance of plant: 73% - Installation: 4%	Based on 2015 data for bottom-fixed offshore wind turbine Based on assumption of 2020 projection for floating wind turbine
Rhodri and Marc, 2015	- Wind turbine: 40% - Balance of plant: 37% - Installation: 23%	- Wind turbine: 42% - Balance of plant: 45.5% - Installation: 12.5%	Based on assumption of a bottom-fixed offshore wind farm Based on assumption of a floating offshore wind farm
Benveniste, et al., 2016	- Development: 4% - Windturbine: 39% - Balance of plant: 31% - Installation: 26%	- Development: 4.8% - Windturbine: 37.6% - Balance of plant: 44.5% - Installation: 13.1%	Based on assumption of a 10 MW bottom-fixed offshore wind turbine Based on assumption of a 10 MW floating offshore wind turbine
Valpy et al., 2017	- Development: 4.7% - Windturbine: 51.3% - Balance of plant: 27.9% - Installation: 16.1%		Based on assumption of a 500 MW bottom-fixed offshore wind farm
Tyler et al., 2019	- Development: 5.1% - Windturbine: 31.9% - Balance of plant :40.9% - Installation: 22.1%	- Development: 4.7% - Windturbine: 24.4% - Balance of plant: 47.1% - Installation: 23.8%	Based on assumption of a 600 MW bottom-fixed offshore wind farm Based on assumption of a 600 MW floating offshore wind farm
Lerch, 2019	- Development: 5% - Windturbine: 40% - Balance of plant: 31% - Installation: 25%	- Development: 5% - Windturbine: 39% - Balance of plant: 50% - Installation: 6%	Based on a 4.14 MW bottom-fixed offshore wind turbine Based on a 10 MW floating offshore wind turbine

As shown in Table 3, the capital costs usually consist of four types of costs: costs for development and management, wind turbine, balance of plant (BOP), and transportation and installation, even though Rhodri and Marc (2015) did not classify development and management cost separately. The development and management cost includes expenses such as development, design, marine environment surveys, management, construction insurance, etc. and varies with the size of the project. In the case of FOWTs, the scope and intensity for a seabed environment survey are less considerable than those in case of bottom-fixed offshore wind turbines since a FOWT is not fixed on the seabed, but the cost of analyzing the weather for deep sea installation may be higher.

The wind turbine cost consists of three elements: rotor, nacelle, and tower. Rotor contains blades, hub, auxiliary systems, and blade bearings, while nacelle is a cover housing that houses most turbine components such as generator, gearbox, drive train, power take-off, control system, and other assemblies. The nacelle and contained components account for the largest share of wind turbine cost, followed by the rotor cost. The compositions of the 5 MW and 10 MW wind turbines' costs are shown in Table 4. When upscaling a wind turbine, while other parts' proportions show small changes, the nacelle cost increases significantly due to especially the generator cost rise. In the case of a gearless-type 10 MW wind turbine, the generator cost is even double that of one with the gearbox (Offshore Renewable Energy Catapult, 2019).

Table 4 Offshore wind turbine cost break-down

Wind turbine cost	5 MW turbine[1]	10 MW turbine[2]
Nacelle:	41.70%	60.61%
- Bedplate and shaft	3.70%	6.06%
- Main bearing	1.30%	3.03%
- Gearbox	16.70%	10.61%
- Generator	4.20%	15.15%
- Power take-off	6.70%	10.61%
- Control system	2.80%	3.79%
- Others	6.30%	11.06%
Rotor:	25.00%	28.79%
- Blade	17.50%	19.70%
- Hub casting	1.30%	2.27%
- Pitch system	2.50%	1.52%
- Others	3.70%	5.15%
Tower:	16.70%	10.61%
- Tower	16.70%	10.61%
Miscellaneous components:	16.70%	NA

[1] Bjerkseter and Agotnes (2013)

[2] Offshore Renewable Energy Catapult (2019)

The BOP cost includes floater of wind turbine, mooring system, anchor, and connecting cable. More than 40 concepts of floaters have been proposed (Spearman and Strivens, 2020), but they can be segmented into 3 main types: spar, semi-submersible and tension leg platform (TLP) (Fig. 6). A spar-type floater is ballast-stabilized structure with a large draft that is suitable for deep water. A TLP is a

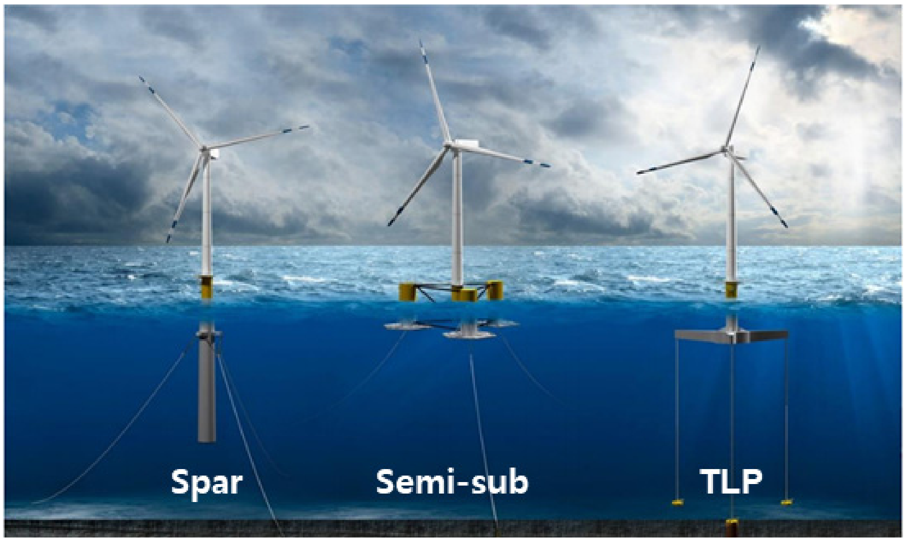

Fig. 6 Main substructure types of offshore floating wind turbine

Table 5 Offshore wind turbine cost breakdown[1)]

Item	Spar	Semi-submersible	TLP
Weight	heavy	heavy	light
Wave sensitivity	low	high	low
Pitch stability	ballast	buoyancy	mooring
MCF[2)]	120%	200%	130%
Water depth	> 100 m	> 50 m	> 50 m

[1)] Jung and Lee (2020)

[2)] MCF (Manufacturing complexity factor): The relative complexity of manufacturing in compare with the bottom-fixed monopile type.

tension-stabilized structure that uses tendons, so the seabed surface needs to be hard enough for tendon installation, and the installation cost increases with water depth. In the case of a semi-submersible substructure, with catenary mooring-stabilized structure, it is suitable for relatively shallow to deep water depth (Table 5).

According to Global Wind energy Council (GWEC) database, by the end of 2020, 67% of floating offshore wind turbines in the market use a semi-submersible floater (Lee and Zhao, 2020). Although spars and TLPs could reduce manufacturing cost due to lighter weight, transportation and installation procedures are more complicated than semi-submersibles' one. A semi-submersible platform needs more complicated manufacturing process and requires more amount of steel but has advantages such as ease of transportation and installation. It can be also installed in shallow water depth.

Bottom-fixed and floating offshore wind turbines show a meaningful difference in the BOP costs. Due to the low complexity of the BOP design, turbine cost accounts for the largest share of the total cost of fixed-bottom offshore wind power generation. In other words, the foundation design of onshore wind power can be applied again to that of fixed-bottom offshore wind turbine. Since it costs so much to design and build a floating substructure, most of the references estimate higher BOP cost t. For instance, according to the research results of the National Renewable Energy Laboratory (NREL) based on a 6 MW wind turbine (Lerch, 2019), the difference between the turbine cost and BOP cost of bottom-fixed offshore wind power is only 9%, but that of FOWT is up to 22.7% as shown in Table 3. The reason for this is that the floating substructure occupies a large share of the BOP cost. As the floating substructure technology develops in terms of design and production, the BOP cost is expected to be reduced gradually.

The transportation and installation cost include the costs for transportation, installation, and decommissioning (Sun, 2020). Transportation and installation cost mainly depend on the types of floating structures. Since a semi-submersible FOWT is assembled on the ground or at the quayside and towed to an installation offshore site, the installation process is simpler and therefore the transportation and installation costs of the semi-submersible FOWTs are more competitive than other types of floaters. A spar floater should be towed a certain distance to have a sufficient water depth and positioned to upright position by a ballasting operation. After then, tower, nacelle, and rotor are assembled to the spar floater step by step. A fully assembled spar-type FOWT is towed to the installation site.

In the case of a TLP-type floater, there are various ways of installation methods. For example, the Germany's GICON TLP can be assembled on the ground by mounting the tower and RNA (rotor nacelle assembly) on the floater and towed by tugboats (wet towing) or transported by special transportation vessel (dry towing) to an installation site or floating slab/towing vessel. Therefore, unlike bottom-fixed offshore wind power, there is no need to hire heavy lift vessel in the installation process of FOWT. The rental fee for a heavy lift vessel is about 150,000 £ or 230 million KRW per day, while that for a fleet of tugboats is only around 30,000 £ (about 47 million KRW) per day (Jame and Costa Ros, 2015).

The operation and maintenance cost is necessary for operating and maintaining a wind turbine over its lifetime. This cost is mainly classified into operation cost and maintenance cost. The portion of the costs are almost same as that of the bottom-fixed offshore wind turbine,

Table 6 Operation and Maintenance cost break-down

O&M cost		Components	% in LCOE
500 MW wind farm[1]	Bottom-fixed	- Material: 15% - Labour: 10% - Equipment: 75%	22.0% (average)
	Floating	- Material: 13% - Labour: 9% - Equipment: 79%	25.0% (average)
600 MW wind farm[2]	Bottom-fixed	- Operation: 23% - Maintenance: 77%	34.3%
	Floating	- Operation: 22% - Maintenance: 78%	29.5%

[1] Bjerkseter and Agotnes (2013)

[2] Tyler et al. (2019)

accounting for about 22–34% of the LCOE (refer to Table 6). A large proportion of operating and maintenance cost is maintenance costs. It is known that the maintenance cost of a geared type turbine is higher than that of a gearless type turbine (direct-driven type turbine) due to complexity of gear system. The semi-submersible FOWT is possible to tow it back to a repair yard whenever maintenance is required. Therefore the semi-submersible FOWT is more advantageous than the bottom-fixed one in terms of the maintenance cost.

3.2 System Integration Cost

System integration cost is commonly referred to the cost of integrating an individual power plant into an electricity system (Lee, 2017). It is classified according to the type of renewable energy system: balancing cost, grid cost, and profile cost (Jang, 2019). The balancing cost comes from the renewable power generation due to weather forecast uncertainty. The grid cost includes connection costs and system reinforcement costs for connecting the generator to the transmission/distribution network. Finally, the profile cost, which is also called utilization cost or backup cost is the cost incurred by the variability of renewable generation.

Even though the LCOE always includes capital expenditure (CAPEX) and operating expenditure (OPEX), the formulas for calculating the system integration cost may be different by country or by project, which may affect the estimation of the LCOE (EWEA, 2016). When the average consumption of wind energy was about 10.2% in Europe in 2014, the balancing cost of wind energy was about 2–3 €/MWh. However, when the consumption increased to 20%, the balancing cost increased to about 4.5 €/MWh (EWEA, 2016). The profile cost, similarly to the balancing cost, elevates as the use of wind energy increases (Jang, 2019). However, these data are based on an onshore wind turbines only and there are few analytical studies on the profile cost of offshore wind case.

The FOWTs usually require higher grid cost than the bottom-fixed offshore wind turbines or onshore wind turbines because they are located farther from the energy consumption sites. According to the OECD NEA (Organization for Economic Co-operation and Development Nuclear Energy Agency), the grid cost in the system integration cost shares about 70% and 46% corresponding to the use of offshore wind power of 10% and 30%, respectively (OECD NEA, 2018). The grid cost of a FOWT is about 24% of the LCOE and can be influenced largely by environmental conditions, the distance from land, water depth, etc. (Myhr et al., 2014).

3.3 Social Cost

In the case of renewable energy, the social cost is not significant since carbon dioxide, air pollution, and radionuclide emissions are not produced. According to the LCOE calculation standard of the Korean Society of Industrial Organization, the social costs include only policy cost. Policy cost includes residential and environmental compensations (Korea Electric Power Corporation, 2018). The project developers of bottom-fixed offshore wind projects have to pay much policy cost to solve the problems related to costal ecosystem, underwater noise, and resident complaints. In contrast, a floating offshore wind turbine installed in the deep sea far from land is relatively free from these problems, and the compensation payment can be minimized.

The policy cost by the Japan Committee of Cost Verification includes human resource development, technology development for efficiency improvement, promotion, additional profits related to FIT (feed-in tariff) purchase price (Choi et al., 2019). A FIT purchase price, also called renewable energy payments, is a policy system designed to support renewable energy producers when market price of renewable energy is lower than the price announced by the government. It is mainly applied in the United States, Japan, and Germany. The Japanese FIT purchase price was maintained at 36 ￥/kWh from 2018 to 2020 for the FOWTs (Korea Energy Economics Institute, 2019).

The Korean Government also used to operate the FIT policy till 2012. The renewable energy portfolio standard (RPS) is now in acts in Korea. The RPS is a system that requires power generation companies with more than 500 MW power generation facilities to produce renewable energy by a certain percentage of total power generation. A power generation operator must either produce renewable energy directly or purchase a renewable energy certificate (REC) to meet the RPS obligation (Yoo, 2018). The REC certifies that power suppliers produced renewable energy. It has different weighting factors according to the renewable energy types (Song, 2012). As shown in Table 7, the weighting factors for the offshore wind power turbines ranges from 2.0 to 3.5 according to the grid connection distances.

Table 7 REC for offshore wind turbines[1]

Grid connection (km)	REC weighting factor
$d < 5$	2.0
$5.0 \leq d < 10.0$	2.5
$10.0 \leq d < 15.0$	3.0
$d \geq 15.0$	3.5

[1] Korea Energy Agency Renewable Energy Center (n.d.)

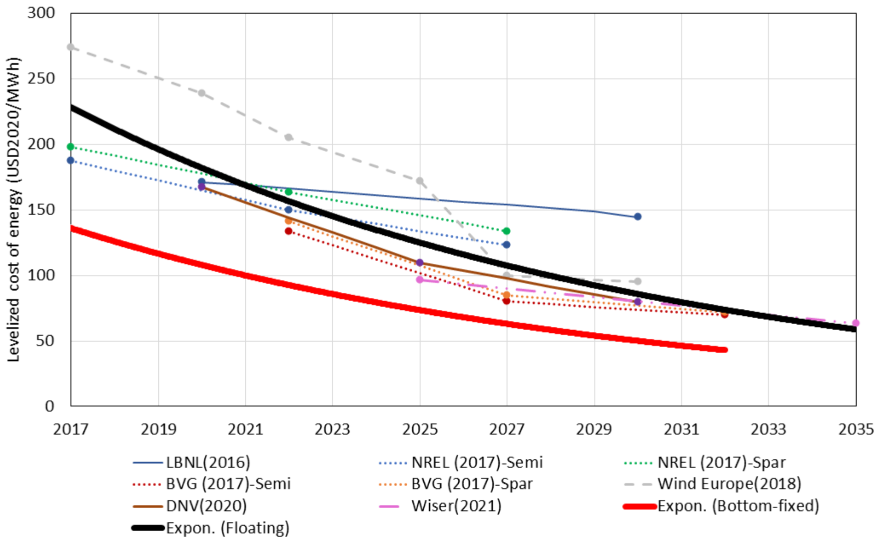

Fig. 7 Global LCOE estimates

3.4 Solutions for Cost Reductions in Offshore Wind Energy Production

As shown in Fig. 7, the LCOEs of the bottom-fixed and floating offshore wind turbines are predicted based on several references (Wiser et al., 2016; Beiter et al., 2017; Hundleby et al., 2017; WindEurope, 2018; DNV GL, 2020; Wiser et al., 2021). The red and black thick solid lines are exponential trend lines for the bottom-fixed and floating offshore wind turbines, respectively. The black thick solid line is more rapid reduction in the LOCE than the red one. This means the LCOE of the FOWTs could decrease faster than that of bottom-fixed wind turbines.

Although the data are based on some pilot farm projects, the LCOE of floating offshore wind farms is about 180–275 $/MWh (Wiser et al., 2016; WindEurope, 2018), which is almost double that of the bottom-fixed wind turbines (130 $/MWh in 2018). The LCOE of floating offshore wind farms is expected to reduce by 135–175 $/MWh after 2022 (Hundleby et al., 2017; WindEurope, 2018). Wiser et al. (2021) even forecasted that the floating offshore wind turbines' LCOE will decrease to about 60 $/MWh by 2035, eliminating the difference between the LCOEs of the bottom-fixed and floating offshore wind turbines.

There are various cost raisers of floating offshore wind power, such as the scale of development, turbine rating, cost of BOP, grid cost, etc. (OREC, 2021). For instance, compared to a pilot project, the capital costs of a commercial-scale project are significantly reduced. As shown in Fig. 8, Carbon Trust (Rhodri and Marc, 2015) estimated that CAPEX of floating offshore wind farm could be reduced by 48% when scaled up from a pilot project to a large commercial farm. Equinor reported that the CAPEX of the world's first floating offshore wind farm Hywind Scotland was reduced by 60–70% compared to the single-unit demonstration project (Equinor, n.d.).

The largest cost saving for the offshore wind farm projects is in the turbine sizes. The turbine capacity has continued to increase, but the floater capacity to support a turbine should follow it. Nevertheless, the commercial maturity of the wind turbine market continues to increase, and the design and manufacturing technology of large turbines continue to advance. As of 2021, 9.6 MW turbines were used in the floating offshore wind farm of WindFloat Kincadine project, and it is expected that 15 MW wind turbines will be used from 2030 in England, along with 20 MW wind turbines from 2037 (Offshore Renewable Energy Catapult, 2021).

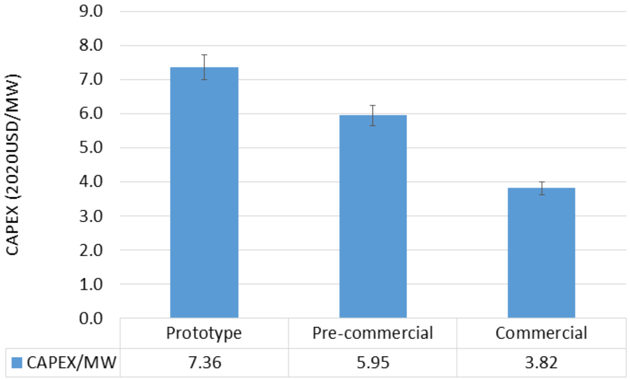

Fig. 8 Capex for floating wind devices by development stages (Rhodri and Marc, 2015)

Continuous innovation in the design and performance of the floating substructure, which accounted for a large proportion in CAPEX, will have significant impact on total costs. In addition, the development of mooring line material and design standardization all have cost-reduction potential. The integrated design concept of an anchor, mooring system, and floating substructure could not only help to reduce cost, but also lessen the time for transportation, installation, and maintenance. For example, the objective of the COREWIND (COst REduction and increase performance of floating WIND technology) project promoted by Horizon 2020 is to reduce the LCOE of floating offshore wind power by 15% through improvements in anchor systems and power cables (Ramboll Group, n.d.).

Currently, because most offshore wind turbines for floaters are modified from the onshore wind turbines, it is necessary to develop some specialized turbines for FOWTs. The geared wind turbines are dominant in markets, but the gearboxes require higher maintenance cost than direct-driven turbines. The gearless or direct-driven turbines wind turbines are more suitable for offshore because it will require low maintenance cost for the rotor parts being directly connected to the generator.

Grid costs make up a large portion of the LCOE. Recently, the Swedish government announced a proposal to reduce the cost of connecting offshore power plants to the national electricity grid for electricity suppliers (Swedish Wind energy Association, 2021). According to the research by Bulder et al. (2021), it is predicted that the LCOE can be reduced by 7.7% through the development and integration of offshore grids for the European markets. Moreover, by producing green hydrogen with electricity produced from floating offshore wind plants, it is possible to dramatically reduce the grid cost of floating offshore wind power. The Dolphyn project in the UK is an example of producing green hydrogen through floating offshore wind power. After starting a 2 MW demonstration in 2024, a 10 MW platform will be installed at the Kincardine floating offshore wind farm in 2027 (Scottish Government, n.d.).

4. Conclusion

Floating offshore wind turbine is developing with a fast-maturing technology, while bottom-fixed offshore wind turbine has many restrictions related to water depth and seabed conditions. Recently, the global cumulative installation capacity of the FOWTs has continued to increase through many studies and pilot/wind-farm projects, but the economic feasibility is still uncertain. For the purpose of confirming the possibility of reducing floating offshore wind power's LCOE, a comparative analysis between bottom-fixed and floating offshore wind power was performed. From a social cost perspective, the LCOE was classified into power plant costs, system integration costs, and social costs. The sub-categories of these costs are broken down and shown in Table 8.

Table 8 LCOE break down under social perspective

Primary category	Second category	Tertiary category
Plant-level cost	Capital cost	Development & management cost
		Turbine cost
		BOP cost
		Transportation & Installation cost
	O&M cost	Operation cost
		Maintenance cost
System integration cost (System cost)	Balancing cost	
	Grid cost	
	Profile cost	
Social cost	Compensation cost	

The main difference between bottom-fixed and floating offshore wind turbines was identified as the proportion of the BOP cost in the power plant level. The wind turbine cost is the largest for the bottom-fixed offshore wind turbines, while the floating offshore wind turbines require much BOP cost among all of costs. Since there are various types of floating substructures, the BOP cost and operation and maintenance cost can also be reduced by technical choice or development of advanced floating substructures that are most suitable for the conditions of the sea area. Floating offshore wind power is expected to be more competitive than bottom-fixed offshore wind power since it has lower ecological survey cost, transportation and installation cost, and maintenance cost.

At the system integration level, analyses of balancing cost and profile cost are still insufficient, and further studies are needed to assess this part. In the case of floating wind power, the competitiveness would be low in terms of grid cost due to the long connecting distance compared to a bottom-fixed one. However, it is predicted that the grid cost of floating wind power can be dramatically reduced through new technology in electricity generation, such as green hydrogen (Power to gas, P2G).

The social costs related to the environment of floating offshore wind power are relatively low because the bottom-fixed offshore wind power requires more compensation for ecosystem impacts, civil complaints, etc. Currently, floating offshore wind power's LCOE is more than double that of bottom-fixed offshore wind power, but through continuous technology development and cost reduction, floating offshore wind power is expected to have an LCOE that is approximately equivalent to that of bottom-fixed offshore wind power by 2035. By reducing LCOE through several methods related to development scale, wind turbine rating, BOP cost reduction, grid cost reduction, it is expected that floating offshore wind power can be a significant driver that can support energy transition in the future.

Conflict of Interest

No potential conflict of interest relevant to this article is reported.

Funding

This work was supported by Korean Institute of Energy Technology Evaluation and Planning (KETEP) and the Ministry of Trade, Industry & Energy (MOTIE) of Korea (No. 20203030020230).

References

Beiter, P., Musial, W., Kilcher, L., Maness, M., & Smith, A. (2017). An Assessment of the Economic Potential of Offshore Wind in the United States from 2015 to 2030 (Technical Report NREL/TP-6A20-67675). National Renewable Energy Laboratory. Retrieved from https://www.nrel.gov/docs/fy17osti/67675.pdf

Benveniste, G., Lerch, M., Prada, M., Kretschmer, M., Berqué, J., López, A., & Pérez, G. (2016). LIFES50+ D2.2: LCOE Tool Description, Technical and Environmental Impact Evaluation Procedure. European Union. Retrieved from https://ec.europa.eu/research/participants/documents/downloadPublic?documentIds=080166e5ad5562e8&appId=PPGMS

Bjerkseter, C., & Agotnes, A. (2013). Levelised Costs of Energy for Offshore floating Wind Turbine Concepts (Master's Thesis). Norwegian University of Life Sciences, Ås, Norway.

Bulder, B.H., Swamy, S.K., & Warnaar, P.M.J. (2021). Pathways to Potential Cost Reductions for Offshore Wind Energy (TNO report TNO 2020 R11926). Topsector Energie. Retrieved from https://www.topsectorenergie.nl/sites/default/files/uploads/Wind%20op%20Zee/Documenten/20210125_RAP_Pathways_to_potential_cost_reduction_offshore_wind_energy_F03.pdf

Choi, Y.S., Ju, H.C., & Won, D.K. (2019). 국내외 균등화발전비용(LCOE) 산출방법 사례 분석 [Case Analysis of Domestic and Foreign Levelized Cost of Electricity (LCOE) Calculation Method]. Korea Electric Power Corporation Planning Division. Retrieved from http://kepcocommunication.com/006/down/13.pdf

DNV GL. (2020). Floating Wind: The Power to Commercialize, Insights and Reasons for Confidence. Norway. Retrieved from https://www.energiesdelamer.eu/wp-content/uploads/2020/12/03_12-020_DNV_GL_Floating_Wind_The_Power_to_Commercialize_FINAL-compresse.pdf

Equinor. (n.d.). The Future of Offshore Qind is Afloat. Retrieved from https://www.equinor.com/en/what-we-do/floating-wind.html

Equinor. (2020). Equinor and ORE Catapult Collaborating to Share Hywind Scotland Operation Data. Retrieved from https://www.equinor.com/en/news/2019-11-28-hywind-scotland-data.html

European Wind Energy Association (EWEA). (2016). Balancing Responsibility and Costs of Wind Power Plants. Retrieved from https://windeurope.org/fileadmin/files/library/publications/position-papers/EWEA-position-paper-balancing-responsibility-and-costs.pdf

Benveniste, G., Lerch, M., Prada, M, D., Kretschmer, M., Berqué, J., López, A., & Pérez, G., (2016). LIFES50+ D2.2: LCOE Tool Description, Technical and Environmental Impact Evaluation Procedure (Ref. Ares(2016)5798062). IREC.

Harries, T., & Grace, A. (2015). Floating Wind: Buoyant Progress, Wind-Research Note. Bloomberg-New Energy Finance.

Hundleby, G., Freeman, K., Logan, A., & Frost, C. (2017). Floating Offshore: 55 Technology Innovations That Will Have Greater Impact on Reducing the Cost of Electricity from European Floating Offshore Wind Farms. KiC InnoEnergy and BVG Associates.

IRENA. (2019). Future of Wind: Deployment, Investment, Technology, Grid Integration and Socio-Economic Aspects (A Global Energy Transformation paper). Abu Dhabi: International Renewable Energy Agency. Retrieved from https://www.irena.org/-/media/Files/IRENA/Agency/Publication/2019/Oct/IRENA_Future_of_wind_2019.pdf

Jame, R., & Costa Ros, M. (2015). Floating Offshore Wind: Market and Technology Review. UK: Carbon trust. Retrieved from https://prod-drupal-files.storage.googleapis.com/documents/resource/public/Floating%20Offshore%20Wind%20Market%20Technology%20Review%20-%20REPORT.pdf

Jang, H.S. (2019). 편익이전 기법을 활용한 간헐성 전원의 계통비용 추정연구 [A Study on Estimating System Cost of Intermittent Power Supply Using Benefit Transfer Technique]. Korea Energy Economics Institute.

Jung, J, H., & Lee, S, J. (2020). 부유식 해상풍력 추진 현황 및 기술개요 [Enforcement Situation of Floating Offshore Wind Power and Technology Overview]. Korea Electric Power Corporation. Retrieved from http://kepcocommunication.com/003/down/11.pdf

Korea Energy Agency (2020). New & Renewable Energy White Paper (11-1410000-001321-11). Korea.

Korea Energy Agency Renewable Energy Center. (n.d.). 공급의무화(RPS) [Renewable Energy Portfolio Standard]. Retrieved from https://www.knrec. or.kr/business/rps_guide.aspx

Korea Energy Economics Institute. (2019). World Energy Market Insight, 19(12), 35–36. Retrieved from http://www.keei.re.kr/keei/download/WEMI1912.pdf

Korea Electric Power Corporation. (2018). 균등화 발전원가 해외사례 조사 및 시사점 분석 [A Study on Oversea Cases of Levelized Electricity Cost].

Korea Institute of Energy Research. (2015). Korea New and Renewable Energy Resource Atlas (2nd ed.). Retrieved from http://www.kier-solar.org/pdf/getFile.do?type=WIND

Lee, C.Y. (2017). 태양광 원가분석을 통한 균등화 비용 [International Comparative Analysis of Equalization Costs through Solar Power Cost Analysis]. Korea Energy Economics Institute.

Lee, G. T., & Kim, K. H., (2020). 재생에너지 공급확대를 위한 중장기 발전단가(LCOE) 전망 시스템 구축 및 운영 [Mid- to Long-Term Power Generation Unit Price Forecast for Expansion of Renewable Energy Supply, System Construction and Operation]. Korea Energy Economics Institute.

Lee, J., & Zhao, F. (2020). Global Offshore Wind Report 2020. Belgium: Global Wind Energy Council (GWEC). Retrieved from http://www.greenbr.org.cn/cmsfiles/1/editorfiles/files/6484a20699b340e8b16d2da0451de83a.pdf

Lerch, M. (2019). LIFES50+ D2.8: Expected LCOE for Floating Wind Turbines 10MW+ for 50m+ Water Depth (Ref. Ares (2019)2889481). IREC.

Ministry of Trade, Industry and Energy (2020). 주민과 함께하고, 수산업과 상생하는 해상풍력 발전 방안 [Plan for Offshore Wind Power Generation in Collaboration with Local Residents and the Fishing Industry]. Korea.

Myhr, A., Bjerkseter, C., Agotnes, A., & Nygaard, T.A. (2014). Levelised Cost of Energy for Offshore Floating Wind Turbines in a Life Cycle Perspective. Renewable Energy, 66, 714–728.

https://doi.org/10.1016/j.renene.2014.01.017

OECD Nuclear Energy Agency (OECD NEA). (2018). The Full Cost of Electricity Provision: Extended Summary (NEA No.7437). France. Retrieved from https://www.oecd-nea.org/upload/docs/application/pdf/2019-12/7437-full-costs-sum-2018.pdf

Offshore Renewable Energy Catapult (OREC). (2019). Guide to an Offshore Wind Farm: Updated and Extended. Retrieved from https://ore.catapult.org.uk/app/uploads/2019/04/BVGA-5238-Guide-r2.pdf

Offshore Renewable Energy Catapult (OREC). (2021). Floating Offshore Wind: Cost Reduction Pathways to Subsidy Free. Floating Offshore Wind Centre of Excellence. Retrieved from https://ore.catapult.org.uk/wp-content/uploads/2021/01/FOW-Cost-Reduction-Pathways-to-Subsidy -Free-report-.pdf

Ramboll Group. (n.d.). COREWIND Aims to Teduce Costs for Floating Offshore Wind Turbines. Retrieved from https://ramboll.com/projects/germany/corewind

Rhodri, J., & Marc, C.R. (2015). Floating Offshore Wind: Market and Technology Review. Prepared for the Scottish Government. Scotland: Carbon Trust. Retrieved fom https://prod-drupal-files.storage.googleapis.com/documents/resource/public/Floating%20Offshore%20Wind%20Market%20Technology%20Review%20-%20REPORT.pdf

Samadi, S. (2017). The Social Costs of Electricity Generation—Categorising Different Types of Costs and Evaluating Their Respective Relevance. Energies, 10(3), 356. https://doi.org/10.3390/en10030356

Scottish Government. (n.d.). National Development Programme: ERM Dolphyn Project. Environmental Resources Management Limited. Retrieved fom https://www.transformingplanning.scot/media/1500/083-environmental-resources-management-limited.pdf

Spearman, D.K., & Strivens, S. (2020). Floating Wind Joint Industry Project - Phase II Summary Report. UK: Carbon Trust. Retrieved from https://prod-drupal-files.storage.googleapis.com/documents/resource/public/FWJIP_Phase_2_Summary_Report_0.pdf

Song, S.O. (2012). ‘REC’를 알아야 RPS가 보인다 [You Need to Know ‘REC’ to See RPS]. Green Energy Times. Retrieved from http://www.gnetimes.co.kr/news/articleView.html?idxno=19386

Sun, M.Y. (2020). 해상풍력 산업과 O&M 기술을 통한 진출방안 [Offshore Wind Power Industry and Progression Plan through O&M Technology]. Proceedings of the 7th Online Market Conference on Offshore Plant Service Industry, Korea, 49–72.

Swedish Wind Energy Association. (2021). Proposal for Reduced Grid Connection Costs for Offshore Wind Power. Retrieved from https://swedishwindenergy.com/press-releases/proposal-for-reduced-grid-connection-costs-for-offshore-wind-power

Tyler, S., Philipp, B., & Patrick D. (2019). Cost of Wind Energy Review (NREL/TP –5000-7847). US: National Renewable Energy Laboratory. ttps://www.nrel.gov/docs/fy21osti/x78471.pdf

Valpy, B., Hundleby, G., Freeman, K., Roberts, A. & Logan, A. (2017). Future Renewable Energy Costs: Offshore Wind, 57 Technology Innovations That Will Have Greater Impact on Reducing the Cost of the Electricity from European Offshore Wind Farms. BVG Associates, Inno Energy. Retrieved from https://bvgassociates.com/wp-content/uploads/2017/11/InnoEnergy-Offshore-Wind-anticipated-innovations-impact-2017_A4.pdf

Weinstein, A. (2014). The WindFloat Journey: Changing the Paradigm Offshore Wind. In 23th WavEC Offshore Renewables Annual Seminar, United States – Portugal: Fostering Transatlantic Growth of Marine Renewables. Retrieved from https://www.wavec.org/contents/files/alla-weinstein-wavec-seminar-2014.pdf

WindEupore. (2017). Floating Offshore Wind Vision Statement. Retrieved from https://windeurope.org/wp-content/uploads/files/about-wind/reports/Floating-offshore-statement.pdf

WindEurope. (2018). Floating Offshore Wind Energy: A Policy Blueprint for Europe. Retrieved from https://windeurope.org/wp-content/uploads/files/policy/position-papers/Floating-offshore-wind-energy-a-policy-blueprint-for-Europe.pdf

Wiser, R., Karen, J., Seel, J., Baker, E., & Hand, M. (2016). Forecasting Wind Energy Costs & Cost Drivers: The View of the World’s Leading Experts (LBNL- 1005717). U.S. Department of Energy. Retrieved from https://www.ea-energianalyse.dk/wp-content/uploads/2020/02/1282_Forecasting-Wind-Energy-Costs-and-Cost-drivers.pdf

Wiser, R., Rand, J., Seel, J., Beiter, P., Baker, E., Lantz, E., & Giman, P. (2021). Expert Elicitation Survey Predicts 37% to 49% Declines in Wind Energy Costs by 2050. Nature Energy, 6, 555–565. https://doi.org/10.1038/s41560-021-00810-z

Yoo, J.M. (2018). RPS제도 + FIT제도 = 한국형 FIT제도 [RPS Policy + FIT Policy = Korean FIT Policy]. Retrieved from http://www.energycenter.co.kr/news/articleView.html?idxno=620

Author ORCIDs

Author name	ORCID
Pham, Thi Quynh Mai	0000-0003-1923-5873
Im, Sungwoo	0000-0001-6792-1953
Choung, Joonmo	0000-0003-1407-9031

Instructions for Authors

General information

To submit a manuscript to the Journal of Ocean Engineering and Technology (JOET), it is advised to first carefully read the aims and the scope section of this journal, as it provides information on the editorial policy and the category of papers it accepts. Unlike many regular journals, JOET usually has no lag in acceptance of a manuscript and its publication. Authors that find a match with the aims and the scope of JOET are encouraged to submit as we publish works from all over the world. JOET adheres completely to guidelines and best practices published by professional organizations, including Principles of Transparency and Best Practice in Scholarly Publishing (joint statement by COPE, DOAJ, WAME, and OASPA (http://doaj.org/bestpractice) if otherwise not described below. As such, JOET would like to keep the principles and policies of those professional organizations during editing and the publication process.

Research and publication ethics

Details on publication ethics are found in http://joet.org/authors/ethics.php. For the policies on research and publication ethics not stated in the Instructions, Guidelines on Good Publication (http://publicationethics.org/) can be applied.

Requirement for membership

One of the authors who submits a paper or papers should be member of the Korean Society of Ocean Engineers (KSOE), except a case that editorial board provides special admission of submission.

Publication type

Article types include scholarly monographs (original research articles), technical articles (technical reports and data), and review articles. The paper should have not been submitted to other academic journal. When part or whole of a manuscript was already published to conference papers, research reports, and dissertations, then the corresponding author should note it clearly in the manuscript.

Copyright

After published to JOET, the copyright of manuscripts should belong to KSOE. A transfer of copyright (publishing agreement) form can be found in submission website (http://www.joet.org).

Manuscript submission

Manuscript should be submitted through the on-line submission website (http://www.joet.org). The date that manuscript was received through on-line website is the official date of receipt. Other correspondences can be sent by an email to the Editor in Chief or secretariat. The manuscript must be accompanied by a signed statement that it has been neither published nor currently submitted for publication elsewhere. The manuscript should be written in English or Korean. Ensure that online submission are in a standard word processing format. Corresponding author must write the manuscript using the JOET template provided in Hangul or MS Word format. Ensure that graphics are high-resolution. Be sure all necessary files have been uploaded/ attached.

Authors' checklist

Please refer to “Authors' Checklist” for details.

Article structure

Manuscript must be edited in the following order: (1) Title, (2) Authors' names and affiliations, (3) Keywords, (4) Abstract, (5) Nomenclature (optional), (6) Introduction, (7) Main body (analyses, tests, results, and discussions), (8) Conclusions, (9) Conflict of interest (optional), (10) Funding (optional), (11) Acknowledgements (optional), (12) References, (13) Appendices (optional), (14) Author’s ORCIDs.

Abstract

A concise and factual abstract is required. The abstract should state briefly the background, purpose and methods of the research, the principal results and conclusions. An abstract should be written in around 300 words. References are not cited in abstract whenever possible. Also, non-standard or uncommon abbreviations should be avoided, but if essential they must be defined at their first mention in the abstract itself.

Keywords

Immediately after the abstract, provide a maximum of 5 or 6 keywords.

Unit

Use the international system units(SI). If other units are mentioned, please give their equivalent in SI.

Equations

All mathematical equations should be c1early printed/typed using well accepted explanation. Superscripts and subscripts should be typed clearly above or below the base line. Equation numbers should be given in Arabic numerals enclosed in parentheses on the right-hand margin.

Tables

Tables should be numbered consecutively with Arabic numerals. Each table should be fully titled. All tables should be referred to in the texts.

Figures

Figures should be numbered consecutively with Arabic numerals. Each figure should be fully titled. All figures should be referred to in the texts. All the illustrations should be of high quality meeting with the publishing requirement with legible symbols and legends.

Conflict of interest

It should be disclosed here according to the statement in the Research and publication ethics regardless of existence of conflict of interest. If the authors have nothing to disclose, please state: “No potential conflict of interest relevant to this article was reported.”

Funding

Funding to the research should be provided here. Providing a FundRef ID is recommended including the name of the funding agency, country and if available, the number of the grant provided by the funding agency. If the funding agency does not have a FundRef ID, please ask that agency to contact the FundRef registry (e-mail: fundref.registry@crossref.org). Additional detailed policy of FundRef description is available from http://www.crossref.org/fundref/. Example of a funding description is as follows:

The study is supported by the Inha University research fund (FundRef ID: 10.13039/501100002632), and the Korea Health Personnel Licensing Examination Institute research fund (FundRef ID: 10.13039/501100003647).

Acknowledgments

Any persons that contributed to the study or the manuscript, but not meeting the requirements of an authorship could be placed here. For mentioning any persons or any organizations in this section, there should be a written permission from them.

References in text

References in texts follow the APA style. Authors can also see how references appear in manuscript text through the ‘Template’.

Reference list

Reference list follows the APA style. Authors can see how references should be given in reference section through the ‘Template’.

Appendices

The appendix is an optional section that can contain details and data supplemental to the main text. If there is more than an appendix, they should be identified as A, B, C, etc. Formulae and equations in appendices should be given separate numbering: Eq. (A1), Eq. (A2), etc.; in a subsequent appendix, Eq. (B1) and so on. Similarly for tables and figures: Table A1; Fig. A1, etc.

ORCID (Open Researcher and Contributor ID)

All authors are recommended to provide an ORCID. To obtain an ORCID, authors should register in the ORCID web site: http://orcid.org. Registration is free to every researcher in the world. Example of ORCID description is as follows:

Joonmo Choung: https://orcid.org/0000-0003-1407-9031

Peer review and publication process

The peer review process can be broadly summarized into three groups: author process, review process, and publishing process for accepted submissions. General scheme is presented in Figure 1.

Check-in process for review

If the manuscript does not fit the aims and scope of the Journal or does not adhere to the Instructions to Authors, it may be rejected immediately after receipt and without a review. Before reviewing, all submitted manuscripts are inspected by Similarity Check powered by iThenticate (https://www.crossref.org/services/similarity-check/), a plagiarism-screening tool. If a too high degree of similarity score is found, the Editorial Board will do a more profound content screening.

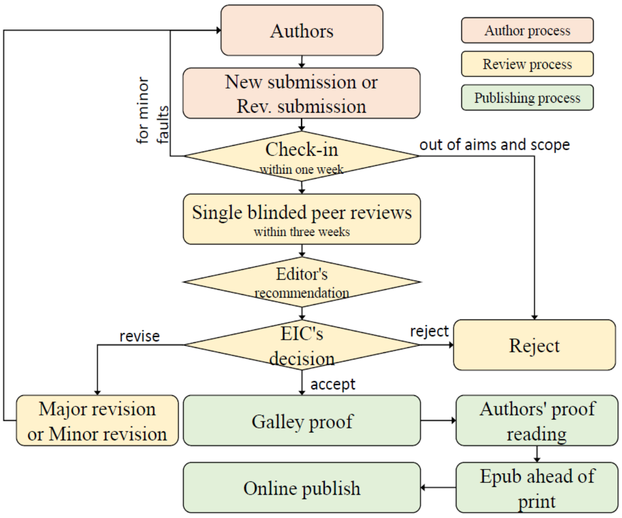

Figure 1 Flow chart of the peer review and publication process of JOET

The criterion for similarity rate for further screening is usually 15%; however, rather than the similarity rate, the Editorial Board focuses on cases where specific sentences or phrases are similar. The settings for Similarity Check screening are as follows: It excludes quotes, bibliography, small matches of 6 words, small sources of 1%, and the Methods section.

Number of reviewers

Reviewers will be selected from the list of reviewers. Manuscripts are then peer reviewed by at least 2 experts in the corresponding field, usually by 2.

Peer review process and the author response to the reviewer comments

JOET adopts single blind review, which means that the authors do not know the identity of the reviews. All papers, including those invited by the Editor, are subject to peer review.

The review period is 4 weeks. Usually the first decision is made within a week after completion of the review. The Editorial Board’s decision after the review will be one of followings: Accept, Minor revision, Major revision, or Rejection. The Editorial Board may request the authors to revise the manuscript according to the reviewers’ comments. If there are any requests for revision of the manuscript by the reviewers, the authors should do their best to revise the manuscript. If the reviewer's opinion is not acceptable or is believed to misinterpret the data, the author should reasonably indicate that. After revising the manuscript, the author should upload the revised files with a separate response sheet to each item of the reviewer's commentary. The author's revisions should be completed within 3 months after the request. If it is not received by the due date, the Editorial Board will notify the author. To extend the revision period beyond 3 months, the author should negotiate that with the Editorial Board. The manuscript review process can be provided for up two rounds. If the authors wish further review, the Editorial Board may consider it. The Editorial Board will make a final decision on the approval of the submitted manuscript for publication and can request any further corrections, revisions, and deletions of the article text if necessary. Statistical editing is also performed if the data requires professional statistical review by a statistician.

Processing after acceptance

If the manuscript is finally accepted, the galley proof will be sent to the corresponding author after professional manuscript editing and English proofreading. Proofreading should be performed for any misspellings or errors by the authors. Proofreading manuscript for publication is provided to the corresponding author, and the corresponding author must review the proofreading manuscript. Corresponding authors are responsible for the content of the proofreading manuscript and any errors. After final proofreading, the manuscript may appear at the journal homepage as an article in press with a unique DOI number for rapid communication. All published articles will be replaced by the replacement XML file and a final PDF.

Feedback after publication

If the authors or readers find any errors, or contents that should be revised, it can be requested from the Editorial Board. The Editorial Board may consider erratum, corrigendum or a retraction. If there are any revisions to the article, there will be a CrossMark description to announce the final draft. If there is a reader's opinion on the published article with the form of Letter to the editor, it will be forwarded to the authors. The authors can reply to the reader's letter. Letter to the editor and the author's reply may be also published.

How the journal handle complaints and appeals

The policy of JOET is primarily aimed at protecting the authors, reviewers, editors, and the publisher of the journal. If not described below, the process of handling complaints and appeals follows the guidelines of the Committee of Publication Ethics available from: https://publicationethics.org/appeals

- *Who complains or makes an appeal?*

Submitters, authors, reviewers, and readers may register complaints and appeals in a variety of cases as follows: falsification, fabrication, plagiarism, duplicate publication, authorship dispute, conflict of interest, ethical treatment of animals, informed consent, bias or unfair/inappropriate competitive acts, copyright, stolen data, defamation, and legal problem. If any individuals or institutions want to inform the cases, they can send a letter via the contact page on our website: https://www.joet.org/about/contact.php. For the complaints or appeals, concrete data with answers to all factual questions (who, when, where, what, how, why) should be provided.

- *Who is responsible to resolve and handle complaints and appeals?*

The Editorial Board or Editorial Office is responsible for them. A legal consultant or ethics editor may be able to help with the decision making.

- *What may be the consequence of remedy?*

It depends on the type or degree of misconduct. The consequence of resolution will follow the guidelines of the Committee of Publication Ethics (COPE).

Article processing charge

Payment due

Article processing charge (APC) covers the range of publishing services JOET provides. This includes provision of online tools for editors and authors, article production and hosting, and customer services. Upon editorial acceptance of an article for the regular review service and upon submission of an article for the fast review service, the corresponding author will be notified that payment is due.

APC

The APC up to 6 pages is ₩200,000 (or ＄200) and ₩550,000 (or ＄550) for the for the regular and fast review services, respectively. An extra APC of $50 per page is charged for papers longer than 6 pages, No taxes are included in this charge. For the fast review service, an advance fee of ₩250,000 ($250) should be paid on submission.

Payment methods

Credit card payment can be made online using a secure payment form as soon as the manuscript has been editorially accepted. We will we send a receipt by email once payment has been processed. Please note that payment by credit card carries a surcharge of 10% of the total APC.

Invoice payment is due within 7 days of the manuscript receiving editorial acceptance. Receipts are available on request.

JOET Templet 2021.02.04.

Journal of Ocean Engineering and Technology 00(0), 000-000, December, 2100
https://doi.org/10.26748/KSOE.2100.000

pISSN 1225-0767
eISSN 2287-6715

Original Research Article, Technical Article, Review Article, etc

Title of Article

Firstname Lastname[1], Firstname Lastname[2] and Firstname Lastname[3]

[1]*Professor, Department of OO, OO School, OO University, Busan, Korea*
[2]*Graduate Student, Department of OO, OO University, Seoul, Korea*
[3]*Senior Researcher, Department of OO, OO Engineering. Corp., Seoul, Korea*

KEY WORDS: Lumped mass line model, Explicit method, Steel lazy wave riser (provide a maximum of 5 or 6 keywords.*)*

ABSTRACT: *A concise and factual abstract is required. The abstract should state briefly the background, purpose and methods of the research, the principal results and conclusions. An abstract should be written in around 300 words. References are not cited in abstract whenever possible. Also, non-standard or uncommon abbreviations should be avoided, but if essential they must be defined at their first mention in the abstract itself.*

Nomenclature (Optional)

ITOC	Increment of total operating cost ($/yr)
LHV	Lower heating value (kJ/kg)
Pw	Power (kW)
T	Temperature (K)
V	Volume (m^3)
ρ	Density (kg/m^3)

1. Introduction

The introduction should briefly place the study in a broad context and highlight why it is important. It should define the purpose of the work and its significance. The current state of the research field should be reviewed carefully and key publications cited. Please highlight controversial and diverging hypotheses when necessary. Finally, briefly mention the main aim of the work and highlight the principal conclusions. As far as possible, please keep the introduction comprehensible to scientists outside your particular field of research.

2. General Information for Authors

2.1 Research and Publication Ethics

Authorship should be limited to those who have made a significant contribution to the conception, design, execution, or interpretation of the reported study. All those who have made significant contributions should be listed as co-authors. Where there are others who have participated in certain substantive aspects of the research project, they should be acknowledged or listed as contributors.

The corresponding author should ensure that all appropriate co-authors and no inappropriate co-authors are included on the paper, and that all co-authors have seen and approved the final version of the paper and have agreed to its submission for publication.

Details on publication ethics are found in the journal's website (http://joet.org/authors/ethics.php). For the policies on research and publication

Received 00 February 2100, revised 00 October 2100, accepted 00 October 2100

Corresponding author Firstname Lastname: +82-51-759-0656, e-mail@e-mail.com

It is a recommended paper from the proceedings of 2019 spring symposium of the Korea Marine Robot Technology (KMRTS).

ethics not stated in the Instructions, Guidelines on Good Publication (http://publicationethics.org/) can be applied.

2.2 Requirement for Membership

One of the authors who submits a paper or papers should be member of The Korea Society of Ocean Engineers (KSOE), except a case that editorial board provides special admission of submission.

2.3 Publication Type

Article types include scholarly monographs (original research articles), technical articles (technical reports and data), and review articles. The paper should have not been submitted to other academic journal. When part or whole of a manuscript was already published to conference papers, research reports, and dissertations, then the corresponding author should note it clearly in the manuscript.

Example: It is noted that this paper is revised edition based on proceedings of KAOST 2100 in Jeju.

2.4 Copyright

After published to JOET, the copyright of manuscripts should belong to KSOE. A transfer of copyright (publishing agreement) form can be found in submission website (http://www.joet.org).

2.5 Manuscript Submission

Manuscript should be submitted through the on-line submission website (http://www.joet.org). The date that manuscript was received through on-line website is the official date of receipt. Other correspondences can be sent by an email to the Editor in Chief or secretariat. The manuscript must be accompanied by a signed statement that it has been neither published nor currently submitted for publication elsewhere. The manuscript should be written in English or Korean. Ensure that online submission are in a standard word processing format. Corresponding author must write the manuscript using the JOET template provided in Hangul or MS Word format. Ensure that graphics are high-resolution. Be sure all necessary files have been uploaded/ attached.

2.5.1 Authoer’s checklist

Authoer’s checklist and Transfer of copyright can be found in submission hompage (http:/www.joet.org).

3. Manuscript

Manuscript must be edited in the following order: (1) Title, (2) Authors' names and affiliations, (3) Keywords, (4) Abstract, (5) Nomenclature (optional), (6) Introduction, (7) Main body (analyses, tests, results, and discussions), (8) Conclusions, (9) Conflict of interest (optional), (10) Funding (optional), (11) Acknowledgements (optional), (12) References, (13) Appendices (optional), (14) Author’s ORCIDs.

3.1 Unit

Use the international system units(SI). If other units are mentioned, please give their equivalent in SI.

3.2 Equations

All mathematical equations should be clearly printed/typed using well accepted explanation. Superscripts and subscripts should be typed clearly above or below the base line. Equation numbers should be given in Arabic numerals enclosed in parentheses on the right-hand margin. The parameters used in equation must be defined. They should be cited in the text as, for example, Eq. (1), or Eqs. (1)–(3).

$$G_{GEV}(x;\mu,\sigma,\xi)=\begin{cases}\exp[-(1+\xi(x-\mu)/\sigma)^{-1/\xi}] & \xi\neq 0\\ \exp[-\exp(-(x-\mu)/\sigma)] & \xi=0\end{cases} \tag{1}$$

in which μ, σ, and ξ represent the location (“Shift” in figures), scale, and shape parameters, respectively.

3.3 Tables

Tables should be numbered consecutively with Arabic numerals. Each table should be typed on a separate sheet of paper and be fully titled. All tables should be referred to in the texts.

Table 1 Tables should be placed in the main text near to the first time they are cited

Item	Buoyancy riser
Segment length1) (m)	370
Outer diameter (m)	1.137
Inner diameter (m)	0.406
Dry weight (kg/m)	697
Bending rigidity (N·m^2)	1.66E8
Axial stiffness (N)	7.098E9
Inner flow density (kg·m^3)	881
Seabed stiffness (N/m/m^2)	6,000

1)Tables may have a footer.

3.4 Figures

Figures should be numbered consecutively with Arabic numerals. Each figure should be fully titled. All the illustrations should be of high quality meeting with the publishing requirement with legible symbols and legends. All figures should be referred to in the texts. They should be referred to in the text as, for example, Fig. 1, or Figs. 1–3.

(a) Description of what is contained in the first panel

(b) Description of what is contained in the first panel

Fig. 1 Schemes follow the same formatting. If there are multiple panels, they should be listed as: (a) Description of what is contained in the first panel; (b) Description of what is contained in the second panel. Figures should be placed in the main text near to the first time they are cited

3.5 How to Describe the References in Main Texts

All references should be listed at the end of the manuscripts, arranged in order of Alphabet. References in texts follow the American Psychological Association (APA) style. The exemplary form of listed references is as follows:

Single author: (Kim, 1998) or Kim (1998)
Two authors: (Kim and Lee, 2000) or Kim and Lee (2000)
Three or more authors: (Kim et al., 1997) or Kim et al. (1997)
Two or more papers: (Lee, 1995a; Lee, 1995b; Ryu et al., 1998)
Year unknown: (Kim, n.d.) or Kim (n.d.)

4. Results

This section may be divided by subheadings. It should provide a concise and precise description of the experimental results, their interpretation as well as the experimental conclusions that can be drawn. Tables and figures are recommended to present the results more rapidly and easily. Do not duplicate the content of a table or a figure with in the Results section. Briefly describe the core results related to the conclusion in the text when data are provided in tables or in figures. Supplementary results can be placed in the Appendix.

5. Discussion

Authors should discuss the results and how they can be interpreted in perspective of previous studies and of the working hypotheses. The findings and their implications should be discussed in the broadest context possible. Future research directions may also be highlighted

6. Conclusions

This section can be added to the manuscript.

Conflict of Interest (Optional)

It should be disclosed here according to the statement in the Research and publication ethics regardless of existence of conflict of interest. If the authors have nothing to disclose, please state: “No potential conflict of interest relevant to this article was reported.”

Funding (Optional)

Please add: “This research was funded by Name of Funder, grant number XXX” and “The OOO was funded by XXX”. Check carefully that the details given are accurate and use the standard spelling of funding agency names at https://search.crossref.org/funding

Acknowledgments **(Optional)**

In this section you can acknowledge any support given which is not covered by the author contribution or funding sections. This may include administrative and technical support, or donations in kind (e.g., materials used for experiments). For mentioning any persons or any organizations in this section, there should be a written permission from them.

References

- Journal name should not be abbreviated.
- A private report with limited access or download availability can not be a reference.
- Include the digital object identifier DOI or URL for all references where available.
- Reference list follows the American Psychological Association (APA) style.

Referring to journal publications:

Author, A.A., Author, B.B., & Author, C.C. (Year). Title of Article. Journal Title, vol(no), pp–pp. https://doi.org/xx.xxxx/xxxxxx

Author, A.A., Author, B.B., Author, C.C. (accepted; in press). Title of Article. Title of Periodical. Retrieved from http://xx.xxx/x.pdf

Lee, T.K., Kim, T.W., Rim, C.W., & Kim, S.C. (2013). A Study on Calculation of Local Ice Pressures for ARAON Based on Data Measured at Arctic Sea. Journal of Ocean Engineering and Technology, 27(5), 88–92. https://doi.org/10.5574/KSOE.2013. 27.5.088

Lee, T.K., Kim, T.W., Rim, C.W., & Kim, S.C. (accepted; in press). A Study on Calculation of Local Ice Pressures for ARAON Based on Data Measured at Arctic Sea. Journal of Ocean Engineering and Technology, Retrieved from http://xxx.xxx/xxx.pdf

Referring to conference proceedings:

Author, A.A., Author, B.B., & Author, C.C. (Year). Title of Article. Proceeding Title, City, Country, pp–pp. https://doi.org/xx.xxxx

Aoki, S., Liu, H., & Sawaragi, T. (1994). Wave Transformation and Wave Forces on Submerged Vertical Membrane. Proceedings of International Symposium Waves - Physical and Numerical Modeling, Vancouver, Canada, 1287–1296.

Tsukamoto, C.L., Lee, W., Yuh, J., Choi, S.K., & Lorentz, J. (1997). Comparison Study on Advanced Thruster Control of Underwater Robots. Proceedings of International Conference on Robotics and Automation, 1845–1850. https://doi.org/110.1109/ROBOT.1997.619056

Referring to books:

Author, A.A. (Year). Title of Book (xx ed.). Location: Publisher.

Strunk, W., & White, E.B. (2000). The Elements of Style (4th ed.). NewYork, USA: Longman.

Schlichting, H. (1968). Boundary Layer Theory (6th ed.). New York, USA: McGraw-Hill.

Referring to theses or dissertations:

Author, A.A. (Year). Title of Doctoral Dissertation or Master’s thesis (Doctoral Dissertation or Master’s thesis). Name of Institution, City, Country.

Giovanni, I. (1998). Modelling and Identification of Underwater Robotic Systems (Ph.D. Thesis). University of Genova, Genova, Italy.

Referring to technical reports, rules, or guidelines:

Author, A.A. (Year). Title of report (Reprot No. xxx), Location: Publisher.

Likhomanov, V. (2010). Full-Scale Ice Trials of the Korean Research Icebreaker ARAON. Daejeon, Korea: Arctic and Antarctic Research Institute (AARI).

ABS. (2011). Guide for Ice Loads Monitoring Systems. Houston, USA: American Bureau of Shipping.

Lloyd's Register. (2011). FDA ICE Fatigue Induced by Ice Loading, ShipRight Design and construction - Fatigue Design Assesment. London, United Kingdom: Lloyd's Register.

Larson, M., & Kraus, N.C. (1989). SBEACH: Numerical Model for Simulating Storm-Induced Beach Change - Report 1 Empirical Foundation and Model Development (Technicla Report CERC-89-9). Coastal Engineering research center Vicksburg Ms.

Referring to patents:

Righsholder, A.A. (Year). Title of Patent. Patent number, Patent office with country.

Dawoo Shipbulding & Maringe Engineering (DSME). (2013). Distance Length Standardization Method for Preventing Interference at the time of Uploading Cell Guide of Container Ship. Unexamined Patent Publication 1020130044635, Korean Interllectual Property Office.

Referring to websites:

Righsholder, A.A. (Year). Title of webpage. Retrieved Month Year from http://xxxx

International Association of Classification Societies (IACS). (2010a). Common Structural Rules for Bulk Carriers. Retrieved July 2010 from http://www.iacs-data.org.uk

US Congressional Hearing. (2009). Strategic Importance of the Arctic in Us Policy. Retrieved June 2019 from https://fas.org/irp/arctic.pdf

Dawoo Shipbulding & Maringe Engineering (DSME). (2013). Distance Length Standardization Method for Preventing Interference at the time of Uploading Cell Guide of Container Ship. Retrieved June 2019 from https://patentimages.storage./pdfs/792.pdf

Referring to software:

Righsholder, A.A. (Year). Title of Software. Downloaded Month Year from http://xxxx

Standard

Organization. (Year). Title of the standard in italics [Translated title – if applicable] (Standard No.). Retrieved from https://...

International Organization for Standardization. (2005). Industrial sewing machines: Safety requirements for sewing machines, units and systems (ISO Standard No. 10821). Retrieved from http://www.standard.no/no/Nettbutikk/produktkatalogen/Produktpresentasjon/?ProductID=113554

Translation

Author, A. A. (Year of publication). Title of work: Capital letter also for subtitle (T. Translator, Trans.). Location: Publisher. (Original work published YEAR). DOI

Ura, T., & Takakawa, S. (2015). All about Submersibles (W.S. Kim, D.S. Kim, Y.H. Choi,.C.H. Park, J.S. Park, P.M. Lee, H.S. Jung, Trans.). Korea: CIR. (Original Work Published in 1994, Japan: Seizan-Shoten Publiching)

in text: (Ura and Takakawa, 1994/2015)

Referring to some exceptional cases:

- when authors are missing, institution can replace authors

National Oceanic and Atmospheric Administration (NOAA). (2015). Deep-ocean Assessment and Reporting of Tsunamis (DART). Retrieved December 2019 from https://nctr.pmel.noaa.gov/Dart/

- when dates or years are missing, it is replaced with "n.d."

National Oceanic and Atmospheric Administration (NOAA). (n.d.). Deep-ocean Assessment and Reporting of Tsunamis (DART).

- when more then seven authors, first 6 authors ... last author.

Yeu, T., Choi, H.T., Lee, Y., Chae, J., Lee, Y., Kim, S.S., ... Lee, T.H. (2019). Development of Robot Platform for Autonomous Underwater Intervention. Journal of Ocean Engineering and Technology, 33(2), 168–177. https://doi.org/10.26748/KSOE. 2019.021

Appendix (Optional)

The appendix is an optional section that can contain details and data supplemental to the main text. For example, explanations of experimental details that would disrupt the flow of the main text, but nonetheless remain crucial to understanding and reproducing the research shown; figures of replicates for experiments of which representative data is shown in the main text can be added here if brief, or as Supplementary data. Mathematical proofs of results not central to the paper can be added as an appendix.

All appendix sections must be cited in the main text. In the appendixes, Figures, Tables, etc. should be labeled starting with ‘A’, e.g., Fig. A1, Fig. A2, etc.

Examples:
https://doi.org/10.26748/KSOE.2019.022
https://doi.org/10.26748/KSOE.2018.4.32.2.095

Author ORCIDs

All authors are recommended to provide an ORCID. To obtain an ORCID, authors should register in the ORCID web site: http://orcid.org. Registration is free to every researcher in the world. Example of ORCID description is as follows:

Author name	**ORCID**
So, Hee	0000-0000-000-00X
Park, Hye-Il	0000-0000-000-00X
Yoo, All	0000-0000-000-00X
Jung, Jewerly	0000-0000-000-00X

Authors' Checklist

The following list will be useful during the final checking of a manuscript prior to sending it to the journal for review. Please submit this checklist to the KSOE when you submit your article.

< Checklist for manuscript preparation >

☐ I checked my manuscript has been 'spell-checked' and 'grammar-checked'.
☐ One author has been designated as the corresponding author with contact details such as
  - E-mail address
  - Phone numbers
☐ I checked abstract 1) stated briefly the purpose of the research, the principal results and major conclusions, 2) was written in around 300 words, and 3) did not contain references (but if essential, then cite the author(s) and year(s)).
☐ I provided 5 or 6 keywords.
☐ I checked color figures were clearly marked as being intended for color reproduction on the Web and in print, or to be reproduced in color on the Web and in black-and-white in print.
☐ I checked all table and figure numbered consecutively in accordance with their appearance in the text.
☐ I checked abbreviations were defined at their first mention there and used with consistency throughout the article.
☐ I checked all references mentioned in the Reference list were cited in the text, and vice versa according to the APA style.
☐ I checked I used the international system units (SI) or SI-equivalent engineering units.

< Authorship checklist >

JOET considers individuals who meet all of the following criteria to be authors:

☐ Made a significant intellectual contribution to the theoretical development, system or experimental design, prototype development, and/or the analysis and interpretation of data associated with the work contained in the article.
☐ Contributed to drafting the article or reviewing and/or revising it for intellectual content.
☐ Approved the final version of the article as accepted for publication, including references.

< Checklist for publication ethics >

☐ I checked the work described has not been published previously (except in the form of an abstract or as a part of a published lecture or academic thesis).
☐ I checked when the work described has been published previously in other proceedings without copyright, it has clearly noted in the text.
☐ I checked permission has been obtained for use of copyrighted material from other sources including the Web.
☐ I have processed Plasgiarism Prevention Check through reliable web sites such as www.kci.go.kr, http://www.ithenticate.com/, or https://www.copykiller.org/ for my submission.
☐ I agree that final decision for my final manuscript can be changed according to results of Plasgiarism Prevention Check by JOET administrator.
☐ I checked one author at least is member of the Korean Society of Ocean Engineers.
☐ I agreed all policies related to 'Research and Publication Ethics'
☐ I agreed to transfer copyright to the publisher as part of a journal publishing agreement and this article will not be published elsewhere including electronically in the same form, in English or in any other language, without the written consent of the copyright-holder.
☐ I made a payment for reviewing of the manuscript, and I will make a payment for publication on acceptance of the article.
☐ I have read and agree to the terms of Authors' Checklist.

Title of article :
Date of submission : DD/MM/YYYY
Corresponding author : signature
Email address :

※ E-mail this with your signature to ksoehj@ksoe.or.kr

Publishing Agreement

ARTICLE DETAILS

Title of article :
Corresponding author :
E-mail address :
DOI : https://doi.org/10.26748/KSOE.2XXX.XXX

YOUR STATUS

I am one author signing on behalf of all co-authors of the manuscript.

ASSIGNMENT OF COPYRIGHT

I hereby assign to the Korean Society of Ocean Engineers, the copyright in the manuscript identified above and any tables, illustrations or other material submitted for publication as part of the manuscript (the “Article”). This assignment of rights means that I have granted to Korean Society of Ocean Engineers the exclusive right to publish and reproduce the Article, or any part of the Article, in print, electronic and all other media (whether now known or later developed), in any form, in all languages, throughout the world, for the full term of copyright, and the right to license others to do the same, effective when the Article is accepted for publication. This includes the right to enforce the rights granted hereunder against third parties.

SCHOLARLY COMMUNICATION RIGHTS

I understand that no rights in patents, trademarks or other intellectual property rights are transferred to the Journal owner. As the author of the Article, I understand that I shall have: (i) the same rights to reuse the Article as those allowed to third party users of the Article under the CC-BY-NC License, as well as (ii) the right to use the Article in a subsequent compilation of my works or to extend the Article to book length form, to include the Article in a thesis or dissertation, or otherwise to use or re-use portions or excerpts in other works, for both commercial and non-commercial purposes. Except for such uses, I understand that the assignment of copyright to the Journal owner gives the Journal owner the exclusive right to make or sub-license commercial use.

USER RIGHTS

The publisher will apply the Creative Commons Attribution-Noncommercial Works 4.0 International License (CC-BY-NC) to the Article where it publishes the Article in the journal on its online platforms on an Open Access basis.

The CC-BY-NC license allows users to copy and distribute the Article, provided this is not done for commercial purposes and further does not permit distribution of the Article if it is changed or edited in any way, and provided the user gives appropriate credit (with a link to the formal publication through the relevant DOI), provides a link to the license, and that the licensor is not represented as endorsing the use made of the work. The full details of the license are available at http://creativecommons.org/licenses/by-nc/4.0/legalcode.

REVERSION OF RIGHTS

Articles may sometimes be accepted for publication but later rejected in the publication process, even in some cases after public posting in “Articles in Press” form, in which case all rights will revert to the author.

☑ I have read and agree to the terms of the Journal Publishing Agreement.

Corresponding author:

name signature

※ E-mail this with your signature to ksoehj@ksoe.or.kr (Papers will not be published unless this form is signed and returned)

Research and Publication Ethics

Journal of Ocean Engineering and Technology (JOET) adheres to the guidelines published by professional organizations, including Committee on Publication Ethics (COPE; https://publicationethics.org/)

1. Authorship

JOET considers individuals who meet all of the following criteria to be authors:

1) Made a significant intellectual contribution to the theoretical development, system or experimental design, prototype development, and/or the analysis and interpretation of data associated with the work contained in the article.
2) Contributed to drafting the article or reviewing and/or revising it for intellectual content.
3) Approved the final version of the article as accepted for publication, including references.

Contributors who do not meet all of the above criteria may be included in the Acknowledgment section of the article. Omitting an author who contributed to your article or including a person who did not fulfill all of the above requirements is considered a breach of publishing ethics.

Correction of authorship after publication: JOET does not correct authorship after publication unless a mistake has been made by the editorial staff.

2. Originality and Duplicate Publication

All submitted manuscripts should be original and should not be in consideration by other scientific journals for publication. Any part of the accepted manuscript should not be duplicated in any other scientific journal without permission of the Editorial Board, although the figures and tables can be used freely if the original source is verified according to the Creative Commons Attribution License (CC BY-NC). It is mandatory for all authors to resolve any copyright issues when citing a figure or table from other journal that is not open access.

3. Conflict-of-Interest Statement

Conflict of interest exists when an author or the author's institution, reviewer, or editor has financial or personal relationships that inappropriately influence or bias his or her actions. Such relationships are also known as dual commitments, competing interests, or competing loyalties. These relationships vary from being negligible to having a great potential for influencing judgment. Not all relationships represent true conflict of interest. On the other hand, the potential for conflict of interest can exist regardless of whether an individual believes that the relationship affects his or her scientific judgment. Financial relationships such as employment, consultancies, stock ownership, honoraria, and paid expert testimony are the most easily identifiable conflicts of interest and the most likely to undermine the credibility of the journal, the authors, or of the science itself. Conflicts can occur for other reasons as well, such as personal relationships, academic competition, and intellectual passion. If there are any conflicts of interest, authors should disclose them in the manuscript. The conflicts of interest may occur during the research process as well; however, it is important to provide disclosure. If there is a disclosure, editors, reviewers, and reader can approach the manuscript after understanding the situation and the background of the completed research.

4. Management Procedures for the Research and Publication Misconduct

When JOET faces suspected cases of research and publication misconduct such as a redundant (duplicate) publication, plagiarism, fabricated data, changes in authorship, undisclosed conflicts of interest, an ethical problem discovered with the submitted manuscript, a reviewer who has appropriated an author's idea or data, complaints against editors, and other issues, the resolving process will follow the flowchart provided by the Committee on Publication Ethics (http://publicationethics.org/resources/flowcharts). The Editorial Board of JOET will discuss the suspected cases and reach a decision. JOET will not hesitate to publish errata, corrigenda, clarifications, retractions, and apologies when needed.

5. Editorial Responsibilities

The Editorial Board will continuously work to monitor and safeguard publication ethics: guidelines for retracting articles; maintenance of the integrity of the academic record; preclusion of business needs from compromising intellectual and ethical standards; publishing corrections, clarifications, retractions, and apologies when needed; and excluding plagiarism and fraudulent data. The editors maintain the following responsibilities: responsibility and authority to reject and accept articles; avoiding any conflict of interest with respect to articles they reject or accept; promoting publication of corrections or retractions when errors are found; and preservation of the anonymity of reviewers.

6. Hazards and human or animal subjects

If the work involves chemicals, procedures or equipment that have any unusual hazards inherent in their use, the author must clearly identify these in the manuscript. If the work involves the use of animal or human subjects, the author should ensure that the manuscript contains a statement that all procedures were performed in compliance with relevant laws and institutional guidelines and that the appropriate institutional committee(s) has approved them. Authors should include a statement in the manuscript that informed consent was obtained for experimentation with human subjects. The privacy rights of human subjects must always be observed.

Ensure correct use of the terms sex (when reporting biological factors) and gender (identity, psychosocial or cultural factors), and, unless inappropriate, report the sex and/or gender of study participants, the sex of animals or cells, and describe the methods used to determine sex and gender. If the study was done involving an exclusive population, for example in only one sex, authors should justify why, except in obvious cases. Authors should define how they determined race or ethnicity and justify their relevance.

7. Secondary publication

It is possible to republish manuscripts if the manuscripts satisfy the conditions of secondary publication. These are:

- The authors have received approval from the Editorial Board of both journals (the editor concerned with the secondary publication must have access to the primary version).
- The priority for the primary publication is respected by a publication interval negotiated by editors of both journals and the authors.
- The paper for secondary publication is intended for a different group of readers
- The secondary version faithfully reflects the data and interpretations of the primary version.
- The secondary version informs readers, peers, and documenting agencies that the paper has been published in whole or in part elsewhere, for example, with a note that might read, "This article is based on a study first reported in the [journal title, with full reference]"
- The title of the secondary publication should indicate that it is a secondary publication (complete or abridged republication or translation) of a primary publication.

8. Complaints and Appeals

The process of handling complaints and appeals follows the guidelines of the COPE available from: https://publicationethics. org/appeals

9. Post-publication discussions and corrections

The post-publication discussion is available through letter to editor. If any readers have a concern on any articles published, they can submit letter to editor on the articles. If there found any errors or mistakes in the article, it can be corrected through errata, corrigenda, or retraction.

KSOE

The Korean Society of Ocean Engineers